

Sister Rod Nondestructive Examination Final Report

Spent Fuel and Waste Disposition

***Prepared for
US Department of Energy
Spent Fuel and Waste Science and
Technology***

***Oak Ridge National Laboratory:
Rose Montgomery, Bruce Bevard,
Robert N. Morris, James Goddard, Jr.,
Susan K. Smith, Jianwei Hu***

***Electric Power Research Institute:
John Beale and Byungsik Yoon***

***December 21, 2018
SFWD-SFWST-2017-000003 Rev. 1
(M2SF-17OR010201021)
ORNL/SPR-2017/484 Rev. 1
(ORNL/SPR-2018/801)***

DISCLAIMER

This information was prepared as an account of work sponsored by an agency of the U.S. Government. Neither the U.S. Government nor any agency thereof, nor any of their employees, makes any warranty, expressed or implied, or assumes any legal liability or responsibility for the accuracy, completeness, or usefulness, of any information, apparatus, product, or process disclosed, or represents that its use would not infringe privately owned rights. References herein to any specific commercial product, process, or service by trade name, trade mark, manufacturer, or otherwise, does not necessarily constitute or imply its endorsement, recommendation, or favoring by the U.S. Government or any agency thereof. The views and opinions of authors expressed herein do not necessarily state or reflect those of the U.S. Government or any agency thereof.

SUMMARY

This report documents work performed under the Spent Fuel and Waste Disposition for the US Department of Energy (DOE) Office of Nuclear Energy (NE) Spent Fuel and Waste Science and Technology program. This work was performed to fulfill the Level 2 Milestone M2SF-17OR010201021, “Documentation of Non-destructive Tests on Sister Pins,” within work package SF-17OR01020102.

The High Burnup Spent Fuel Data Project, sponsored by DOE-NE, is focused on understanding the effects of long-term storage and transportation on high burnup (HBU) (>45 gigawatt days per metric ton uranium) light water reactor fuel. The goals of the project are to “provide confirmatory data for model validation and potential improvement, provide input to future spent nuclear fuel (SNF) dry storage cask design, support license renewals and new licenses for Independent Spent Fuel Storage Installations (ISFSIs), and support transportation licensing for high burnup SNF” [1]. In support of project goals, 25 sister rods were removed from fuel assemblies at the North Anna Power Station. Nine rods were removed from the project assemblies, and 16 rods were removed from similar HBU assemblies. The 25 sister rods were shipped to Oak Ridge National Laboratory (ORNL) Irradiated Fuels Examination Laboratory (IFEL) in early 2016 for detailed nondestructive examination (NDE) and destructive examination (DE). The detailed examinations will provide essential information on the physical state of the HBU rods and the fuel contained in the rods prior to loading, drying, and long-term dry storage [1]. Similar tests will be performed at the end of the long-term storage period to identify any changes in the fuel rods’ properties during the dry storage period [1].

This report documents the conclusion of the Phase I testing of the sister rods and provides a report of the NDE tasks performed and the data collected, as guided by the sister rod test plan [2]. The NDE scope and general findings are summarized in Table S-1. In addition to the sister rod program’s NDE scope, two additional radiation scanning projects performed for the National Nuclear Security Administration (NNSA) and completed using the sister rods are also summarized. Also, a specialized eddy current examination for measurement of cladding hydrogen content (F-SECT) was performed on 19 of the 25 sister rods by the Electric Power Research Institute (EPRI) and a summary of that exam is provided. Destructive testing of the sister rods is expected to begin in April 2018.

Visual examinations of all 25 sister rods were completed in May 2017. The images are available in three user-viewable formats:

- (1) 784 individual, unprocessed photos per sister rod, for a total of 19,600 photos (the source data for the other two image sets),
- (2) 25 compiled user-interactive Shockwave Flash (SWF) collage files (one per sister rod), each containing 784 individual photos per sister rod, with each labeled for searching and observation, and
- (3) 96 flattened 40 mm axial segment collages per sister rod (2,400 total images) obtained by filtering and stitching together the individual azimuthal photos.

Waterside surface features relevant to the specification of future NDE and DE were identified via visual examination and tabulated. No weld failures, obvious cladding breaches, or other significant defects were observed. Rod identification and bar codes are visible on all rods except for F35P17 and F35K13 since bar codes were not used when these two rods were fabricated. A typical striated surface texture appearance which is visible in the images as alternating axial light and dark bands is present to varying degrees in all cases, with the more heavily oxidized rods having the appearance of deeper striations. The visual examination indicated that shallow grid-to-rod fretting (GTRF) marks are common, and a few rods have deep GTRF marks. Several rods appear to have patches of Chalk River Unidentified Deposits (CRUD) and/or spalling oxide. Peeling oxide was identified on M5 and ZIRLO sister rods. Rod insertion (pre-irradiation) and rod removal from the parent fuel assembly produced long axial scratches on most

rods. Interactions with grid springs and dimples may have scraped off CRUD or oxides along the length of the rods during assembly removal at the orthogonal grid spring locations.

Three sets of integrated radiation measurements were completed, including (1) one-dimensional scans using the Advanced Diagnostics and Evaluation Platform (ADEPT) sodium iodide (NaI) detector, (2) high resolution gamma spectroscopy using a high-purity germanium (HPGe) detector, and (3) gamma and neutron measurements using a fission/ionization chamber-based fork detector. The one-dimensional gamma scans of all 25 sister rods performed specifically for the sister rod project were completed using ADEPT in 2 energy ranges: 400 to 800 keV for examination of the fuel stack, and 1,100 to 1,600 keV for examination of the structural components. The two energy ranges were collected simultaneously. Data were collected in 1 mm increments along the axis of the rod and were indexed to the bottom of the rod. The scan signal exhibited the expected behavior without any sign of fission product accumulation or migration. The axial profile of the rods was as expected, and depressions in burnup were easily observed at the spacer grid locations. Pellet-pellet interface locations were also observable, so an estimate of the number of pellets in each rod could be made. The spring in the plenum region was visible, so an estimate of the length of the plenum region was also made. Some small fuel stack gaps were observed via the gamma scanning. The largest was estimated as 5 mm on sister rod 6U3P16. The HPGe and fork detector measurements were performed for the DOE NNSA Office of Nonproliferation and Arms Control (NPAC) and are summarized in this report for completeness. There is very good agreement in the general trends and locations of grid burnup depressions. Differences up to 7% were observed between the fork gamma counts and the HPGe total gamma counts near the rod bottom, likely due to the fact that a collimator is not used in the fork measurement. There is good agreement among all three detectors in the higher burnup regions of the rod. Radiochemical assay of selected rod locations will provide additional definitive (within measurement uncertainty) burnup measurements.

The overall length of each sister rod was measured multiple times and was within the expected range, with the longest rod measured at 3,894 mm and the shortest rod measured at 3,881 mm in length.

Profilometry measurements were taken using two pairs of linear variable differential transformers (LVDTs) to measure the fuel rod diameter as a function of axial location. The two sets of measurements are 90° apart and can provide information on the extent to which the rod is out of round (*ovality*). Overall, within the accuracy of the device and given the actual surface condition of the rods, no significant ovality (>0.04 mm) was noted in the rods. In general, the expected diametrical trends were observed. Some rods had very thick oxide with large spalled areas (see Section 3.1). Rods with the thickest oxide layers appear to have some locally erratic diameter measurements. In particular, assemblies 3A1 and F35 show the expected increasing diameter from the bottom to the top of the rod (referenced to the true bottom for the F35 rods), but there is a large amount of point-to-point variation in the higher rod elevations due to the uneven spalling CRUD/oxide layer. A large (~¾ pellet length) reduced diameter (~0.5 mm) region was noted in the profilometry scan for rod 6U3P16 that is associated with the ~5 mm pellet-pellet gap identified during gamma scanning. Bambooning, which is a small diameter variation with a period of about 10 mm (the pellet length), was observed in all rods.

All sister rods were extensively photographed during the visual examination. The visuals camera was also used to photograph the profilometry calibration rod, and the information obtained was used to resolve boundary pixel criteria and to scale the pixel count in each sister rod visual to a rod diameter. The diameter was measured in 40 mm increments along the length of the rod at 0-, 45-, 90-, 135-, 180-, 225-, 270-, and 315-degree rotations. The diameter measurements based on the visuals were compared with the LVDT measurements and the features identified by gamma scan. Although these measurements are not considered to be as accurate as the LVDT measurements in total, they are useful in verifying trends, measuring the ends of the rods that cannot be measured with the LVDTs, and for additional observations around the circumference of the rod. Overall, this method gives reasonable agreement with the LVDT data, and the overall accuracy appears to be better than 0.05 mm. Optimization of the optical path and

camera optics, along with a fixed reference point for picture-by-picture calibration, could lead to a non-contact fast measurement system.

Two eddy current examinations were completed: (1) a campaign using traditional eddy current methods to measure oxide/CRUD thickness and remaining cladding thickness and to identify flaws, and (2) an EPRI campaign using their F-SECT technique to measure the hydrogen content of the cladding. The traditional eddy current measurements were completed in November 2017 and the F-SECT measurements were completed late in July 2017. The EPRI F-SECT measurements indicated an alloy-average peak lift-off of ~130, 105, 45, and 17 μm of lift-off on the Zircaloy-4 (Zirc-4), low tin Zirc-4 (LT Zirc-4), ZIRLO and M5-clad sister rods, respectively, while the traditional eddy current examinations performed indicated an alloy-average maximum lift-off of 146, 151, 48, and 19 μm on the Zirc-4, LT Zirc-4, ZIRLO and M5-clad rods, respectively. The differences in results obtained using the two different techniques are likely related to the fact that the F-SECT technique measured only selected locations, while the traditional eddy current measurements were more exhaustive. Significant wall thinning (17 – 22%) due to uniform oxidation was observed in the Zirc-4 and LT Zirc-4 rods in the higher burnup regions of the rod, and the minimum remaining cladding wall thickness was measured as ~0.462 mm on these rods. The EPRI F-SECT technique estimated a maximum hydrogen content of just under 1,000 wppm at an elevation of ~3,000 mm on a Zirc-4 sister rod. The elevation of the maximum hydrogen is consistent with the elevation of the peak lift-off measured using traditional eddy current methods.

A comparison of previously-reported EPRI poolside measurements of the two F35 rods in 2002 with the traditional eddy current lift-off measured in hot cell yields an average difference of 15 – 25%. As circumferential variation in the oxide thickness is expected and these two very HBU Zirc-4-clad rods have a very large amount of oxide spalling from their four cycles in reactor, a conclusion about the veracity of either the poolside EPRI or the ORNL traditional eddy current data cannot be drawn. The metallography samples that will be examined during the destructive examinations of the sister rods are expected to provide a definitive oxide thickness measurement for each sister rod. Therefore, while the NDE lift-off data appear to be valid for use in the primary purpose of guiding the DE specimen selection process, it should not be cited where a precision measurement of the total oxide thickness is required.

No deep defects that would indicate through-wall penetration were noted during the encircling coil scans. Several defect scan indications were characteristic of pellet-pellet gaps (sharp rod outer diameter [OD] reductions) or large GTRF marks (local indication of cladding cross-sectional volume reduction) and tended to confirm the visual, gamma scanning, and profilometry findings.

The surface temperature of several rods was measured at the axial mid-plane over several days. The maximum temperature measured, for sister rod 5K7P02, was 31.2 °C in the hot cell storage array.

Table S-1. NDE scope and summary of findings.

NDE	Summary of findings
NDE.01: Visuals of the complete exterior surface of each rod with a digitally created user-viewable montage of the surface, and the location and appearance of any physical abnormalities (e.g., chemical attack, blisters, cracks, heavy or uneven oxide layers, weld failures, or clad distortions)	No apparent cladding breach. Several rods appear to have patches of CRUD and/or spalling oxide. Peeling oxide was identified on M5 and ZIRLO sister rods. Pellet-pellet gaps (confirmed by gamma scan) are visible as dark bands on the surface of rods 3D8E14, 6U3P16, and F35P17. GTRF marks are visible on almost every sister rod. The images are only available in digital format.
NDE.02: Gamma scanning to nondestructively: a. obtain relative axial burnup profiles b. identify any gross migration of fission products or large pellet cracks c. identify any pellet stack gaps d. measure the pellet stack height e. identify the location and magnitude of any burnup depressions due to grid spacers	The scan signals exhibited the expected behavior without any sign of fission product accumulation or migration. The axial profile of the rods was as expected, and depressions in burnup were easily observed at the spacer grid locations. Pellet-pellet interface locations were also observable, so an estimate of the number of pellets in each rod could be made. The spring in the plenum region was visible, so an estimate of the length of the plenum region was also made. Three relatively large fuel stack gaps (>3 mm) were observed on rods 6U3P16, 3D8E14, and F35P17 and can also be observed visually. The measured pellet stack length varied from 3,674 to 3,699 mm.
NDE.03: Fuel rod overall length measurements	The overall rod length varied from 3,881 to 3,894 mm.
NDE.04: Eddy current scans to obtain information on clad mechanical macroscopic defects and estimate oxide/CRUD waterside thickness	Significant wall thinning (17 – 22%) due to uniform oxidation was observed in the Zirc-4 and LT Zirc-4 rods in the higher burnup regions of the rod, and the minimum remaining cladding wall thickness was measured as ~0.462 mm on these rods. The largest cladding defect noted was a 7% reduction in cladding total cross-sectional volume related to an identified pellet-pellet gap on rod F35P17, detected with eddy current as a cladding OD reduction (indicated as a 35% through wall flaw). Several 1 – 3% cladding total cross-sectional volume reductions were indicated at observed GTRF marks on other rods. The maximum rod average measured lift-off for M5-clad, ZIRLO-clad, and Zirc-4/LT Zirc-4-clad sister rods was 27, 69, and 164 μm , respectively.
NDE.05: Profilometry measurements providing the rod OD as a function of axial location	The maximum OD measured for M5-clad, ZIRLO-clad, and Zirc-4/LT Zirc-4-clad sister rods was 9.52, 9.55, and 9.63 mm, respectively.
NDE.06: Rod surface temperature measurements	The maximum waterside surface temperature measured on the sister rods in the hot cell (in storage and on the ADEPT) was 31.2 °C.

ACKNOWLEDGMENTS

Many thanks to our US Department of Energy Office of Nuclear Energy (DOE-NE) sponsor, Ned Larson. The gamma and neutron scanning described in Sections 3.2.2 and 3.2.3 was possible due to the generosity of the International Nuclear Safeguards Technology Program, part of DOE NNSA NPAC. We also appreciate the Electric Power Research Institute's contributions in the area of eddy current examinations. To Pan Guirong of Westinghouse, John Strumpell of Framatome, and Tom Brookmire of Dominion, many thanks and much gratitude for their support, information provided, and time spent reviewing this document. We also wish to acknowledge the ORNL Irradiated Fuels Examination Laboratory for their support and cooperation in the handling and examination of the sister rods and Framatome for their support on the eddy current campaign.

This page is intentionally left blank.

CONTENTS

SUMMARY	iii
ACKNOWLEDGMENTS	vii
LIST OF FIGURES	x
LIST OF TABLES.....	xvi
RECORD OF REVISIONS	xvii
ACRONYMS.....	xix
1. INTRODUCTION.....	1
2. NDE SCOPE	3
3. NDE RESULTS.....	5
3.1 NDE.01: Visual Examinations	5
3.1.1 General Condition.....	5
3.1.2 Typical Waterside Cladding Appearance of M5-Clad Rods.....	18
3.1.3 Typical Waterside Cladding Appearance of ZIRLO-Clad Rods	20
3.1.4 Typical Waterside Cladding Appearance of Zircaloy-4 and LT Zircaloy-4- Clad Rods.....	23
3.2 NDE.02 Gamma and Neutron Scanning	25
3.2.1 One-Dimensional Sodium Iodide Gamma Scanning	26
3.2.2 HPGe Detector Scanning	38
3.2.3 Fork Detector Gamma and Neutron Scanning.....	43
3.3 NDE.03: Fuel Rod Overall Length	48
3.4 NDE.04: Eddy Current Examinations.....	48
3.4.1 F-SECT Measurements	48
3.4.2 Traditional Eddy Current Measurements	51
3.4.2.1 Eddy current calibration.....	51
3.4.2.2 Scan Speed and Data Acquisition	51
3.4.2.3 Scan Frequencies	52
3.4.2.4 Cladding Defect Scan Results.....	52
3.4.2.5 Lift-Off Scan Results	58
3.5 NDE.05: Profilometry Measurements.....	88
3.5.1 LVDT Measurements.....	88
3.5.2 Visual Profilometry.....	90
3.6 NDE.06: Surface Temperature Measurements.....	103
4. SUMMARY OF RESULTS.....	105
5. REFERENCES	108
Appendix A.....	A-1
Appendix B	B-1
Appendix C	C-1

LIST OF FIGURES

Figure 1. Example of Visible Rod Labeling and Bar Coding (Partial Shown).....	8
Figure 2. Striated Surface Texture (Alternating Longitudinal Light and Dark Bands) Observed for (a) Highly Oxidized Rods and (b) a Lightly Oxidized M5 Rod, and (c) Dark Patches Associated with Spacer Grid Locations (“Flow Marking”).	8
Figure 3. Typical Appearance of Orthogonal Longitudinal Scratches Consistent with Spacer Grid Spring/Dimple Interaction during Rod Insertion and Withdrawal from the Fuel Assembly.....	9
Figure 4. Example of Circumferential Striping at Pellet-Pellet Interfaces (6U3P16).....	9
Figure 5. Typical Appearance of End Cap Welds, M5 Rod 30AE14 (Left) and ZIRLO Rod 6U3L08 (Right).	9
Figure 6. Typical Appearance of ADEPT Handling Marks (Left) and Manipulator Scratches (Right).	9
Figure 7. Illustration of Visible Features on an M5 Sister Rod using (a) the Unprocessed Individual Photo, (b) the Interactive SWF, and (c) the Flattened and Filtered Collage and a ZIRLO Sister Rod using (d) the Unprocessed Individual Photo, (e) the Interactive SWF, and (f) the Flattened and Filtered Collage.....	10
Figure 8. Selected Visual Observations from Assembly 30A.....	18
Figure 9. Selected Visual Observations from Assembly 5K7.....	19
Figure 10. Selected Visual Observations from Assembly 3D8.....	20
Figure 11. Selected Visual Observations from Assembly 6U3.....	21
Figure 12. Selected Visual Observations from Assembly 3F9.	22
Figure 13. Selected Visual Observations from Assembly F35.	23
Figure 14. Selected Visual Observations from Assembly 3A1.....	24
Figure 15. Comparison of Gamma Count Rates Collected by Three Different Detectors for Sister Rod 30AE14: HPGe, fork, and NaI. The Normalized Predicted Average Assembly Axial Fuel Burnup is Also Plotted for Reference.....	25
Figure 16. Gamma Scans for Sister Rod from Fuel Assembly 30A.	30
Figure 17. Gamma Scans for Sister Rod from Fuel Assembly 5K7.	31
Figure 18. Gamma Scans for Sister Rod from Fuel Assembly F35.....	32
Figure 19. Gamma Scans for Sister Rod from Fuel Assembly 3A1.	33
Figure 20. Gamma Scans for Sister Rod from Fuel Assembly 3F9.....	34
Figure 21. Gamma Scans for Sister Rod from Fuel Assembly 3D8.	35
Figure 22. Gamma Scans for Sister Rod from Fuel Assembly 6U3.	36
Figure 23. Typical Pellet Ridging on a Fuel Rod Observed Via Gamma Scanning; Scales are Magnified to Show the Detail. The Typical Pellet is Approximately 10mm Long.....	37
Figure 24. Diagram of the Measurement Geometry for the HPGe Campaign.....	38
Figure 25. Picture of the HPGe Detector during Spectroscopy Measurements.....	39
Figure 26. HPGe Sum Spectrum of Sister Rod 30AD05.....	40
Figure 27. HPGe-derived Axial Scan of Sister Rod 30AD05 Using the Gross Peak Counts from the 661.6 keV Peak of ^{137}Cs	41
Figure 28. Superimposed Spectra of Coaxial Ge, NaI, and LaBr ₃ Detectors.....	42
Figure 29. Comparison of the Cooling Time and Burnup of Rod 3D8B2 by Detector Type.....	42
Figure 30. (a) Fork Detector Head, (b) Fission and Ionization Chambers, (c) Rear View of Fork Detector Head (with Back Plate Removed).....	43
Figure 31. Measurement of a Spent Fuel Assembly in a Pool Using a Fork Detector [8].....	43
Figure 32. Set Up for Calibrating the Fork Detectors at ORNL’s RASCAL Facility.	44
Figure 33. Set Up for Measuring a Full-Length Sister Rod Using a Fork Detector in IFEL Hot Cell.	45

Figure 34. Set Up for Measuring a 5×5 Array of 25 Full-Length Spent Fuel Rods Using a Fork Detector at ORNL's IFEL Hot Cell, All Locations Filled with Sister Rods (Left) and 8 Partially Vacant Locations (Right).....	45
Figure 35. Normalized Fork Neutron and Gamma Count Rates along the Length of Fuel Rod 30AE14.....	46
Figure 36. Comparisons between the Fork Gamma and Neutron Count Rates with the Corresponding Calculated Neutron and Gamma Source Intensities in 9 Fuel Rods.	47
Figure 37. The F-SECT Bench Installed in the IFEL Hot Cell.....	49
Figure 38. Representative Sister Rod Lift-Off Data for Each Cladding Type.	50
Figure 39. F-SECT Estimated Hydrogen Content for Sister Rod F35K13, an Example of HBU Zirc-4 Rods with High Corrosion.....	50
Figure 40. Lift-Off Measured in All Four Quadrants, Sister Rod 6U3O05.	61
Figure 41. A Comparison of the Average Measured Lift-Off for Two Scans Completed on Rod 30AG09, Both at 10 mm/sec.	62
Figure 42. A Comparison of the Average Measured Lift-Off for Two Scans Completed on Rod F35P17, both at 10 mm/sec.	63
Figure 43. Average Measured Lift-Off for Sister Rods from Fuel Assembly 3D8.	64
Figure 44. Average Measured Lift-Off for Sister Rods from Fuel Assembly 3F9.	65
Figure 45. Average Measured Lift-Off for Sister Rods from Fuel Assembly 6U3.	66
Figure 46. Average Measured Lift-Off for Sister Rods from Fuel Assembly 5K7.	67
Figure 47. Average Measured Lift-Off for Sister Rods from Fuel Assembly 30A.	68
Figure 48. Average Measured Lift-Off for Sister Rods from Fuel Assembly F35.	69
Figure 49. Average Measured Lift-Off for Sister Rods from Fuel Assembly 3A1.	70
Figure 50. Average Measured Lift-Off for All M5-Clad Sister Rods.....	71
Figure 51. Average Measured Lift-Off for All ZIRLO-Clad Sister Rods.	72
Figure 52. Average Measured Lift-Off for All Zirc-4 and Low-Tin Zirc-4-Clad Sister Rods.	73
Figure 53. A Comparison of the Trends Observed in the Average Measured Gamma Scan, Profilometry, and Lift-Off Scans for Sister Rod 3F9N05.	74
Figure 54. A Comparison of the Trends Observed in the Average Measured Gamma Scan, Profilometry, and Lift-Off Scans for Sister Rod 5K7O14.....	75
Figure 55. A Comparison of the Trends Observed in the Average Measured Gamma Scan, Profilometry, and Lift-Off Scans for Sister Rod F35P17.	76
Figure 56. Rod Bambooning Is Observable in the Lift-Off Data in Lower Oxide/CRUD Thickness Regions (Main Graph) and is Less Discernable Where the Oxide/CRUD Thickness Is Large (See the Inset), As Shown for Sister Rod 3A1B16.	77
Figure 57. An Example of Lift-Off Measurements Where Significant Spalling Is Present (Four Quadrant Lift-Off, Sister Rod F35K13).	78
Figure 58. Rotational Eddy Current Lift-Off Scans of 3A1B16 at 791 mm.	79
Figure 59. A 3D Surface Plot Illustrating the Variations in Measured Lift-Off Over the Circumference of Sister Rod 3F9D07 in Higher Burnup Elevations Compared with Visible Rod Features.	80
Figure 60. Rotational Eddy Current Lift-Off Scan of 3F9N05 at 3,209 mm.	81
Figure 61. Rotational Eddy Current Lift-Off Scans of 6U3P16 at 3,434 mm.	82
Figure 62. Rotational Scan of Sister Rod 3F9D07 at 2,279 mm Elevation.	83
Figure 63. Rotational Scan of Sister Rod 3F9D07 at 1,765 mm Elevation Indicating Depth of a Partially Oxidized Fretting Mark and Axial Scratches in the Waterside Surface of the Rod.	84
Figure 64. Rotational Scans of Flow Markings at the Exit of a Spacer Grid, F35P17 at 3,650 mm.	85
Figure 65. An Example of An Abrupt Shift in Lift-Off Magnitude Associated with Either the Coil Sticking in Its Housing or an Accumulation of Debris Under the Coil Head.	86

Figure 66. A Comparison of the 1992 EPRI-Reported Poolside Average Lift-Off Measurements and the ORNL Hot Cell Lift-off Measurements for Sister Rods F35K13 And F35P17 [9].	87
Figure 67. Profilometry Scans for Assembly 30A.	91
Figure 68. Profilometry Scans for Assembly 5K7.	92
Figure 69. Profilometry Scans for Assembly F35.	93
Figure 70. Profilometry Scans for Assembly 3A1.	94
Figure 71. Profilometry Scans for Assembly 3F9.	95
Figure 72. Profilometry Scans for Assembly 3D8.	96
Figure 73. Profilometry Scans for Assembly 6U3.	97
Figure 74. Typical Pellet Ridging on a Fuel Rod via LVDT-Based Profilometry; Scales are Magnified to Show the Detail. The Typical Pellet is Approximately 10mm long.	98
Figure 75. Individual LVDT Measurements for Rod 30AG09 Illustrating the Difference in Measurements for the Two Pairs between 900 and 1,600 mm.	99
Figure 76. Average Diameter Reduction in Rod 6U3P16; This Reduction Nearly Aligns with the Pellet Stack Gap Noted in the Gamma Scan.	100
Figure 77. Example of LVDT Measurements and Visuals Diameter Measurements as Compared with Features Indicated by the Gamma Scans for Rod F35K13.	101
Figure 78. Observed Sinusoidal Trend in Visual Profilometry Data with Angle of Rod Rotation.	102
Figure 79. Cross-Sectional View of the Thermocouple Isolation Housing Used to Measure the Surface Temperature of Selected Sister Rods.	103
Figure 80. 24-Hour Measurement of Surface Temperature of Sister Rod 5K7P02 at Midplane, in the Temperature Housing and on the ADEPT (Not in the Storage Array).	104
Figure A.1. Rod 3A1B16 LVDT Diameter Measurements.	A-2
Figure A.2. Rod 3A1F05 LVDT Diameter Measurements.	A-3
Figure A.3. Rod 3D8B02 LVDT Diameter Measurements.	A-4
Figure A.4. Rod 3D8E14 LVDT Diameter Measurements.	A-5
Figure A.5. Rod 3F9D07 LVDT Diameter Measurements.	A-6
Figure A.6. Rod 3F9N05 LVDT Diameter Measurements.	A-7
Figure A.7. Rod 3F9P02 LVDT Diameter Measurements.	A-8
Figure A.8. Rod 5K7C05 LVDT Diameter Measurements.	A-9
Figure A.9. Rod 5K7K09 LVDT Diameter Measurements.	A-10
Figure A.10. Rod 5K7O14 LVDT Diameter Measurements.	A-11
Figure A.11. Rod 5K7P02 LVDT Diameter Measurements.	A-12
Figure A.12. Rod 6U3I07 LVDT Diameter Measurements.	A-13
Figure A.13. Rod 6U3K09 LVDT Diameter Measurements.	A-14
Figure A.14. Rod 6U3L08 LVDT Diameter Measurements.	A-15
Figure A.15. Rod 6U3M03 LVDT Diameter Measurements.	A-16
Figure A.16. Rod 6U3M09 LVDT Diameter Measurements.	A-17
Figure A.17. Rod 6U3O05 LVDT Diameter Measurements.	A-18
Figure A.18. Rod 6U3P16 LVDT Diameter Measurements.	A-19
Figure A.19. Rod 30AD05 LVDT Diameter Measurements.	A-20
Figure A.20. Rod 30AE14 LVDT Diameter Measurements.	A-21
Figure A.21. Rod 30AG09 LVDT Diameter Measurements.	A-22
Figure A.22. Rod 30AK09 LVDT Diameter Measurements.	A-23
Figure A.23. Rod 30AP02 LVDT Diameter Measurements.	A-24
Figure A.24. Rod F35K13 LVDT Diameter Measurements.	A-25
Figure A.25. Rod F35P17 LVDT Diameter Measurements.	A-26

Figure B.1. Rod 3A1B16 LVDT Profilometry, Visual Profilometry, and Gamma Scan Data.....	B-2
Figure B.2. Rod 3A1F05 LVDT Profilometry, Visual Profilometry, and Gamma Scan Data.	B-3
Figure B.3. Rod 3D8B02 LVDT Profilometry, Visual Profilometry, and Gamma Scan Data.....	B-4
Figure B.4. Rod 3D8E14 LVDT Profilometry, Visual Profilometry, and Gamma Scan Data.	B-5
Figure B.5. Rod 3F9D07 LVDT Profilometry, Visual Profilometry, and Gamma Scan Data.	B-6
Figure B.6. Rod 3F9N05 LVDT Profilometry, Visual Profilometry, and Gamma Scan Data.	B-7
Figure B.7. Rod 3F9P02 LVDT Profilometry, Visual Profilometry, and Gamma Scan Data.	B-8
Figure B.8. Rod 5K7C05 LVDT Profilometry, Visual Profilometry, and Gamma Scan Data.....	B-9
Figure B.9. Rod 5K7K09 LVDT Profilometry, Visual Profilometry, and Gamma Scan Data.....	B-10
Figure B.10. Rod 5K7O14 LVDT Profilometry, Visual Profilometry, and Gamma Scan Data.....	B-11
Figure B.11. Rod 5K7P02 LVDT Profilometry, Visual Profilometry, and Gamma Scan Data.	B-12
Figure B.12. Rod 6U3I07 LVDT Profilometry, Visual Profilometry, and Gamma Scan Data.	B-13
Figure B.13. Rod 6U3K09 LVDT Profilometry, Visual Profilometry, and Gamma Scan Data.....	B-14
Figure B.14. Rod 6U3L08 LVDT Profilometry, Visual Profilometry, and Gamma Scan Data.	B-15
Figure B.15. Rod 6U3M03 LVDT Profilometry, Visual Profilometry, and Gamma Scan Data.....	B-16
Figure B.16. Rod 6U3M09 LVDT Profilometry, Visual Profilometry, and Gamma Scan Data.....	B-17
Figure B.17. Rod 6U3O05 LVDT Profilometry, Visual Profilometry, and Gamma Scan Data.....	B-18
Figure B.18. Rod 6U3P16 LVDT Profilometry, Visual Profilometry, and Gamma Scan Data.	B-19
Figure B.19. Rod 30AD05 LVDT Profilometry, Visual Profilometry, and Gamma Scan Data.....	B-20
Figure B.20. Rod 30AE14 LVDT Profilometry, Visual Profilometry, and Gamma Scan Data.	B-21
Figure B.21. Rod 30AG09 LVDT Profilometry, Visual Profilometry, and Gamma Scan Data.....	B-22
Figure B.22. Rod 30AK09 LVDT Profilometry, Visual Profilometry, and Gamma Scan Data.....	B-23
Figure B.23. Rod 30AP02 LVDT Profilometry, Visual Profilometry, and Gamma Scan Data.	B-24
Figure B.24. Rod F35K13 LVDT Profilometry, Visual Profilometry, and Gamma Scan Data.	B-25
Figure B.25. Rod F35P17 LVDT Profilometry, Visual Profilometry, and Gamma Scan Data.....	B-26

Figure C.1. Lift-Off Measured in All Four Quadrants, Sister Rod 3A1B16.....	C-2
Figure C.2. Lift-Off Measured in All Four Quadrants, Sister Rod 3A1F05.....	C-3
Figure C.3. Lift-Off Measured in All Four Quadrants, Sister Rod 3D8B02.....	C-4
Figure C.4. Lift-Off Measured in All Four Quadrants, Sister Rod 3D8B14.....	C-5
Figure C.5. Lift-Off Measured in All Four Quadrants, Sister Rod 3F9D07.....	C-6
Figure C.6. Lift-Off Measured in All Four Quadrants, Sister Rod 3F9N05.....	C-7
Figure C.7. Lift-Off Measured in All Four Quadrants, Sister Rod 3F9P02.....	C-8
Figure C.8. Lift-Off Measured in All Four Quadrants, Sister Rod 5K7C05.....	C-9
Figure C.9. Lift-Off Measured in All Four Quadrants, Sister Rod 5K7K09.	C-10
Figure C.10. Lift-Off Measured in All Four Quadrants, Sister Rod 5K7O14.	C-11
Figure C.11. Lift-Off Measured in All Four Quadrants, Sister Rod 5K7P02.....	C-12
Figure C.12. Lift-Off Measured in All Four Quadrants, Sister Rod 6U3I07.....	C-13
Figure C.13. Lift-Off Measured in All Four Quadrants, Sister Rod 6U3K09.	C-14
Figure C.14. Lift-Off Measured in All Four Quadrants, Sister Rod 6U3L08.....	C-15
Figure C.15. Lift-Off Measured in All Four Quadrants, Sister Rod 6U3M03.....	C-16
Figure C.16. Lift-Off Measured in All Four Quadrants, Sister Rod 6U3M09.....	C-17
Figure C.17. Lift-Off Measured in All Four Quadrants, Sister Rod 6U3O05.	C-18
Figure C.18. Lift-Off Measured in All Four Quadrants, Sister Rod 6U3P16.....	C-19
Figure C.19. Lift-Off Measured in All Four Quadrants, Sister Rod 30AD05.	C-20
Figure C.20. Lift-Off Measured in All Four Quadrants, Sister Rod 30AE14.....	C-21
Figure C.21. Lift-Off Measured in All Four Quadrants, Sister Rod 30AG09.	C-22
Figure C.22. Lift-Off Measured in All Four Quadrants, Sister Rod 30AK09.	C-23
Figure C.23. Lift-Off Measured in All Four Quadrants, Sister Rod 30AP02.....	C-24
Figure C.24. Lift-Off Measured in All Four Quadrants, Sister Rod F35K13.....	C-25
Figure C.25. Lift-Off Measured in All Four Quadrants, Sister Rod F35P17.....	C-26

Figure C.26. Rotational Eddy Current Lift-Off Scans for 30AE14 at Elevations of 229 mm (Top) and 3,861 mm (Bottom).	C-27
Figure C.27. Rotational Eddy Current Lift-Off Scans for 30AE14 at Elevations of 3,781 mm (Top) and 2,461 mm (Bottom).	C-28
Figure C.28. Rotational Eddy Current Lift-Off Scans for 30AE14 at Elevations of 3320 mm (Top) and 235 mm (Bottom).	C-29
Figure C.29. Rotational Eddy Current Lift-Off Scans for 30AE14 at elevation of 33 mm.	C-30
Figure C.30. Rotational Eddy Current Lift-Off Scans from 30AG09 at 530 mm.	C-30
Figure C.31. Rotational Eddy Current Lift-Off Scans from 30AG09 at 670 mm.	C-31
Figure C.32. Rotational Eddy Current Lift-Off Scans of 3A1B16 at 3,100 mm.	C-31
Figure C.33. Rotational Eddy Current Lift-Off Scans of 3A1B16 at 3,100 mm at 1 RPM (Top) and 10 RPM (Bottom).	C-32
Figure C.34 Rotational Eddy Current Lift-Off Scans of 3A1B16 at 791 mm.	C-33
Figure C.35. Rotational Eddy Current Lift-Off Scans of F35P17 at 1,365 mm.	C-33
Figure C.36. Rotational Eddy Current Lift-Off Scans of F35P17 at 1,805 mm (Top) and 2,263 mm (Bottom).	C-34
Figure C.37. Rotational Eddy Current Lift-Off Scans of F35P17 at 3,080 mm (Top) and 3,650 mm (Bottom).	C-35
Figure C.38. Rotational Eddy Current Lift-Off Scans of F35K13 at 1,139 (Top) and 3,403 mm (Bottom).	C-36
Figure C.39. Rotational Eddy Current Lift-Off Scans of 6U3M03 at 3213mm	C-37
Figure C.40. Rotational eddy current lift-off scan of 3F9D07 at 3,333 mm.	C-37
Figure C.41. Rotational eddy current lift-off scan of 3F9D07 at 3,200 mm.	C-38
Figure C.42. Rotational eddy current lift-off scan of 3F9D07 at 3,295 mm.	C-38
Figure C.43. Rotational Eddy Current Lift-Off Scans of 3F9D07 at 1,765 mm (Top) and 2,279 mm (Bottom).	C-39
Figure C.44. Rotational Eddy Current Lift-Off Scans of 6U3K09 at 310 mm (Top) and 322 mm (Bottom).	C-40
Figure C.45. Rotational eddy current lift-off scan of 6U3K09 at 330 mm.	C-41
Figure C.46. Rotational eddy current lift-off scan of 6U3K09 at 3630 mm.	C-41
Figure C.47. Rotational Eddy Current Lift-Off Scans of 6U3K09 at 371 mm (Top) and 3537 mm (Bottom).	C-42
Figure C.48. Rotational eddy current lift-off scan of 3F9N05 at 3209 mm.	C-43
Figure C.49. Rotational eddy current lift-off measurement of 6U3I07 at 3432 mm.	C-43
Figure C.50. Rotational eddy current lift-off measurements of 6U3I07 at 35 mm (lower end cap).	C-44
Figure C.51. Rotational eddy current lift-off measurements of 6U3I07 at 65 mm.	C-44
Figure C.52. Rotational Eddy Current Lift-Off Scans of 6U3L08 at 3659 mm (Top) and 3435 mm (Bottom).	C-45
Figure C.53. Rotational Eddy Current Lift-Off Scans of 6U3L08 at 35 mm (Top) and 38 mm (Bottom).	C-46
Figure C.54. Rotational eddy current lift-off scan of 6U3L08 at 55 mm.	C-47
Figure C.55. Rotational Eddy Current Lift-Off Scans of 6U3L08 at 3,364 mm.	C-47
Figure C.56. Rotational Eddy Current Lift-Off Scans of 6U3P16 at 449 mm (Top) and 516 mm (Bottom).	C-48
Figure C.57. Rotational Eddy Current Lift-Off Scans of 6U3P16 at 398 mm (Top) and 3835 mm (Bottom).	C-49
Figure C.58. Rotational eddy current lift-off scan of 6U3P16 at 3,434 mm.	C-50
Figure C.59. Rotational eddy current lift-off scan of 3F9P02 at 3,201 mm.	C-50
Figure C.60. Rotational Eddy Current Lift-Off Scans of 3F9P02 at 3664 mm (Top) and 2281 mm (Bottom).	C-51

Figure C.61. Rotational Eddy Current Lift-Off Scans of 3F9P02 at 2116 mm (Top) and 307 mm (Bottom).	C-52
Figure C.62. Rotational eddy current lift-off scan of 3F9P02 at 3835 mm.	C-53
Figure C.63. Rotational Eddy Current Lift-Off Scans of 3F9P02 at 2281 mm (rescan).	C-53

LIST OF TABLES

Table S-1. NDE scope and summary of findings.....	vi
Table 1. Visual observations by sister rod elevation, ZIRLO rods.	11
Table 2. Visual observations by sister rod elevation, M5 rods.	13
Table 3. Visual observations by sister rod elevation, Zirc-4 and LT Zirc-4 rods.	16
Table 4. Results of gamma scanning grouped by rod type (± 1.5 mm, except for rod length, ± 0.5 mm).	28
Table 5. Fuel stack gaps observed through gamma scanning (± 1 mm).	29
Table 6. Summary of Remaining Wall Thickness and Maximum Lift-off.....	53
Table 7. Summary of defect scan results	56
Table 8 Summary of sister rod outer diameter measurements.....	89
Table 9 Summary of Findings.....	107

RECORD OF REVISIONS

Date	Changes
9/15/2017	<ul style="list-style-type: none">• Initial release
3/30/2018	<ul style="list-style-type: none">• The Summary was updated to include eddy current and temperature measurement results.• A description of flow marking and a corresponding typical image were added to Section 3.1.• Table 4 was updated to include campaign average rod lengths.• Section 3.4.1 was updated to include F-SECT hydrogen content results for an example Zirc-4 sister rod.• Section 3.4.2 was completely revised to discuss the results of the traditional eddy current measurements, and Appendix C was added to include the data collected.• Section 3.6 was completely revised to include the surface temperature measurements taken.• Section 4, Summary of Results, was added.• Minor editorial edits and clarifications were made throughout the document. All changes are indicated with lines in the document margins.
5/8/2018	<ul style="list-style-type: none">• Added color-coding to Tables 1, 2, and 3 to allow better visualization of features.• Throughout the document, revised all English units to metric.• In section 3.1.4, summarized GTRF findings.• In Table 4 and Table 8, revised the number of decimal places shown to correctly reflect the measurement precision.
5/16/2018	<ul style="list-style-type: none">• Removed link to Curie image storage.

This page is intentionally left blank.

ACRONYMS

ADEPT	Advanced Diagnostics and Evaluation Platform
BU	burnup
CRUD	Chalk River Unidentified Deposits
DE	destructive examination
DOE	US Department of Energy
FY	fiscal year
GTRF	grid-to-rod fretting
HBU	high burnup
HPGe	high purity germanium
IAEA	International Atomic Energy Agency
IFEL	Irradiated Fuels Examination Laboratory
ISFSI	Independent Spent Fuel Storage Installation
LT	low tin
LVDT	linear variable differential transformers
MTU	metric ton of uranium
MW	megawatt
NaI	sodium iodide
NE	Office of Nuclear Energy
NDE	nondestructive examination
NNSA	National Nuclear Security Administration
NPAC	Office of Nonproliferation and Arms Control
OD	outer diameter
ORNL	Oak Ridge National Laboratory
PWR	pressurized water reactor
RASCAL	Radiation Standards Calibration
ROI	region of interest
SNF	spent nuclear fuel
SFWD	Spent Fuel and Waste Disposition
SFWST	Spent Fuel and Waste Science and Technology
SWF	Shockwave Flash

This page is intentionally left blank.

SPENT FUEL AND WASTE SCIENCE AND TECHNOLOGY SISTER ROD NONDESTRUCTIVE EXAMINATION ANNUAL REPORT FY2017

1. INTRODUCTION

The High Burnup Spent Fuel Data Project, sponsored by the US Department of Energy (DOE) Office of Nuclear Energy (NE), is focused on understanding the effects of long-term storage and transportation on high burnup (HBU) (>45 gigawatt days per metric ton uranium) light water reactor fuel. The goals of the project are to “provide confirmatory data for model validation and potential improvement, provide input to future SNF dry storage cask design, support license renewals and new licenses for Independent Spent Fuel Storage Installations (ISFSIs), and support transportation licensing for high burnup SNF” [1].

In support of the project goals, 25 sister rods were removed from fuel assemblies at the North Anna Power Station. Nine rods were removed from the project assemblies, and 16 rods were removed from similar HBU assemblies. The 25 sister rods were shipped to Oak Ridge National Laboratory (ORNL) in early 2016 for detailed nondestructive examination (NDE) and destructive examination (DE) in the Irradiated Fuels Examination Laboratory (IFEL). The detailed examinations will provide essential information on the physical state of the HBU rods and the fuel contained in the rods prior to loading, drying, and long-term dry storage [1]. Similar tests will be performed at the end of the long-term storage period to identify any changes in the properties of the fuel rods during the dry storage period [1].

This report documents the conclusion of the Phase I testing of the sister rods and provides a report of the NDE tasks performed and the data collected, as guided by the sister rod test plan [2].

This page is intentionally left blank.

December 21, 2018

2. NDE SCOPE

The sister rod program's NDE scope includes visual examinations of the rods' external surfaces and gross dimensional measurements [2]. All 25 sister rods have undergone extensive nondestructive examination using ORNL's Advanced Diagnostics and Evaluation Platform (ADEPT) for the following:

- NDE.01: Visuals of the complete exterior surface of each rod with a digitally created, user-viewable montage of the surface, and the location and appearance of any physical abnormalities (e.g., chemical attack, blisters, cracks, heavy or uneven oxide layers, weld failures, or clad distortions)
- NDE.02: Gamma scanning to nondestructively:
 - a. obtain relative axial burnup profiles
 - b. identify any gross migration of fission products or large pellet cracks
 - c. identify any pellet stack gaps
 - d. measure the pellet stack height
 - e. identify the location and magnitude of any burnup depressions due to grid spacers;
- NDE.03: Fuel rod overall length measurements
- NDE.04: Eddy current scans to obtain information on clad mechanical macroscopic defects and estimated oxide/CRUD thickness as a function of axial location
- NDE.05: Profilometry measurements providing the rod outer diameter as a function of axial location
- NDE.06: Rod surface temperature measurements

In addition to the sister rod program's NDE scope, two additional radiation scanning projects performed for the National Nuclear Security Administration (NNSA) were completed and are summarized in Sections 3.2.2 and 3.2.3. Also, a specialized eddy current examination for measurement of cladding hydrogen content was performed on 19 of the 25 sister rods by the Electric Power Research Institute (EPRI), and a summary of that exam is also provided in Section 3.4.1.

This page is intentionally left blank.

3. NDE RESULTS

3.1 NDE.01: Visual Examinations

Visual examinations of all 25 sister rods were completed in May 2017. Three sets of images are available:

- 784 individual unprocessed photos per sister rod, for a total of 19,600 photos (the source data for the other two image sets),
- 25 compiled user-interactive Shockwave Flash (SWF) collage files (one per sister rod) containing 784 individual photos per sister rod, with each labeled for searching and observation, and
- 96 flattened 40 mm axial segment collages per sister rod (2,400 total images) obtained by filtering and stitching together the individual azimuthal photos.

All three sets of images are available in digital format only and are stored on ORNL's CURIE.ORNL.gov resource [3]. The file name nomenclature for individual digital photos is:

XXXZZZ-YYYYMMDD01-A###-D----_S***.jpg,

where:

XXX	is the sister rod parent assembly ID,
ZZZ	is the sister rod lattice location in the parent assembly,
YYYY	is the year the image was captured,
MM	is the month the image was captured,
DD	is the day the image was captured,
###	indicates the azimuthal orientation, in degrees, at which the image was captured,
----	indicates the axial elevation at which the image was captured, in mm, from the bottom of the fuel rod, with the exception of rods F35P17 and F35K13, which were loaded into the shipping container and hot cell backwards, so their elevations are from the tops of the rods, and
***	is a tracking number issued by the software.

The file name nomenclature used for the flattened collage sections is:

stitched_XXXZZZ-YYYYMMDD01-Axxx-D----_Sxxx.png, and

the nomenclature used for the interactive SWF files is:

XXXZZZ-Collage_out.swf,

where the variables are those previously defined for the individual photos. The SWF files are opened using a web browser and appear to work best with Microsoft Internet Explorer.

Figure 1 through Figure 6 provide a collection of general observations ordered by assembly number. The majority of the images presented in this section include white arrows meant to indicate the visual feature discussed in the text. While most images present the full section of the rod in the imaging view in a horizontal axial orientation on the page, some images have been rotated or cropped for space.

3.1.1 General Condition

No weld failures, obvious cladding breaches, or other significant defects were observed. Rod identification and bar codes are visible on the rods (an example is shown in Figure 1), except on F35P17 and F35K13 since bar codes were not used when these two rods were fabricated. The visual examination indicated that shallow grid-to-rod fretting (GTRF) marks are common, and a few rods have patches of Chalk River Unidentified Deposits (CRUD) and/or spalling oxide. A typical striated surface texture

appearance, visible in the images shown in Figure 2 (a) and (b) as alternating axial light and dark bands, is present to varying degrees in all cases, with the more heavily oxidized rods having the appearance of deeper striations. Figure 2c shows large dark oval or U-shaped patches that occur near spacer grid locations that are visible on many sister rods. These markings could indicate locally thinner oxidation (likely, as discussed in Section 3.4.2) or they could be thin patches of CRUD. In either case, the proximity of the markings to spacer grids suggests that they are related to coolant flow distributions in the spacer grids and are therefore termed “flow markings.”

For the Zircaloy-4 (Zirc-4), low tin (LT) Zirc-4, and ZIRLO fuel rods, when the parent fuel assembly was fabricated, the fuel rods were pulled or pushed through the spacer grids with the springs/dimples engaged. Interaction with the spacer grid springs and dimples during rod insertion can produce long, shallow axial scratches along much of the rod’s length at the azimuthal locations of the grid springs/dimples. These are visible on the rod as oxidized scratches, as shown in Figure 3. Likewise, in many cases, interaction with the spacer grid springs and dimples during rod removal created long axial scratches along much of the rod length at orthogonal locations consistent with the location of the grid springs/dimples, removing surface CRUD and perhaps some oxide. Because the rods are not expected to rotate significantly in the reactor, it is likely that the rod removal scratches are collocated with the rod insertion scratches; however, two sets of scratches were noted in at least one sister rod. The rod insertion scratches oxidize in the reactor and the presence of oxide in the scratch would indicate that it occurred during fuel assembly fabrication. In contrast, for the Framatome Advanced Mark-BW fuel assembly design, the M5 fuel rods were inserted into the assembly using a method called “keying,” in which the springs and dimples are depressed to prevent scratching of the cladding during assembly fabrication. Therefore, it is likely that any axial scratches observed on the M5 rods occurred only during rod removal.

The pellet-pellet interfaces are frequently visible in the rod external surface images as circumferential dark stripes, as illustrated in Figure 4. During in-reactor operation, the cladding at the pellet-pellet interface is slightly cooler, and hydrogen is known to migrate to these cooler regions. Also, oxidation is slightly lower at the cooler pellet-pellet interfaces. The combination of these two effects creates a band of deeper coloration at the pellet-pellet interfaces. End cap welds are also clearly visible, as illustrated in Figure 5.

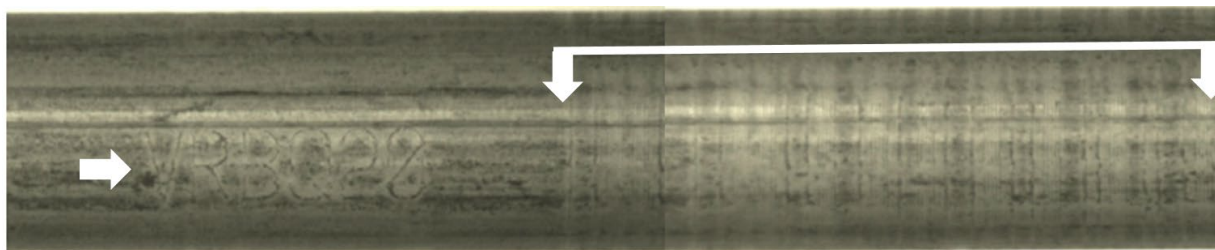
During the visual examination, the rods are moved and rotated to the position in front of the camera using the ADEPT system. The large amount of rod handling required for the photos can introduce some rubbing or polishing to the cladding’s outer surfaces, resulting in minor visual artifacts that could be confused with pellet-pellet interfaces. Since the pellets are approximately 10 mm long, banding that is spaced at a frequency other than 10 mm is likely a result of clad polishing during handling. Additionally, necessary handling of the rods using the in-cell manipulators can produce scratches, typically visible as bright diagonal marks on the rod’s surface, as illustrated in Figure 6. Some additional examples of handling marks are provided in Tables 1 and 4. Finally, the profilometry measurements (see Section 3.5) were completed prior to the visual examinations. Based on previous experience with contact probes such as the LVDTs used for the profilometry exam, the profilometry scans may have removed some CRUD or left some markings on the rod, although no such markings were identified as of this review.

Due to their dark matte black appearance, it is difficult to detect features on the surface of the M5 rods using the interactive images or the raw images. As an illustration, Figure 7(a)(b)(c) shows side by side images of the same rod with an elevation and rotation having a burnishing mark (a very shallow fretting wear mark). The burnishing mark is clearly visible in the flattened and contrast filtered collage, but it is barely discernible in the SWF format. Features on the Zirc-4, LT Zirc-4, and ZIRLO rods are also generally more discernible in the flattened collage format, as well, but some features can become less apparent due to the large format and high contrast filtering used, as illustrated in Figure 7(d)(e)(f).

Tables 1, 2 and 3 provide a summary of the visible features identified using the visual exam data for ZIRLO, M5 and Zirc-4/LT Zirc-4 sister rods, respectively. Typical oxidation patterning is not annotated

in the tables, but the visual appearance of thicker than expected oxide, oxide spalling, oxide peeling, and flow marking are noted. The rod insertion/removal scratches are likewise not annotated, as they are present on all rods at almost every elevation. Also, the severity of the feature is not annotated (e.g., fretting is noted, but it is not categorized as shallow, moderate, or deep in the tables). In some areas there is an appearance of depth to the markings that resembles debris, and this has been noted in the table. However, at this time, no debris indication has been confirmed. As mentioned previously, feature visibility varies depending upon the image set. The majority of the data listed in the tables is based on a survey of the flattened images. The tables are not considered to be an exhaustive listing, but they do provide a good overall summary of the variety of features present for each sister rod.

Sections 3.1.2, 3.1.3, and 3.1.4 provide a general discussion by alloy type and parent fuel assembly.



Two images — 3F9N05-2017050901-A000_D3811_S768.jpg and 3F9N05-2017050901-A000_D3771_S753.jpg — are stitched together. Although these images are from the same rod and are adjacent photos, there is an obvious difference in image contrast (right vs left) due to instantaneous lighting conditions.

Figure 1. Example of Visible Rod Labeling and Bar Coding (Partial Shown).

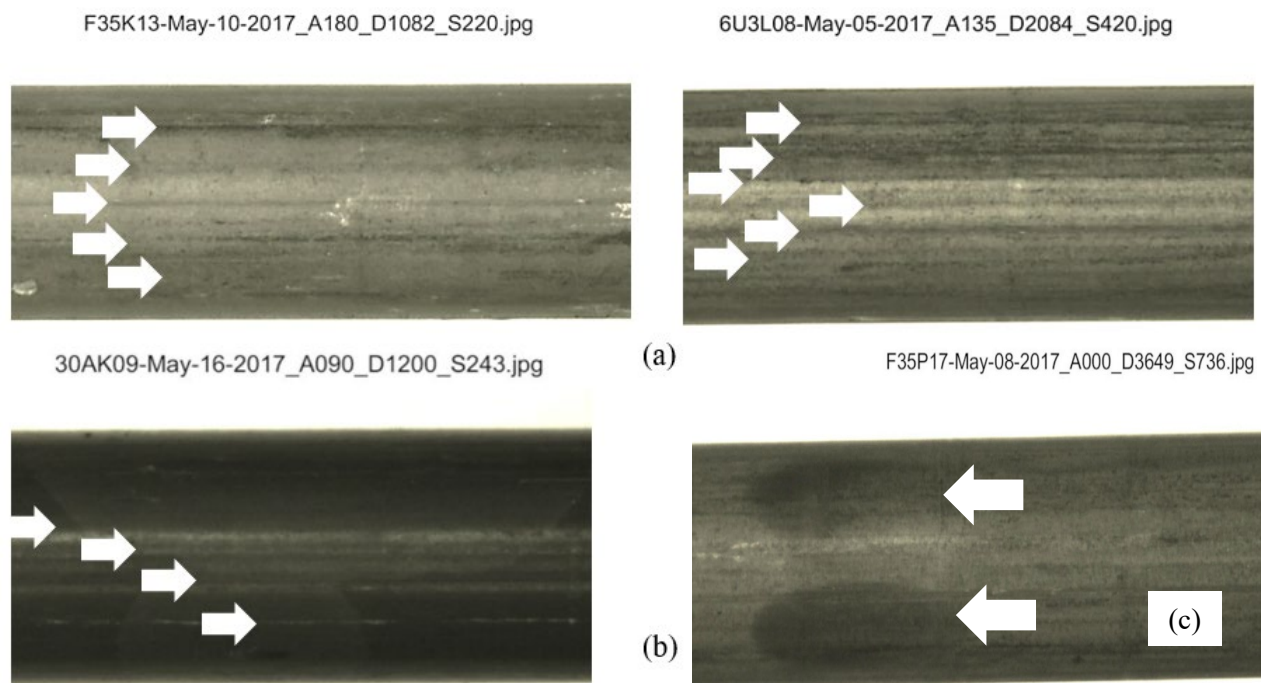


Figure 2. Striated Surface Texture (Alternating Longitudinal Light and Dark Bands) Observed for (a) Highly Oxidized Rods and (b) a Lightly Oxidized M5 Rod, and (c) Dark Patches Associated with Spacer Grid Locations (“Flow Marking”).

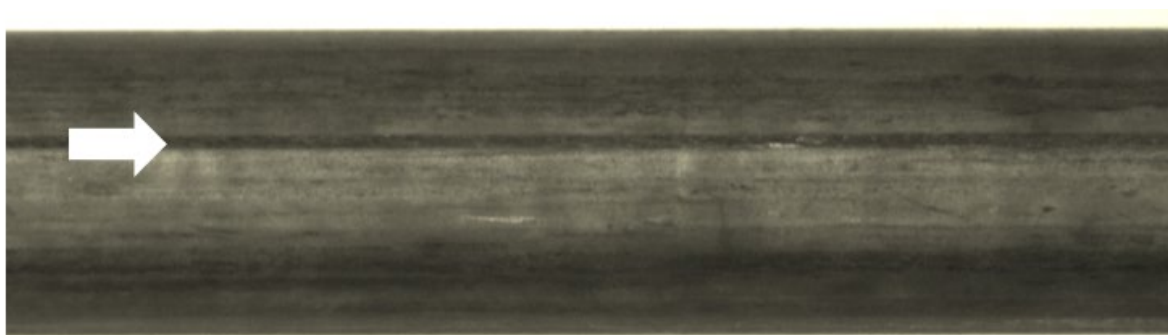


Figure 3. Typical Appearance of Orthogonal Longitudinal Scratches Consistent with Spacer Grid Spring/Dimple Interaction during Rod Insertion and Withdrawal from the Fuel Assembly.

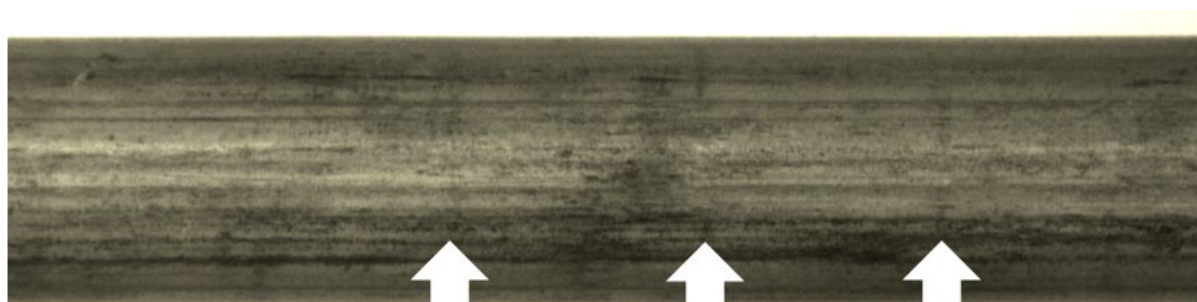


Figure 4. Example of Circumferential Striping at Pellet-Pellet Interfaces (6U3P16).

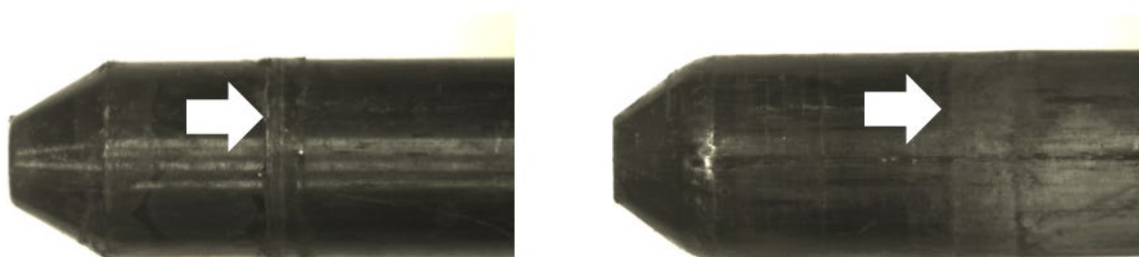


Figure 5. Typical Appearance of End Cap Welds, M5 Rod 30AE14 (Left) and ZIRLO Rod 6U3L08 (Right).

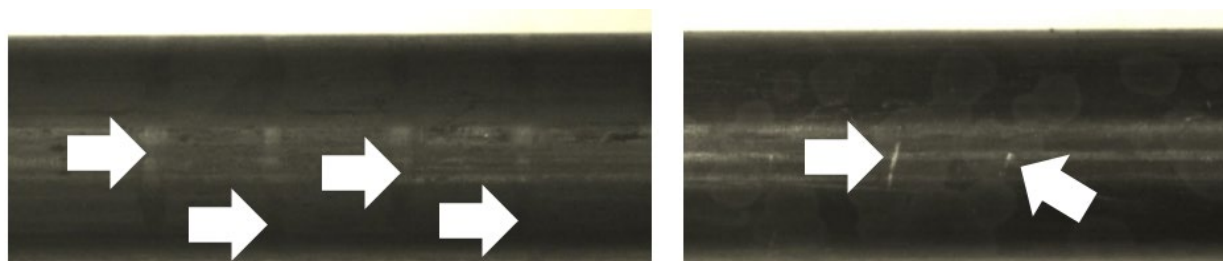
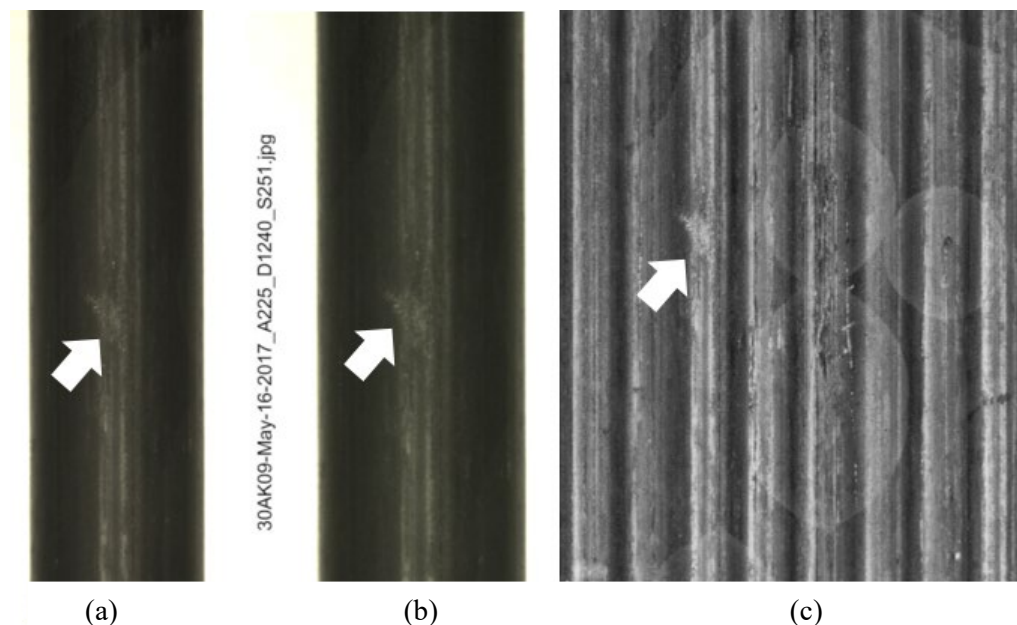
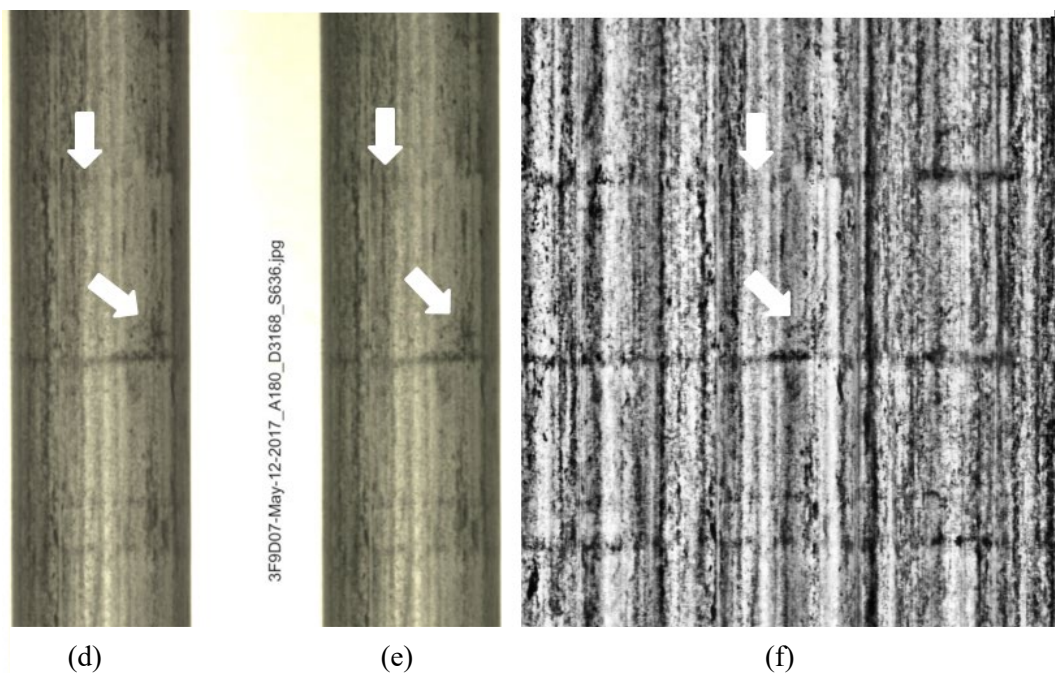


Figure 6. Typical Appearance of ADEPT Handling Marks (Left) and Manipulator Scratches (Right).



On the matte black M5 rods above, features such as the fretting mark (as indicated by the arrow) and the circular patches of oxidation become more visible.



On the shiny grey surfaces of the Zirc-4, LT Zirc-4 and ZIRLO rods, the flattened and filtered image can make some features such as the pellet-pellet boundaries more visible, while some features, such as the dark patch highlighted with the arrow, become indistinct.

Figure 7. Illustration of Visible Features on an M5 Sister Rod using (a) the Unprocessed Individual Photo, (b) the Interactive SWF, and (c) the Flattened and Filtered Collage and a ZIRLO Sister Rod using (d) the Unprocessed Individual Photo, (e) the Interactive SWF, and (f) the Flattened and Filtered Collage.

Table 1. Visual observations by sister rod elevation, ZIRLO rods.

Key: **F**=fretting, **FM**=flow marking, **HS**=handling scratches, **HM**= handling marks, **DP**=dark patch, **LP**=light patch, **HO**=heavy oxide, **SO**=spalling or peeling oxide, **PB**=pellet banding, **FL**=flaky appearance, **UPC**=rod bar code, **DB**=debris, **DS**= dark "scratches", **OR**=peeling oxide rings, **BR**=burnishing; a question mark (?) is meant to imply uncertainty about the observation immediately preceding it. Typical oxidation patterning is not included. Blank cells mean that no features beyond typical were observed.

[illegible]

Table 2. Visual observations by sister rod elevation, M5 rods.

Key: **F**=fretting, **FM**=flow marking, **HS**=handling scratches, **HM**= handling marks, **DP**=dark patch, **LP**=light patch, **HO**=heavy oxide, **SO**=spalling or peeling oxide, **PB**=pellet banding, **FL**=flaky appearance, **UPC**=rod bar code, **DB**=debris, **DS**= dark "scratches", **OR**=peeling oxide rings, **BR**=burnishing; a question mark (?) is meant to imply uncertainty about the observation immediately preceding it. Typical oxidation patterning is not included. Blank cells mean that no features beyond typical were observed.

Elevation from rod bottom (approx. mm)	5K7C05	5K7K09	5K7O14	5K7P02	30AD05	30AE14	30AG09	30AK09	30AP02
0000									
0040	HS	HS	HS	HS	HS	HS	F HS	HS	HS
0080	HS	HS	HS	F	HS		HS	HS F	HS
0120	HS OR	HS OR	HS F		HS	HS		F	F
0160	HS OR	HS OR	HS	HS	HS				
0200	HS OR	OR	HS	HS	HS	OR			
0240	HS OR		HS	HS		OR			HS
0280	HS OR		LP	HS					
0320	HS UPC	UPC	UPC	HS	UPC	UPC	UPC LP	UPC	UPC
0360	HS FL	UPC	UPC	UPC	UPC	UPC	UPC HS	UPC FL	UPC HS
0400	FL (CRUD?)	F Heavy FL (CRUD?)	HS DP			UPC	HS		
0440	FL (CRUD?)	Heavy FL (CRUD?)	FL						HS
0480	Heavy FL (CRUD?)		Heavy FL (CRUD?)		HS		HS		HS
0520	Heavy FL (CRUD?)		HS	Heavy FL (CRUD?)	HS				HS
0560	FL (CRUD?)	LP	HS	Heavy FL (CRUD?) F			HS		HS
0600			Heavy FL (CRUD?)	F		HS DB?	F deep rod removal scratch	HS	
0640				HS		HS	HS	HS F	
0681	F	F	F	F	F	HS	HS	F	F
0721		F	F HS	F	HS BR	F	HS	F HS	F
0761	HS		HS	F	HS BR		HS	HS	
0801			HS PB	F HS PB		HS	HS	HS	
0841			HS	PB			HS		
0881	LP				LP	LP	HS		
0921	LP						HS	F HS	
0961						LP (wear?)			PB
1001			HS		LP	LP (wear?)	PB		PB
1041			LP				F		PB
1081	HS		PB		HS				
1121					HS BR	HS F	deep rod removal scratches	HS	
1161		F				F	HS	BR	
1201	OR F DB?		F	F	F	F HS	HS	F	F
1241	OR F		F	F	F	LP HS	F	F	F
1281				F		LP HS		F	
1321				F	BR				BR
1361	HS					LP	F		HS
1401			HS LP		BR		F	F	BR
1441			HS LP						
1481					HS				
1521	PB DB? HS	PB	OR	PB HS		LP PB	PB	PB	PB
1561	PB	PB LP	OR PB	PB LP HS HM		HS PB	PB	PB	PB
1601	PB	PB LP	PB	PB OR		HS PB	PB	PB BR	PB
1641	PB	PB LP				PB	PB	PB	PB HS

Elevation from rod bottom (approx. mm)	5K7C05	5K7K09	5K7O14	5K7P02	30AD05	30AE14	30AG09	30AK09	30AP02
1681		F	PB F	HS F		PB F HS	PB	PB	BR PB
1721	F	F	F	F	PB		PB	PB	F PB
1761		F	HS F	F PB	HS PB	F HS PB	PB	PB	F PB
1801			F	F PB	PB	PB	PB	PB	
1841	PB			PB	PB	PB	PB	PB	
1881			F	F PB	PB	PB	PB	PB	
1921		F	F	F PB	PB	PB	PB HS	PB	
1962		Local striping	PB	F PB	PB	PB	HM	PB	
2002		Local striping	PB	F PB	PB F	PB	HM	PB	F
2042	F		PB	PB		PB	HM	PB	
2082		LP	PB	PB		PB	HM	PB	
2122			PB	PB	HM	PB	F PB HM	PB	
2162			PB	PB	HM	PB	HM PB	PB	
2202	LP (DB?)		F	PB	PB	PB	PB	PB HS	
2242			F	F	PB	PB	PB	PB	F
2282		F		F PB	PB F	PB	PB	PB	
2322					PB	PB	F PB	PB HS F HM	
2362	LP	HS			PB	PB	F PB	HM	
2402	LP HS	PB			PB	PB HS	PB	HM	
2442		F		HM	PB	HS F HM	PB HM	HM	
2482		F		HM F	HM	HS F HM	PB HM	HM BR	
2522	F	LP PB	F	F HM	HM	Local striping PB HM	PB HM	HM	
2562			F PB	F HM	HM	HM		HM	
2602	HM HS			HM	HM	HM FL PB		HM	
2642	HS	HS		HM	HM	HM HS		HM	
2682				HM	HM	HM	DP HM	HM	
2722	HS	F PB		HM	HM	HM	Heavy HM	HM	
2762	HS	LP		HM	HM	HM HS PB F	Heavy HM	HM	F HS
2802	BR F	F		F HM	HM	F HM	Heavy HM	HM	HS F
2842				HM	HM	HM	Heavy HM	HM	HM
2882		LP		HM	HM	HM PB	Heavy HM	HM	HM
2922		HM		HM	HS HM	HS	Heavy HM	HM	HM
2962				HM	HM	HM HS PB	Heavy HM	HM F	HM
3002	BR		F	HM	HM	HM HS DB?	Heavy HM	HM F	HM
3042	HM HS	F HM	F	F	HM	F HM	HM	HM	F HM
3082	HS	F HM LP	F	HM	HM	F HM	HM	HM	HM
3122	HM	HM		HM	HM	HM	F or DB HM	HM	HM
3162	HM HS	HM		HM		HM	HM	HM	HM
3202	HM HS DB?	HM		HM		HM HS	HM	HM	HM
3243	F HM	HM		HM		HM	HM	HM	HM
3283		HM	F	F HM		HM	HM	HM	HM
3323	BR F		F	F HM	F	HM	HM	HM	HM
3363	HM		HM	HM	HM	HM	HM	HM	HM
3403	FM HM	FM HM	HM	HM	HM	HM HS	HM	HM	HM
3443	HM		HM LP	HM	HM	HM	HM	HM	HM
3483	HS	HM DP DB?	HM HS	HM	HM	HM	HM	HM	HM
3523	HS	HM	HM	HM	HM	HM	HM DP	HM	HM
3563		HM	HM DP	HM	HM	HM	HM	HM	HM
3603		HM	HM OR	HM	HM	HM	HM	HM	HM
3643	FM	FM		HM	HM	HM	HM	HM	HM
3683	HS			HM	HM	HM	HM	HM	HM

December 21, 2018

15

Elevation from rod bottom (approx. mm)	5K7C05	5K7K09	5K7O14	5K7P02	30AD05		30AE14		30AG09	30AK09	30AP02
3723	Locally increased oxide		OR		HM	HS	HM			HM	HM
3763	Locally increased oxide		Locally HO				HM	Locally HO		HM	HM
3803		OR			HS		HM			HM	HM
3843	HS						HM	HS		HM	HS
3891											

Table 3. Visual observations by sister rod elevation, Zirc-4 and LT Zirc-4 rods.

Key: **F**=fretting, **FM**=flow marking, **HS**=handling scratches, **HM**= handling marks, **DP**=dark patch, **LP**=light patch, **HO**=heavy oxide, **SO**=spalling or peeling oxide, **PB**=pellet banding, **FL**=flaky appearance, **UPC**=rod bar code, **DB**=debris, **DS**= dark "scratches", **OR**=peeling oxide rings, **BR**=burnishing; a question mark (?) is meant to imply uncertainty about the observation immediately preceding it. Typical oxidation patterning is not included. Blank cells mean that no features beyond typical were observed.

Elevation from rod bottom (for rods 3A1B16 and 3A1F05) and from rod top for rods F35K13 and F35P17 (approx. mm)	3A1B16	3A1F05	F35K13 (backward)	F35P17 (backward)
0000				
0040		HS LP	HS	HS
0080		HS F		DS HS
0120				HS
0160				
0201				
0241			FM	
0281				
0321		HS		SO FL
0361				SO FL
0401				SO FL
0441			SO	SO FL
0481	HS	HM F HS FM	SO FL	SO FL
0521	HS		SO	SO FL
0562	HS	HS DP	SO	SO
0602		HS F	SO	SO
0642	F	HS DP HM	SO	SO FL
0682		HS DP	SO	SO FL FL
0722		DP LP	SO	SO FL FL
0762	HS	DP LP		SO FL FL
0802		HS DP	SO	SO FL FL
0842		HS	SO	SO FL FL
0882			SO	SO FL FL
0923		PB	SO FL	SO FL FL
0963			SO	SO FL FL
1003			SO FL	SO FL FL
1043	DP		SO FL	SO FL FL
1083			SO	SO
1123		F		SO
1163			SO	SO FL
1203	F		SO FL	SO FL
1244	BR	HS	SO	SO FL
1284			SO	SO FL
1324		FM	SO FL	SO FL
1364			SO FL	SO FL
1404			SO FL	SO FL
1444			SO FL	SO FL
1484	PB		SO FL	SO FL
1524	PB		SO	SO FL
1564	HS	PB or HM	SO	SO
1605	PB LP			
1645	PB	PB		
1685	PB	PB	SO	SO
1725	PB	PB	SO	SO FL
1765	PB HS	PB	SO	SO FL
1805	PB	PB	SO	SO FL
1845	PB	PB	SO	SO FL
1885	PB	PB	SO	SO FL
1925	PB	PB	SO	SO FL
1966	PB	PB		SO FL
2006	PB	PB		SO

December 21, 2018

17

Elevation from rod bottom (for rods 3A1B16 and 3A1F05) and from rod top for rods F35K13 and F35P17 (approx. mm)	3A1B16			3A1F05		F35K13 (backward)		F35P17 (backward)	
2046	PB			PB				SO	
2086	PB			PB					
2126	PB			PB	FL				
2166	PB			PB	FL			HS	
2206	PB			PB	FL				
2246	PB	HO						PB	
2286									
2327				PB					
2367				PB	FL				
2407				PB	FL				
2447	PB	SO		PB	FL				
2487	PB	SO		PB	FL				
2527	PB	SO	HM	PB	FL	HS			
2567	PB		SO	PB	SO				
2607	PB		SO	PB	SO				
2647	PB	SO	HM	FL	PB	SO			
2688	PB	SO	HM	FL	PB	SO			
2728	PB	SO	HM	FL	PB	SO			
2768				PB	SO	F		HS	
2808	PB			PB	SO			PB	
2848				PB	SO				
2888	SO		FL	PB	SO				
2928	HO		FL	PB	SO				
2968	HO		FL	PB	SO				
3009	SO		FL	PB	SO				
3049	SO		FL	PB	SO				
3089	HO		FL	PB	SO				
3129				PB	SO				
3169				PB	SO	HS		FM	
3209				PB	SO	HS			
3249				PB	SO	HS			
3289				PB	SO	HS	DS		
3329				PB	SO	DS			
3370				HO	FL			HM	
3410	FM	SO				FM		FM	
3450									
3490						HS			
3530								HS	
3570								HS	
3610									
3650	FM	HM		FM		FM		FM	
3690	HM								
3731	HM							HS	
3771	HM	UPC		HM	UPC	HS			
3811	UPC			UPC		HS	HM		
3851	HM	UPC		HM	UPC	HS		HS	
3891									

3.1.2 Typical Waterside Cladding Appearance of M5-Clad Rods

Figure 8 and Figure 9 provide a summary of images representative of the M5 visible features. The M5 rods typically exhibited very light waterside oxide visible in the majority of the images as irregular, somewhat circular patches. Some areas also include an interior circular patch that appears to have peeling oxide, as illustrated in Figure 9(i). Some shallow GTRF marks are visible, along with rod removal scratches. Some localized areas of the M5 rods have thin CRUD layers, presenting with the appearance of a peeling thin skin, as shown in Figure 9(a) and (b). Most of the M5 rods have shallow-to-moderate GTRF marks at the axial locations corresponding to the spacer grid elevations. Also, since not all of the spacer grids in the Framatome-designed assemblies are fixed axially, some GTRF marks have an extended length, as shown in Figure 9(e).

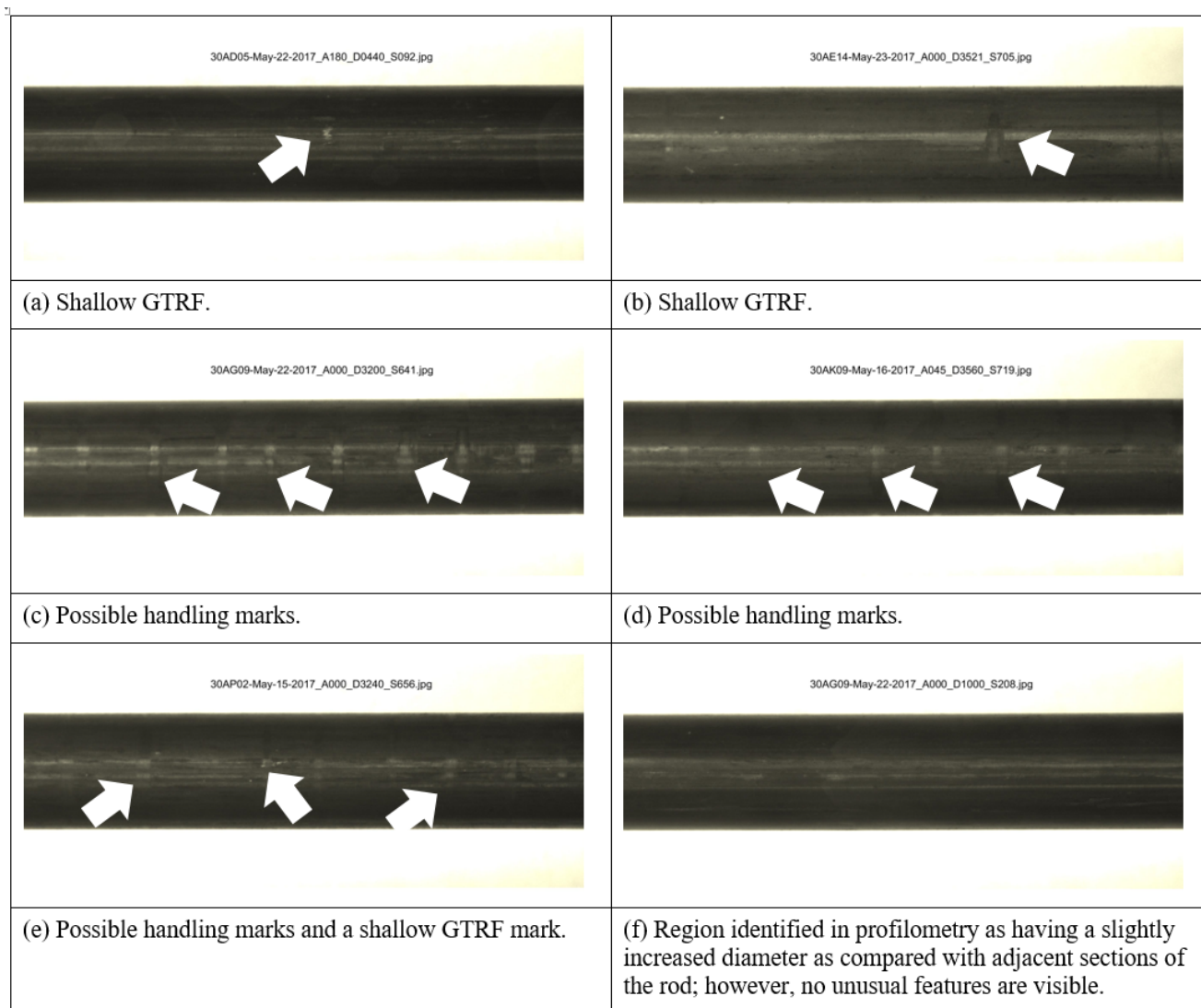


Figure 8. Selected Visual Observations from Assembly 30A.

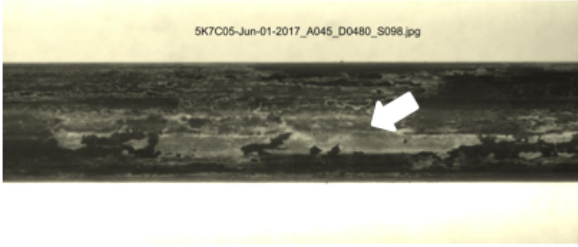
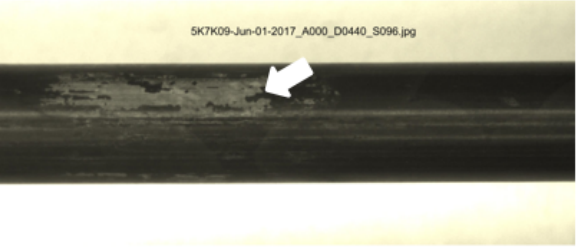
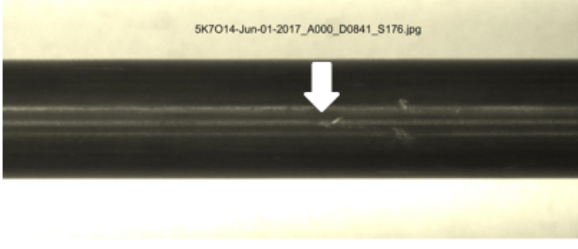
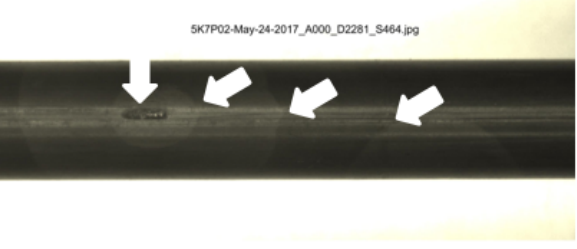
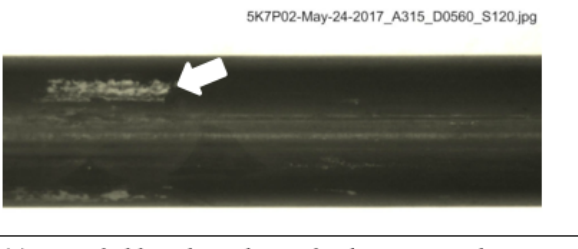
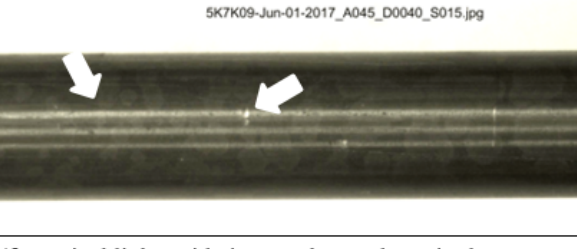
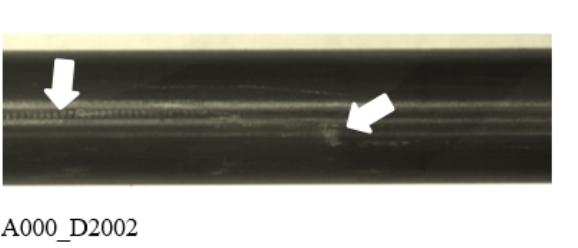
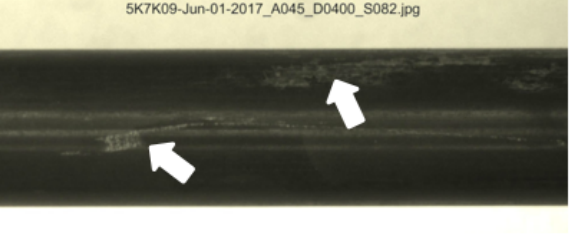
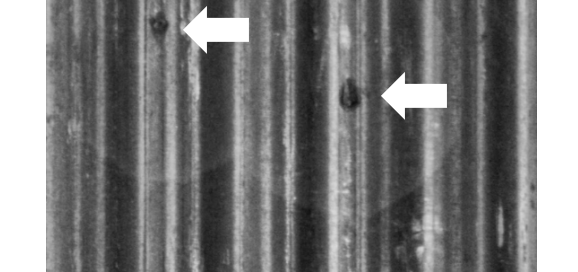
	
(a) Localized CRUD peeling.	(b) Localized CRUD peeling.
	
(c) Shallow GTRF	(d) Shallow GTRF with light oxidation in circular patches.
	
(e) Extended length moderate depth GTRF mark.	(f) Typical light oxidation patches and manipulator scratches.
 <p>A000_D2002</p>	
(g) Typical rod removal scratch and a shallow GTRF mark.	(h) Shallow GTRF with rod removal scratch and peeling CRUD.
	<p>(i) an example of center peeling oxide rings (note the image was extracted from a flattened collage and the axial direction of the rod is oriented perpendicular to the other images shown on this page).</p>

Figure 9. Selected Visual Observations from Assembly 5K7.

3.1.3 Typical Waterside Cladding Appearance of ZIRLO-Clad Rods

The ZIRLO-clad rods have a moderate-to-heavy oxide layer, with some oxide peeling and spalling observed. GTRF marks are present on most rods and range in severity from shallow to deep. Figure 10 to Figure 12 illustrate these details. No visible signs of through-wall cladding damage were observed. Darker regions are present at grid elevations, indicating either CRUD or possibly a thinner oxidation layer (attributed to better heat transfer in those areas due to flow turbulence). A dark band on rod 6U3P16 is clearly a pellet-pellet gap as identified by gamma scan, as noted in Figure 11(h).

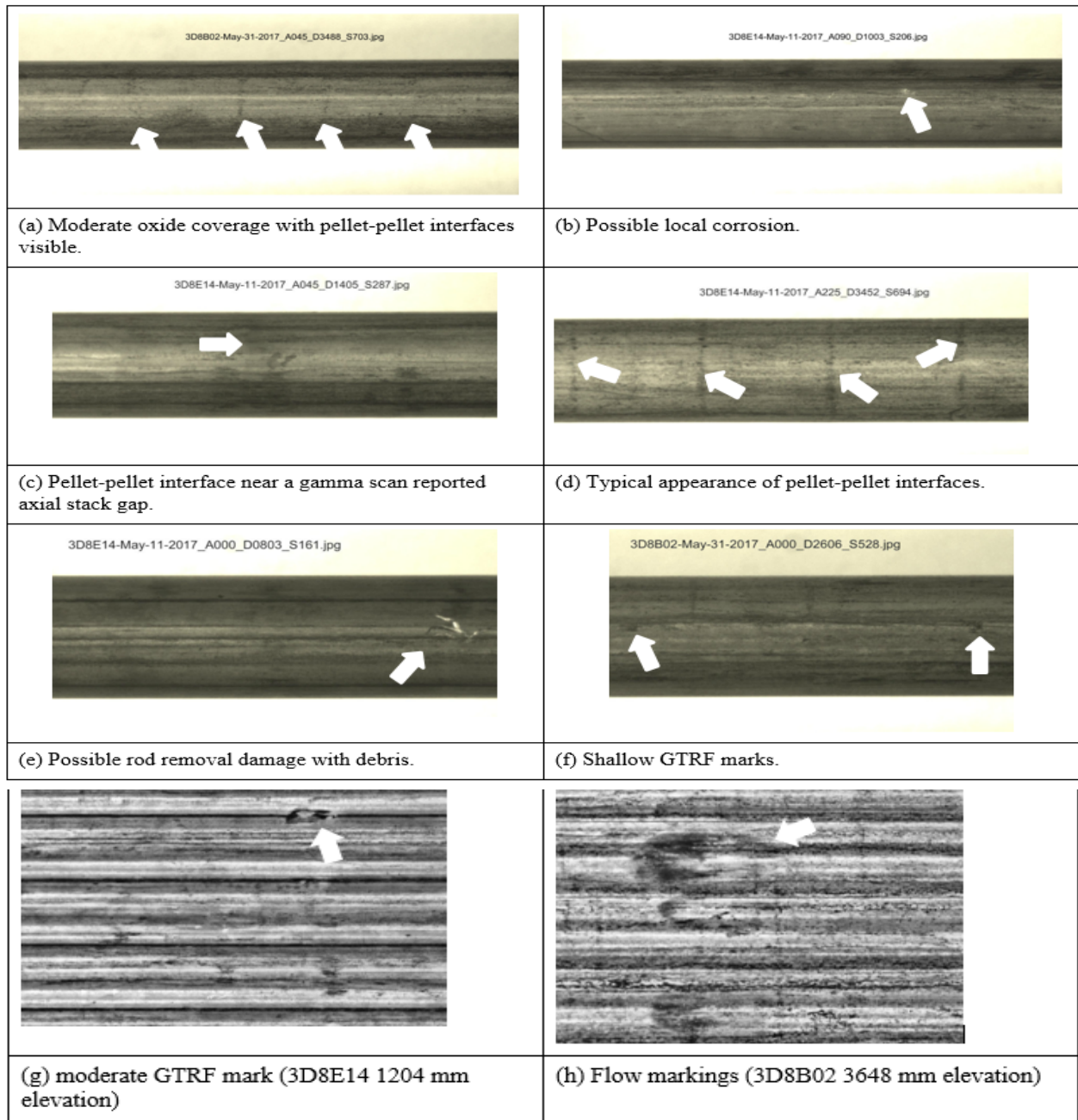


Figure 10. Selected Visual Observations from Assembly 3D8.



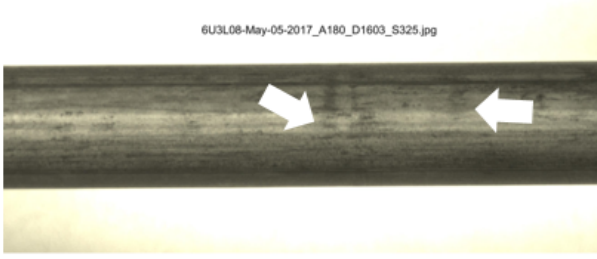



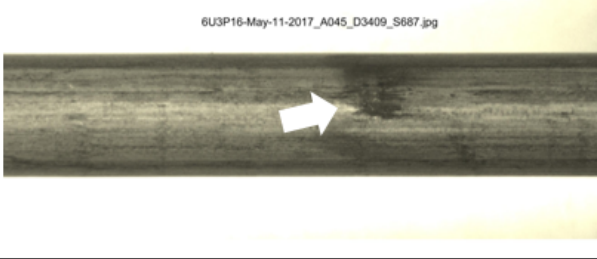
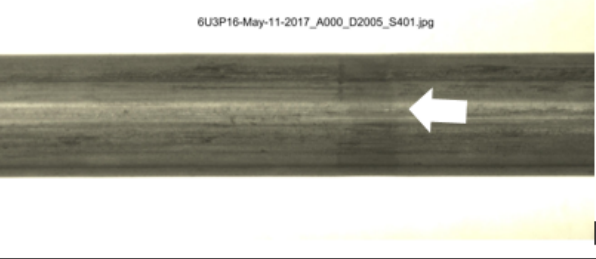
	
(a) Relatively deep GTRF.	(b) Moderate GTRF.
	
(c) Possible handling marks and pellet-pellet interface bands.	(d) Possible handling marks and pellet-pellet interface bands.
	
(e) Rod insertion or removal scratch with shallow GTRF.	(f) Possible handling marks.
	
(g) Flow marking (darker region) associated with turbulent flow around a spacer grid with a shallow GTRF mark.	(h) Banded region is pellet-pellet gap (~5 mm) noted by gamma scan and measured by profilometry.

Figure 11. Selected Visual Observations from Assembly 6U3.

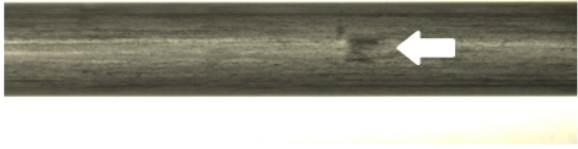
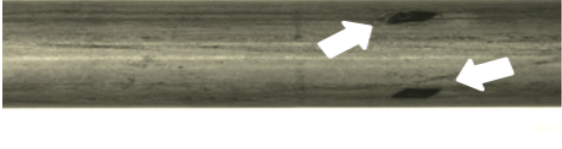
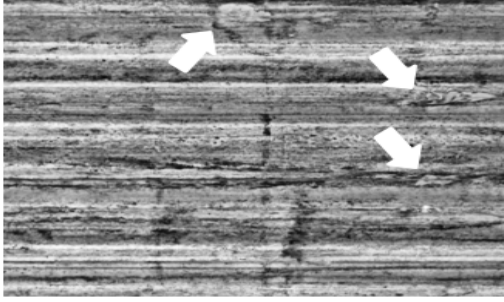
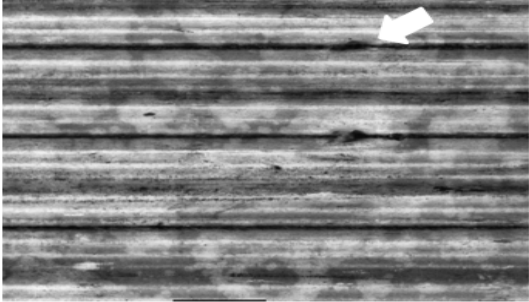
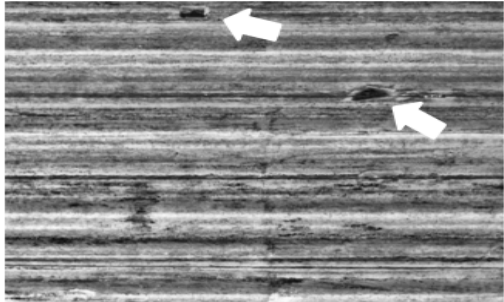
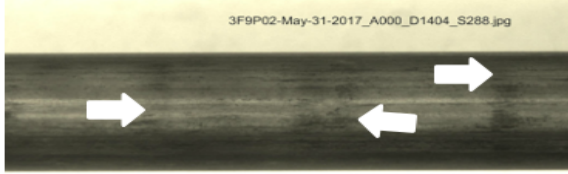
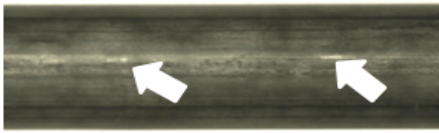
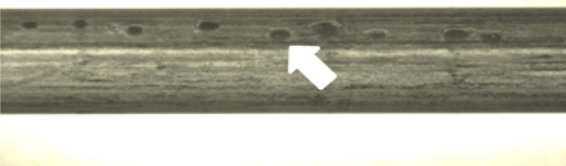

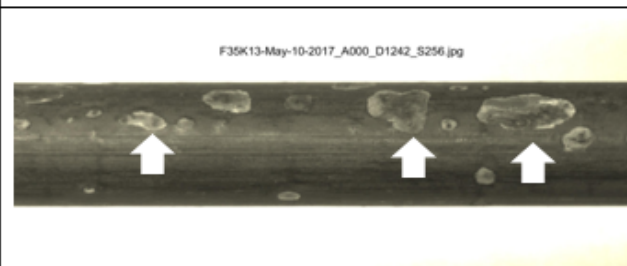
	
(a) Shallow GTRF.	(b) Deep GTRF.
	
(c) Moderate GTRF, completely oxidized, and a patch of locally heavy oxidation.	(d) Moderate GTRF.
	
(e) Moderate GTRF that likely occurred during an early cycle since the mark appears to be partially oxidized.	(f) Typical appearance of pellet-pellet interfaces; this section near a gamma scan-reported axial stack gap (~3 mm).
	
(g) Very shallow apparent GTRF.	(h) Some oxide peeling was noted.
	(i) Unwrapped image (all azimuthal locations at 2246 mm elevation) of 3F9D07, moderate to deep fretting wear.

Figure 12. Selected Visual Observations from Assembly 3F9.

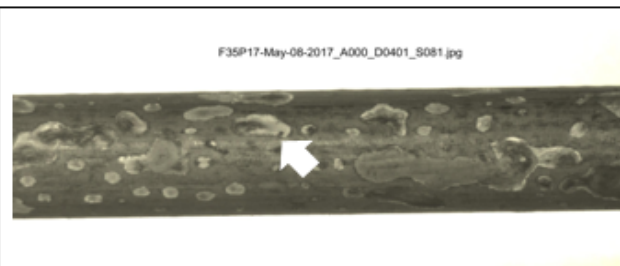
3.1.4 Typical Waterside Cladding Appearance of Zircaloy-4 and LT Zircaloy-4-Clad Rods

Assemblies 3A1 and F35 (Figure 13 and Figure 14) appeared to have the greatest amount of oxide buildup/spalling. No visible signs of through-wall damage or large areas of clad degradation were found. A thin layer of CRUD appears to be visible in spalled regions, having the appearance of a black rim around the base of the spalled area, as shown in Figure 13(d). Some areas of significant oxidation have a flake-like appearance, as shown in Figure 14(g) and (h). Some shallow GTRF marks are visible, and some features that appear to be GTRF marks that have oxidized in later cycles are visible (see Figure 63 for an example). In the case of the oxidized GTRF marks, it is not possible to estimate depth, and eddy current measurements are relied upon to detect deep oxidized GTRF marks (see Section 3.4.2).

These rods were loaded into the shipping packaging and hot cell backwards and consequently were scanned in the opposite direction from the other sister rods. The distance is measured from the top of the rod rather than the bottom.



(a) Significant oxide spalling; some pellet-pellet interface bands are visible.



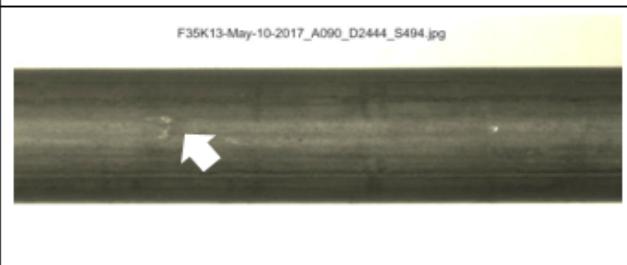
(b) Significant oxide spalling.



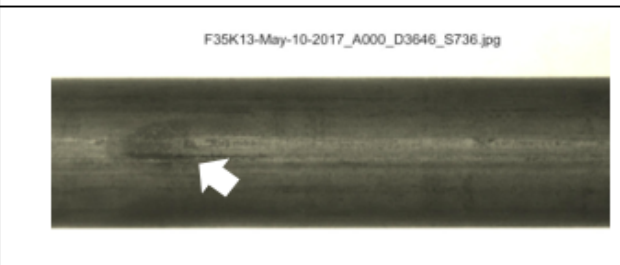
(c) Shallow GTRF.



(d) Significant oxide spalling with CRUD; an indication of the oxide thickness is visible at the upper edge of the rod image.



(e) Shallow GTRF.



(f) Flow pattern at a grid elevation.

Figure 13. Selected Visual Observations from Assembly F35.


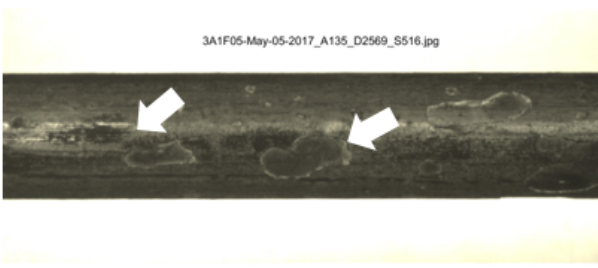
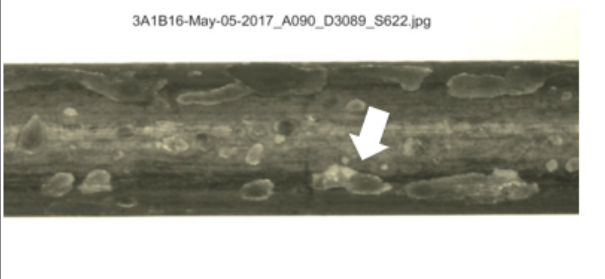
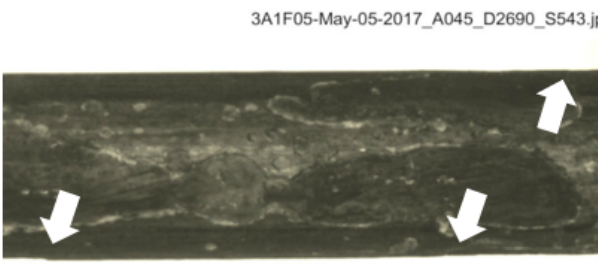

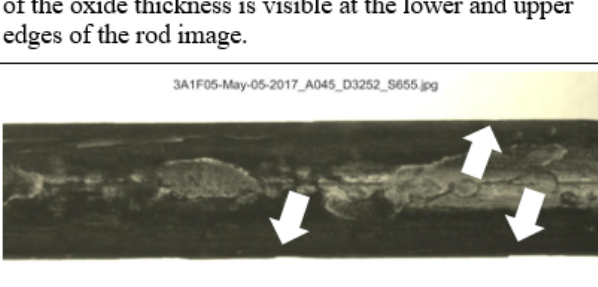
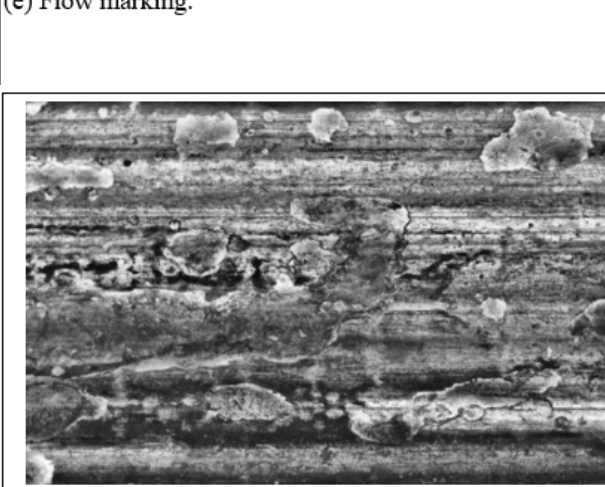
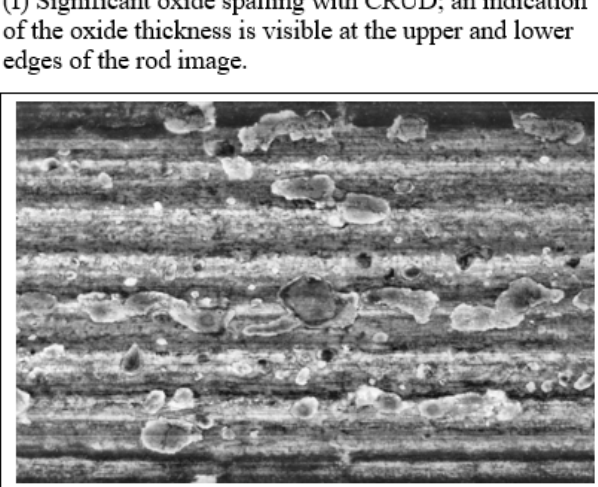
	
(a) Moderate GTRF mark.	(b) Significant oxide spalling with some peeling CRUD.
	
(c) Significant spalling oxide.	(d) Significant oxide spalling with CRUD; an indication of the oxide thickness is visible at the lower and upper edges of the rod image.
	
(e) Flow marking.	(f) Significant oxide spalling with CRUD; an indication of the oxide thickness is visible at the upper and lower edges of the rod image.
	
(g) Unwrapped image (full rod circumference shown at 3252 mm elevation) of 3A1F05, heavy oxide layer with spalling.	(h) Unwrapped image (all azimuthal locations at 3089 mm elevation) of 3A1B16, heavy oxide layer with spalling.

Figure 14. Selected Visual Observations from Assembly 3A1.

3.2 NDE.02 Gamma and Neutron Scanning

Three sets of integrated radiation measurements were completed, including: (1) one-dimensional scans using the ADEPT's sodium iodide (NaI) detector; (2) high resolution gamma spectroscopy using a high-purity germanium (HPGe) detector, and (3) gamma and neutron measurements using a fission/ionization chamber-based fork detector. The HPGe and fork detector measurements were performed for the NNSA, Office of Nonproliferation and Arms Control (NPAC), and are summarized here for completeness.

Figure 15 compares the four normalized gamma count rate data sets for sister rod 30AE14 measured using the three different detectors (the HPGe measurements include two gamma counts, ^{137}Cs and total). For reference, the normalized predicted average assembly axial burnup profile is also plotted. There is very good agreement in the general trends and locations of spacer grid burnup depressions. Up to 7% differences were observed between the fork gamma counts and the HPGe total gamma counts near the rod bottom, likely due to the fact that a collimator is not used in the fork measurement, but even so, there is good agreement between all three detectors in the higher burnup regions of the rod. Radiochemical assay of selected rod locations will provide additional definitive (within measurement uncertainty) burnup measurements.

The following sections describe the results afforded by each gamma/neutron measurement campaign.



Figure 15. Comparison of Gamma Count Rates Collected by Three Different Detectors for Sister Rod 30AE14: HPGe, fork, and NaI. The Normalized Predicted Average Assembly Axial Fuel Burnup is Also Plotted for Reference.

3.2.1 One-Dimensional Sodium Iodide Gamma Scanning

A one-dimensional gamma scan (resolution of ~1mm obtained using a long, adjustable-width collimator) was completed using the ADEPT on all 25 rods in 2 energy ranges: 400 to 800 keV for examination of the fuel stack and 1,100 to 1,600 keV for examination of the structural components. ADEPT's special purpose sodium iodide (NaI) detector is 152.4 mm long and 12.7 mm in diameter for maximum detection of the signal from the region of interest. The NaI detector was selected so that ADEPT can maximize the gamma signal at the expense of energy resolution.

The count time used for sister rod measurements was 20s each except for the first rod, which was scanned for only 15s. Although the 15s scan was judged sufficient based on the results for the first rod and the rod was not rescanned, the count time was increased to 20s for conservatism for the remainder of the rods. The signal from this lower scan time was later scaled for comparison with the other rods. The longer scan time was chosen after the results from the first rod were obtained because the facility's operating schedule limited the rod change intervals, and the longer scan time allowed for maximum data collection in the allocated time. During the scan, the rod was translated axially, but it was not rotated. The two energy ranges were collected simultaneously. Data were collected in 1 mm increments along the axis of the rod and were indexed to the bottom of the rod.

The results of the gamma scanning length measurements are summarized in Table 4. The activity signal exhibited the expected behavior without any sign of fission product accumulation or migration. The axial profile of the rods was as expected, and depressions in burnup were easily observed at the spacer grid locations. Figure 16 through Figure 22 provide graphs of the gamma scanning data and summarize the measurement data obtained for the sister rod (note that the length data indicated in the graphs are those measured during the gamma scans only, see Table 4). The graphs plot the rod activity as a function of axial length, and although the rod burnup cannot be estimated based on the gamma scans, the axial profile is analogous to the axial burnup of the fuel. In addition to the gross gamma counts measured for each sister rod, the graphs also plot the utility-predicted assembly average burnup (where available), normalized and scaled to a corresponding average gamma count, for comparison with the measured axial profiles. As a first order approximation, the gamma total counts tend to trend with the average pin burnup; however, other factors such as cooling time influence the total gamma counts.

The rod length was measured by the ADEPT apparatus during the gamma scanning as a part of the rod indexing. The uncertainty of the overall rod length is determined by the positional accuracy of the ADEPT resolvers, 0.5mm, derived through repeated measurements of the same rod and applicable over the total length of the fuel rod (on the order of 3,900 mm). The uncertainty of the gamma-determined lengths/locations is influenced by both the uncertainty associated with the gamma collimator width (1 mm) and the positional uncertainty of the ADEPT apparatus (0.5 mm). The total uncertainty of gamma-determined lengths/locations is therefore conservatively estimated as the absolute value of the sum of the individual uncertainties, 1.5 mm (the movement uncertainty depends on rod friction with the drive and resolver wheels and is difficult to characterize).

The overall rod length measurement (see Section 3.3) facilitated the measurement of axial rod components that do not produce a gamma signal (e.g., bottom-end plug, top-end plug). Because of the very weak signal, the bottom-end plug's length (location) was determined by the start value of the pellet stack. The top-end plug length (location) was determined by subtracting the end value of the spring location from the rod's length.

Both the fuel stack length and the plenum length (spring) were inferred from the gamma scan data. The plenum region has a much lower gamma signature, since there is no fuel in that region. However, the gamma source provided by the fission gases and activation of the plenum spring allow the plenum region to be differentiated from the top-end plug. Note that none of the sister rods have a lower plenum spring. The top and bottom of the pellet stack produce a gamma scattering effect that is observable as a sharp reduction in the scan count rate.

Since the dish and chamfer regions are large enough to provide a significant drop in gamma source term, the gamma scan allows for differentiation of every pellet in the rod. This is visible in the full-length rod graphs (Figure 16 through Figure 22) as chatter in the data. Zooming into a specific segment of the rod, as illustrated in Figure 23, provides differentiation of each pellet. An estimate of the number of pellets in each fuel rod was determined by spectral methods in which the gamma scanning data were examined for shallow reductions in the fuel stack gamma count associated with pellet end geometry (chamfers and dishes). The average pellet length was determined by dividing the pellet stack length by the number of pellets counted. Since partial pellets are not used, the fractional estimated number of pellets was rounded off to the nearest integer value.

Because each pellet is visible, axial gaps in the stack (either pellet-pellet gaps or pellet end capping, which is material missing from the ends of the pellet resulting from die or handling issues during manufacture) can also be observed, and the gap length can be estimated. Where the gamma count is significantly lower than observed for normal pellet end effects, the data on each side of the count rate reduction were examined, and the length of the pellet-pellet gap was estimated. The results are summarized in Table 5. The uncertainty of the gap measurements is evaluated as ± 1.5 mm since the observation is a product of both rod length and gamma measurements. However, as discussed previously, the ± 0.5 mm resolver uncertainty is distributed over the entire length of the rod, and the local uncertainty for the gap measurement is nearer to ± 1 mm. Since some of stack gaps reported in Table 5 are 1 mm in length, the uncertainty of ± 1 mm implies that these stack gaps may not exist, or they may be as large as 2 mm. Likewise, for all locations where a gap was not indicated, there is a possibility that a 1 mm gap exists but was not detected.

No serious structural defects were noted in any of the rods because of the gamma scanning; some small fuel stack gaps were observed, and the largest was estimated as 5 mm on sister rod 6U3P16.

Table 4. Results of gamma scanning grouped by rod type (± 1.5 mm, except for rod length, ± 0.5 mm).

Rod	Average pellet length (mm)	Estimated number of pellets in the stack	Average pellet length for type (mm)	Average pellet number for type	Bottom plug length (mm)	Top plug length (mm) ^{Note 1}	Plenum length (mm)	Average plenum length for type (mm)	Fuel stack length (mm)	Average fuel stack length for type (mm)	Overall Rod Length (mm) ^{Note 1}	Overall Rod Length (mm) ^{Note 2}	Average rod length for type (mm) ^{Note 2}
30AE14	10.3	357	10.2	359	14	9	184	182	3,674	3,677	3,881	3,881	3,882
30AK09	10.2	361			14	10	178		3,679		3,881	3,881	
30AD05	10.3	358			14	10	185		3,677		3,886	3,886	
30AG09	10.2	359			13	10	185		3,674		3,882	3,881	
30AP02	10.3	359			14	9	179		3,679		3,881	3,881	
6U3O05	9.9	372	9.9	372	20	12	182	179	3,676	3,679	3,890	3,890	3,890
6U3I07	9.9	373			20	13	175		3,680		3,888	3,888	
6U3M03	9.9	372			20	12	178		3,682		3,892	3,892	
6U3M09	9.9	372			18	13	183		3,675		3,889	3,889	
6U3K09	9.9	372			19	12	179		3,679		3,889	3,889	
6U3L08	9.9	373			19	13	175		3,683		3,890	3,890	
6U3P16	9.9	371			20	12	179		3,679		3,890	3,890	
5K7C05	10.2	362	10.1	363	14	9	180	181	3,680	3,679	3,883	3,884	3,884
5K7K09	10.2	362			14	10	185		3,675		3,884	3,884	
5K7O14	10.1	364			14	10	176		3,684		3,884	3,884	
5K7P02	10.1	364			14	9	182		3,678		3,883	3,882	
3A1B16	10.0	370	9.9	371	10	9	193	192	3,680	3,682	3,892	3,892	3,893
3A1F05	9.9	371			10	10	190		3,684		3,894	3,894	
3F9D07	9.9	374	9.9	374	20	12	174	177	3,684	3,682	3,890	3,890	3,891
3F9N05	9.8	374			20	13	178		3,681		3,892	3,892	
3F9P02	9.9	373			19	13	178		3,681		3,891	3,891	
3D8B02	10.0	367	10.1	367	20	12	174	175	3,683	3,685	3,889	3,889	3,891
3D8E14	10.1	367			19	12	175		3,687		3,893	3,894	
F35K13	13.7	269	13.7	270	10	9	178	175	3,690	3,695	3,887	3,887	3,888
F35P17	13.6	272			11	8	172		3,699		3,890	3,890	

Notes on Table 4:

1. Calculation is based on the average overall rod length measured during the gamma scanning.
2. Based on multiple length measurements taken over the whole NDE campaign.

Table 5. Fuel stack gaps observed through gamma scanning (± 1 mm).

Rod*	Location from rod bottom (mm)	Estimated gap width (mm)
30AD05	3,635	1
	3,646	2
	3,657	2
	3,667	1
	3,678	2
6U3P16	2,010	5
6U3K09	453	1
5K7P02	448	1
5K7C05	755	2
	948	1
	1,559	2
3F9D07	462	2
3F9P02	1,303	2
	1,313	1
	1,373	2
3D8E14	1,403	3
F35P17	1,655	3

*Rods not listed did not have an observed stack gap (within the stated ± 1 mm uncertainty).



Figure 16. Gamma Scans for Sister Rod from Fuel Assembly 30A.



Figure 17. Gamma Scans for Sister Rod from Fuel Assembly 5K7.

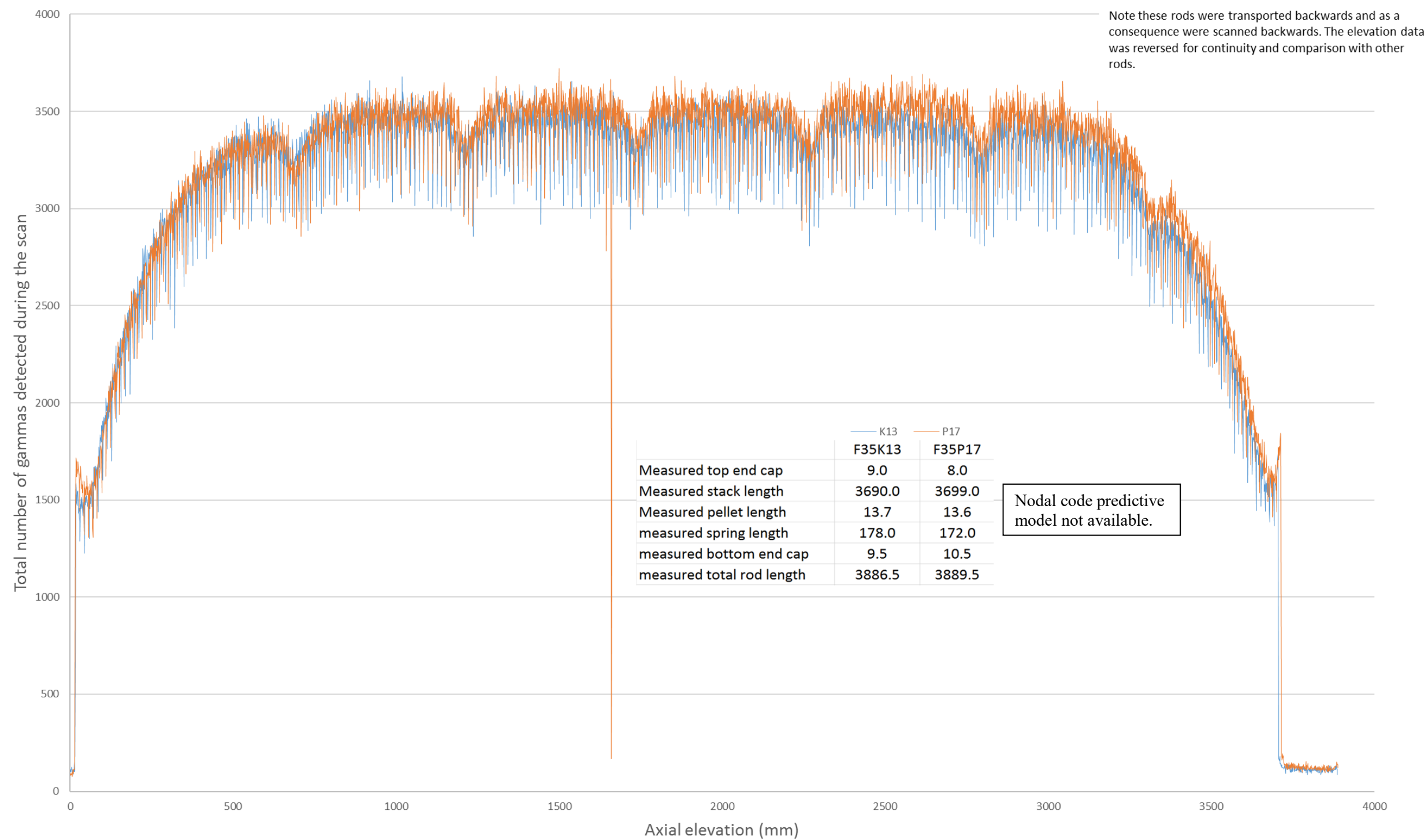


Figure 18. Gamma Scans for Sister Rod from Fuel Assembly F35.

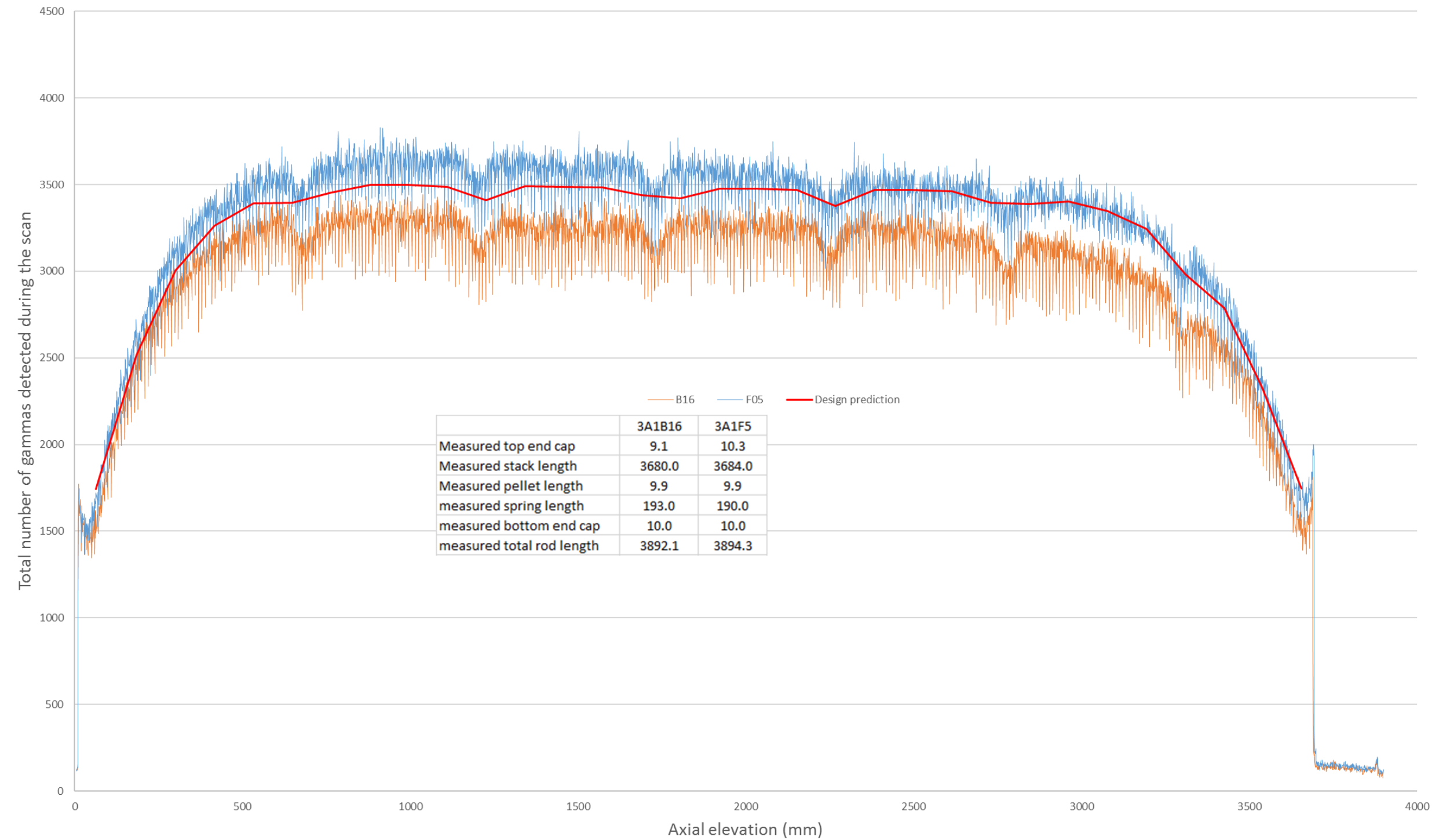


Figure 19. Gamma Scans for Sister Rod from Fuel Assembly 3A1.



Figure 20. Gamma Scans for Sister Rod from Fuel Assembly 3F9.



Figure 21. Gamma Scans for Sister Rod from Fuel Assembly 3D8.

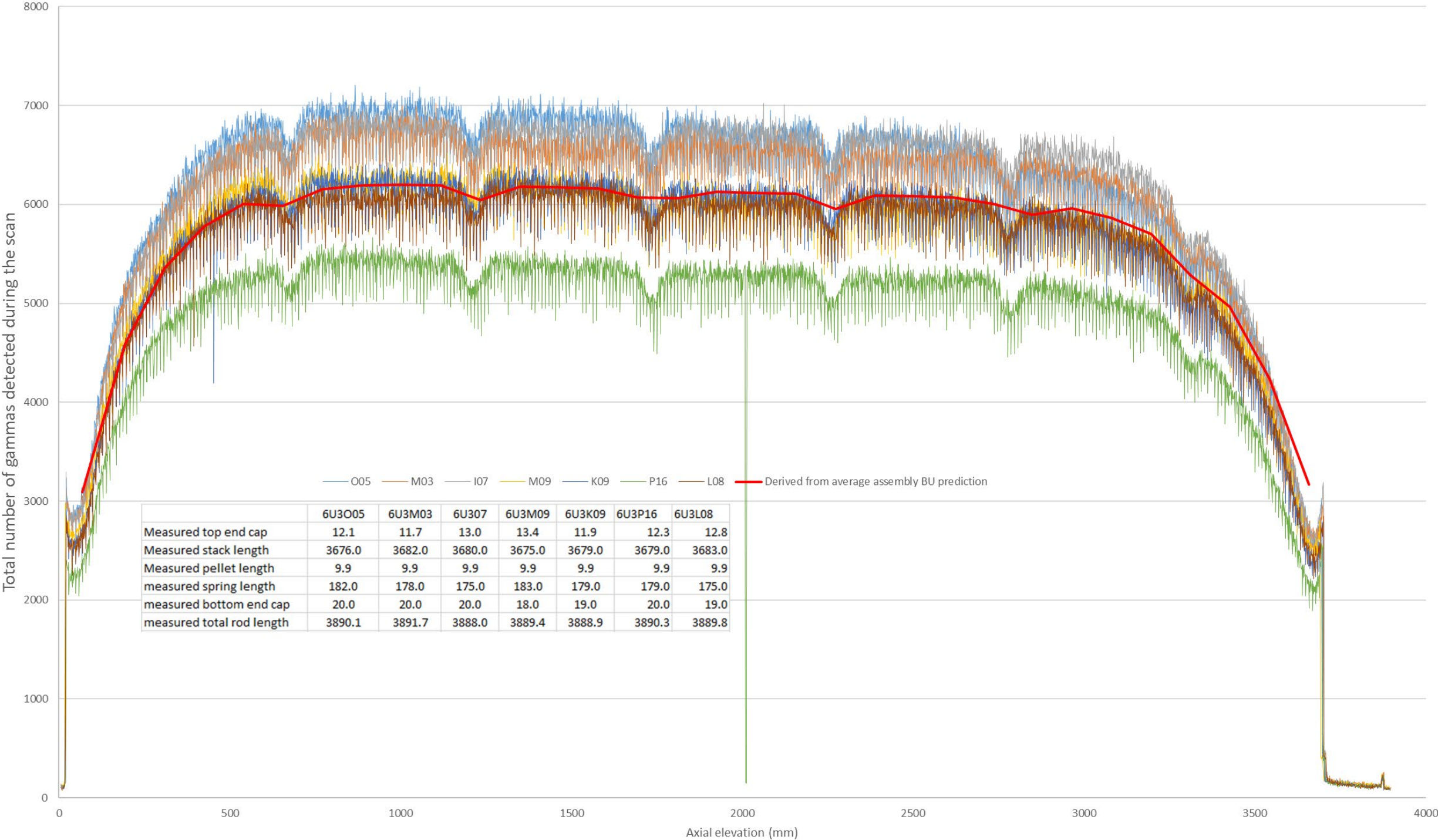


Figure 22. Gamma Scans for Sister Rod from Fuel Assembly 6U3.

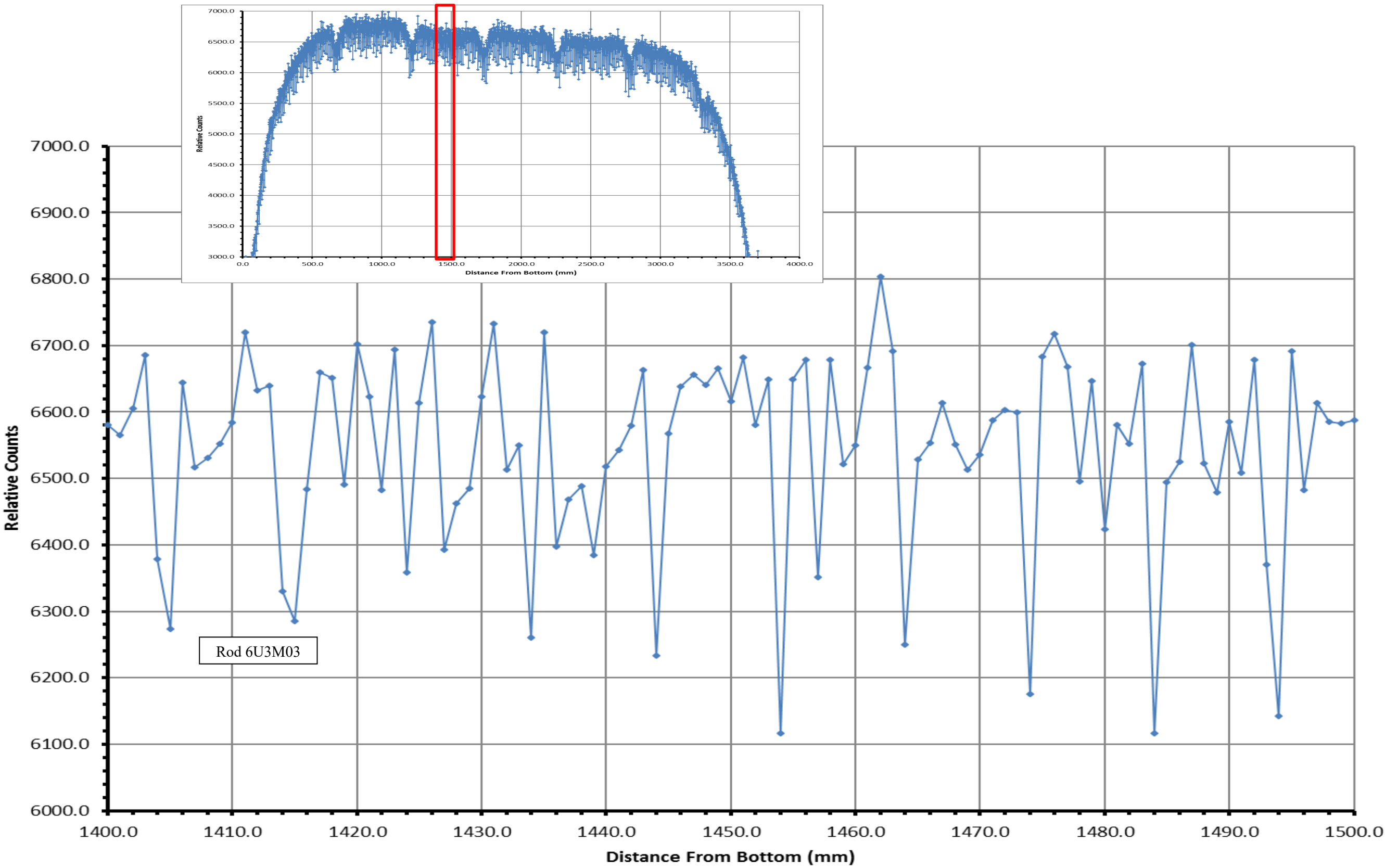


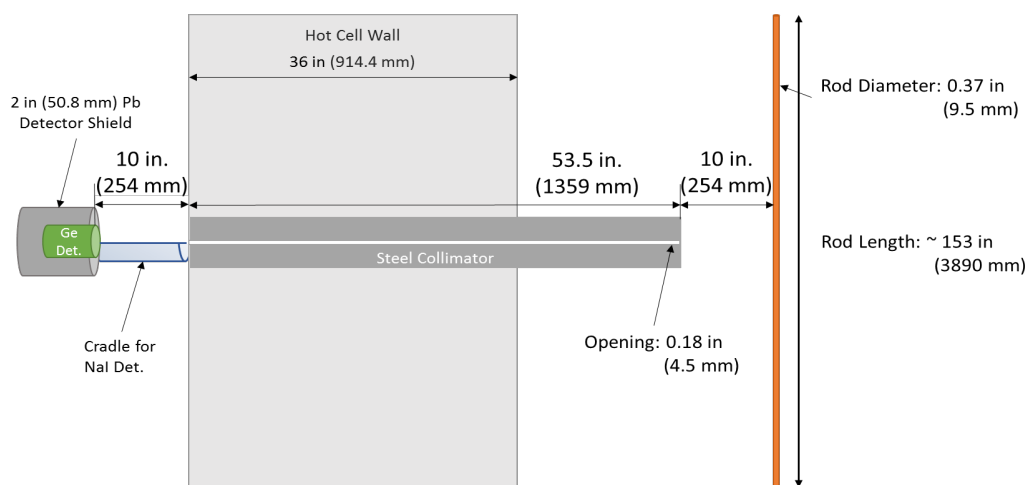
Figure 23. Typical Pellet Ridging on a Fuel Rod Observed Via Gamma Scanning; Scales are Magnified to Show the Detail. The Typical Pellet is Approximately 10mm Long.

3.2.2 HPGe Detector Scanning

International nuclear safeguards use NDE techniques to verify the declared characteristics of SNF assemblies. These characteristics usually include initial fuel enrichment, assembly average burnup, and irradiation history. A recurring requirement for the use of high-resolution gamma spectroscopy as a technique for safeguards verification is the calibration of the gamma-ray peak intensities or areas to the isotopic content of the fuel at discharge. Typically this is accomplished through simulation or measurement of several known SNF assemblies. Two questions are raised by these methods of calibration: (1) to what extent are the simulation codes sufficiently validated against real spectroscopy measurements, and (2) how can the burden of independent SNF calibration measurements taken during a facility inspection be reduced? Measurement of the sister rods using the HPGe detector provides a unique opportunity to begin addressing both calibration concerns. This section describes a preliminary evaluation of the spectra performed thus far. A report on the HPGe scanning with a catalog of the spectra collected can be found in Smith et al. [4].

All 25 sister rods were scanned using a high-resolution HPGe gamma spectrometer. The measurement dwell time was restricted by the working hours of the hot cell facility, and only two rods could be scanned in 24 h, one during the daytime and the second overnight. Scans could not be performed over the weekends, but the time was used to take long background measurements of the hot cell with and without a dummy rod. The purpose of the dummy rod is to get a better estimate of how much background from the hot cell is directly blocked by the SNF rod. Background subtraction is preferred because it reduces the possibility of overestimating the background contributions when doing the spectrum analysis.

Figure 24 and Figure 25 illustrate the detector measurement geometry and configuration for the HPGe measurement campaign. The detector chosen for the measurements is a large p-type semi-planar HPGe manufactured by Canberra Industries (model BE3820), also known as a broad-energy germanium detector (BEGe). The energy resolution of the BE3820 is nominally <750 eV at 122 keV and <1900 eV at 1332 keV. The collimator's NaI detector cradle cannot be removed, and because the HPGe detector is larger in diameter than the NaI detector, it does not fit into the NaI cradle. Therefore, it had to be placed 254 mm from the face of the collimator. The sliding wedge aperture of the collimator was opened to approximately 4.5 mm such that the full diameter of the rod was in the field of view.



The steel collimator extends through and beyond the hot cell concrete wall to within 10 in of the fuel rod. A cradle is built onto the end of the collimator for the NaI detector measurements and could not be removed for the HPGe detector measurements.

Figure 24. Diagram of the Measurement Geometry for the HPGe Campaign.

Since the area of the HPGe detector used is much larger than the aperture, it is the collimator that determines the count rate. A 50.8 mm thick modular lead shielding and positioning assembly was used to shield potential room background and improve measurement reproducibility.

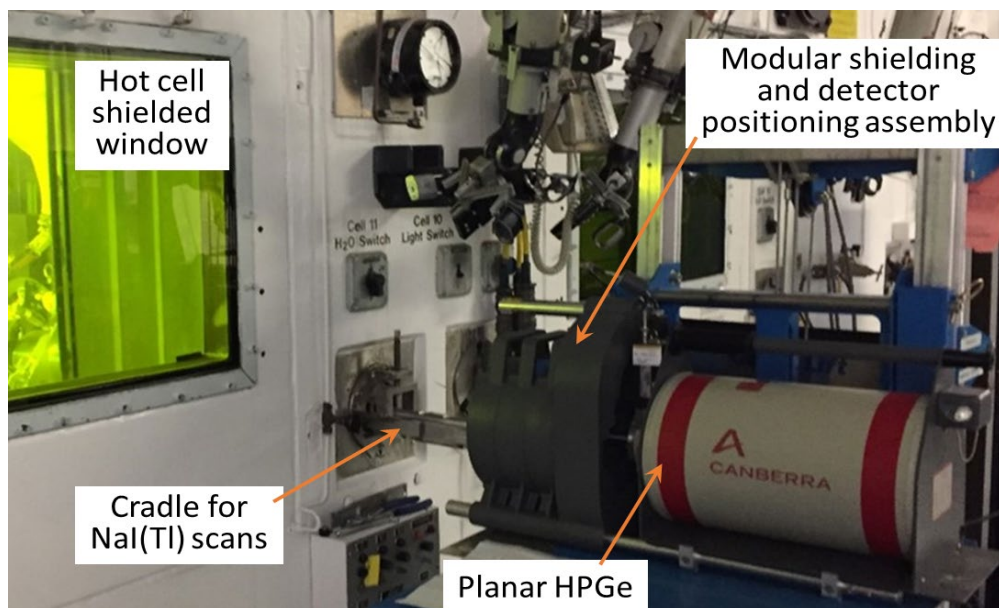


Figure 25. Picture of the HPGe Detector during Spectroscopy Measurements.

The IFEL was equipped with a CANBERRA DSA 2000 multichannel analyzer and CANBERRA Genie 2000 software V3.2.1 to perform the data acquisition. The digital signal processing settings were configured to acquire a spectrum of 8,192 channels and an energy range from 0-3,045 keV. Live time correction was enabled, so a reference pulser/source was not used to correct for dead time.

For the axial scans, 700 spectra were collected in discrete steps of approximately 5.56 mm along the entire length of the fuel rod (3,890 mm). Typically, an 18s live time was used for scans performed during the workday, and a 50s live time was used for scans performed overnight. These settings were selected as a tradeoff between count time and dead time to ensure that two rods could be measured each calendar day. The elapsed exam time was measured in terms of live time, so it varied somewhat with incoming count rate.

The individual spectrum from each measurement point was collected using a user-defined prefix, the date, and the position of the rod during that measurement file naming scheme. The data collected associated with sister rod 30AD05 are discussed in this summary report to illustrate the results obtained. For a complete discussion of the data and results, please see Smith et al. [4].

Assembly 30A has average declared burnup of 52 GWd/MTU and was discharged from the reactor core 6–7 years ago. It was expected that the spectra for 30AD05 would be dominated by the three long-lived fission products that emit gamma rays: ^{134}Cs , ^{137}Cs , and ^{154}Eu . Figure 26 illustrates the energy spectrum of a single point selected from the 700 axial point spectra acquired with the HPGe detector along the length of rod 30AD05 using the PeakEasy Software program [5]. The summed spectrum shown in Figure 26 clearly shows these isotopes. Additionally, the radiation-induced x-rays from uranium are clearly visible. Above the 1,596 keV ^{154}Eu gamma ray, the spectrum is dominated by small peaks from random coincidence summing.

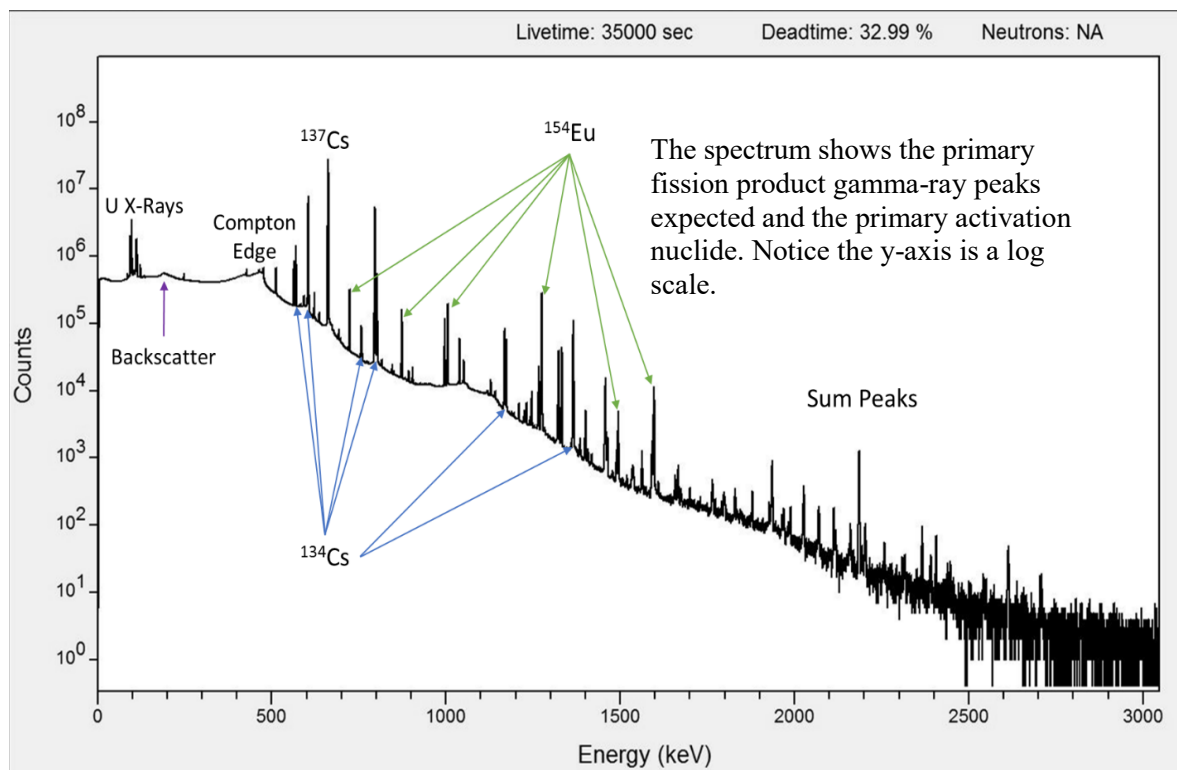


Figure 26. HPGe Sum Spectrum of Sister Rod 30AD05.

From the axially collected 700 point spectra, individual dead time-corrected total counts from an energy region of interest (ROI) can be plotted against the axial rod position where the data were acquired. It is expected that the total count rates will be approximately constant (within statistics) along the central portions of the sister rod that contain fuel (drop off is expected at the ends of the fuel stack), consistent with an efficient in-reactor use of the fuel. The fuel rod plenum region is dominated by ^{60}Co from the irradiation of the spring in the plenum.

Figure 27 shows the axial scan gross counts for sister rod 30AD05 for a ROI around the 661.6 keV peak from ^{137}Cs . Spacer grid depressions in burnup are visible as reductions in the total count rates. The overall burnup profile measured using the HPGe detector agreed very well with the results achieved using the NaI detector. However, the sliding wedge aperture of the collimator was only opened to 1 mm for the NaI scans. Because of the narrow width of the collimator used with the NaI detector, count rate reductions could be seen in the data corresponding to the transition between individual fuel pellets (see Section 3.2.1). Because the HPGe detector has a lower efficiency and required a much larger aperture opening, this granularity was not achieved.

With the support of the NNSA's Office of Global Material Security, additional measurements were performed to determine whether scintillator detectors could be used for burnup calculation. A coaxial HPGe detector, a 50.8×50.8 mm NaI detector, and a lanthanum bromide (LaBr_3) detector were used to measure sister rod 3D8B02 at a single location (2,000 mm from the bottom) using essentially identical detector positions. The coaxial HPGe and BEGe detector measurements were performed in the same position as the BEGe in the axial scans previously described. The NaI and LaBr_3 were placed in the cradle at respective distances of 54.0 mm and 50.8 mm from the steel collimator. The rod was measured with each detector for a live time of 30 minutes.

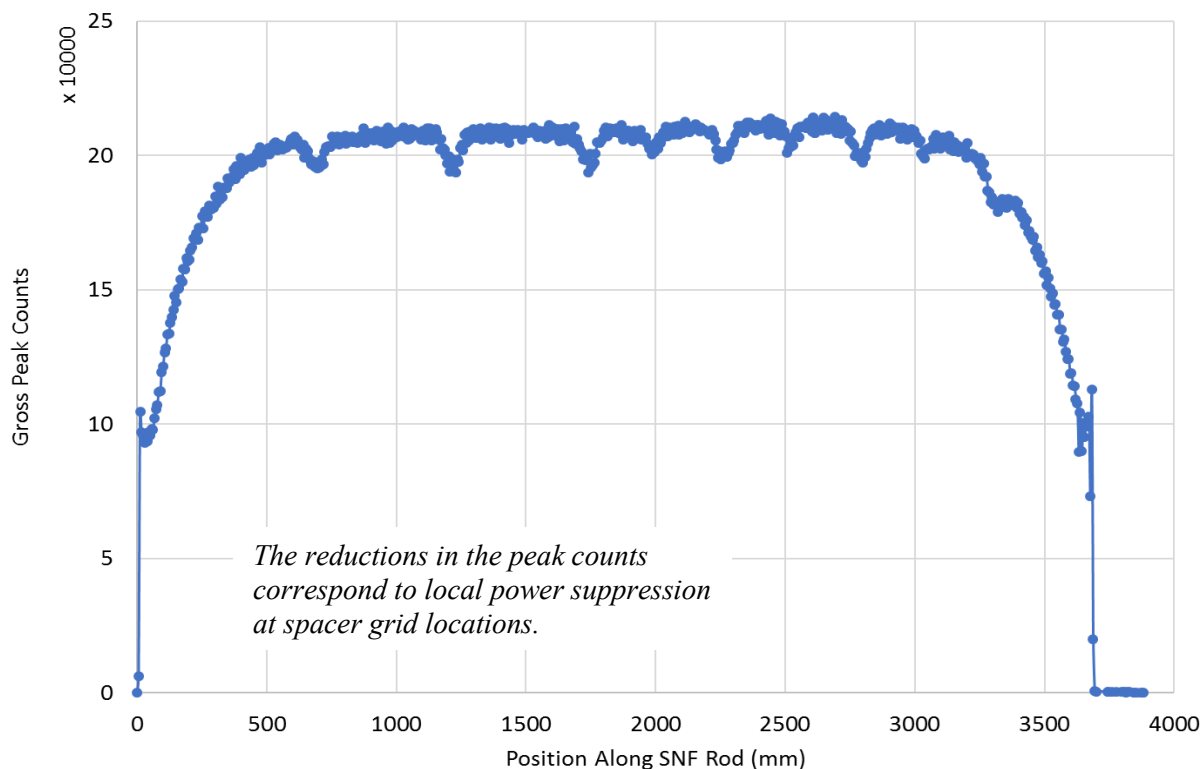


Figure 27. HPGe-derived Axial Scan of Sister Rod 30AD05 Using the Gross Peak Counts from the 661.6 keV Peak of ^{137}Cs .

Figure 28 shows the difference in the spectra produced by each detector as analyzed using PeakEasy [5]. The peaks from ^{134}Cs and ^{154}Eu could not be distinguished with the NaI spectra, so quantitative analysis of that spectrum was not possible.

A preliminary quantitative analysis of the 30-minute spectra obtained from the BEGe, the coaxial HPGe, the LaBr₃ detectors, and the summed spectrum from the full-length axial scan of 3D8B02 (called “Full Length BeGe” in Figure 29) was completed. The mass ratios calculated from the spectra were run through simulations in INDEPTH [6] at a constant power of 40 MW/MTU to generate a calculated burnup and cooling time. The mass ratios used in the INDEPTH simulations were calculated from the average activity ratios of ^{154}Eu and ^{134}Cs with respect to ^{137}Cs . The net count rate was determined using the ROI fit analysis in PeakEasy and the branching ratios from the TORI [7] database.

A comparison of the simulation results from INDEPTH using the HPGe 30-minute measurement as the reference is shown in Figure 29. The results from the LaBr₃ detector were not consistent with the results from the HPGe detectors. In particular, the cooling time calculated from the LaBr₃ detector differed by about 50%. The results from the HPGe detectors were consistent, with only a 3% difference for the predicted cooling times and a 9% difference in predicted burnup. A comparison to the known characteristics of the rod will be completed at a later date.

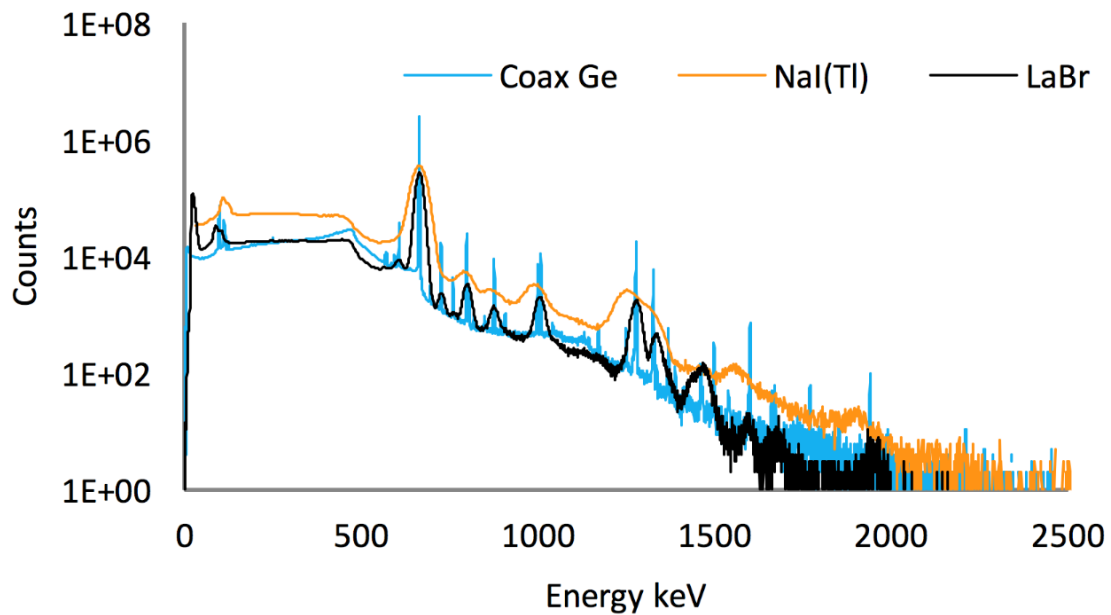
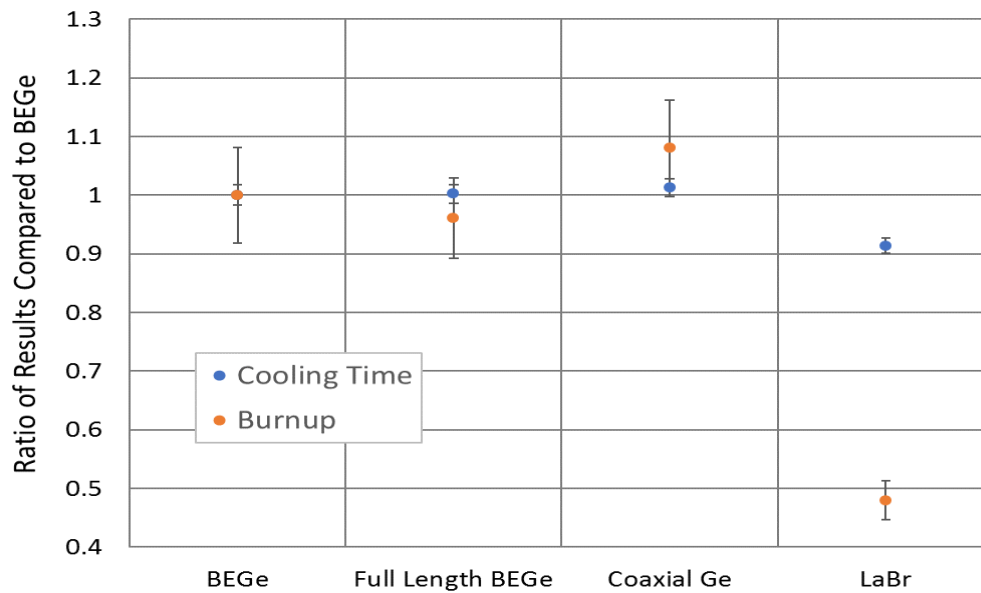


Figure 28. Superimposed Spectra of Coaxial Ge, NaI, and LaBr₃ Detectors.



INDEPTH [6] simulation used flat power of 40MW/MTU and mass ratios were calculated from the gamma spectra.

Figure 29. Comparison of the Cooling Time and Burnup of Rod 3D8B2 by Detector Type.

3.2.3 Fork Detector Gamma and Neutron Scanning

The fork detector is one of two primary instruments routinely used for spent fuel safeguards inspections by international safeguards authorities, including the International Atomic Energy Agency (IAEA) and Euratom [8]. The fork detector is mostly used to measure the neutron and gamma radiation from a spent fuel assembly in a pool, in order to verify the fuel assembly's burnup and cooling time and to check for removal or substitution of fuel rods from a subject fuel assembly. In this project, we explore the application of the fork detector in a hot cell environment, which is relevant to the safeguards at a spent fuel encapsulation plant for geological repository. Two fork detectors, (1) a standard fork detector and (2) a modified fork detector with alternate neutron and gamma detectors, were used to measure the 25 sister rods in this project.

Figure 30. depicts the fork detector, and Figure 31 illustrates the detector measuring a spent fuel assembly in a utility spent fuel pool. Each of the two tines of the fork detector includes two fission chambers and one ionization chamber. The signals from the four fission chambers (two in each tine) are combined to measure two neutron energy groups: one designed for measuring fast neutrons, and the other for measuring thermal neutrons. Similarly, the two ionization chambers (one in each tine) are combined to form one gamma measurement. The number of neutrons emitted by a spent fuel assembly is proportional to approximately the 4th power of the assembly average burnup, and the gamma emission is highly dependent on the fuel's cooling time.

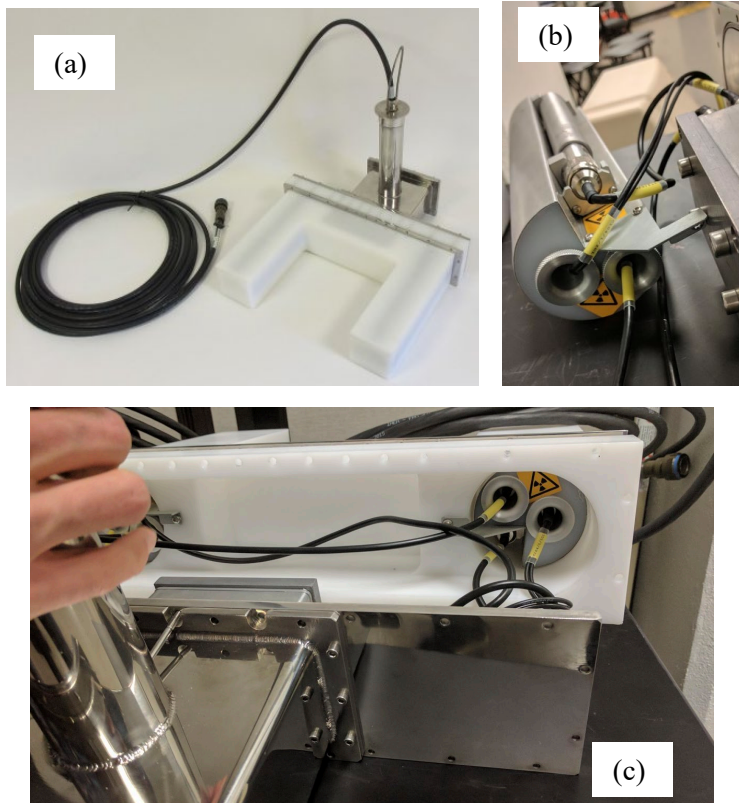


Figure 30. (a) Fork Detector Head, (b) Fission and Ionization Chambers, (c) Rear View of Fork Detector Head (with Back Plate Removed).



Figure 31. Measurement of a Spent Fuel Assembly in a Pool Using a Fork Detector [8].

Before the fork detectors were loaded into the hot cell, they were tested and calibrated in ORNL's Radiation Standards Calibration (RASCAL) facility (Figure 32) using a strong ^{252}Cf neutron source ($\sim 3.0\text{E}8$ neutrons/s) and ^{137}Cs gamma source ($\sim 1,000$ curies and $\sim 3.2\text{E}13$ photons/s).

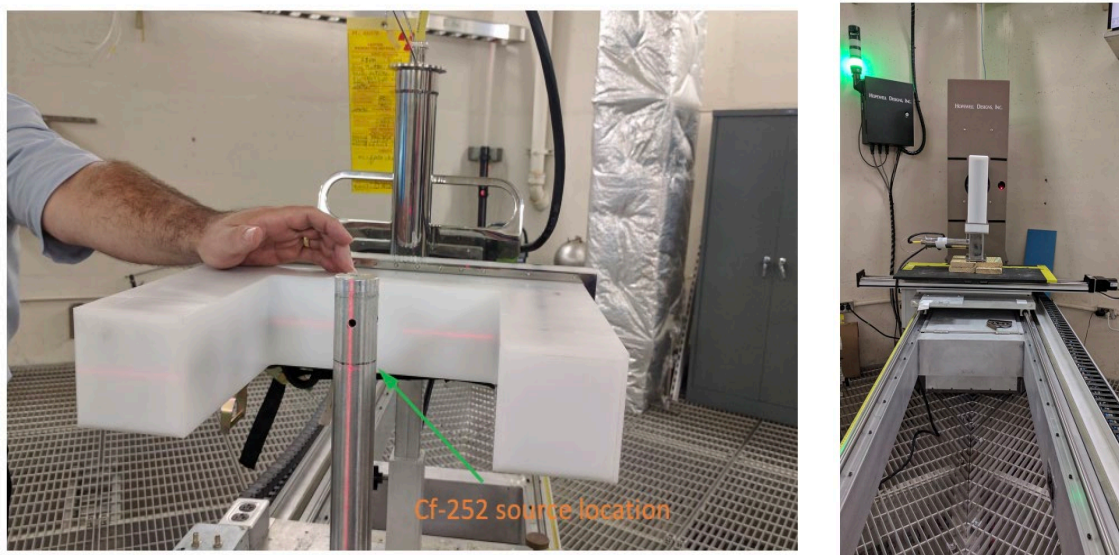
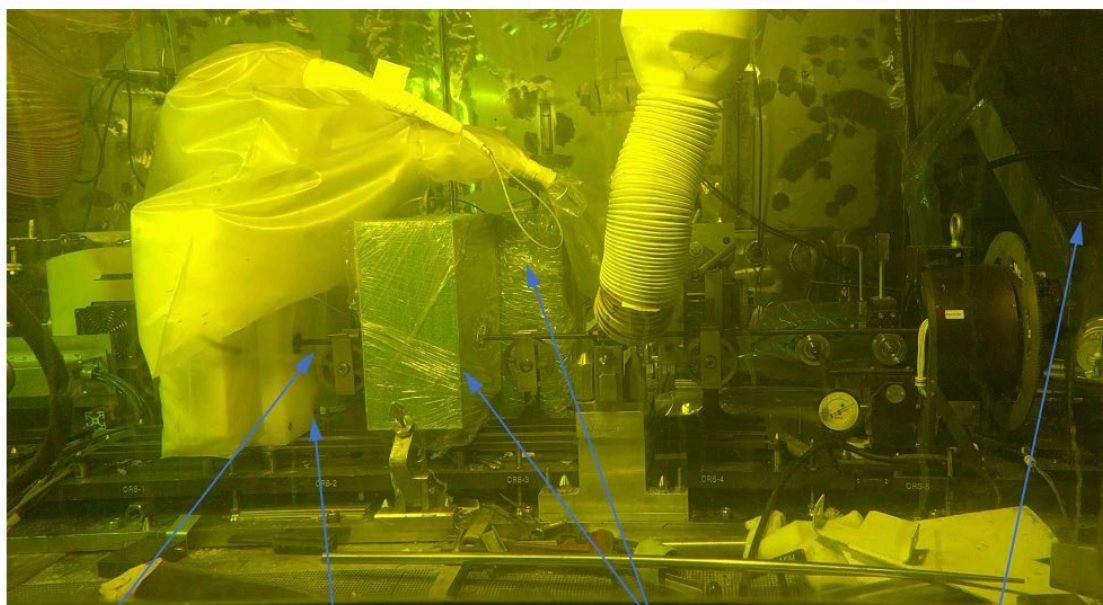


Figure 32. Set Up for Calibrating the Fork Detectors at ORNL's RASCAL Facility.

After the calibration, the fork detectors were loaded into ORNL's IFEL hot cell to measure the sister rods. The fork detectors were first used to measure the individual fuel rods (~ 3.96 m long) in both moderated and unmoderated conditions. Figure 33 shows the measurement of a single fuel rod in the moderated configuration. Polyethylene (poly) blocks were used as moderating material. Aluminum liners were used to prevent transfer of the poly to the fuel rods. For most rods, measurements were taken at 12 locations along the rod length to capture the variations of the axial burnup profile. ORNL's ADEPT system was used for rod positioning. The specific location of the rod relative to the fork detector was always known. No collimator was used in this measurement, so neutron and gamma signals from other parts of the fuel rod cannot be ignored. Such effects can be accounted for using simulations.

After single rod measurements were completed, the sister rods were placed into several different arrays to mimic the neutron and gamma interactions between the rods in a fuel assembly, including 2×2 , 3×3 , and 5×5 arrays. For the 5×5 array, two partial defect scenarios were created and tested. Figure 34 (left) shows the fork measurement of the 5×5 rod array. Four sets of aluminum support structures were specially designed and manufactured to assemble the rods into arrays. Great care was taken to avoid any potential damage to the fuel rods during assembly. The movement of each rod was carefully tracked and recorded, and each sister rod was tagged when used in the arrays.

To create the partial defect scenarios, stainless steel rods were used in place of the fuel rods in the 5×5 array. Measurements were performed with this array at 6 axial locations along the length. Measurements were taken with 4 stainless steel rod substitutions and with 8 stainless steel rod substitutions. Figure 34 (right) shows the 5×5 array from the north end with eight fuel rods missing from view. Short stainless-steel rods (4.5 feet long instead of 13 feet long) were used in this work for easier maneuvering in the hot cell. The short rods also accommodated measurement of an additional configuration in which part of the array had fuel rods missing without substitutions. Measurements were performed at 6 locations along the length of the array.



A spent fuel
rod

Poly block for moderation

Borated poly blocks with
Cd liner for shielding

Near end of the fuel rod
storage casks

The fork detector was enclosed in two layers of poly bags to reduce contamination. A poly block (white) was placed around the fuel rod to provide neutron moderation. Two borated poly blocks with cadmium liners were placed beside the detector to block neutrons emitted from other sister rods stored in the hot cell.

Figure 33. Set Up for Measuring a Full-Length Sister Rod Using a Fork Detector in IFEL Hot Cell.

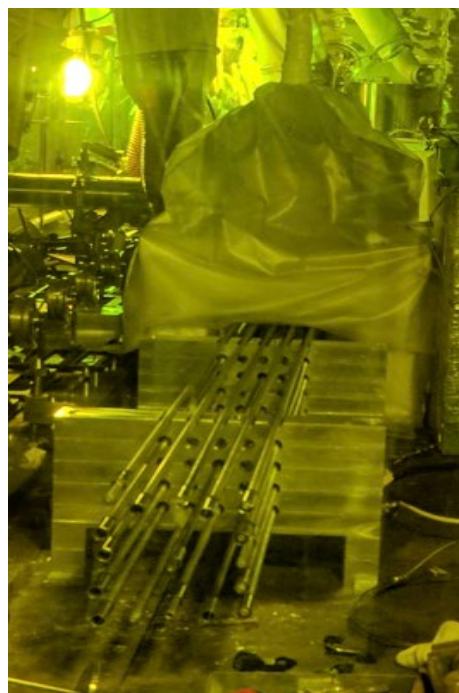
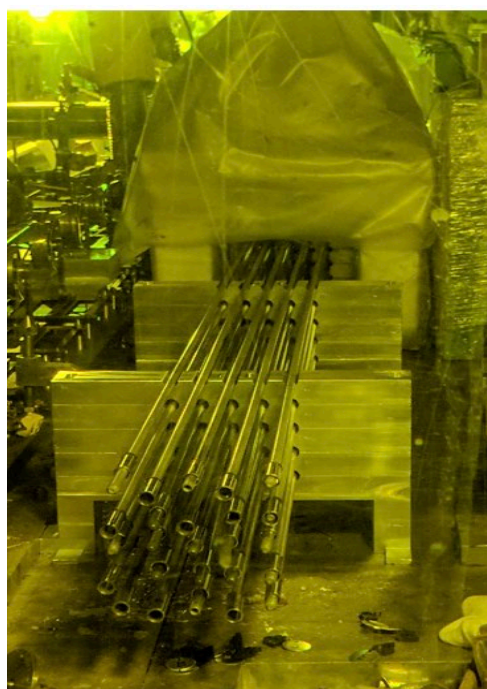


Figure 34. Set Up for Measuring a 5×5 Array of 25 Full-Length Spent Fuel Rods Using a Fork Detector at ORNL's IFEL Hot Cell, All Locations Filled with Sister Rods (Left) and 8 Partially Vacant Locations (Right).

Figure 35 depicts the normalized fork neutron and gamma count rates (with background subtracted) along the length of sister rod 30AE14. The axial burnup profile derived from the average assembly burnup prediction for rod 30AE14's parent assembly was also included for comparison. Axial fuel rod burnup profiles are not available for individual sister rods. Both the neutron and gamma count rates followed the expected trends, increasing from the bottom of the fuel rod to the center section. Due to space restrictions in the hot cell, the fork detector was not able to reach the top end of the fuel rod.

There is good agreement between the gamma measurement and the axial burnup in the middle of the fuel rod. Similar trends were observed in other fuel rods. As mentioned previously, SNF neutron emissions trend with the 4th power of the burnup, while gamma emissions are somewhat linear with burnup. This is evident in the steeper neutron slope shown in Figure 35. In theory, there should be a very close agreement between the fork detector gamma count rates and the predicted axial burnup profile. Different factors can contribute to the discrepancies observed, such as: (1) the predicted assembly average axial burnup plotted in Figure 35 is somewhat different from the sister rod burnup and does not capture localized neutron spectra differences, and (2) a collimator was not used for the fork measurements, which allowed gammas from other sections of the fuel rod to contribute to the signal. During safeguards inspections, fork measurements are usually performed only at the middle of a fuel assembly without the use of a collimator.

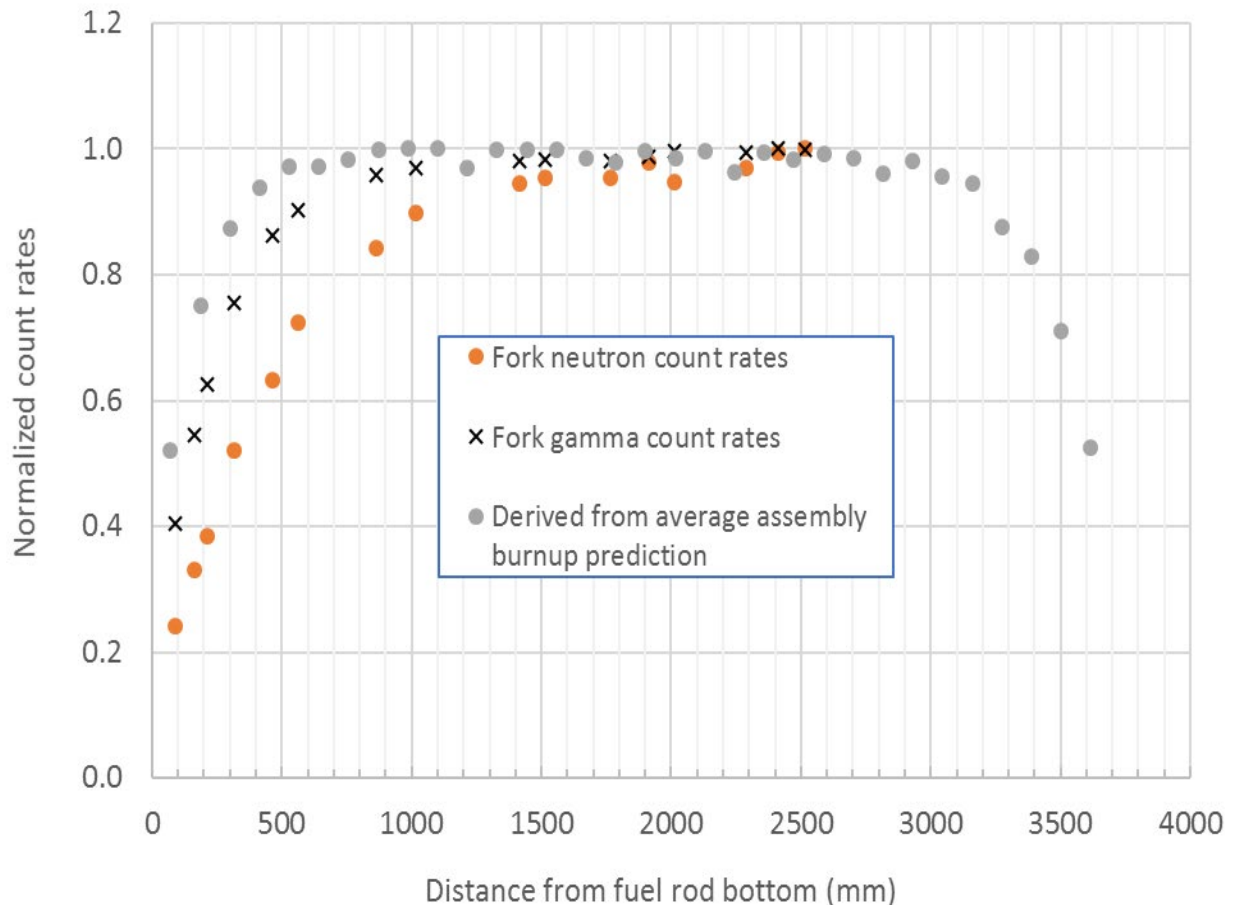


Figure 35. Normalized Fork Neutron and Gamma Count Rates along the Length of Fuel Rod 30AE14.

Figure 36 compares the fork count rates and the corresponding calculated neutron and gamma source intensities (not presented here) based on the fuel design data and the operating histories of the 9 sister rods. The measured count rates are based on the fork measurement at the 1,500 mm position near the axial center of the rod. The measured count rates are expected to be linear with the calculated source intensities for all sister rods because the same measurement geometry was maintained for all fuel rods. As seen in Figure 36, the measured fork neutron and gamma count rates trend very well with the corresponding calculated source intensities. The calculations were performed based on the reported fuel burnup and cooling time. These results demonstrate that the fork detector measurements verified the fuel burnup and cooling time.

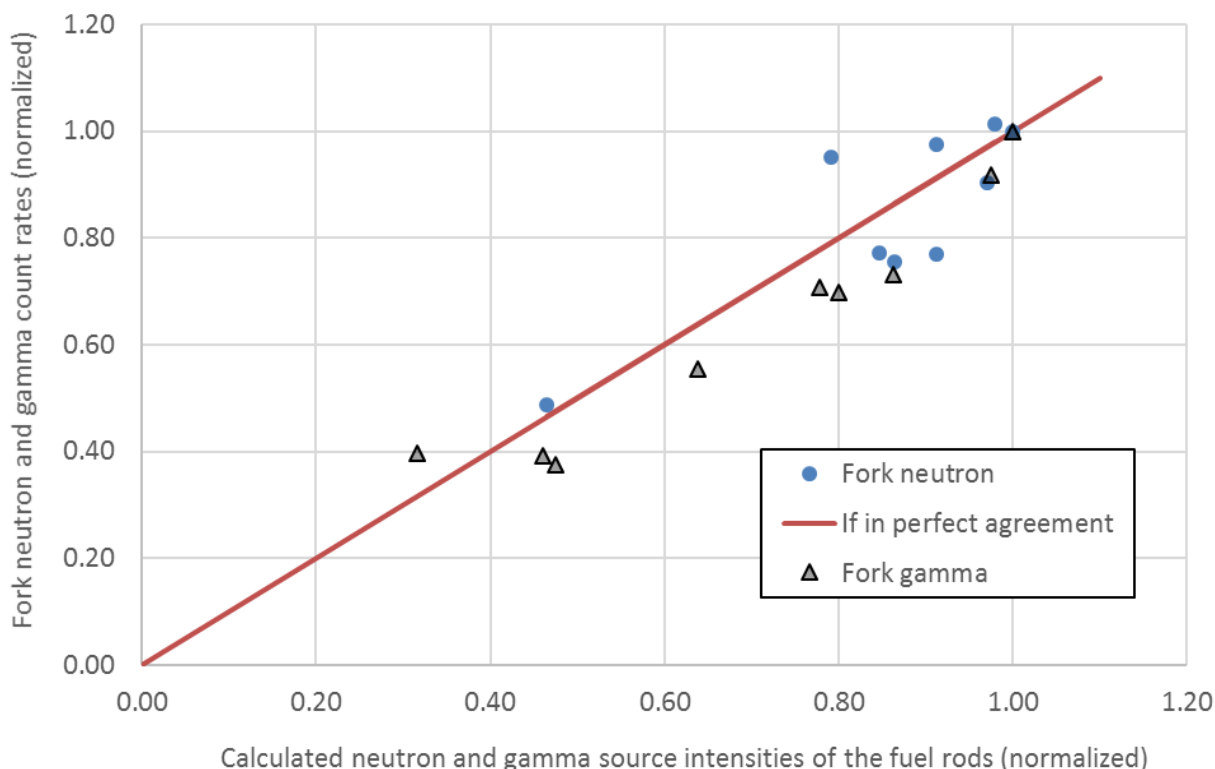


Figure 36. Comparisons between the Fork Gamma and Neutron Count Rates with the Corresponding Calculated Neutron and Gamma Source Intensities in 9 Fuel Rods.

For measurements in which stainless steel rods were substituted for four fuel rods, an 8–14% reduction in the neutron count rate and a 13–16% reduction in the gamma count rate were observed as compared to the rates of the full 5×5 array, depending on the axial locations where the array measurement was performed. When eight fuel rods were replaced with stainless steel rods, the reduction in the neutron count rate was 19–28%, and the reduction in the gamma count rate was 31–34%. It should be noted that the fuel rods that were replaced with steel rods had shorter cooling times than the majority of the rods in the array.

In-air spent fuel fork detector measurements present unique challenges. The sister rods provided a unique opportunity to test the fork detector's in-air measurement performance and to validate ORNL software for use by IAEA and Euratom to predict fork neutron and gamma count rates in real time. The initial results show that the fork detector performs well in air, its gamma count rates are consistent with other data sets, it can verify reported burnup and cooling time of the fuel, and it is sensitive to the quantity of fuel material.

3.3 NDE.03: Fuel Rod Overall Length

The average overall lengths for the 25 sister rods that were measured over the entire NDE campaign are reported in Section 3.2.1, Table 4. Because ADEPT is indexed using the overall rod length, each rod is measured every time it is placed on ADEPT. During the NDE campaign, each sister rod has been measured from 4 to 16 times on different dates. For example, before each gamma scan, the length of each sister rod was measured as needed for machine indexing, and the average was used to calculate the rod's upper end plug length. A calibration rod was also measured periodically.

3.4 NDE.04: Eddy Current Examinations

Two eddy current examinations were completed: (1) a campaign using traditional eddy current methods to measure oxide/CRUD thickness and remaining cladding thickness and to identify flaws, and (2) an EPRI campaign using their F-SECT technique to measure the hydrogen content of the cladding. The traditional eddy current measurements were completed in November 2017, and the F-SECT measurements were completed late in July 2017.

3.4.1 F-SECT Measurements

EPRI performed Frequency-Scanning Eddy Current Technique (F-SECT) measurements on the sister rods in the IFEL hot cell. Due to industry expectations for higher fuel reliability and the emphasis on determining fuel reliability margins, EPRI has advanced development of NDE characterization techniques capable of quantifying hydrogen content, the residual wall thickness of the zirconium alloys, and oxide/CRUD thickness. These techniques could be deployed poolside at a nuclear power plants. The F-SECT has been developed specifically to nondestructively estimate cladding hydrogen content using refined eddy current techniques based on point measurements of electrical conductivity. It has been tested in hot cell and poolside environments on components fabricated with zirconium alloys, including channel box, water rod, spacer, and fuel cladding.

The F-SECT system measures eddy current impedance over a range of frequencies which provides data at different penetration depths into the cladding. The probe must stay in contact with the surface of the rod at the measurement location for approximately 2 seconds to allow for the completion of the 24-frequency sequence and acquisition of the electrical impedance versus frequency spectrum. The F-SECT eddy current impedance measurements are used in conjunction with rigorous electrical conductivity models to determine the amount of hydrogen precipitated in the cladding. Since the cladding's electrical impedance is affected by its alloy composition, heat treatment, and operational history, hydrogen precipitate modeling using electrical impedance must consider these parameters. For pressurized water reactor (PWR) cladding, the primary challenge is compensation for neutron fluence and hydride rim formation. To date, electrical conductivity modeling and F-SECT have been used to estimate hydrogen content in Zircaloy-2 and Zircaloy-4. The presence of ferromagnetic CRUD can also influence the measured electric impedance, and as a consequence, it influences the measured lift-off and estimated hydrogen content. Therefore, EPRI has also developed a magnetic saturation technique to compensate for the effects of ferromagnetic CRUD. Usually PWR fuel does not have a substantial amount of ferromagnetic CRUD, and the sister rods in particular are not expected to have ferromagnetic CRUD. The F-SECT measurement includes point measurements of the combined zirconium oxide and CRUD thickness (the *lift-off*).

An F-SECT measurement bench was designed and installed in the IFEL hot cell to accommodate the work. The bench included an integral magnetic loop coil and an F-SECT probe mounted on a swing arm to allow the fuel rod to be freely moved as shown in Figure 37. A total of 19 sister rods were successfully measured over 3 consecutive days, including ZIRLO, M5, Zirc-4, and LT Zirc-4 clad rods. The detailed results will be reported by EPRI and are summarized here for information only.

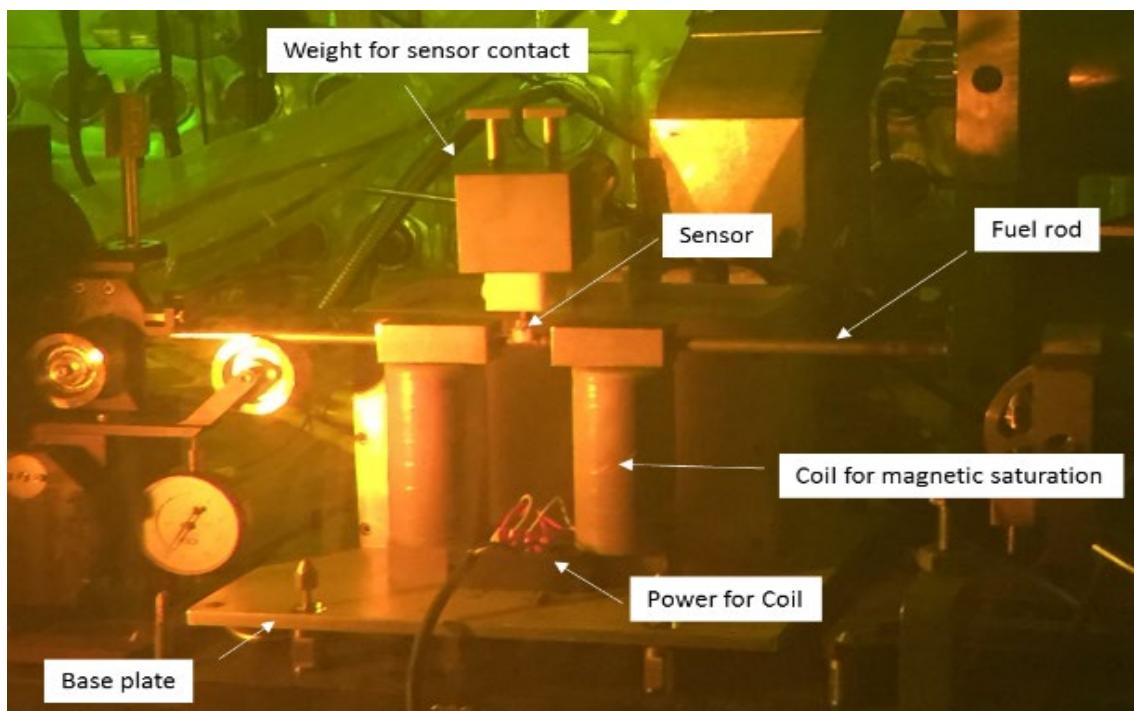


Figure 37. The F-SECT Bench Installed in the IFEL Hot Cell.

Measurements were conducted every 200 mm along the rods. Most rods were measured from lower to higher elevation. At one end of each rod, mostly the lower elevation of the rods, a 500 mm region from the rod end was unable to be measured due to ADEPT limitations. Since F-SECT measurements are point scans, the peak lift-off location can be missed. To reduce this possibility, additional measurements were performed for most rods in higher measured lift-off regions and included both additional axial and azimuthal data. Each position was typically measured twice to check for magnetic CRUD components—once with the magnetic saturation coil off and once with it on. No substantial magnetic component to the CRUD was found.

The F-SECT system requires rigorous and frequent calibration to ensure data accuracy. The calibration typically uses a sample of the cladding alloy being measured with an applied nonconductive spacer material in three known thicknesses. Also, a known lower conductivity nickel alloy is used as an independent standard. For the sister rods, unirradiated base cladding samples of ZIRLO, Zirc-4, and M5 were used as calibration standards. The Zirc-4 standard was used when measuring LT Zirc-4. The stability of the F-SECT requires periodic calibration checks to sustain data quality due to the potential for drift in the electronics resulting from factors such as temperature changes. Calibrations were performed before and after each sister rod was measured. The system was predominantly stable during the sister rod examinations.

Representative lift-off data for each cladding type are shown in Figure 38. As expected, based on previously published industry data, lift-off varies as a function of cladding material. When the CRUD contains magnetic components, the thickness of the CRUD alone can be estimated. However, for the sister rods, where no magnetic CRUD components were found, the CRUD thickness cannot be separated from the zirconium oxide thickness. The highest lift-off observed was between rod elevations of ~3,100 and ~3200 mm for all clad four types. As expected, the Zirc-4-clad sister rods had the highest lift-off overall. The two F35 Zirc-4 rods are atypical in that they were demonstration rods and were operated aggressively for four cycles to HBU. Figure 39 shows the estimated hydrogen content for sister rod F35K13 (Zirc-4) using two different models: a neutron fluence compensation model and a hydride rim

detection model. The transition from one model to the other occurs at $\sim 1,800$ mm axial elevation. In general, it appears that the measured hydrogen content using these modeling techniques is over-predicted for the sister rods, based on previous industry experience with these alloys. The destructive evaluations from the sister rod program are expected to provide data that can be used to improve the accuracy of the F-SECT electrical impedance models.

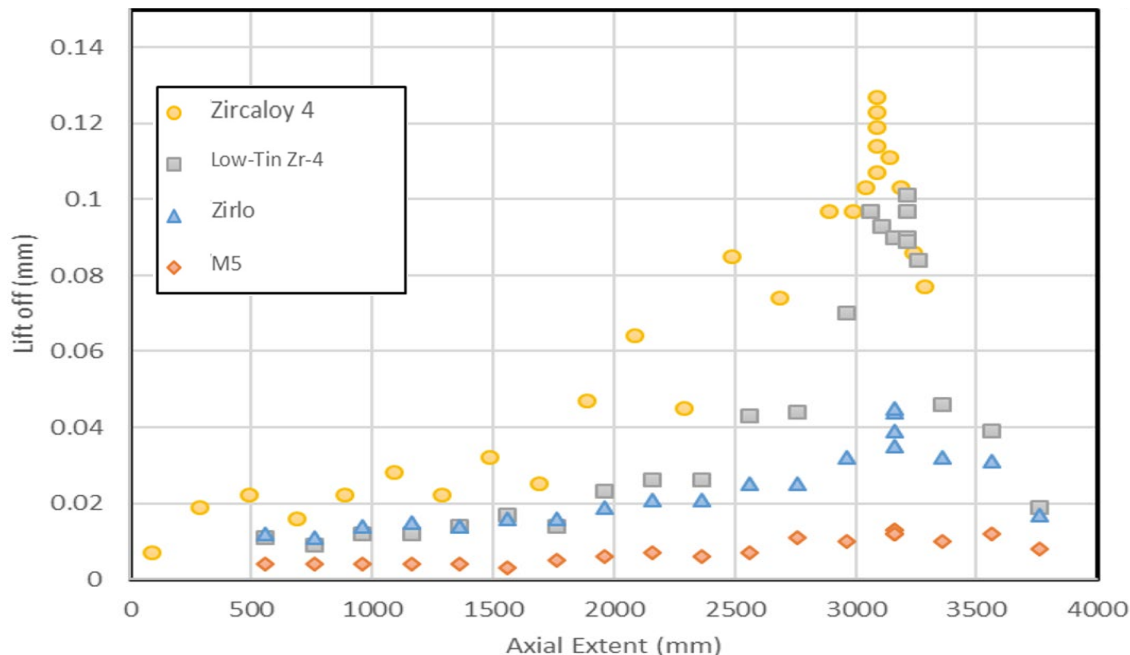


Figure 38. Representative Sister Rod Lift-Off Data for Each Cladding Type.

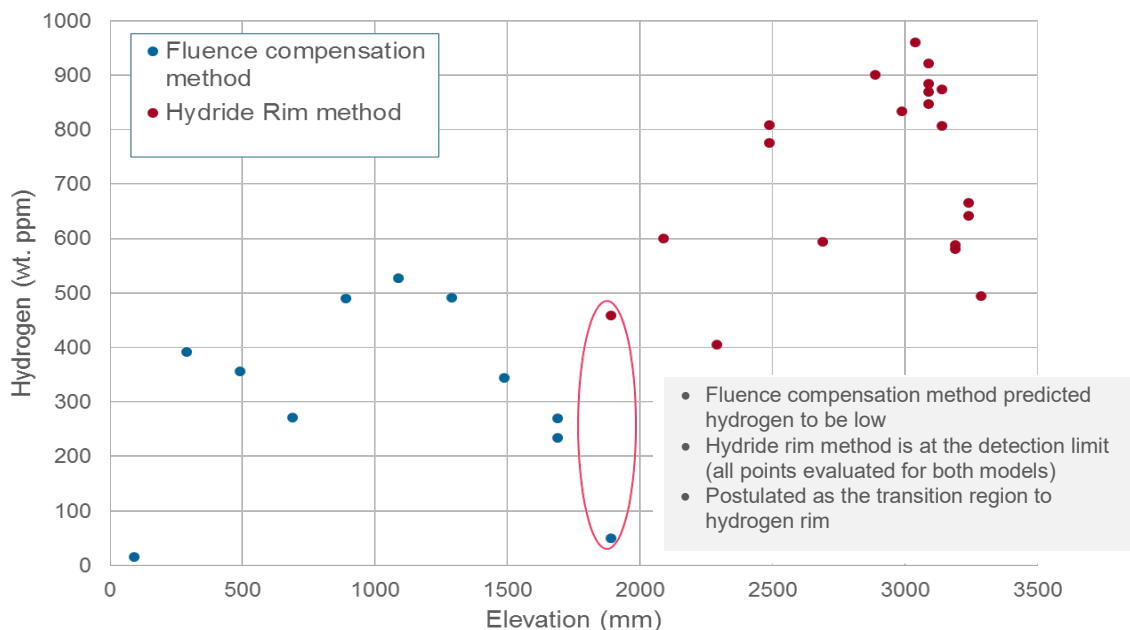


Figure 39. F-SECT Estimated Hydrogen Content for Sister Rod F35K13, an Example of HBU Zirc-4 Rods with High Corrosion.

3.4.2 Traditional Eddy Current Measurements

During the eddy current examination, the cladding is scanned for defects (e.g., breach, through-wall defects, outside and inside diameter discontinuities, wall thinning, localized large increases in cladding diameter) and combined CRUD/oxide thickness (the *lift-off*). Table 6 and Table 7 summarize the results of the eddy current examinations.

3.4.2.1 Eddy current calibration

Except for lift-off measurement, the examination is accomplished using an encircling eddy current coil. The lift-off measurements are obtained using a pancake coil. The eddy current examination technique relies heavily on signal response calibration. The calibration standards used for the ORNL measurements included unirradiated M5, Zirc-4, and ZIRLO examples. A low-tin Zirc-4 example was not available. Each calibration standard was specifically fabricated to include a range of the expected types of defects. A surrogate for the lift-off was used. The calibration standards with the included simulated defects and lift-off were measured and certified by the ORNL Metrology & Measurement Standards department.

Each defect or lift-off has a different voltage reaction to the applied eddy currents. A loss of cladding material or the presence of a nonconductive layer (oxide thickness) results in a signal voltage rise. A voltage calibration curve is generated for the encircling and pancake coils used based on their response to the calibration standard. The Zirc-4 calibration standard was used as a substitute for the low-tin Zirc-4 calibration standard. As mentioned in Section 3.4.1, the presence of ferromagnetic CRUD can bias the results of the scans; however, PWR CRUD typically does not contain ferromagnetic constituents. The absence of ferromagnetic CRUD on the sister rods was confirmed by EPRI's F-SECT examination, as reported in Section 3.4.1.

The encircling coil was calibrated for the alloy to be measured at the beginning of each day of measurement and was checked for drift at the end of the day or when the measurements on rods with that type of alloy were complete. Because the pancake coil is more prone to measurement drift, it was calibrated before and after every fuel rod measurement using the calibration standard for the specific alloy being measured.

3.4.2.2 Scan Speed and Data Acquisition

All 25 sister rods were scanned with the encircling coil. The encircling coil does not contact the rod surface and the entire length of the rod could be scanned. The encircling coil scan is in effect continuous, in that the signal is acquired at a high rate, and the rod travel is not stopped during the scan. Some rods were redundantly scanned at other speeds to determine if a faster scan rate was possible. Rod 5K7P2 was scanned with the encircling coil at 25 mm/sec, 10 mm/sec, and 5 mm/sec. After reviewing the data, it was decided that a slower scan speed was necessary, and the remaining rods were scanned at a rate of 5 mm/sec. All information was collected with a single scan. For all encircling coil scans, the axial location associated with the scan signal was determined based on the scan speed and time elapsed.

All sister rods were scanned multiple times with the pancake coil. As each sister rod was scanned for the first time the 0-degree orientation was marked at the upper end cap and in later eddy current exams this 0-degree orientation was maintained. The pancake coil was in contact with the rod during the scan, so all lift-off measurements begin at approximately 21 mm from the end of the rod. The lift-off scan was in effect continuous in that the signal was acquired at a high rate and the rod travel was not stopped during the scan. The signal data were averaged as they were acquired and were tabulated in ~0.5 mm increments. Each sister rod was scanned axially at 90° rotations (a total of 4 axial traces per sister rod). The lift-off scans were completed serially: 1) the rod was placed under the probe, 2) the probe was lowered to the rod surface, 3) the rod was moved axially to scan the full length, 4) the probe was retracted, 5) the rod was moved axially back to the starting location 6) the rod was rotated to the next azimuthal location. It should be noted that ADEPT can induce some rotational motion as the rod travels axially. While care was taken to realign the rod at the start of each scan, the lift-off measurements cannot be fully characterized as a

straight trace along a single azimuthal location. This helical motion is not relevant to the encircling coil scans, as they represent a cross-sectional measurement. Lift-off scans were performed at a speed of 10 mm/sec. Several rods were redundantly scanned at a speed of 25mm/sec to determine if a faster scan rate was possible, but the faster scan speed resulted in excessive noise, although the average result was not significantly affected.

In addition to the axial scans, selected locations were scanned rotationally. The rod was not moved axially, but rather was rotated 360° at a fixed elevation to examine circumferential variations in lift-off. The rod was moved to the elevation of interest, the pancake coil was lowered to contact the rod surface, and the rod was rotated. Rotational scans were completed at a speed of 1 rpm, with some redundant scans at 10 rpm.

3.4.2.3 Scan Frequencies

For the encircling coil scans, the fuel rods were examined with both absolute and differential signals at four frequencies: 500 and 800 kHz, and 1.0 and 1.2 MHz. Multiple frequencies were used to look for defects at various depths in the cladding. For example, the penetration depth of the eddy current is greater at low frequency, but shallow flaws can be missed at low frequency. Absolute inspection compared the inspection coil to the reference coil, whereas the differential inspection compared the inspection coil signal to the signal from a parallel mounted coil within the encircling inspection coil housing. The absolute coil signal is more useful for gradual changes, such as cladding wall thinning, whereas the differential signal is used for detection of rapid changes such as small holes. Defect sizes were estimated by comparing the voltage and phase angle response of the signal for each frequency to the response from the calibration standard.

3.4.2.4 Cladding Defect Scan Results

Table 6 summarizes the defects noted in the encircling coil scans. No deep defects that would indicate through-wall penetration were noted during the encircling coil scans. Significant wall thinning (>10%) due to uniform oxidation was observed in the Zirc-4 and LT Zirc-4 rods in the higher burnup regions of the rod, and the minimum remaining cladding wall thickness was measured as ~0.462 mm on these rods.

Several defect scan findings indicative of sharp rod OD reductions or large GTRF marks are summarized in Table 6. The GTRF mark identified on sister rod 3F9D07 was indicated as a 2% material loss, which would be equivalent to a single wear mark ~16 µm deep. However, the depths of these two GTRF marks were later measured using the pancake coil and were found to be greater than 16 µm deep (see Section 3.4.2.5). The encircling coil reports loss of material, while the pancake coil measures distance from the metal surface.¹ Since the combined material removed by the GTRF wear is greater than the 2% reported by the encircling coil scan, it appears that the material was relocated to the edges of the wear mark, rather than removed from the rod cladding. The pancake coil scans (see Section 3.4.2.5) tend to support this conjecture.

The many instances of moderate or shallow GTRF noted in the visual examinations were not detected with the encircling coil used. Upon investigation, it appears that to detect these small cladding defects an additional eddy current coil tuned to shallow defects would be required. Since the smaller defects can be identified using the visual examinations, it was decided that a back-fit of the eddy current system to provide shallow defect detection would not be performed.

¹ The pancake coil was not calibrated for measuring depth and there could be significant measurement uncertainty associated with the reported values, as discussed in Section 3.4.2.5.

Table 6. Summary of Remaining Wall Thickness and Maximum Lift-off

Sister Rod	Span average maximum reduction in total cladding cross-sectional volume, ^{Note 1} (%)	Minimum remaining cladding wall thickness, ^{Note 2} (mm)	Maximum rod average measured lift-off, ^{Note 3} (μm)	Elevation of maximum rod average measured lift-off ^{Note 4} (mm)	Axial peak measured lift-off ^{Note 5} (μm)	Elevation of axial peak measured lift-off ^{Note 6} (mm)	Variance of the peak measured lift-off in the 4 quadrants (μm)	Rotational Scan results, peak/minimum/average lift-off @ elevation measured ^{Note 7} (μm/μm/μm @ mm)
30AD05	3	0.569	20	3245	21	3245	1	N/A
30AE14	3	0.569	27	3445	31	3445	2	27 / -0 / 7 @ 33 12 / -0 / 4 @ 229 13 / 2 / 5 @ 235 14 / 2 / 7 @ 2,461 26 / 19 / 23 @ 3,320 25 / 13 / 18 @ 3,781 17 / 9 / 13 @ 3,861
30AG09	3	0.569	20	3405	23	3225	1	15 / 1 / 52 @ 670 21 / 15 / 19 @ 3,351
30AK09	2	0.574	16	3425	20	3865	1	N/A
30AP02	2	0.574	18	3465	22	3705	1	N/A
3A1B16	17	0.490	138	3135	149	3135	3	148 / 52 / 123 @ 3,100 147 / 42 / 122 @ 3,100 (repeat scan at 10 RPM) 150 / 22 / 115 @ 3,101 142 / 43 / 112 @ 3,168
3A1F05	22	0.462	164	3115	185	3105	8	N/A
3D8B02	6	0.551	36	3145	41	3105	1	N/A
3D8E14	5	0.556	64	3205	72	3165	4	N/A
3F9D07	8	0.541	69	3115	87	3255	8	24 / -8 / 18 @ 1,765 30 / -28 / 19 @ 2,279 79 / 45 / 61 @ 3,200 67 / 37 / 50 @ 3,295 71 / 36 / 50 @ 3,333
3F9N05	7	0.546	65	3075	85	3115	8	87 / 38 / 63 @ 3,209

Sister Rod	Span average maximum reduction in total cladding cross-sectional volume, ^{Note 1} (%)	Minimum remaining cladding wall thickness, ^{Note 2} (mm)	Maximum rod average measured lift-off, ^{Note 3} (μm)	Elevation of maximum rod average measured lift-off ^{Note 4} (mm)	Axial peak measured lift-off ^{Note 5} (μm)	Elevation of axial peak measured lift-off ^{Note 6} (mm)	Variance of the peak measured lift-off in the 4 quadrants (μm)	Rotational Scan results, peak/minimum/average lift-off @ elevation measured ^{Note 7} (μm/μm/μm @ mm)
3F9P02	5	0.556	33	3175	41	3235	2	32 / 9 / 20 @ 307 42 / 0 / 18 @ 2,116 16 / 1 / 9 @ 2,281 18 / 12 / 15 @ 2,281 (repeat scan) 43 / 29 / 34 @ 3,201 24 / 15 / 19 @ 3,664 19 / 7 / 14 @ 3,835
5K7C05	2	0.574	17	3365	22	3545	2	N/A
5K7K09	3	0.569	20	3405	21	3405	1	N/A
5K7O14	3	0.569	19	3435	22	3355	1	N/A
5K7P02	2	0.574	18	3445	19	3465	1	N/A
6U3I07	5	0.556	29	3085	32	3465	2	34 / 11 / 21 @ 35 (lower end cap) scan may have included the paint mark put on the rod for 0° location 31 / -0 / 5 @ 65 20 / 8 / 13 @ 2,201 28 / 22 / 25 @ 3,432
6U3K09	6	0.551	38	3135	42	3255	2	10 / 3 / 6 @ 352 9 / 4 / 7 @ 371 33 / 24 / 28 @ 3,630
6U3L08	8	0.541	47	3245	62	3245	9	33 / 12 / 22 @ 35 25 / 8 / 14 @ 38 45 / 33 / 38 @ 3,364 62 / 34 / 45 @ 3,435 34 / 22 / 26 @ 3,659 25 / 8 / 14 @ 3,834
6U3M03	8	0.541	50	3165	60	3195	6	57 / 39 / 46 @ 3,213

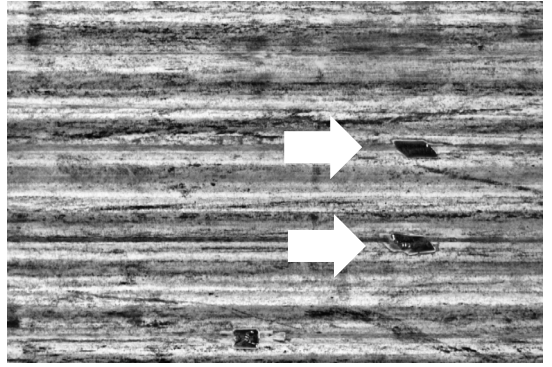
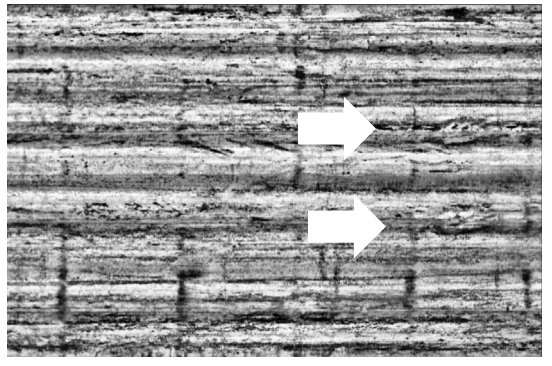
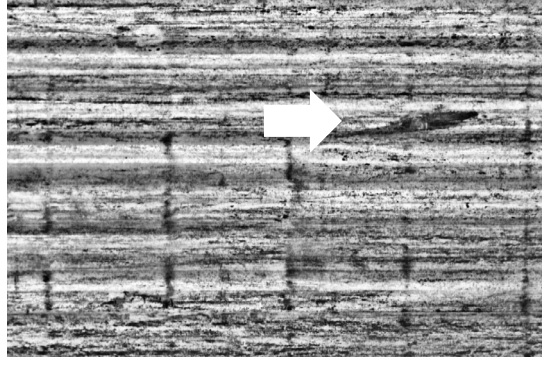
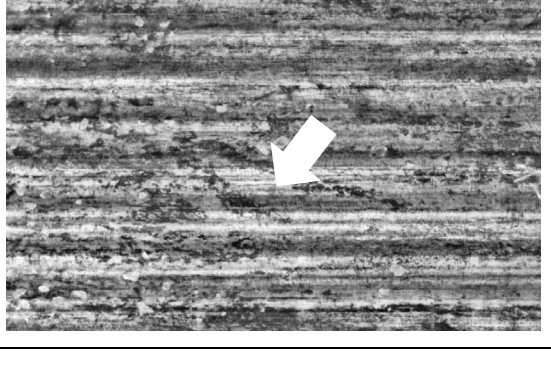
December 21, 2018

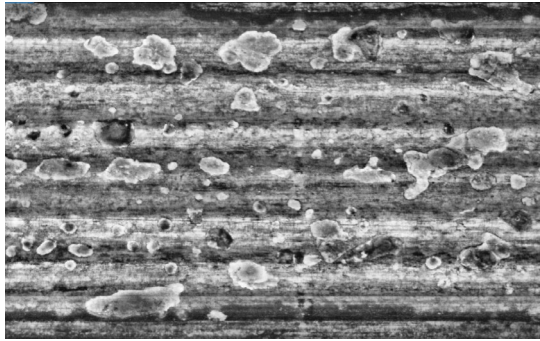
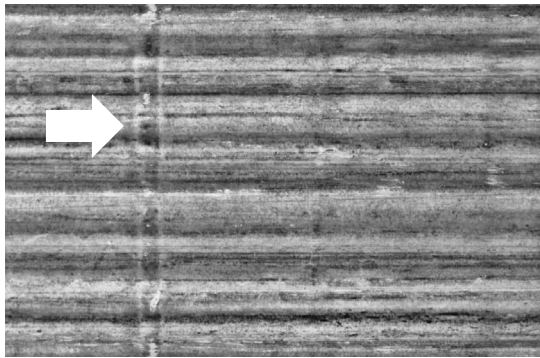
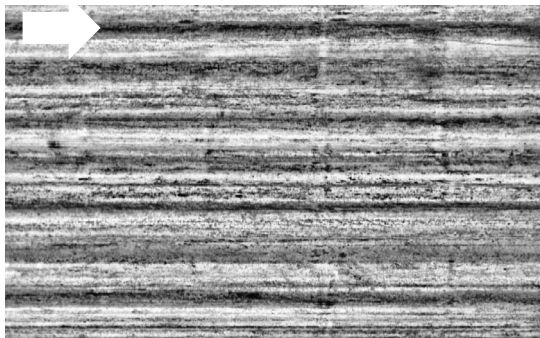
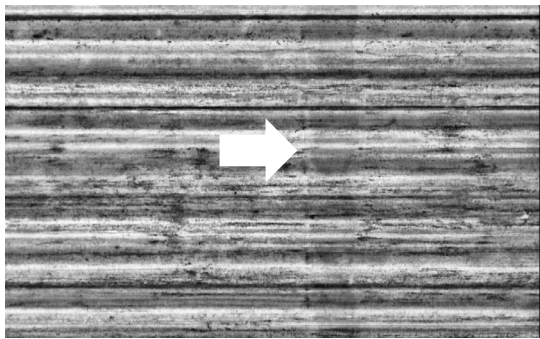
Sister Rod	Span average maximum reduction in total cladding cross-sectional volume, ^{Note 1} (%)	Minimum remaining cladding wall thickness, ^{Note 2} (mm)	Maximum rod average measured lift-off, ^{Note 3} (μm)	Elevation of maximum rod average measured lift-off ^{Note 4} (mm)	Axial peak measured lift-off ^{Note 5} (μm)	Elevation of axial peak measured lift-off ^{Note 6} (mm)	Variance of the peak measured lift-off in the 4 quadrants (μm)	Rotational Scan results, peak/minimum/average lift-off @ elevation measured ^{Note 7} (μm/μm/μm @ mm)
6U3M09	6	0.551	48	3125	53	3305	2	8 / 1 / 4 @ 310 7 / 0 / 4 @ 322 8 / 2 / 4 @ 330
6U3O05	9	0.533	62	3165	66	3245	2	N/A
6U3P16	6	0.551	35	3175	44	3155	4	15 / -0 / 4 @ 378 7 / -0 / 3 @ 398 7 / 0 / 3 @ 449 8 / -0 / 3 @ 516 48 / 24 / 34 @ 3,434 17 / 9 / 13 @ 3,835
F35K13	20	0.472	141	3085	156	3045	7	42 / 22 / 35 @ 1,139 117 / 98 / 108 @ 3,403
F35P17	21	0.467	150	3055	161	3085	7	68 / 53 / 60 @ 1,365 65 / 50 / 56 @ 1,805 54 / 39 / 47 @ 2,263 173 / 123 / 153 @ 3,080 66 / 55 / 60 @ 3,650

Notes on Table 6:

1. The span average maximum reduction was calculated over an interval of approximately 550 mm, representative of the distance between spacer grids in the assembly. The elevations of mid-span mixing grids/intermediate flow mixing grids, if present, were not reflected in the span intervals. The total cladding cross-sectional volume measurement was made using the encircling coil.
2. The minimum remaining cladding wall thickness is the minimum measured for the rod using the encircling coil.
3. For the maximum average measured lift-off, the four quadrant data is averaged individually over 10 mm elevation intervals, and then the four quadrants are averaged. The maximum is the maximum observed for the whole rod.
4. The elevation reported is that corresponding to the location where the maximum average lift-off was measured.
5. The reported peak is the maximum from any one of the quadrant average measured lift-offs. The data in each quadrant is averaged individually over 10 mm elevation intervals.
6. The elevation reported is that corresponding to the location where the peak average lift-off was measured for any single quadrant.
7. See the scan traces with images of the location scanned for more detail. Where a -0 is listed, the scan generally indicated some penetration into the base cladding less than 0.5 μm in depth.

Table 7. Summary of defect scan results

Sister rod	Elevation of defect (mm) ^{Note 1}	Defect type	Image from location of interest
3F9D07	2,264	GTRF: 2% depth through the remaining wall. Estimated depth based on 2% is 16 μm . Marks were later measured with the pancake coil as 18 and 28 μm deep (see Section 3.4.2.5).	
3F9D07	3,299	Likely oxidized GTRF: 3% local reduction in total cladding cross-sectional volume. A rotational scan in this region shows a $\sim 30 \mu\text{m}$ higher lift-off that would be consistent with base metal relocation as discussed in Section 3.4.2.5.	
3F9D07	3,332	GTRF: 1% local reduction in total cladding cross-sectional volume.	
3A1B16	3,309	Likely oxidized GTRF: 1% local reduction in total cladding cross-sectional volume	

Sister rod	Elevation of defect (mm) ^{Note 1}	Defect type	Image from location of interest
3A1B16	3,129	Low phase angle indication consistent with GTRF. No visual confirmation and the location is not consistent with expected grid elevations. Likely this indication is a spalled location.	
F35P17	1,604* 1,632* (repeated scan) *F35 rods are reversed in the cell, location is adjusted to be consistent with other sections	OD reduction due to a pellet-pellet gap, 35% through wall and 7% reduction in total cladding cross-sectional volume.	
6U3O05	3,032	23 mm long scratch with a 2% reduction in total cladding cross-sectional volume, likely deeper than typical rod insertion scratch.	
6U3P16	2,003	OD reduction due to a pellet-pellet gap.	

Notes on Table 7:

- The elevations cited have not been modified for rod slippage during scanning and are approximate only. See the discussion in Section 3.4.2.5.

3.4.2.5 Lift-Off Scan Results

The results of the lift-off eddy current measurements are summarized in Table 6.

As discussed previously, the axial locations recorded for the eddy current measurements during the scans were based on the rod speed and the elapsed time during the measurement. However, the speed of rod movement is known to vary somewhat with humidity and dust in the hot cell. For many of the sister rods the total travel length reported for the lift-off scan (the product of scan speed and elapsed time, as adjusted by the starting position of the scan) was somewhat shorter than the average measured rod length (see Section 3.3 and Table 4), indicating that some slippage of the rod occurred during the lift-off scan. Since one purpose of the eddy current measurements was to guide specimen selection for DE, the axial elevations associated with the lift-off scans have been linearly adjusted based on the measured rod lengths for each sister rod. The adjusted length is used in all lift-off graphs and data listings in this report.

Plots of all lift-off data taken during the eddy current campaign, including axial and rotational scans, are provided in Appendix C. Figure 40 provides an example of the typical four quadrant lift-off measurements. To obtain an average lift-off, the data from each of the four quadrant scans were averaged in 10 mm elevation increments, and then the four quadrant scans were averaged at each elevation to obtain a single rod average scan for each sister rod. Figure 41 and Figure 42 plot the rod average measured lift-off for rods 30AG09 and F35P17. Redundant scans were completed for these two rods, and the graphs provide an illustration of the repeatability observed for the hot cell lift-off measurements. The rod average lift-off measured for two scans at the same speed (10 mm/sec) and taken on different days are within 6 μm .

Figure 43 through Figure 49 provide graphs of the rod average measured lift-off for each sister rod grouped by parent fuel assembly. Figure 50 through Figure 52 plot the rod average lift-off of each sister rod by cladding alloy type. The lift-off measurements exhibited the expected trends, and features observed using gamma scanning and profilometry, such as grid depressions and diameter reductions, are also typically visible in the lift-off scans, as illustrated in Figure 53, Figure 54, and Figure 55 for a typical ZIRLO, M5 and Zirc-4/low-tin Zirc-4 clad sister rod, respectively. Similar to the gamma scanning (Section 3.2.1) and profilometry (Section 3.5) data, bambooing, a small diameter variation with a period of about 10 mm (the pellet length), is observable in the lift-off data, although it becomes much less discernible as the oxide/CRUD thickness increases. An example of the bambooing is plotted in Figure 56 for sister rod 3A1B16.

In most cases, the lift-off followed a smoothly increasing and decreasing trend. However, where oxide spalling or peeling is present, the lift-off measurements appear very noisy, with very high thickness measurements alternating with very low thickness measurements where the oxide has spalled or peeled off. As observed in both the visual and profilometry examinations, there is a large amount of spalling on some of the sister rods. Spalling/peeling oxide is observable on the lift-off traces as alternating high and low lift-off and is particularly significant in the higher elevations of rods 3A1B16, 3A1F05, F35K13, F35P17, and 3F9N05. An example of the lift-off data obtained in spalled areas of the rod is provided in Figure 57 for rod F35K13. As mentioned previously, several rotational scans were completed at discrete rod elevations. Figure 58 provides an example of a rotational scan in spalled areas of rod 3A1B16.

Sister rod 3F9D07 was additionally axially scanned at 75° over the upper high burnup rod elevations. This rod's additional axial data, along with its 0°, 90°, 180°, and 270° data, were used to generate a rod average lift-off surface plot. The surface plot shown in Figure 59 illustrates the lift-off variation in the higher burnup elevations of the rod, where thermal and flow mixing effects and GTRF related to the spacer grid locations produced local reductions in oxide thickness.

In the high burnup rod elevations (~3,000 to 3,500 mm), many of the rods appear to have circumferential variations in lift-off. Asymmetric oxide thickness is expected to form on some rods, as in-reactor flow and temperature conditions are known to vary circumferentially and axially depending on the location of the

rod in its fuel assembly, with corner and peripheral rods being more susceptible. For example, sister rod 3F9N05 was measured rotationally at an elevation of 3,209 mm, revealing an increase from $\sim 50\text{ }\mu\text{m}$ to $\sim 85\text{ }\mu\text{m}$. The locally high oxide thickness produced some spalling, as shown in Figure 60. A second example is provided in Figure 61 for sister rod 6U3P16.

The rotational scans are also useful in estimating the depth and extent of the spalling and GTRF marks. The depth that can be measured with the pancake coil is limited by the coil head geometry, and the coil was not specifically calibrated for depth measurements. Thus, any depth measurements using the pancake coil should be regarded as informational only. As illustrated in Figure 62, the two GTRF marks visually identified on sister rod 3F9D07 at an elevation of 2,279 mm were measured in a rotational scan as 28 and 18 μm deep as compared with the estimated average depth of 16 μm based on the encircling coil scan. The ridging measured on each side of the GTRF marks may indicate that the cladding material was ploughed to the sides of the spacer grid springs, as opposed to removal of the material and release to the reactor coolant as small fines. Since the material was not removed from the cladding, the encircling coil tends to underestimate the depth of the fretting marks.

A second GTRF location on 3F9D07, 1,765 mm, was also measured rotationally, with the depth of two GTRF marks and two axial rod insertion/removal scratches measured, as shown in

Figure 63. The grid insertion/removal axial scratches are visible as square-bottomed features in most of the rotational traces, typically $\sim 3\text{ }\mu\text{m}$ deep, and serve to align the images with the rotational trace. The larger GTRF mark visible at 1,765 mm is partially oxidized (indicating that GTRF was not active in later cycles) with a maximum depth indication of 8 μm . The rotational trace seems to indicate that the smaller wear scar had very little depth ($\sim 2\text{ }\mu\text{m}$) and in fact did not appear to penetrate the oxide layer to the metal surface. However, the image indicates a matte black metal surface in the center of the wear scar. Based on the image, it is likely that the rotational trace missed the deeper portions of the larger wear scar and completely missed the smaller wear scar. For GTRF marks, the lift-off technique requires that the GTRF mark be aligned with the tip of the pancake probe, and the alignment relied on visual confirmation looking through the hot cell window. Given the inaccuracies associated with the alignment, it is evident that the scans did not always measure the desired location on the rod. The measured depths of the axial scratches at the 1,765 mm elevation on 3F9D07 are 2 – 3 μm .

Several rotational scans were taken at grid exit locations, where visible flow patterns were observed. As illustrated in Figure 64, for sister rod F35P17, the difference in lift-off around the circumference resulting from differential flow at a spacer grid location is about 10 μm . This was consistent for the sister rods measured at this type of visible flow patterns.

The rotational scans can also be used to verify the axial scan's reported lift-off magnitude at the rotational elevations measured. In all cases, the rotationally measured scan magnitudes were within 5 μm of those reported by the axial scans. A summary is provided in Table 6.

In some cases, the lift-off trace appears to shift, as illustrated in Figure 65. There are two likely sources of this shift: (1) sticking of the pancake coil in its spring-loaded fixture and (2) the accumulation of debris underneath the contact surface of the coil that is dislodged later in the scan. Although it is possible for signal drift to affect the scan results, it is unlikely to be the source of these observed deviations, as the post-rod calibration was successful in all cases. Furthermore, signal drift is typically a gradual process and would not be expected to result in abrupt shifts in the trace. These data were not discarded, but the averaging of the four quadrants tends to minimize the effects of the shift.

Two sister rods, F35P17 and F35K13, were previously measured at poolside after reactor discharge [9]. Figure 66 compares the poolside lift-off measurements with the average hot cell lift-off measurements. While the trends between the EPRI and ORNL measurements are very similar, the difference in the average lift-off magnitude is fairly significant. The differential of the ORNL lift-off measurements from the EPRI reported "Avg.02" value at the peak lift-off location is 23 μm for F35P17 and 34 μm for

F35K13, a difference of 15 – 25%. Similar to the ORNL hot cell scans, the EPRI scans also included an axial scan in each quadrant. A comparison of the EPRI 0°, 90°, 180° and 270° reported lift-off at each elevation yields an average difference of 12% and an average variance of 12 μm around the circumference of the rod, with as much as a 25% difference and a 75 μm variance in the hottest operating spans. As circumferential variation in the oxide thickness is expected and these two very HBU Zirc-4-clad sister rods have a very large amount of oxide spalling from their four cycles in reactor, a conclusion about the veracity of either the poolside EPRI or the ORNL traditional data cannot be drawn. As a final comparison, previous oxide thickness measurements [The metallography samples that will be examined during the destructive examinations of the sister rods are expected to provide a definitive oxide thickness measurement for each sister rod. Therefore, while the NDE lift-off data appear to be valid for use in the primary purpose of guiding the DE specimen selection process, it should not be cited where a precision measurement of the total oxide thickness is required.

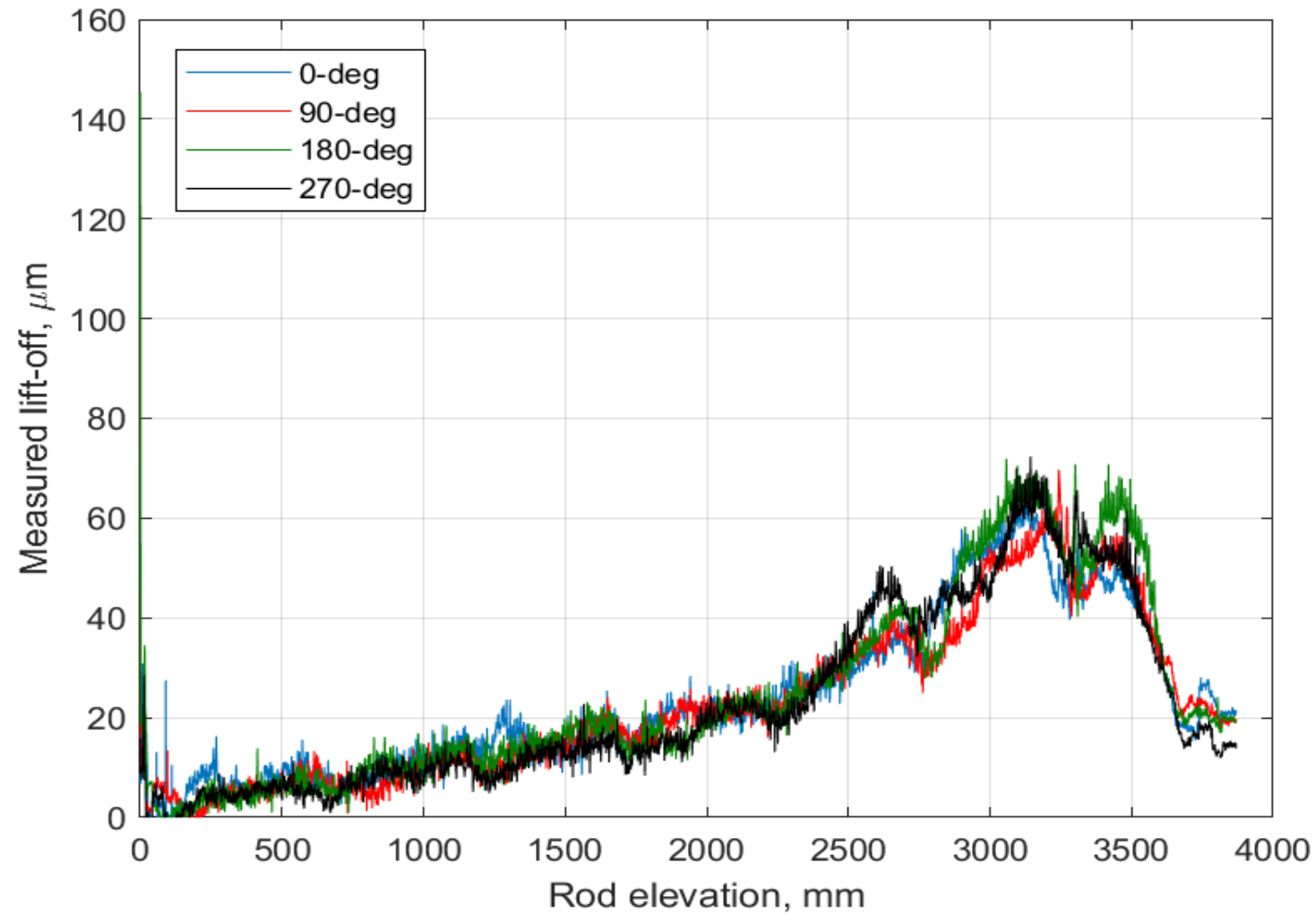


Figure 40. Lift-Off Measured in All Four Quadrants, Sister Rod 6U3O05.

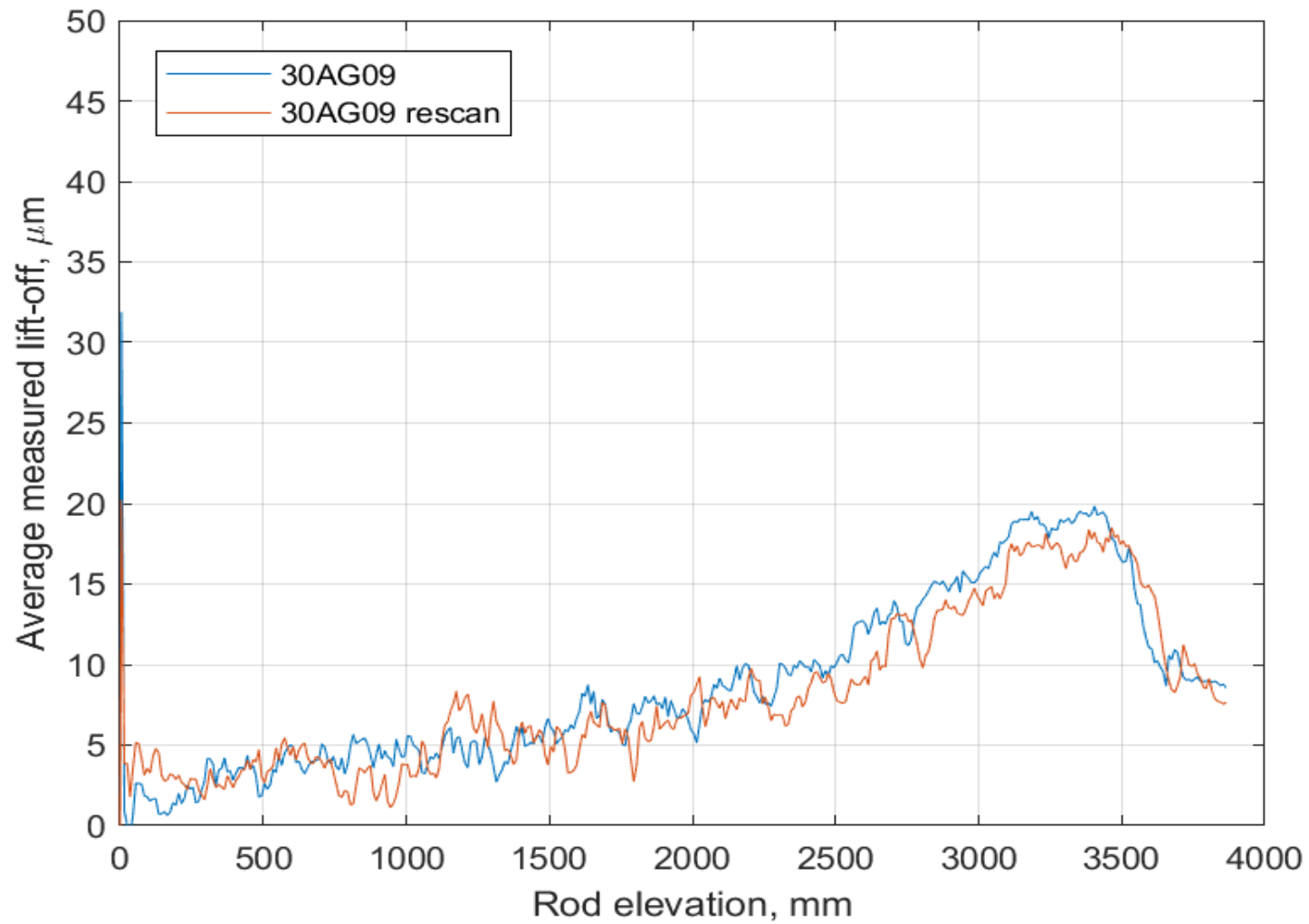


Figure 41. A Comparison of the Average Measured Lift-Off for Two Scans Completed on Rod 30AG09, Both at 10 mm/sec.

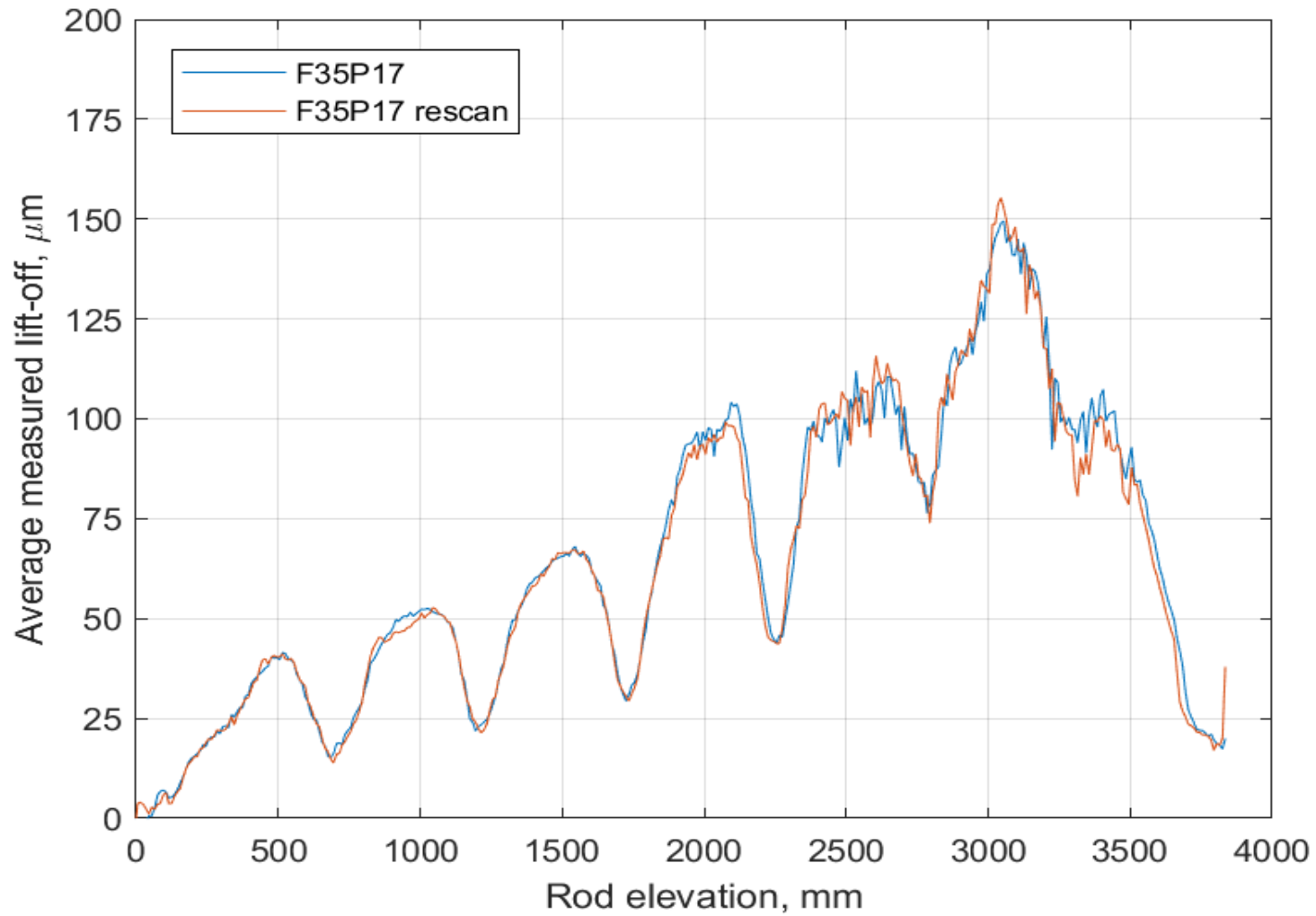


Figure 42. A Comparison of the Average Measured Lift-Off for Two Scans Completed on Rod F35P17, both at 10 mm/sec.

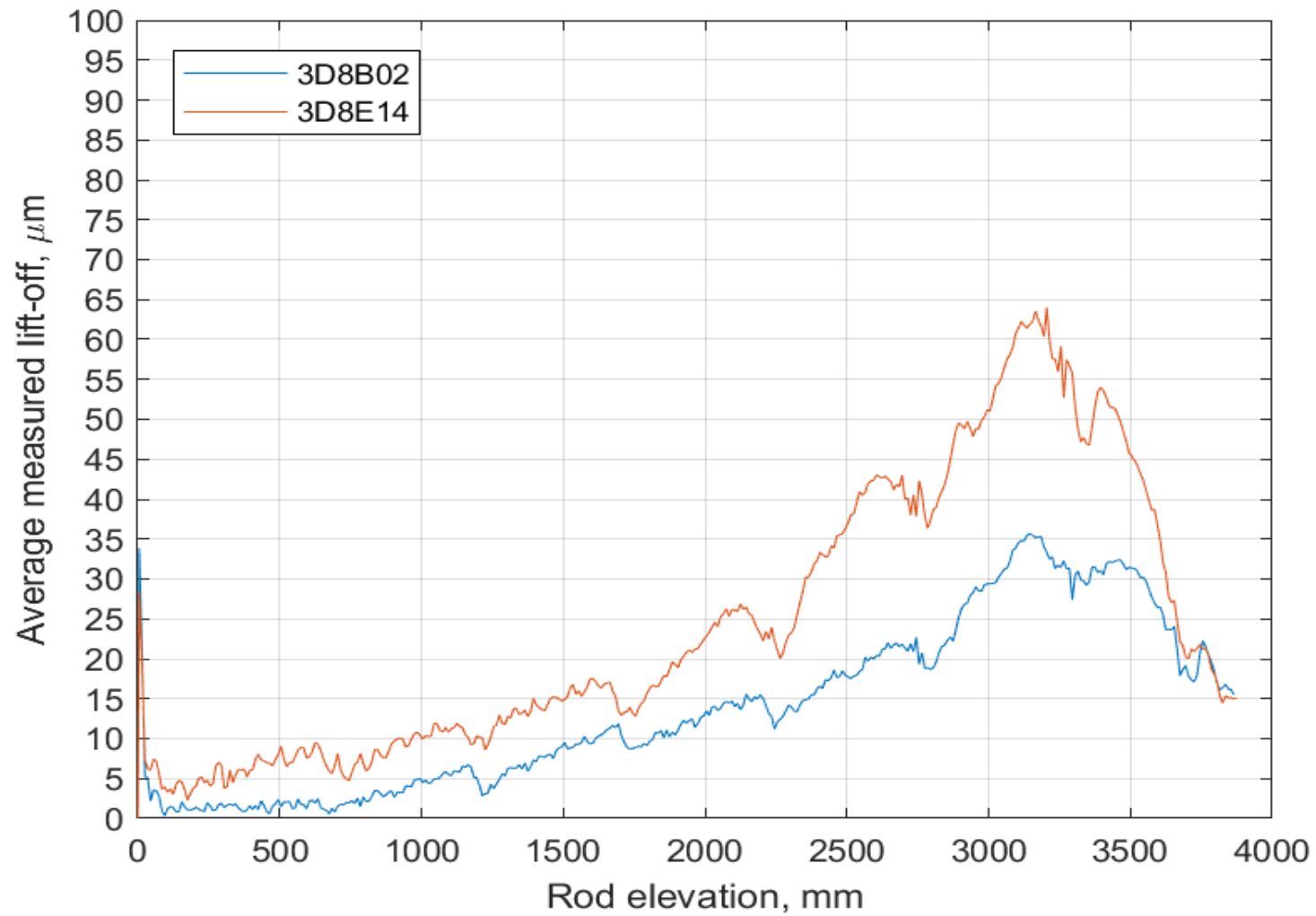


Figure 43. Average Measured Lift-Off for Sister Rods from Fuel Assembly 3D8.

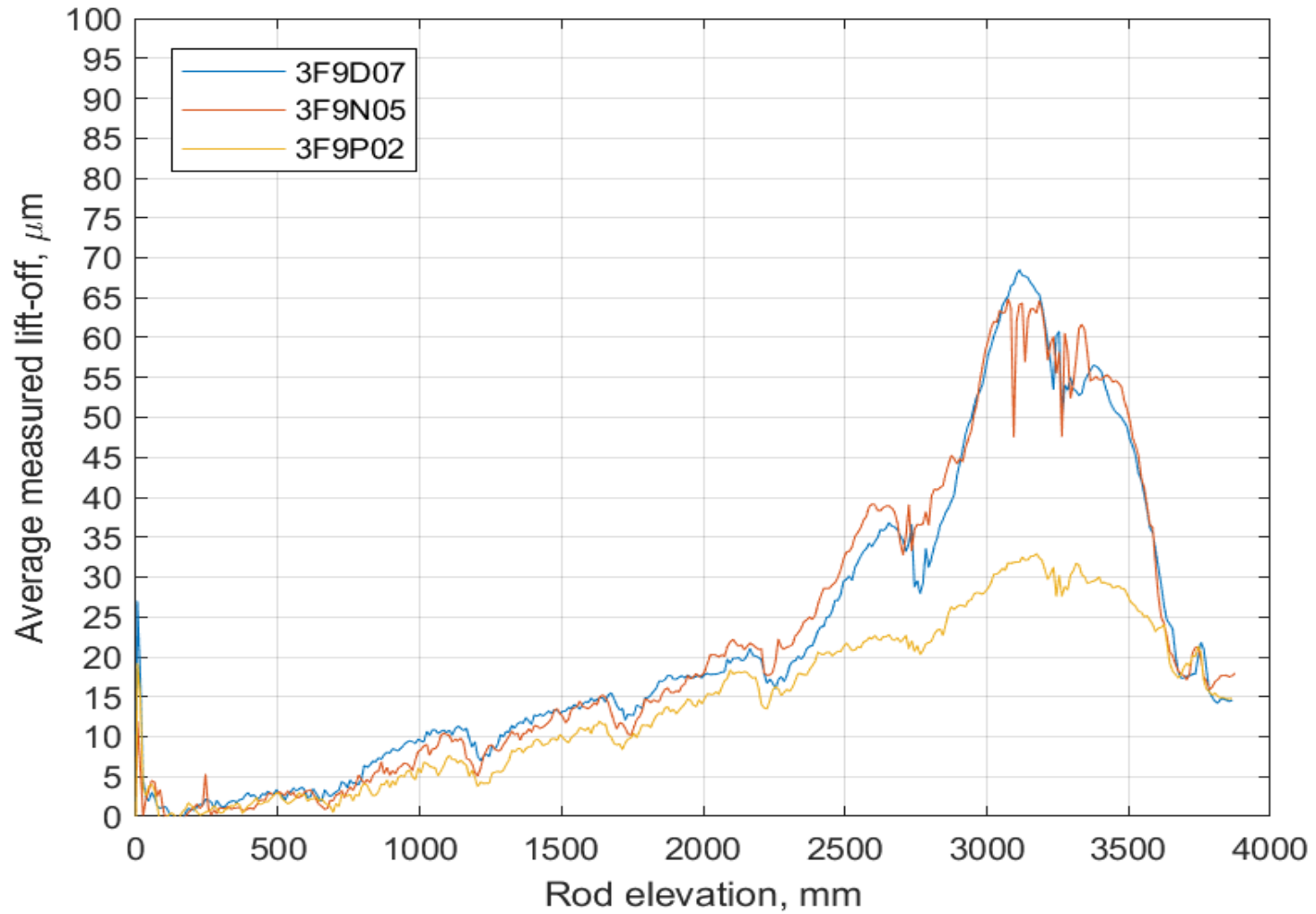


Figure 44. Average Measured Lift-Off for Sister Rods from Fuel Assembly 3F9.

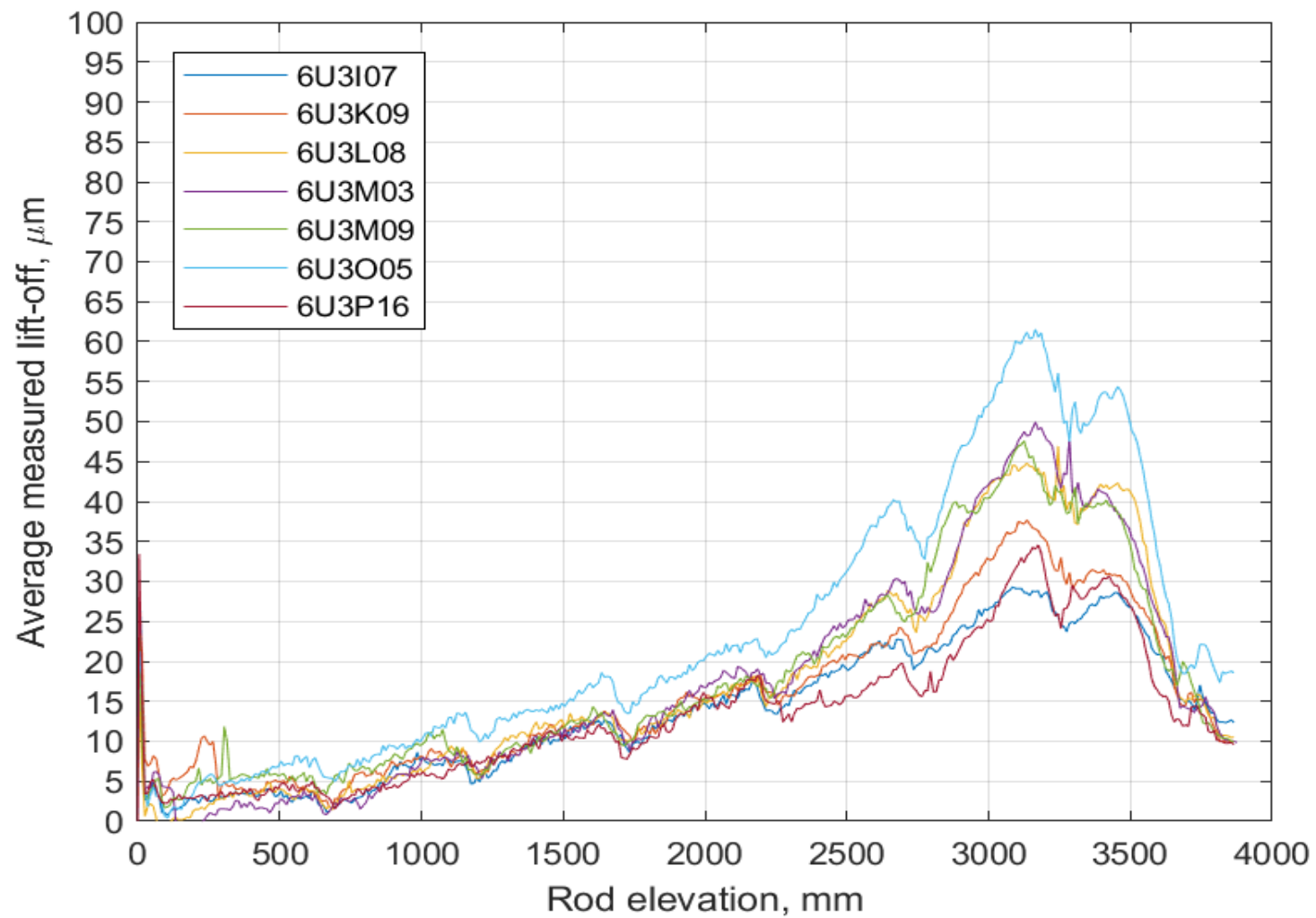


Figure 45. Average Measured Lift-Off for Sister Rods from Fuel Assembly 6U3.

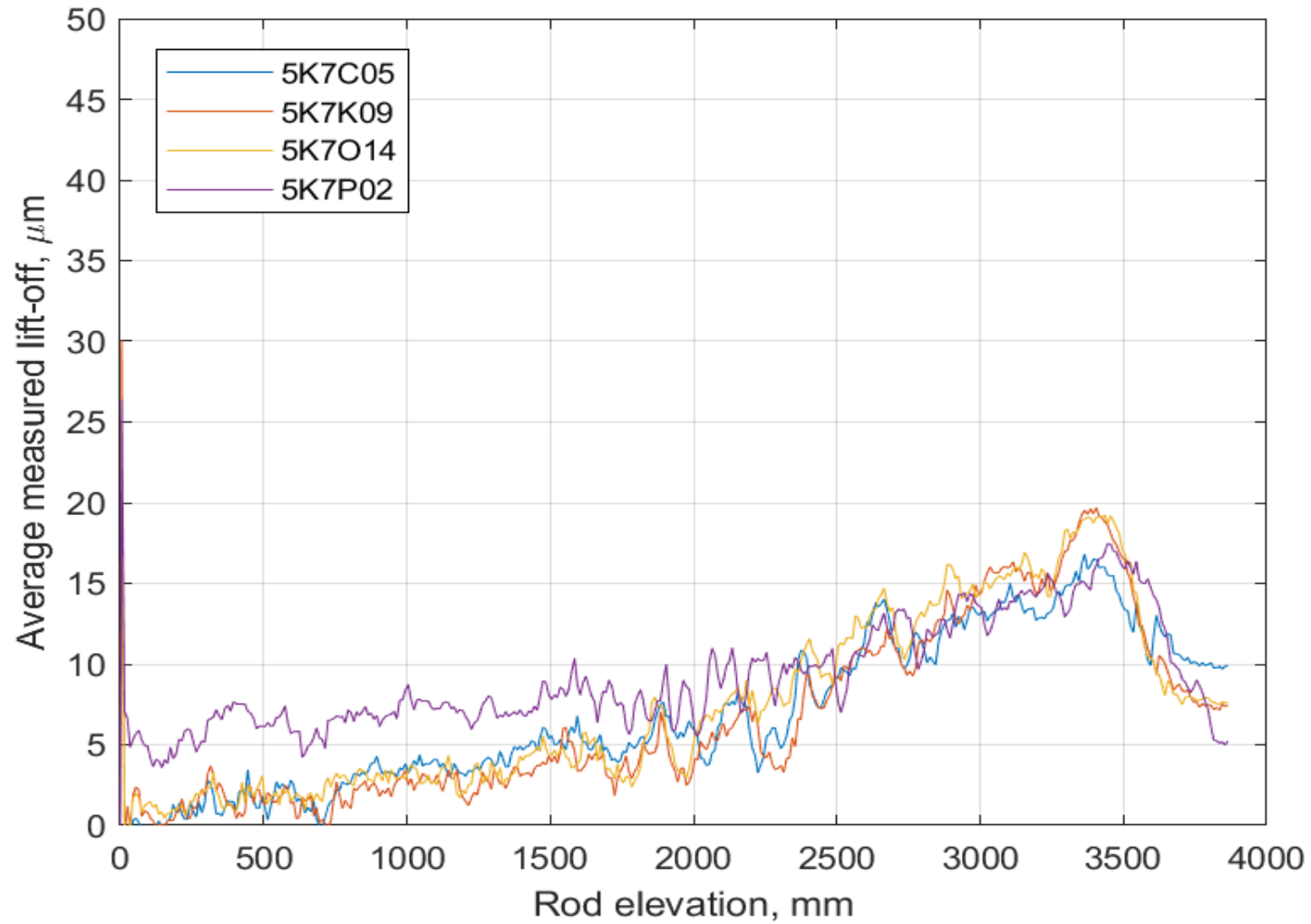


Figure 46. Average Measured Lift-Off for Sister Rods from Fuel Assembly 5K7.

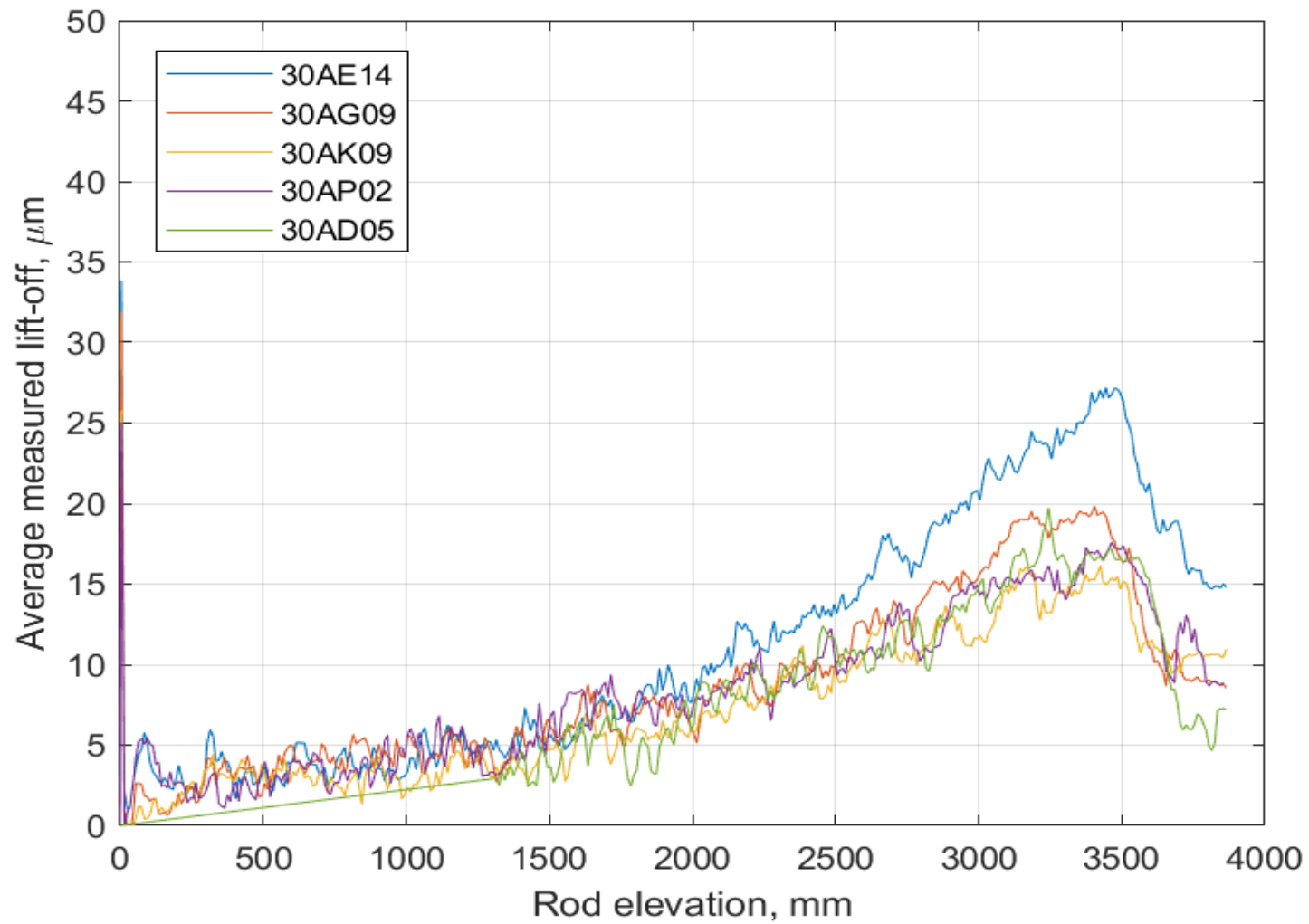


Figure 47. Average Measured Lift-Off for Sister Rods from Fuel Assembly 30A.

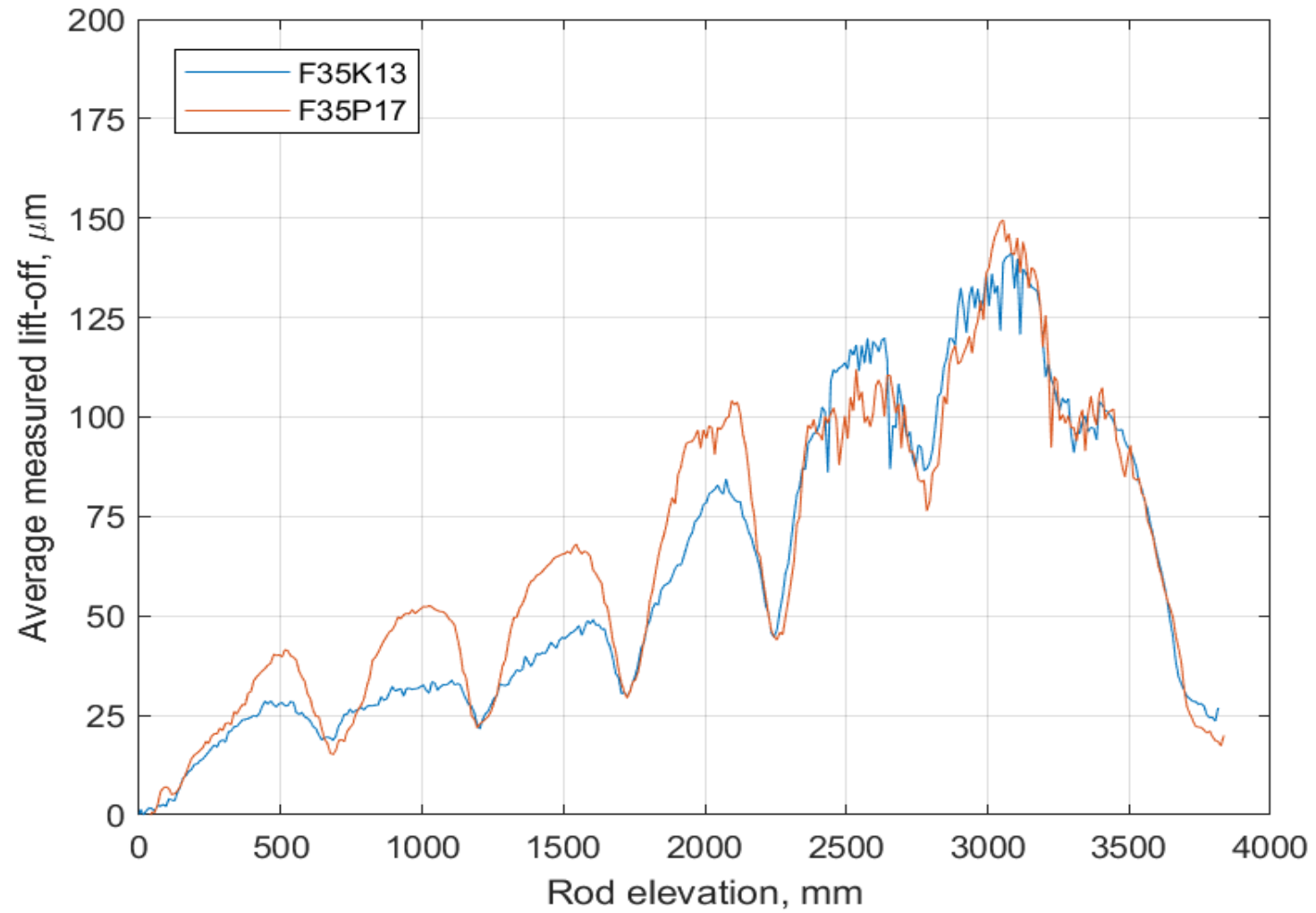


Figure 48. Average Measured Lift-Off for Sister Rods from Fuel Assembly F35.

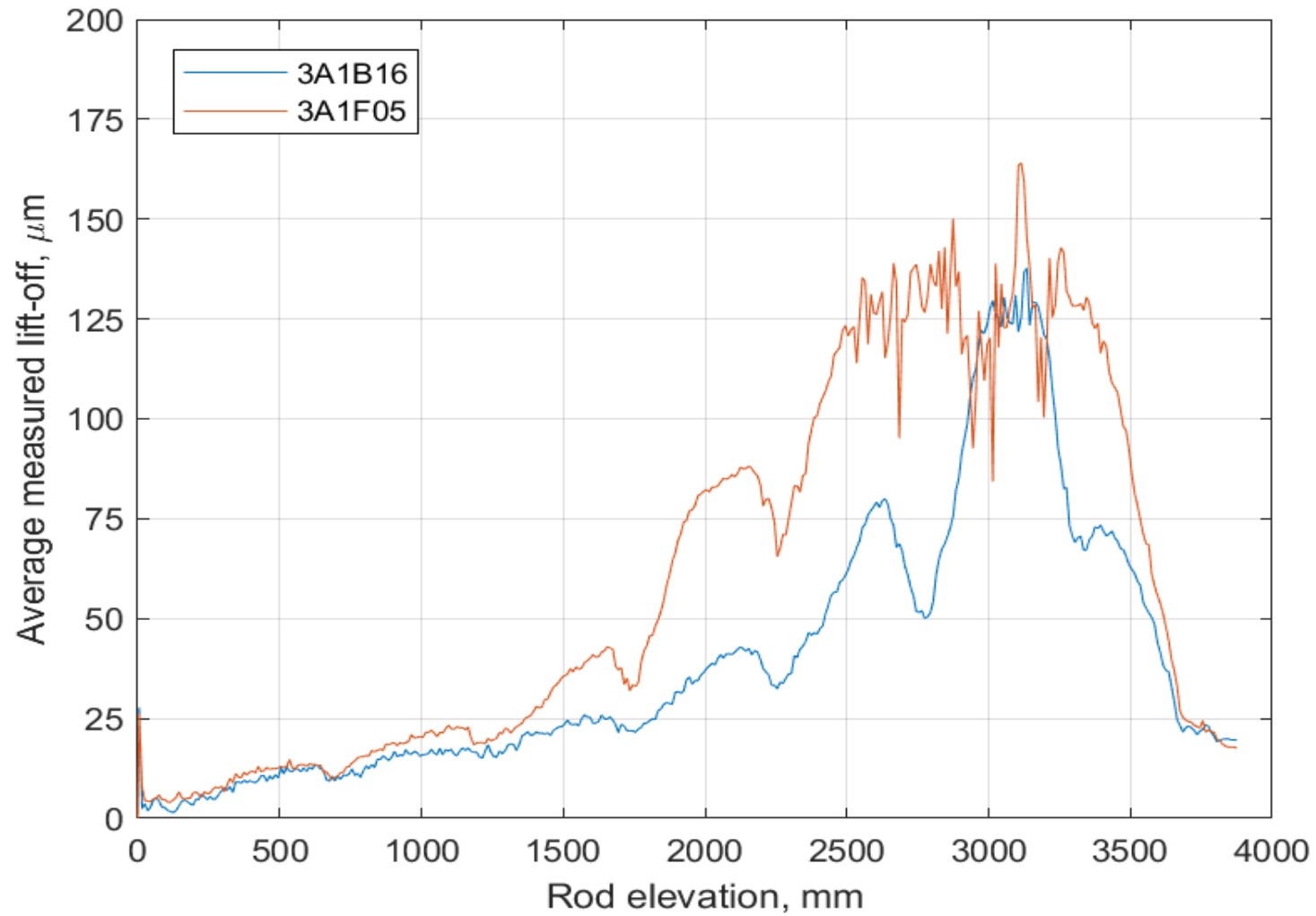


Figure 49. Average Measured Lift-Off for Sister Rods from Fuel Assembly 3A1.

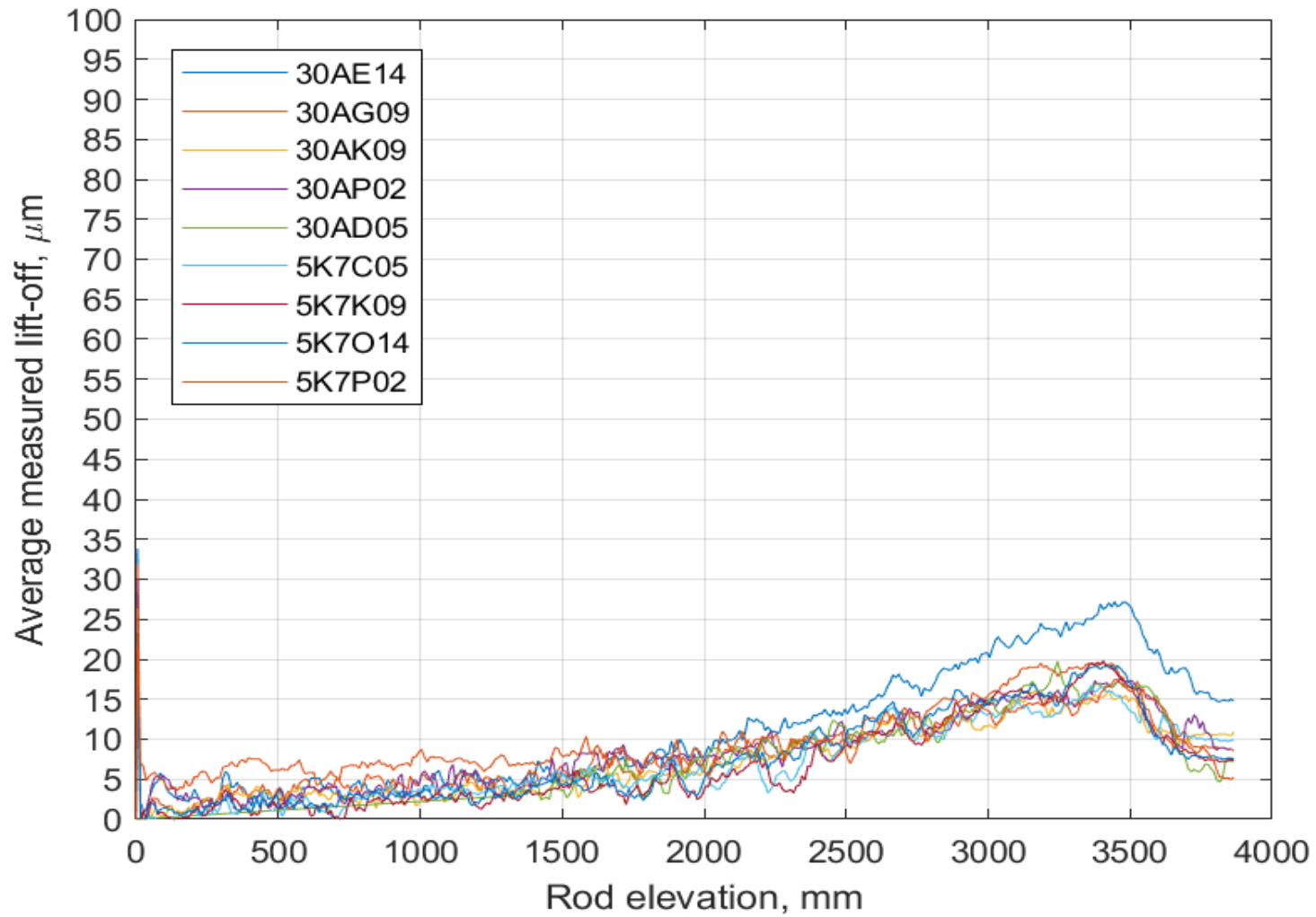


Figure 50. Average Measured Lift-Off for All M5-Clad Sister Rods.

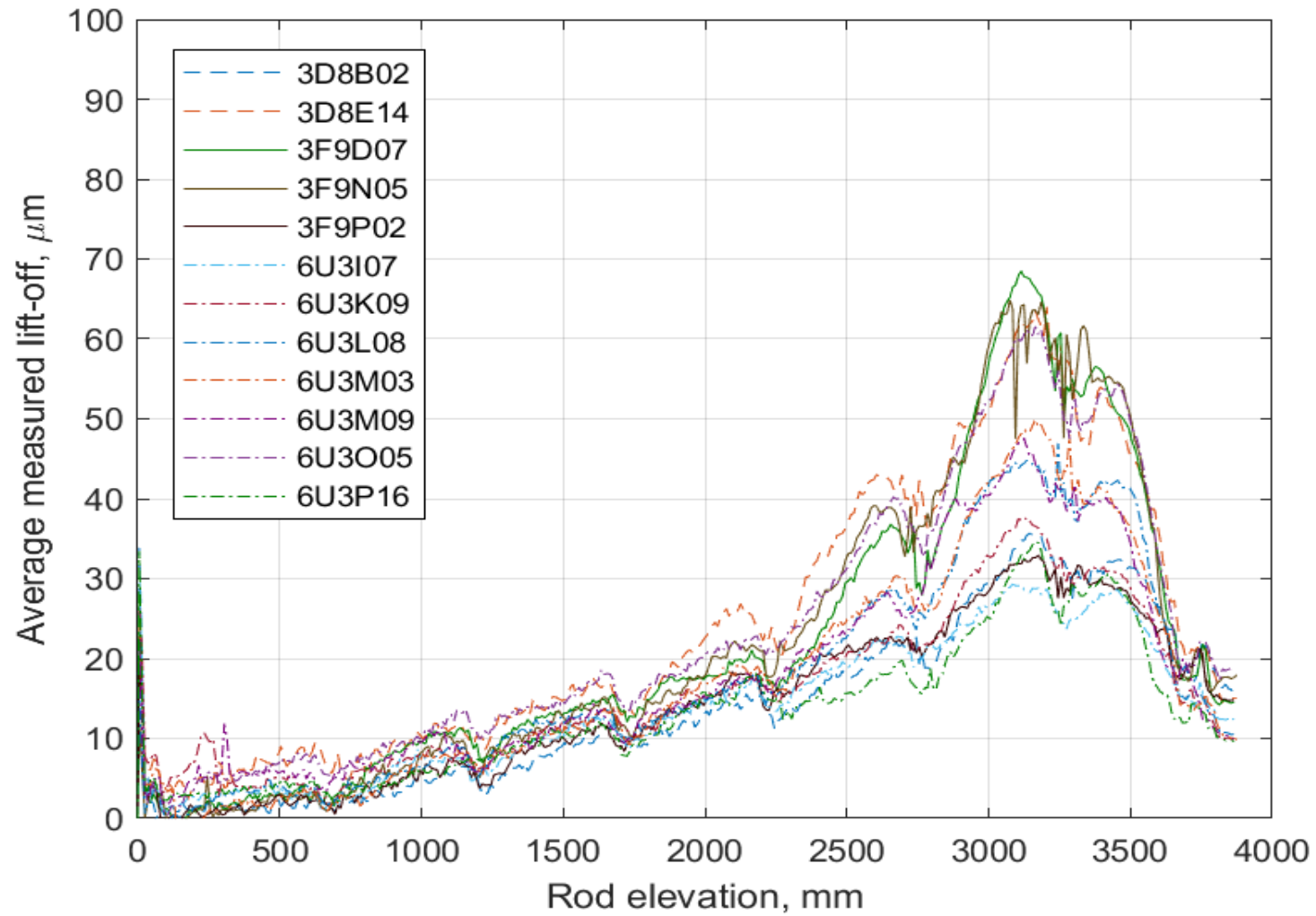


Figure 51. Average Measured Lift-Off for All ZIRLO-Clad Sister Rods.

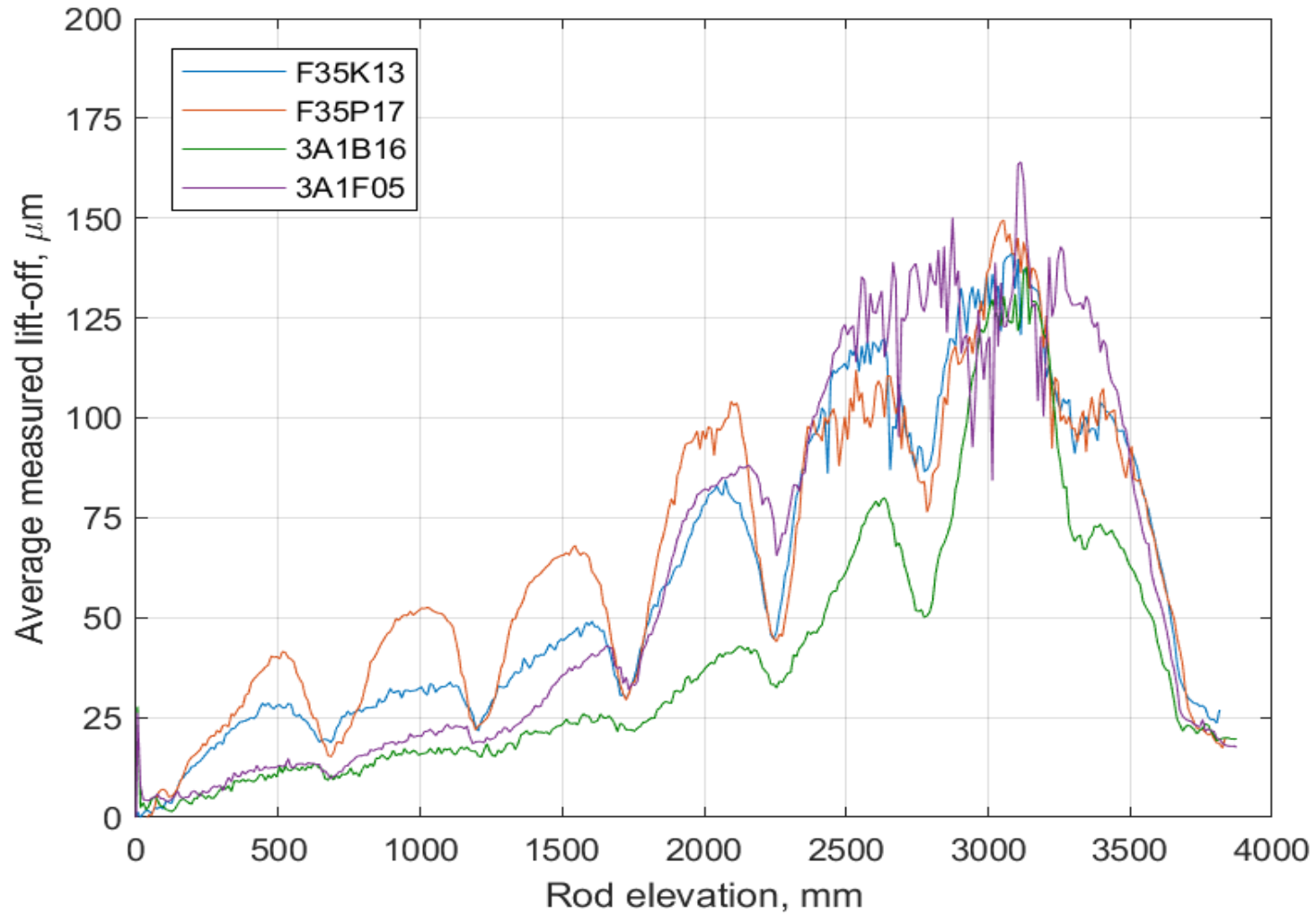


Figure 52. Average Measured Lift-Off for All Zirc-4 and Low-Tin Zirc-4-Clad Sister Rods.

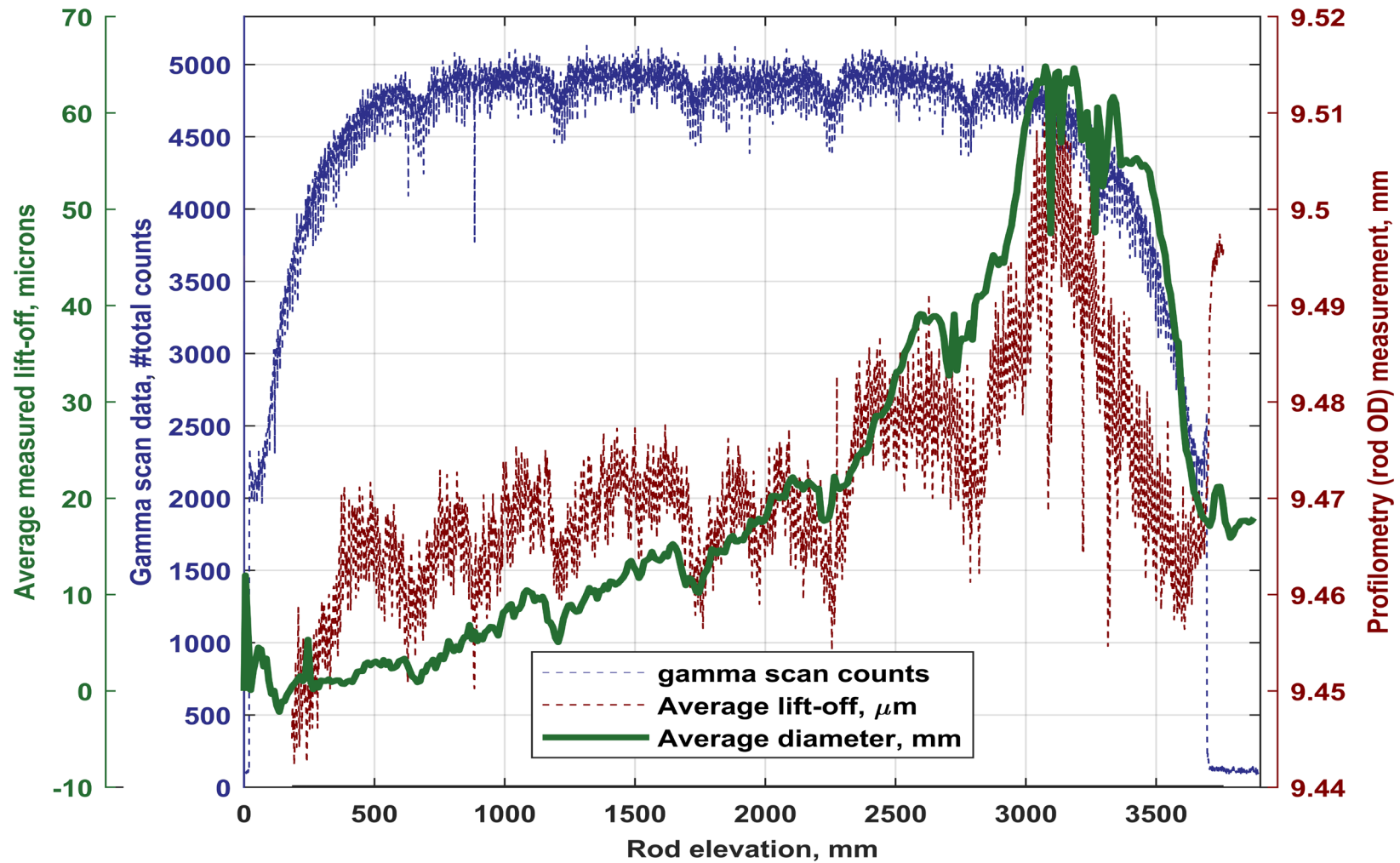


Figure 53. A Comparison of the Trends Observed in the Average Measured Gamma Scan, Profilometry, and Lift-Off Scans for Sister Rod 3F9N05.

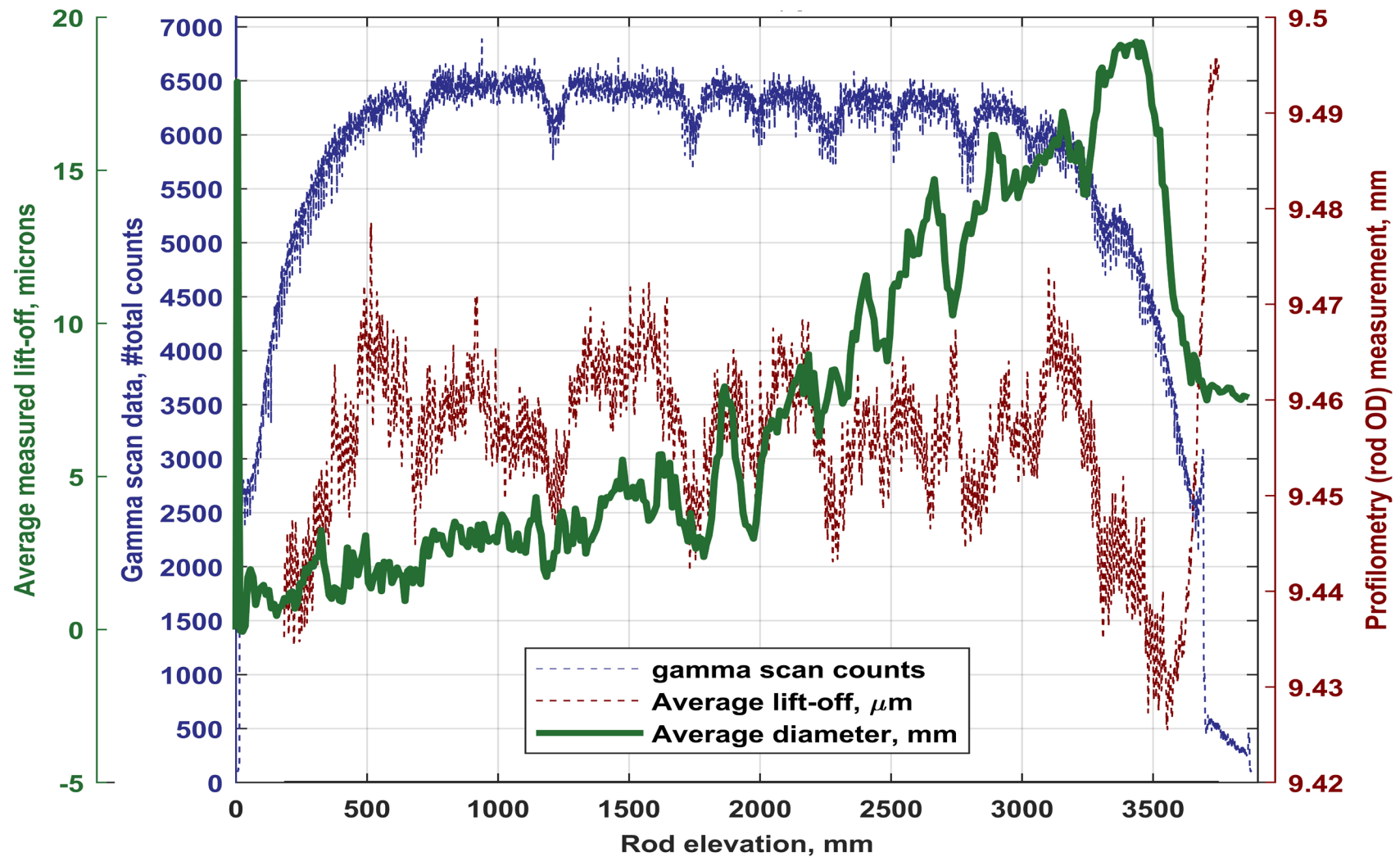


Figure 54. A Comparison of the Trends Observed in the Average Measured Gamma Scan, Profilometry, and Lift-Off Scans for Sister Rod 5K7O14.

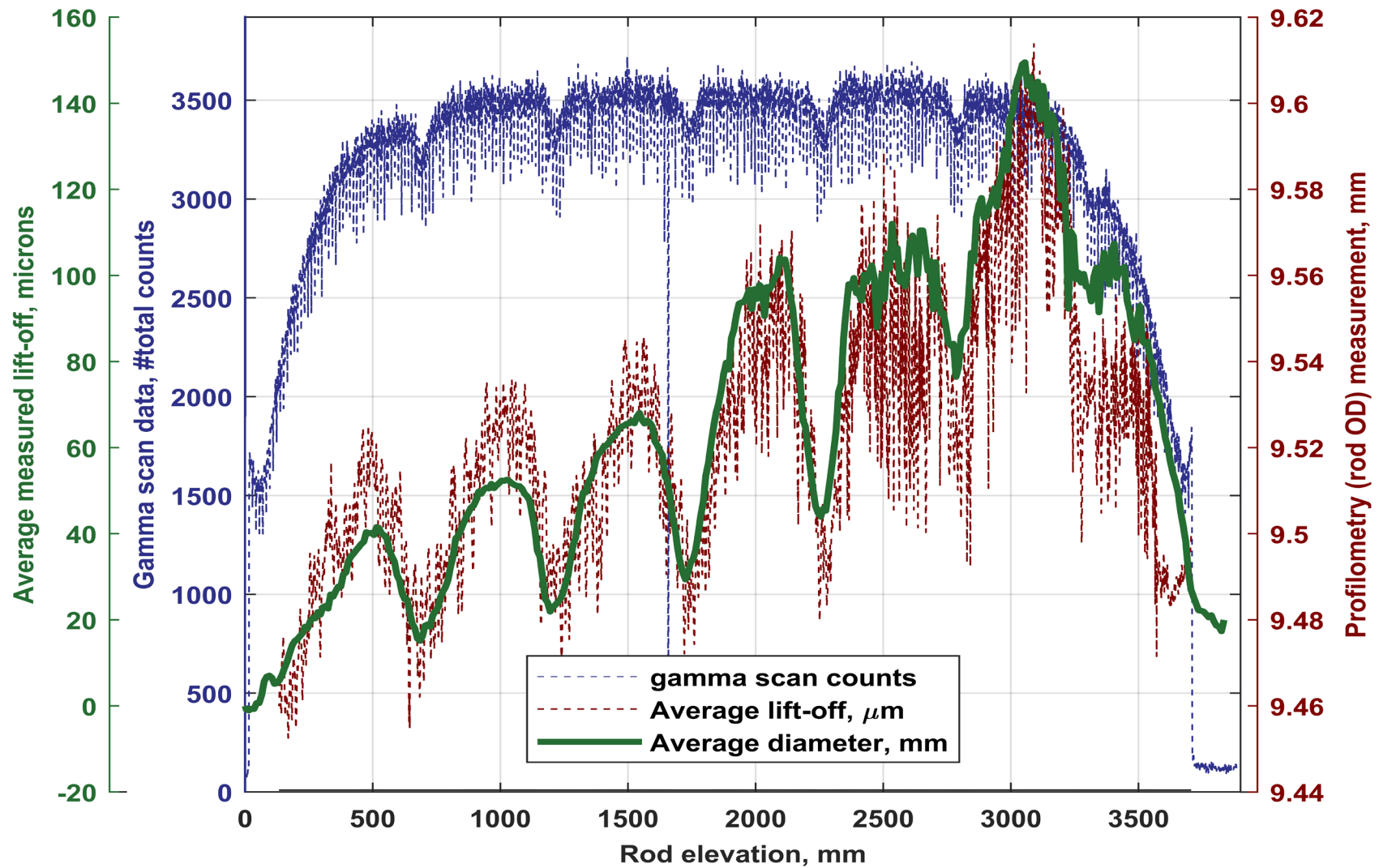


Figure 55. A Comparison of the Trends Observed in the Average Measured Gamma Scan, Profilometry, and Lift-Off Scans for Sister Rod F35P17.

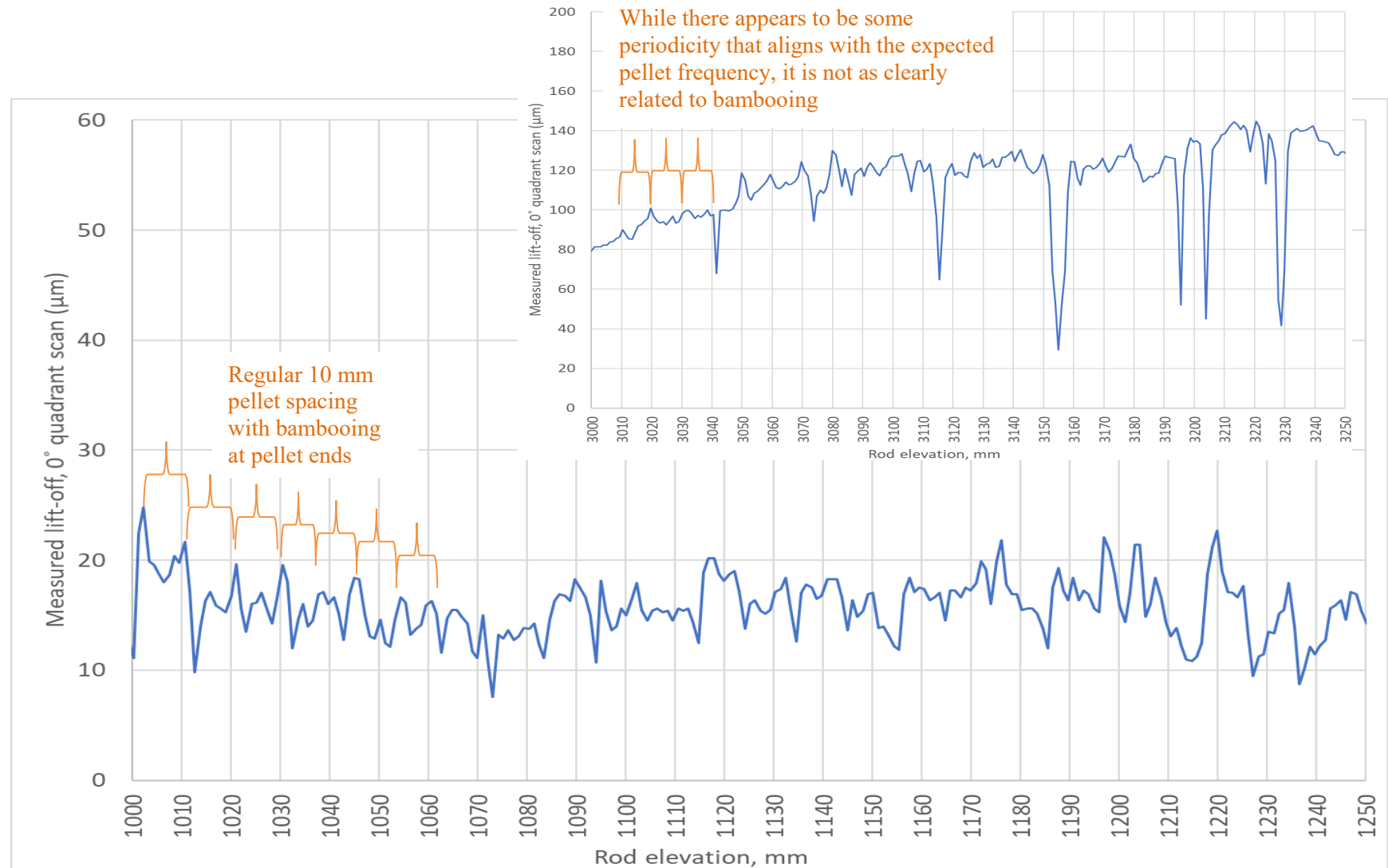


Figure 56. Rod Bambooning Is Observable in the Lift-Off Data in Lower Oxide/CRUD Thickness Regions (Main Graph) and is Less Discernable Where the Oxide/CRUD Thickness Is Large (See the Inset), As Shown for Sister Rod 3A1B16.

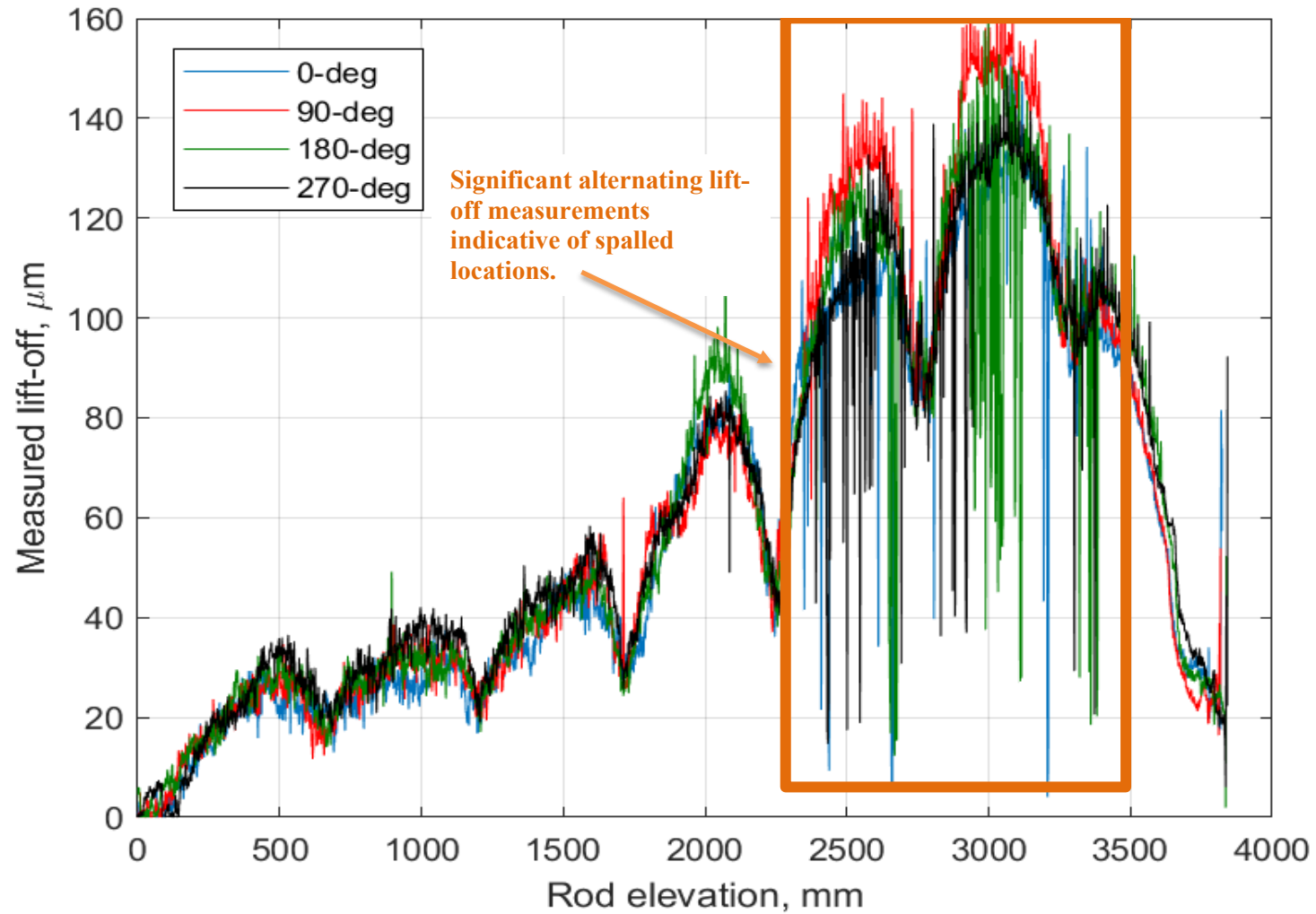


Figure 57. An Example of Lift-Off Measurements Where Significant Spalling Is Present (Four Quadrant Lift-Off, Sister Rod F35K13).

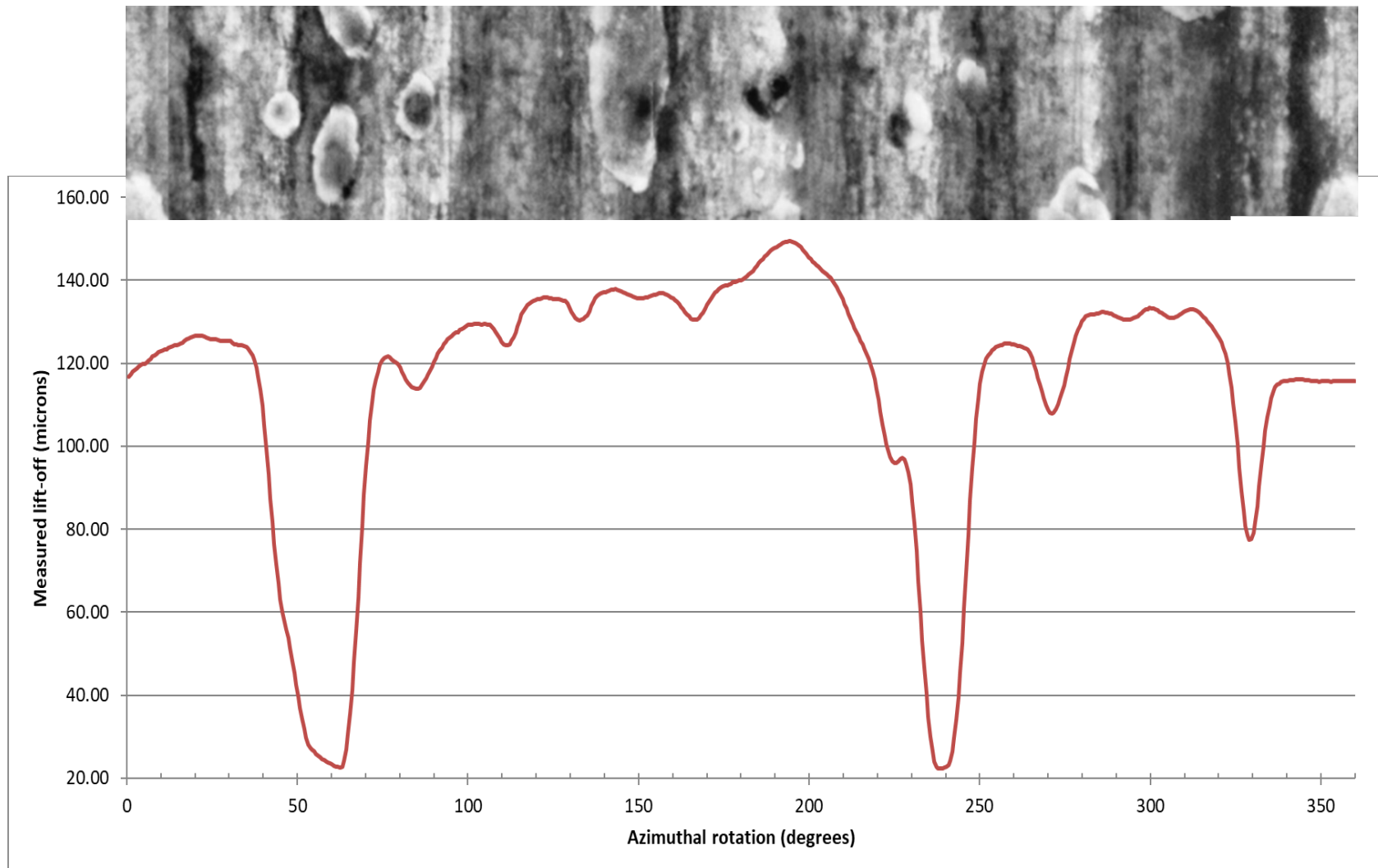


Figure 58. Rotational Eddy Current Lift-Off Scans of 3A1B16 at 3,101 mm.

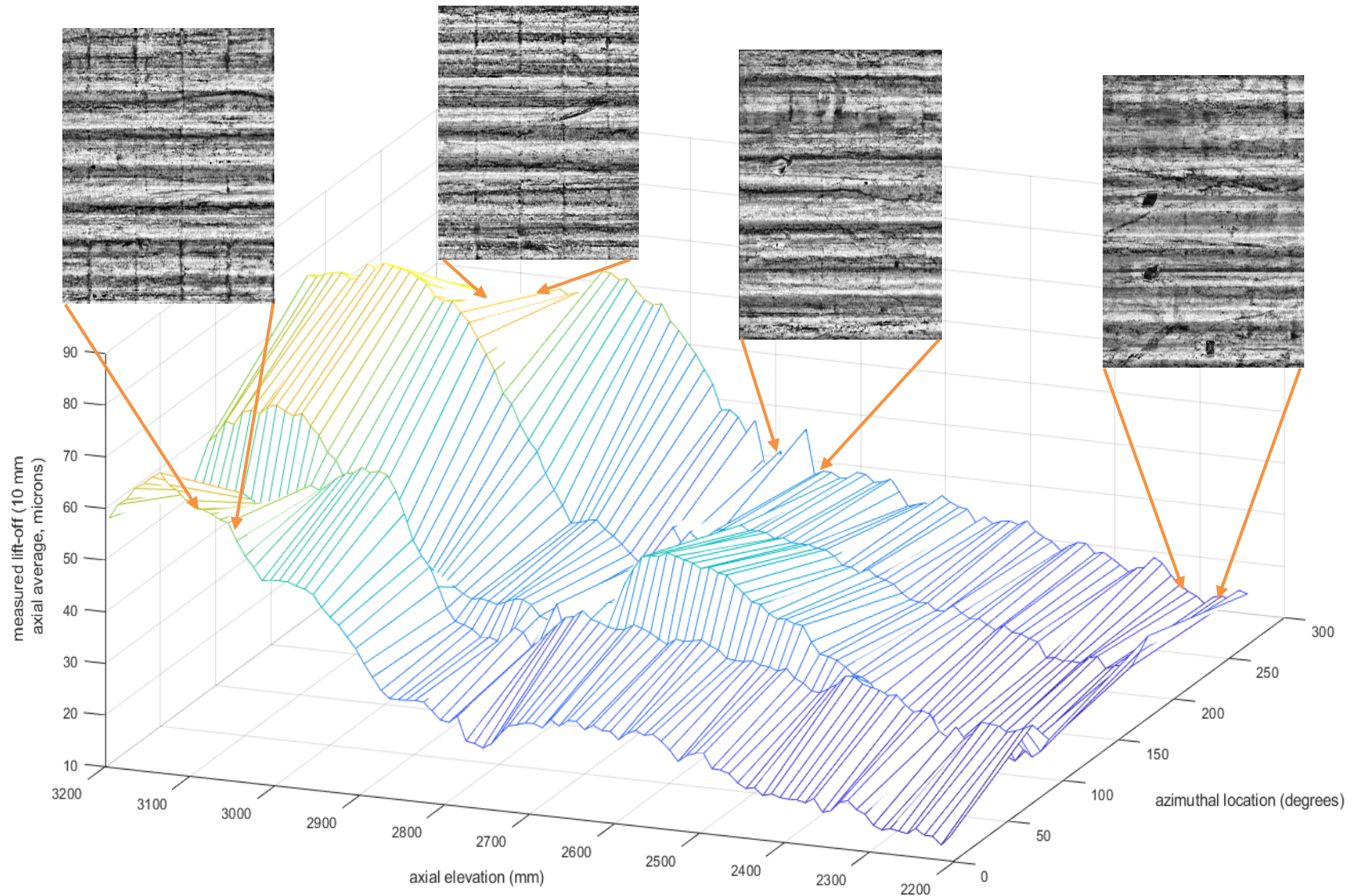


Figure 59. A 3D Surface Plot Illustrating the Variations in Measured Lift-Off Over the Circumference of Sister Rod 3F9D07 in Higher Burnup Elevations Compared with Visible Rod Features.

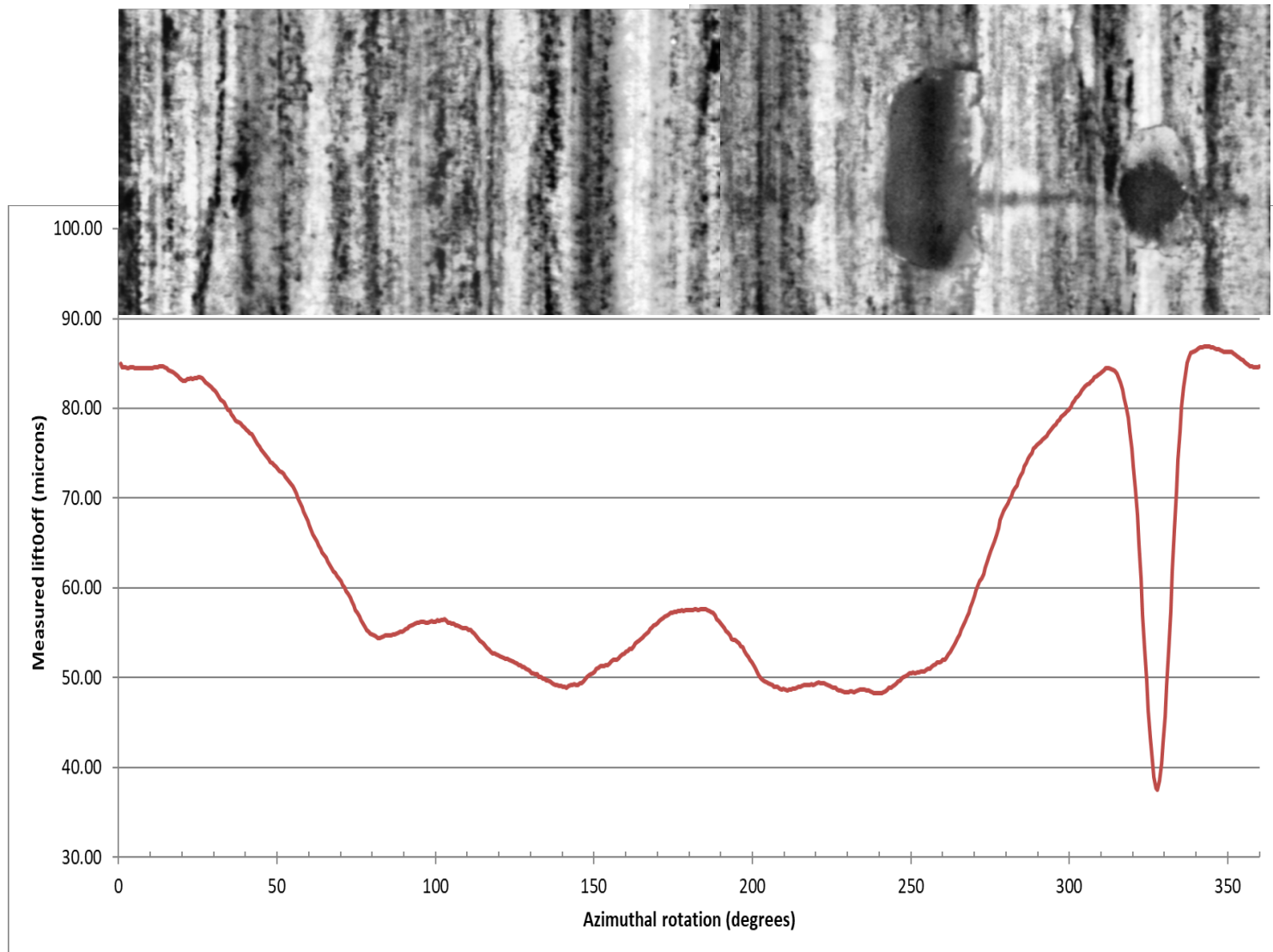


Figure 60. Rotational Eddy Current Lift-Off Scan of 3F9N05 at 3,209 mm.

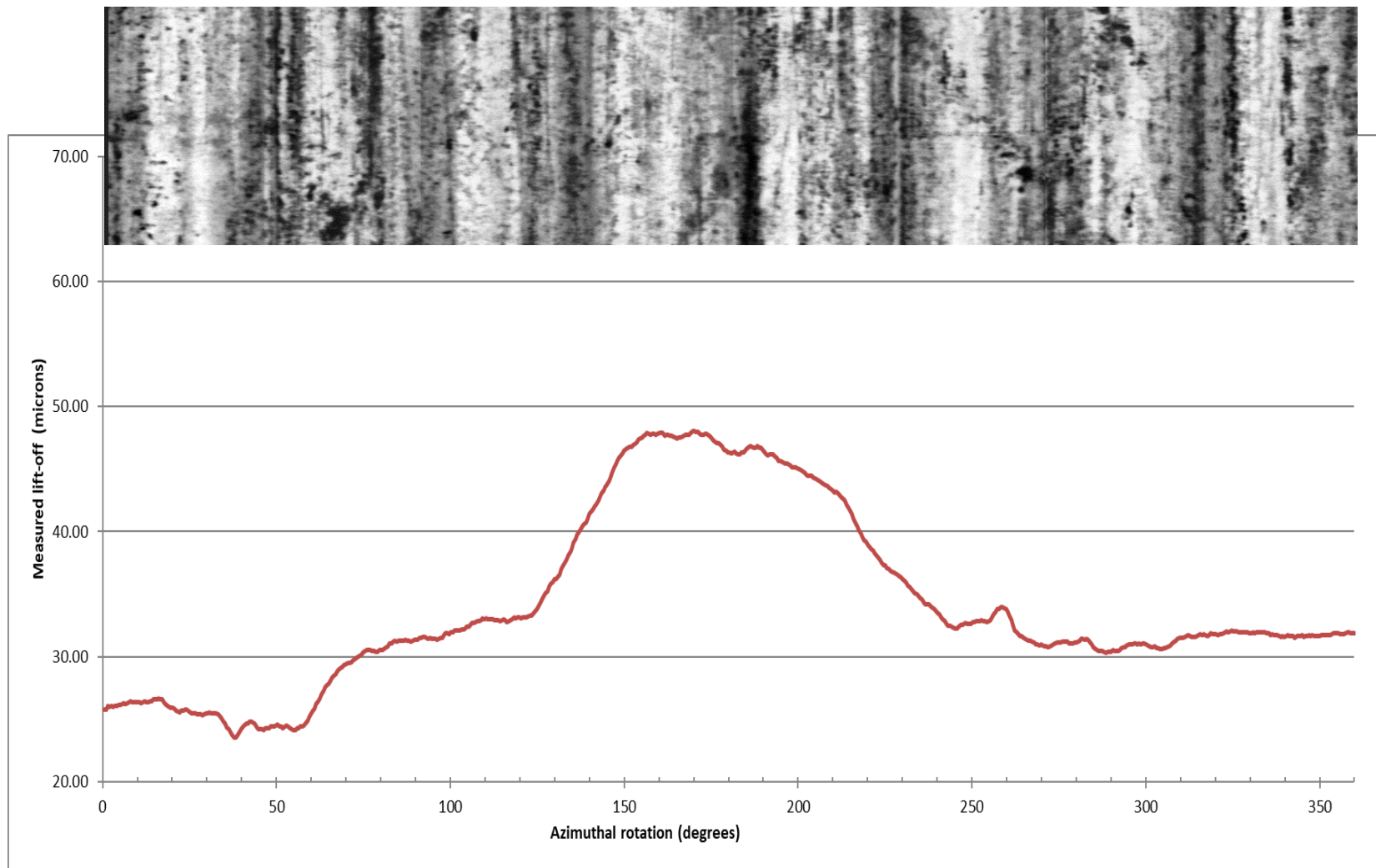


Figure 61. Rotational Eddy Current Lift-Off Scans of 6U3P16 at 3,434 mm.

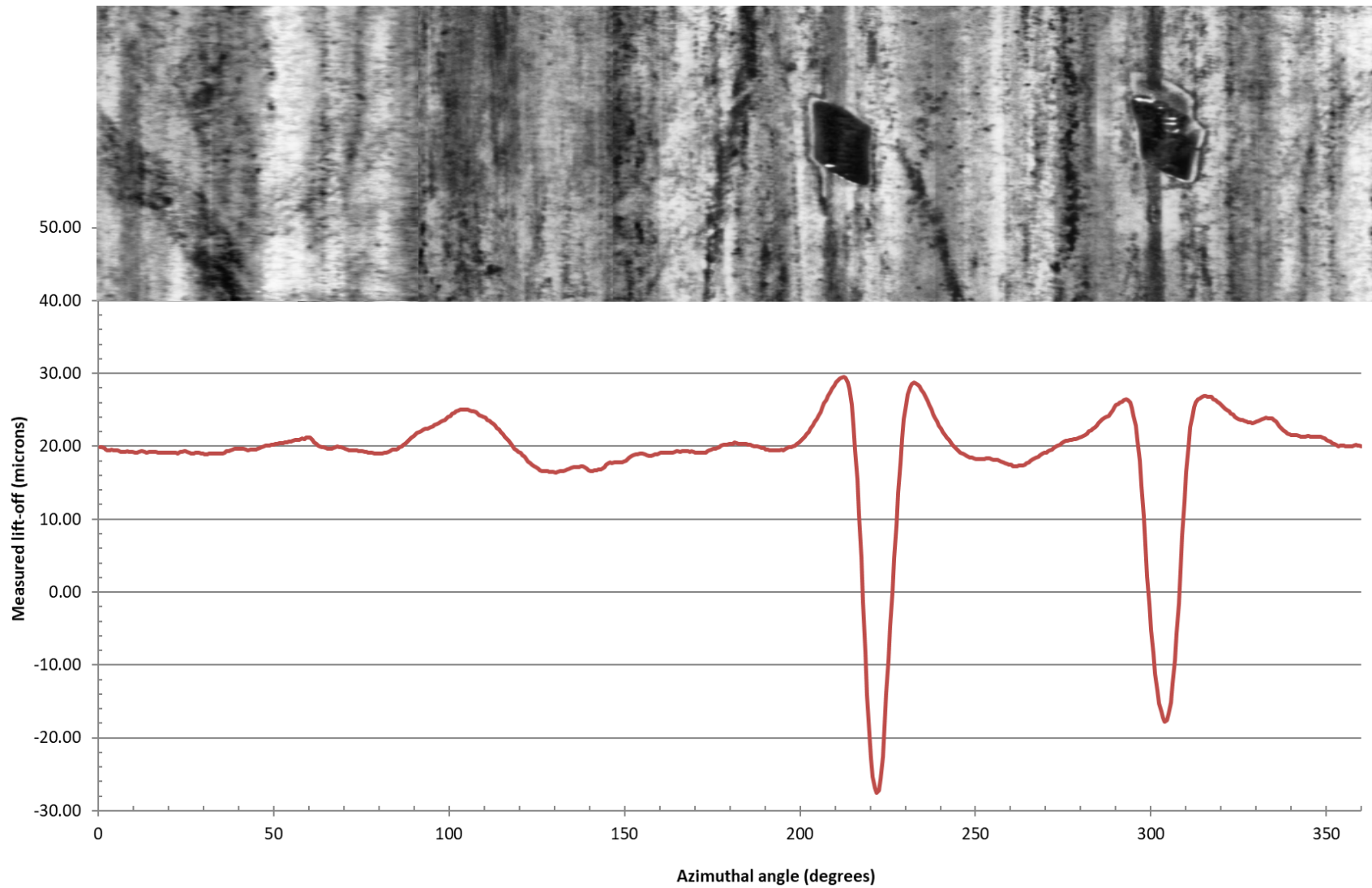


Figure 62. Rotational Scan of Sister Rod 3F9D07 at 2,279 mm Elevation.

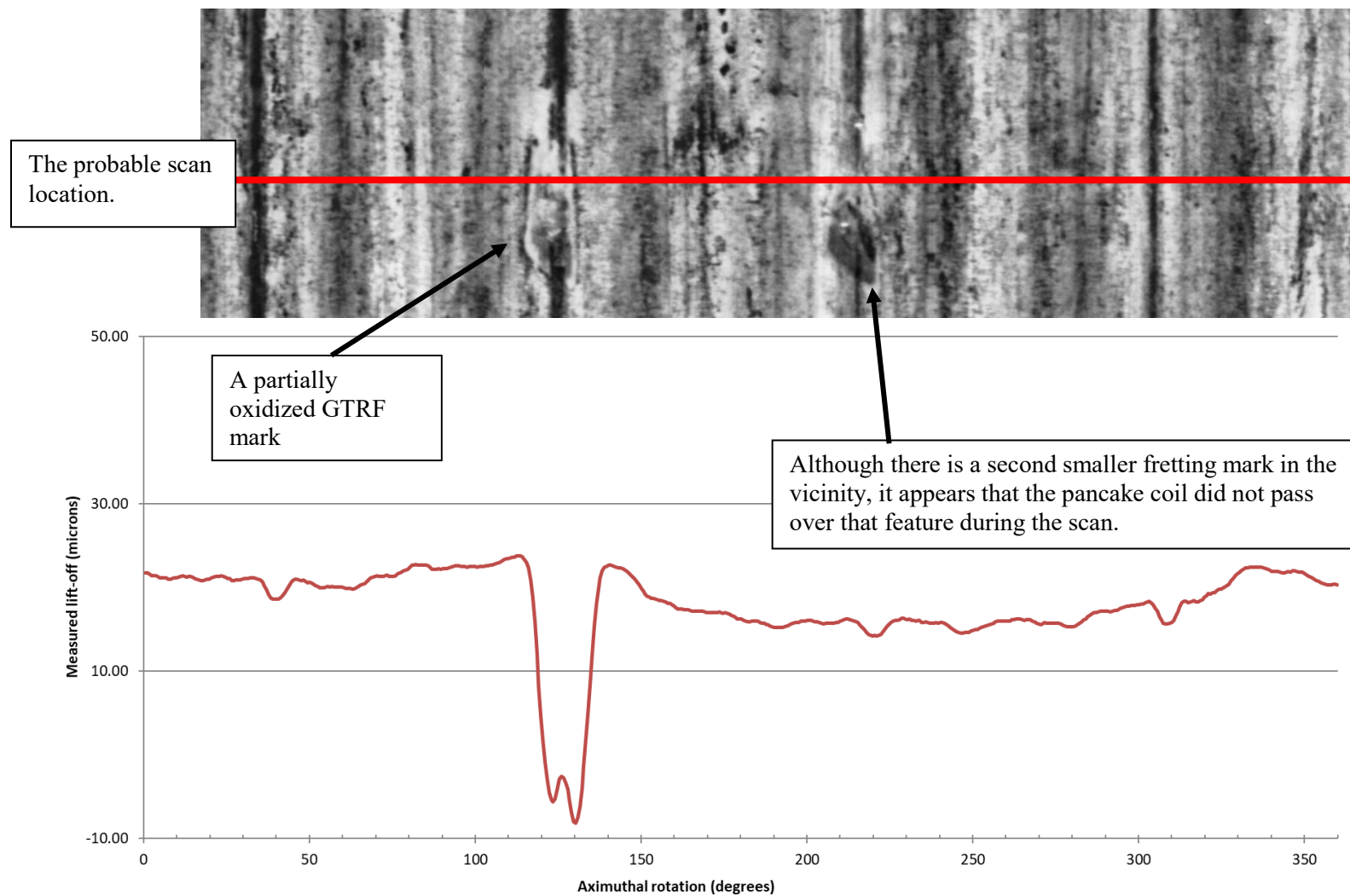


Figure 63. Rotational Scan of Sister Rod 3F9D07 at 1,765 mm Elevation Indicating Depth of a Partially Oxidized Fretting Mark and Axial Scratches in the Waterside Surface of the Rod.

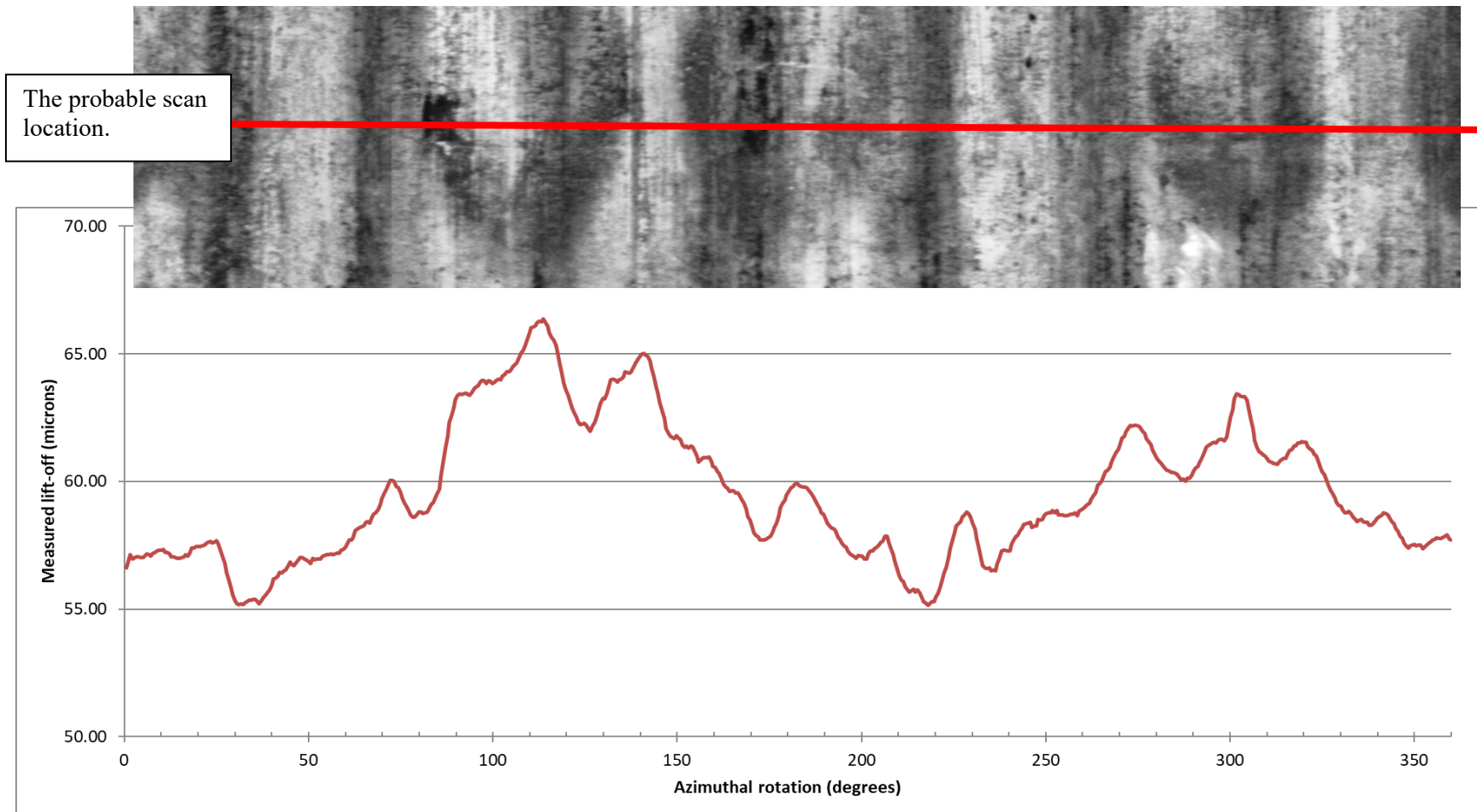


Figure 64. Rotational Scans of Flow Markings at the Exit of a Spacer Grid, F35P17 at 3,650 mm.

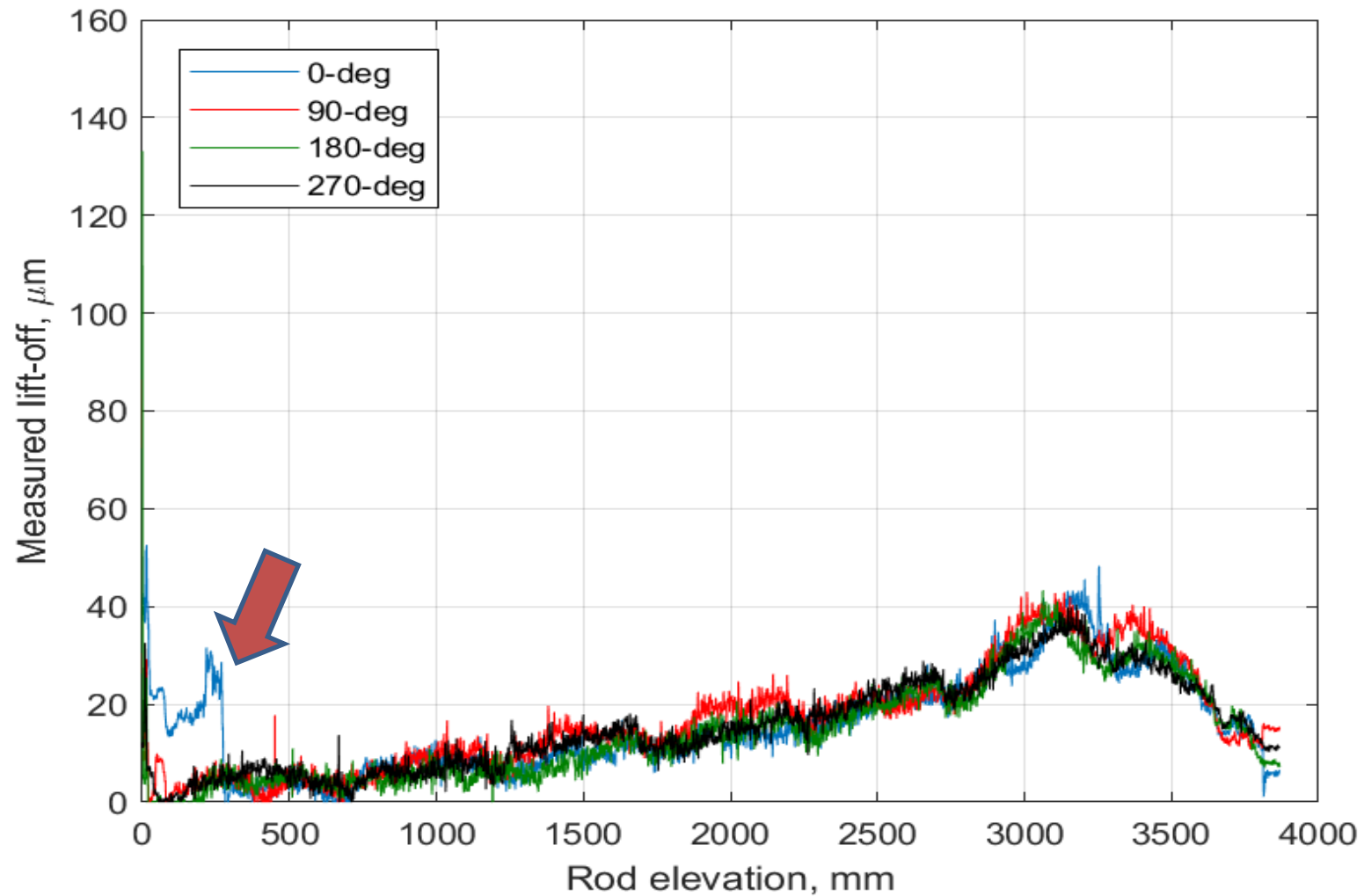


Figure 65. An Example of An Abrupt Shift in Lift-Off Magnitude Associated with Either the Coil Sticking in Its Housing or an Accumulation of Debris Under the Coil Head.

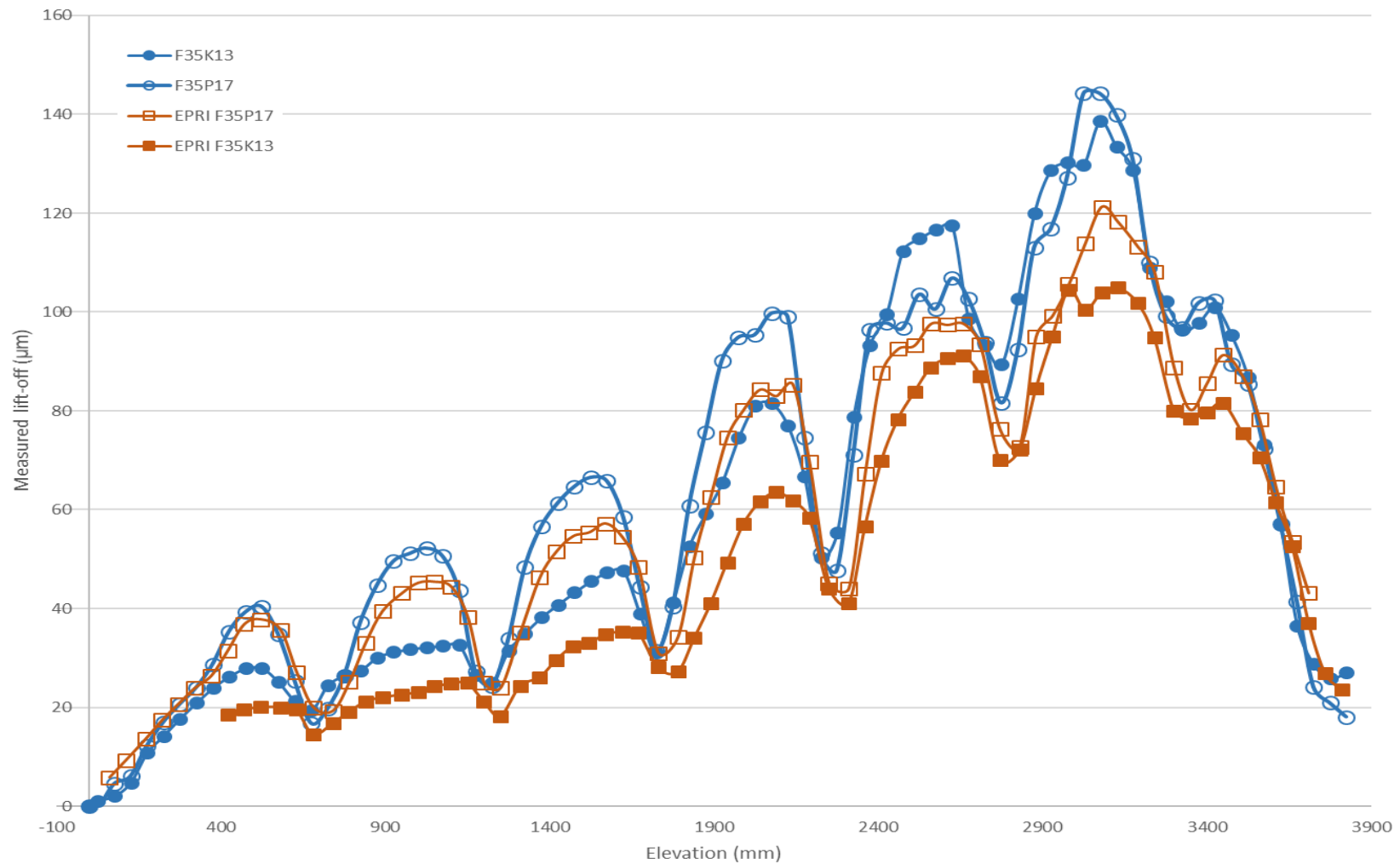


Figure 66. A Comparison of the 1992 EPRI-Reported Poolside Average Lift-Off Measurements and the ORNL Hot Cell Lift-off Measurements for Sister Rods F35K13 And F35P17 [9].

3.5 NDE.05: Profilometry Measurements

The fuel rod diameters were measured at two orthogonal points along their lengths using two sets of linear variable differential transformers (LVDTs). Since numerous photographs of each rod were available, the visual information was also processed to obtain diameter measurements. Section 3.5.1 describes the LVDT measurements taken, and Section 3.5.2 describes the diameter measurements derived from the photos.

3.5.1 LVDT Measurements

LVDT profilometry measurements were completed in April 2017. Two pairs of LVDTs are used: LVDT-1 and LVDT-2 measure 45 degrees off the horizontal plane, and LVDT-3 and LVDT-4 measure 45 degrees off the vertical plane. The two sets of measurements are 90° apart and can provide information on the extent to which the rod is out of round (ovality). The LVDT pairs are slightly offset axially for clearance. Using the LVDTs, the rods can only be measured to within about 200 mm of the end caps due to limitations of the rod-guiding mechanics. The 0.02 mm target accuracy of the LVDT apparatus was achieved. Calibration rods were used to calibrate the LVDTs and to check accuracy. For the sister rod measurements, it was found that one pair of LVDTs (3 and 4) consistently read slightly low, so a correction was applied post-measurement.

Figure 67 through Figure 73 provide the average measured rod diameter as a function of axial rod location grouped by assembly, and Table 8 provides a summary. Overall, within the accuracy of the device and given the actual surface condition of the rods, none of the rods were found to be significantly out of round (0.04 mm). Generally, the average is sufficient to identify significant diametrical changes, but the measurements from the two pairs of LVDTs can be slightly out of phase, and averaging can eliminate the peaks and valleys associated with the pellet ridging. Localized features such as spalling depth, surface dents, and pellet ridging can be identified using (1) individual LVDT traces, which occur only at 2 orthogonal locations along the length, (2) gamma scans, which provide a cross sectional indication only, and (3) visual profilometry, which can have limited resolution capability. A combination of these measurements can also be used. The traces for both pairs of LVDTs are provided in Appendix A.

There were no indications of significant rod swelling or clad major defects. In general, the expected diametrical trends were observed: the rod's diameter is larger in higher burnup regions and smaller in lower burnup regions. However, given the higher burnup of these rods, it is surprising that not many expanded beyond the as-fabricated rod's OD. Only the Zirc-4 and LT Zirc-4 rods appear to have positive diametrical strains on the order of 1%. Several of the M5 and ZIRLO rods never regained their pre-irradiation OD. As expected, the diameter of the rod in the plenum region is very near the as-fabricated cladding OD. Although they could not be measured with the LVDTs, the top- and bottom-end cap diameters are also near the as-fabricated end cap diameters (measured using the visual diameter analysis, see Section 3.5.2 and Appendix B).

Some rods had very thick oxide layers with large spalled areas (see Section 3.1). Rods with the thickest oxide layers appear to have erratic diameter measurements. In particular, Assemblies 3A1 and F35 show the expected increasing diameter from the bottom to the top of the rod (referenced to the true bottom for the F35 rods), but there is a large amount of point-to-point variation in the higher rod elevations due to the uneven spalling oxide layer.

Bambooing — a small diameter variation with a period of about 10 mm (the pellet length) — was observed in all rods. Figure 74 shows a portion of the bottom region of rod 6U3P16, where bambooing caused by pellet-cladding interaction during operation can be observed.

The average LVDT-measured rod diameter for rod 30AG09 displayed a region of increased diameter near 1,000 mm; the visual exam showed nothing unusual in this region. Upon examination of the individual LVDT data shown in Figure 75, it is evident that the spike in diameter was only measured by the

LVDT-1/LVDT-2 pair. Inspection of the diametrical data obtained with the visuals (see Section 3.5.2) does not indicate an increased diameter in any direction, but the difference in diameter between the two sets of LVDTs was only about 0.03 mm, which is only marginally larger than the expected accuracy of the pairs. This difference may have come from some small debris that was carried along by the LVDT, momentary sticking of the LVDT, or a larger-than-expected off-center shift of the rod as it went through the LVDTs, moving the rod out of the optimal measuring range. Thus, this particular local diameter increase is considered a spurious measurement.

Finally, a fairly large ($\sim 3/4$ pellet length) reduced diameter (~ 0.5 mm) region was noted in the profilometry scan for rod 6U3P16, as shown in Figure 76. The reduction was measured by both pairs of LVDTs, but it is not observable in the visual profilometry. This is likely due to the visual method's lower axial resolution, which only has measurements every 40 mm. This reduced diameter region aligns well with the reported gamma scan pellet gap (see Table 5) and is likely the same feature.

Table 8 Summary of sister rod outer diameter measurements

Sister rod	Alloy	Rod maximum OD (mm)	Rod minimum OD (mm)	Rod average OD (mm)
30AD05	M5	9.50	9.38	9.43
30AE14	M5	9.50	9.41	9.45
30AG09	M5	9.52	9.42	9.46
30AK09	M5	9.51	9.42	9.46
30AP02	M5	9.51	9.41	9.45
5K7C05	M5	9.49	9.40	9.46
5K7K09	M5	9.49	9.40	9.45
5K7O14	M5	9.51	9.41	9.46
5K7P02	M5	9.51	9.39	9.45
3D8B02	ZIRLO	9.52	9.42	9.46
3D8E14	ZIRLO	9.54	9.43	9.49
3F9D07	ZIRLO	9.51	9.42	9.46
3F9N05	ZIRLO	9.52	9.43	9.47
3F9P02	ZIRLO	9.50	9.41	9.44
6U3I07	ZIRLO	9.55	9.42	9.45
6U3K09	ZIRLO	9.52	9.42	9.47
6U3L08	ZIRLO	9.51	9.41	9.45
6U3M03	ZIRLO	9.52	9.42	9.46
6U3M09	ZIRLO	9.55	9.41	9.47
6U3O05	ZIRLO	9.52	9.41	9.46
6U3P16	ZIRLO	9.52	9.38	9.45
3A1B16	LT Zirc-4	9.59	9.40	9.47
3A1F05	LT Zirc-4	9.63	9.36	9.49
F35K13	Zirc-4	9.61	9.41	9.49
F35P17	Zirc-4	9.63	9.44	9.52

3.5.2 Visual Profilometry

All of the sister rods were extensively photographed. The camera used was in a fixed location, and the rods in the ADEPT were at a constant distance with respect to the camera. While rod bow and ADEPT handling features can induce some small off-axis movements, the distance from the rod to the camera can only vary an estimated 3.2 mm in an approximately 216 cm optical path. The visual camera was also used to photograph the profilometry calibration rod which has a known nominal diameter of 9.53 ± 0.0025 mm. Although the axial variation of the calibration rod diameter is unknown, it is likely in the range of 0.0025–0.0127 mm. The photographs of the calibration rod (diameter) were used to determine the length-to-pixel ratio for the images. This information was used to resolve boundary pixel criteria (edge of rod versus background) and to scale the pixel count to diameters. The diameter was measured in 1 mm increments along the length of the rod at 0-, 45-, 90-, 135-, 180-, 225-, 270-, and 315-degree rotations. An average diameter was calculated at 40 mm intervals by (1) averaging the 1 mm measurements contained within the interval for each rotation angle and (2) averaging all rotations at that elevation. This provided 97 average diameter measurements along the length of the sister rod. An example of the measurements is provided in Figure 77 as compared with the LVDT measurements and features identified by gamma scan.

Although these measurements are not considered to be as accurate as the LVDT measurements in total, they are useful in verifying trends, measuring the ends of the rods that cannot be measured with the LVDTs, and for additional observations around the circumference of the rod. For example, the discrepancy in the local measurement of rod 30AG09 (mentioned above) was verified using the visual data. However, there appears to be a measurement effect related to the angle of view, as the data tend to exhibit a sinusoidal trend with the rod rotation angle, as shown in Figure 78. The effect, roughly ± 0.05 mm, could be related to a lens distortion, or it is more likely due to an ADEPT off-center rotational effect combined with uneven lighting/background making the edge determination inconsistent. However, it seems that calibration with the imaging must be completed for each angle of rotation to ensure better accuracy, and work beyond the scope of this program would be required to process these data. The averaging mentioned above eliminates some of this effect.

Appendix B presents the visual profilometry plots compared with the average LVDT profilometry measurements and features from the gamma scanning data for all sister rods. Overall, this method gives reasonable agreement with the LVDT data, and the overall accuracy appears to be generally much better than the identified 0.05 mm. Optimization of the optical path and camera optics, along with a fixed reference point for picture-by-picture calibration, could lead to a non-contact fast measurement system.

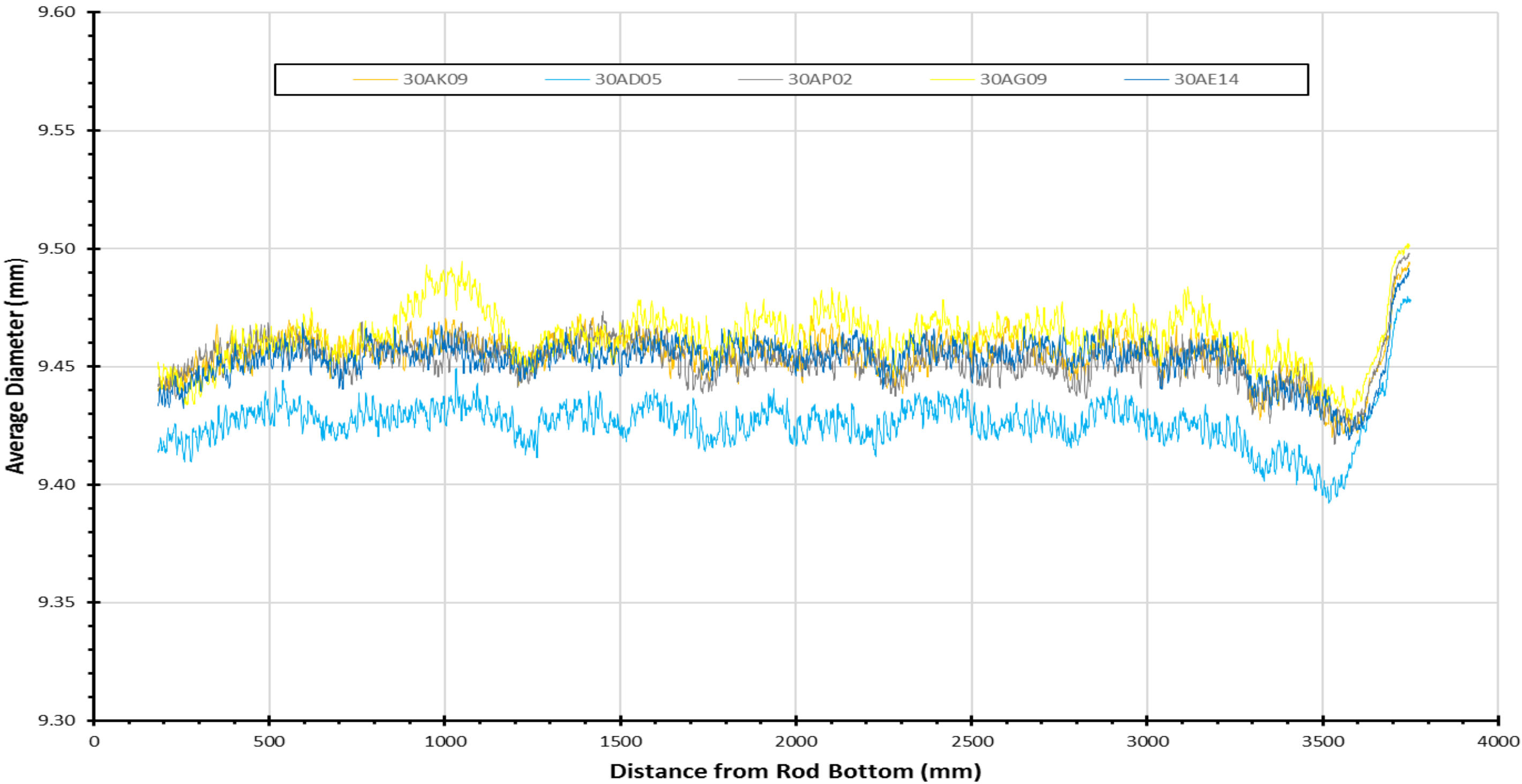


Figure 67. Profilometry Scans for Assembly 30A.

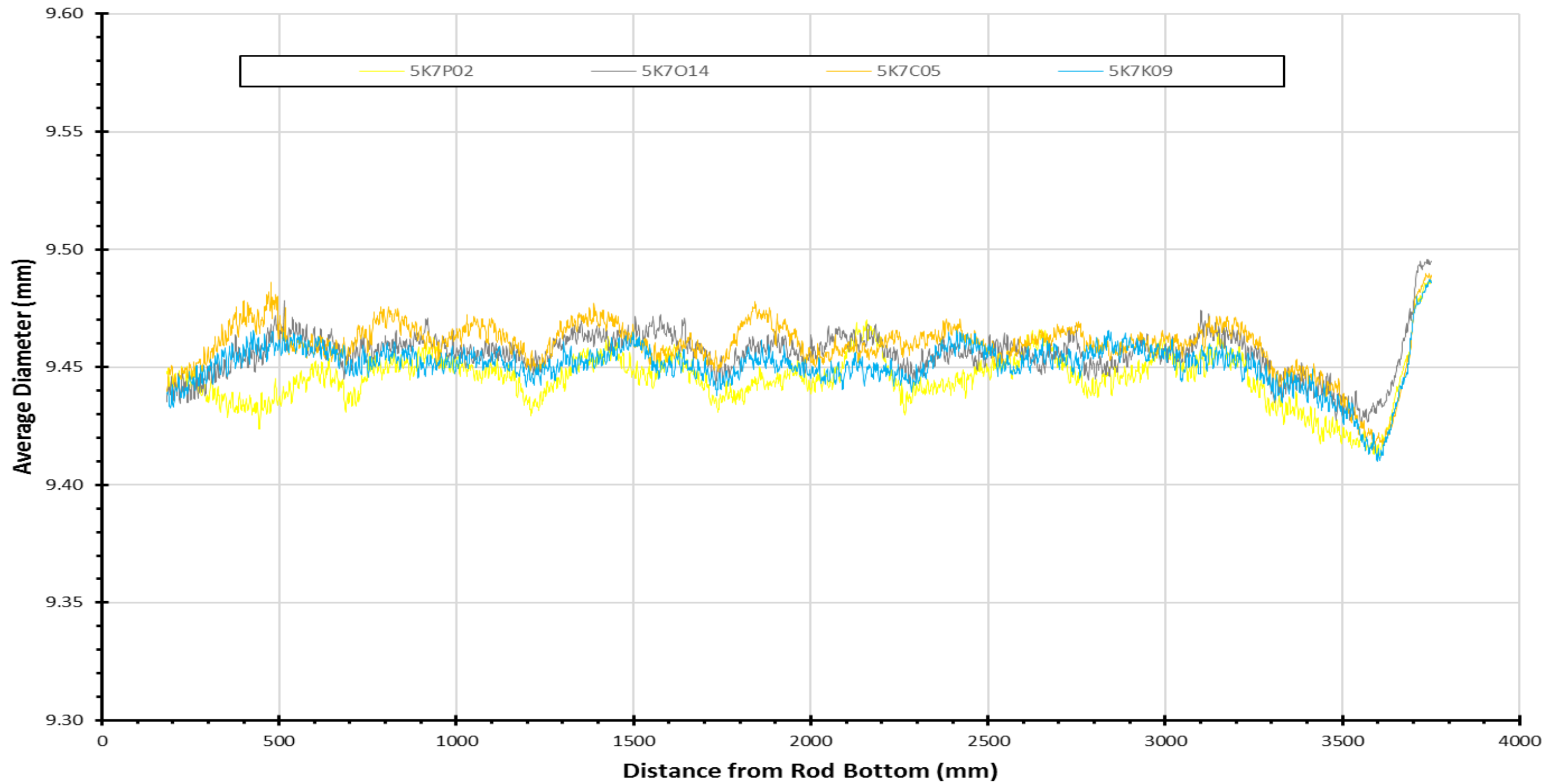


Figure 68. Profilometry Scans for Assembly 5K7.

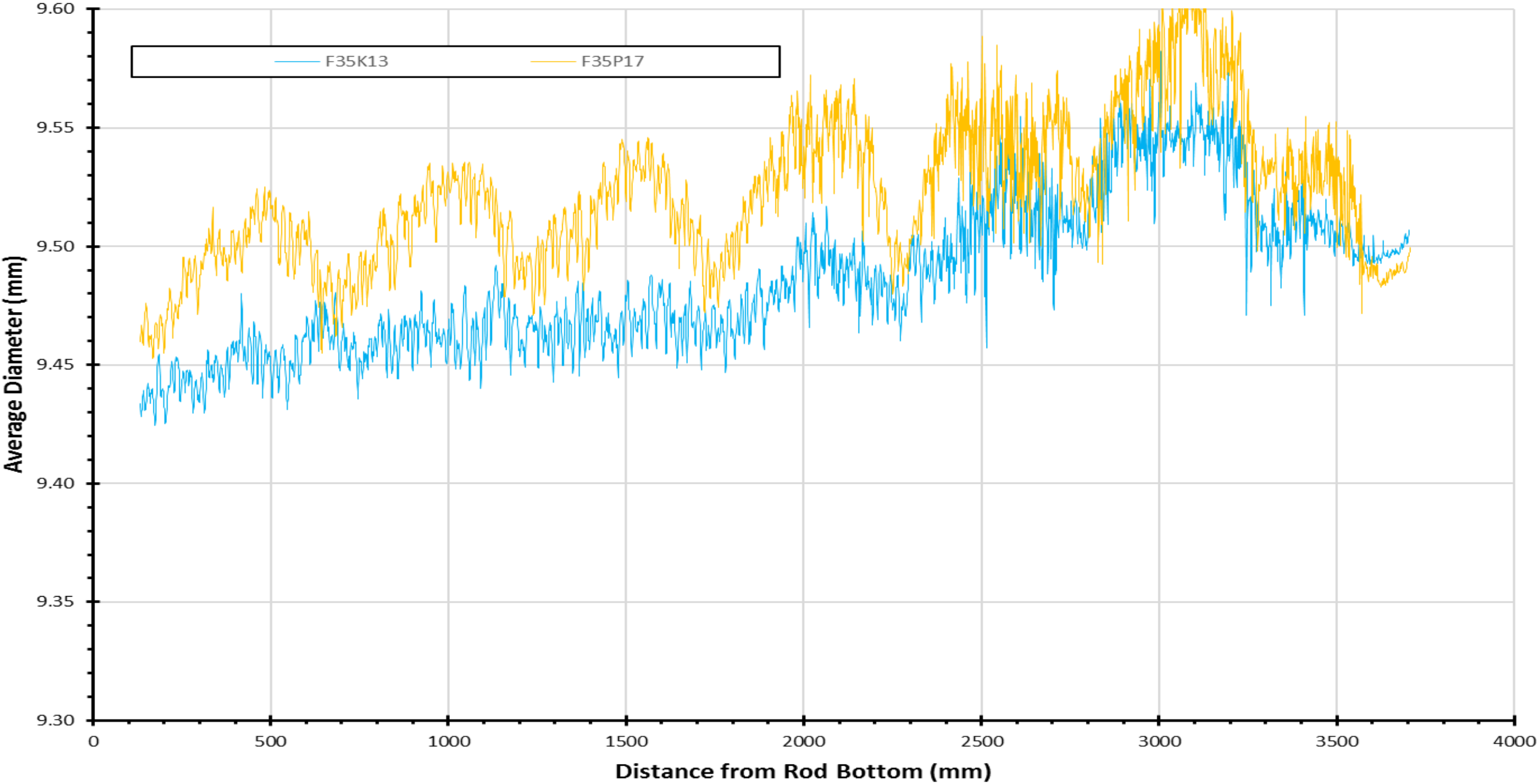


Figure 69. Profilometry Scans for Assembly F35.

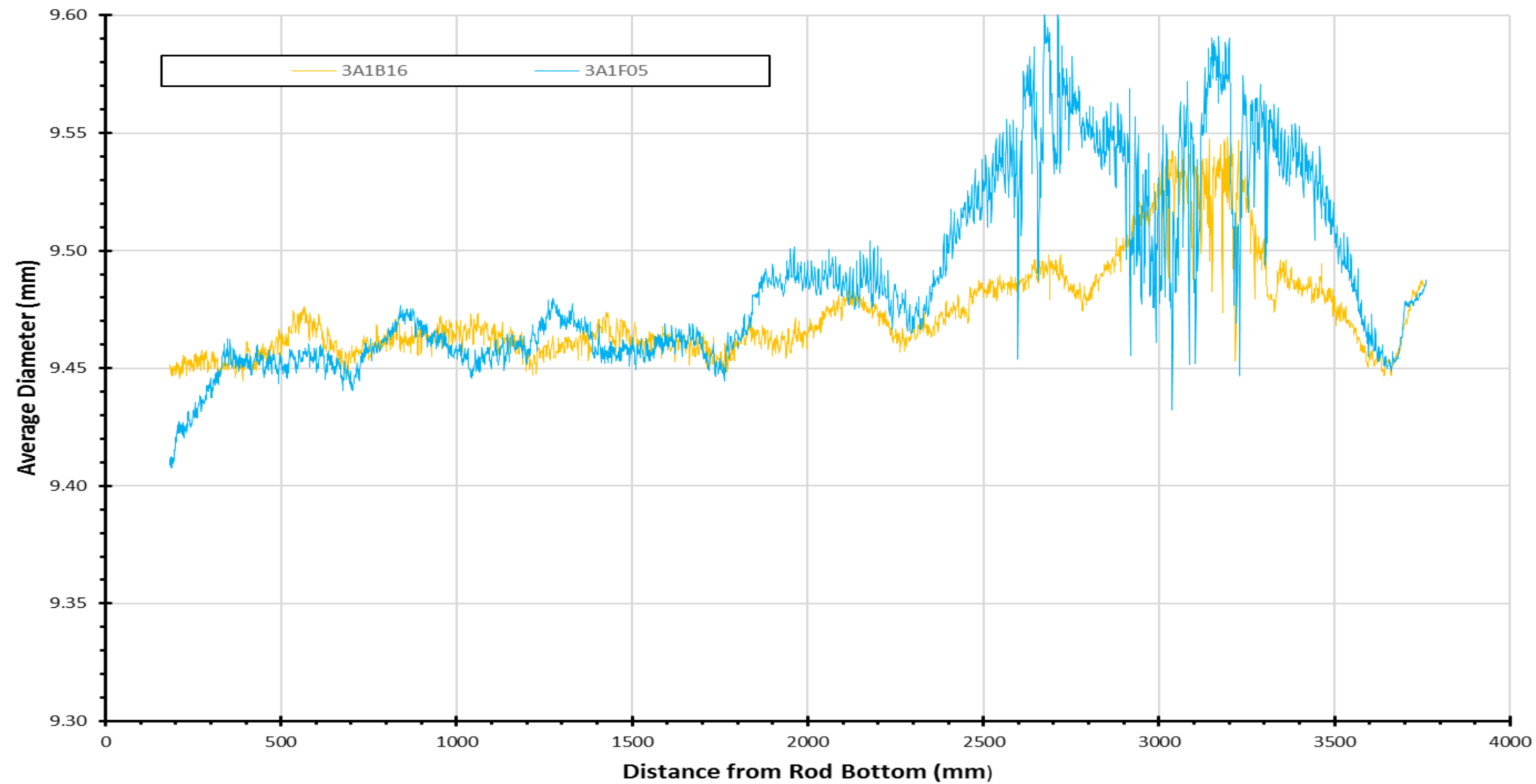


Figure 70. Profilometry Scans for Assembly 3A1.

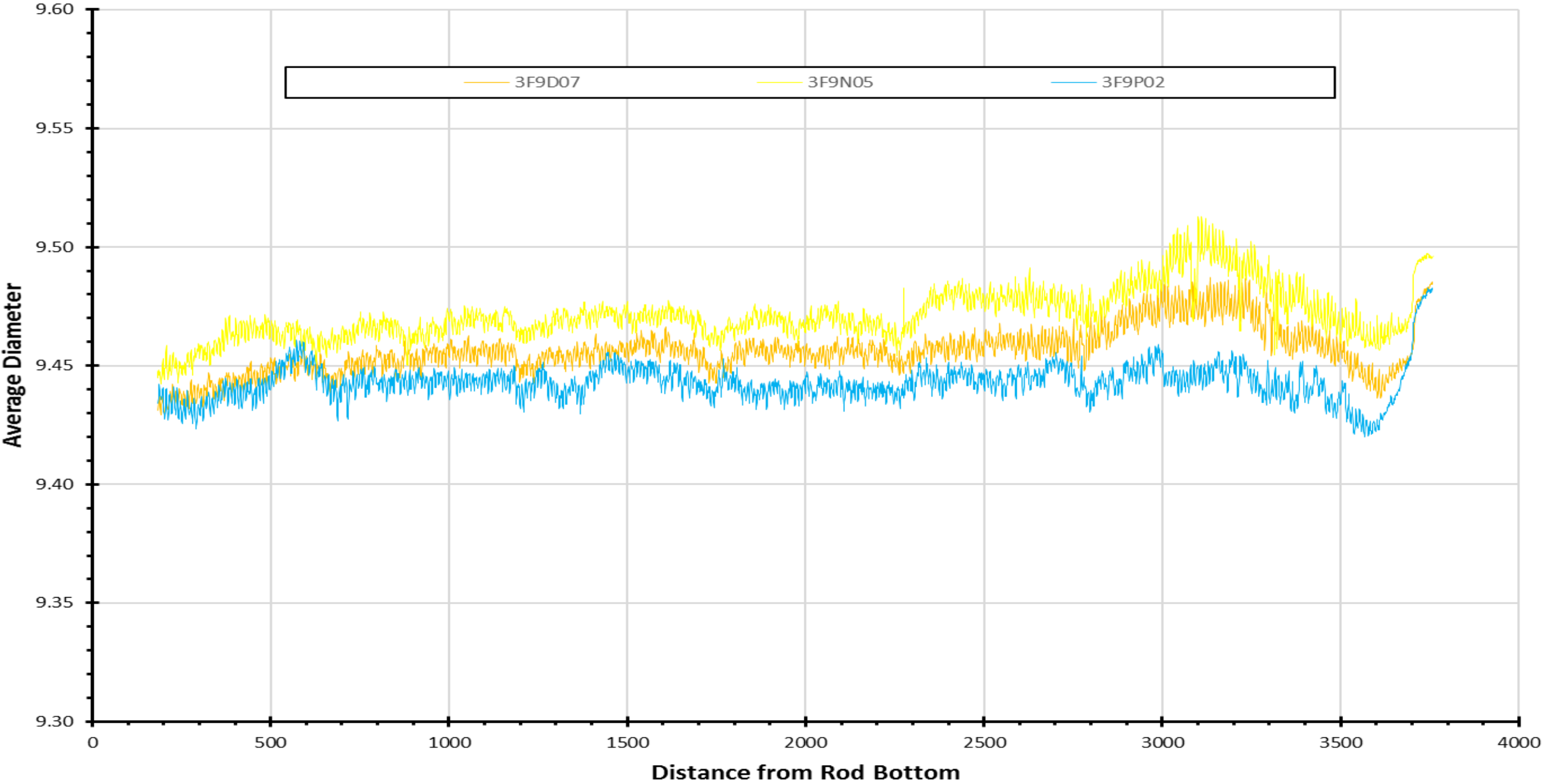


Figure 71. Profilometry Scans for Assembly 3F9.

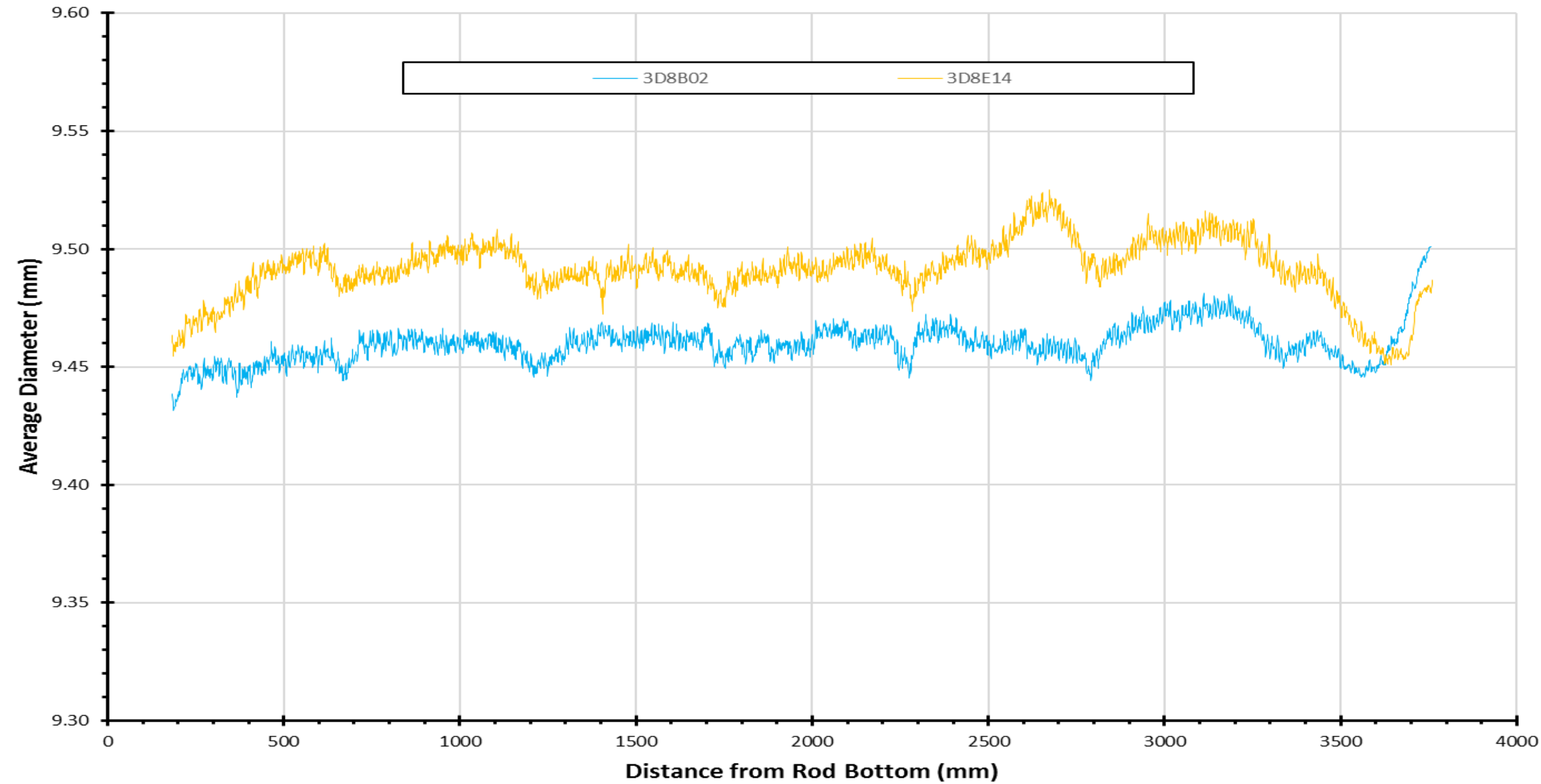


Figure 72. Profilometry Scans for Assembly 3D8.

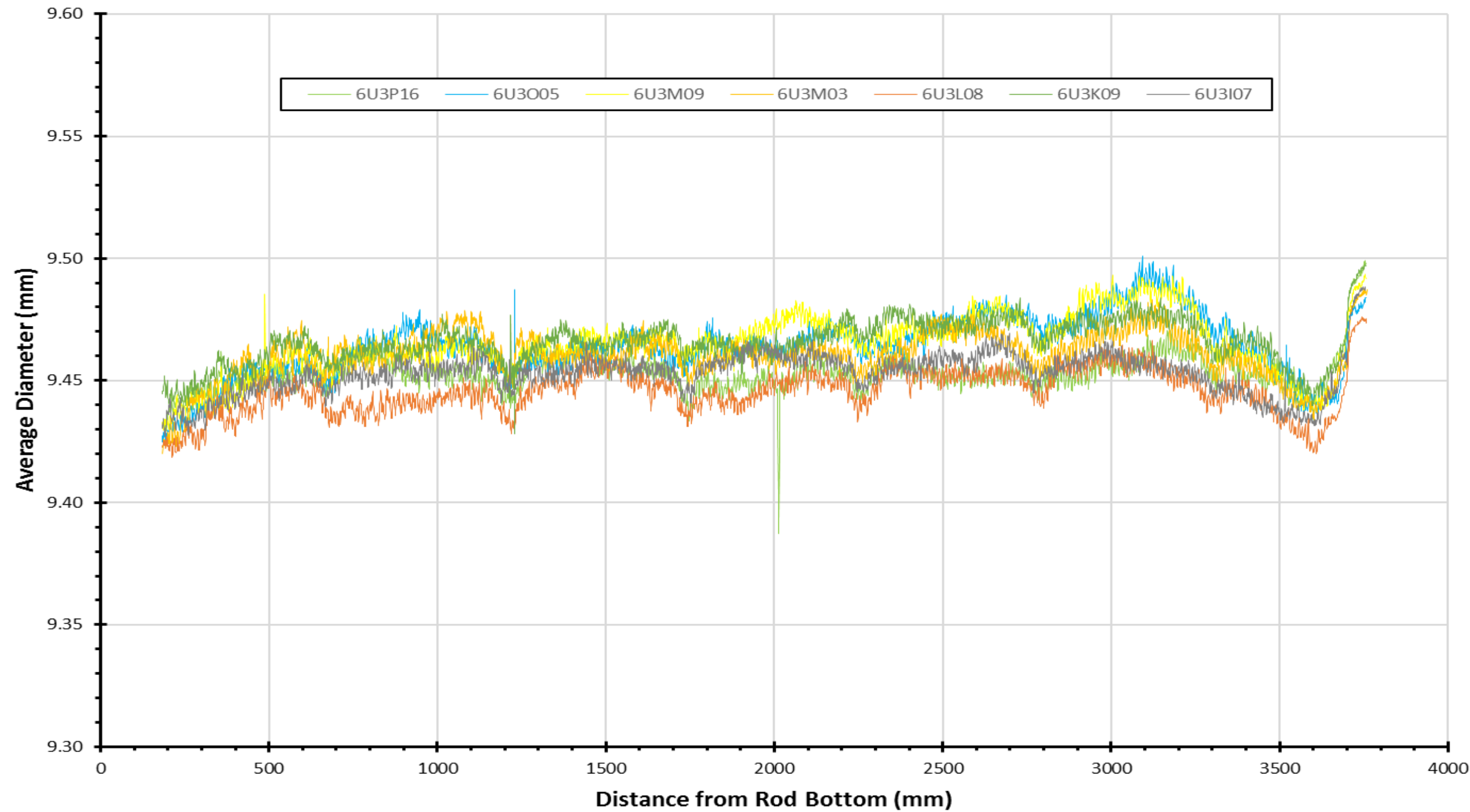


Figure 73. Profilometry Scans for Assembly 6U3.

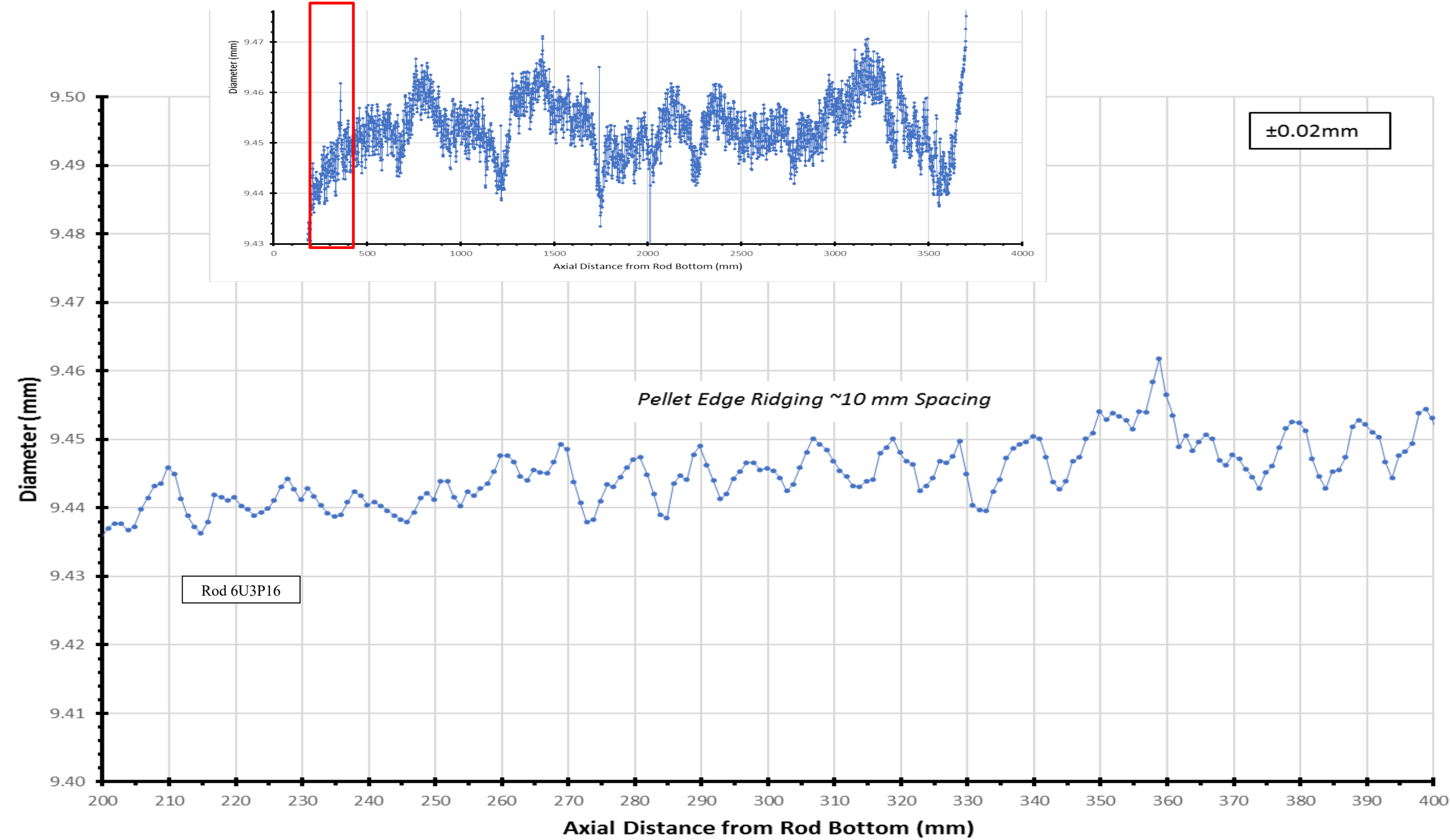


Figure 74. Typical Pellet Ridging on a Fuel Rod via LVDT-Based Profilometry; Scales are Magnified to Show the Detail. The Typical Pellet is Approximately 10mm long.

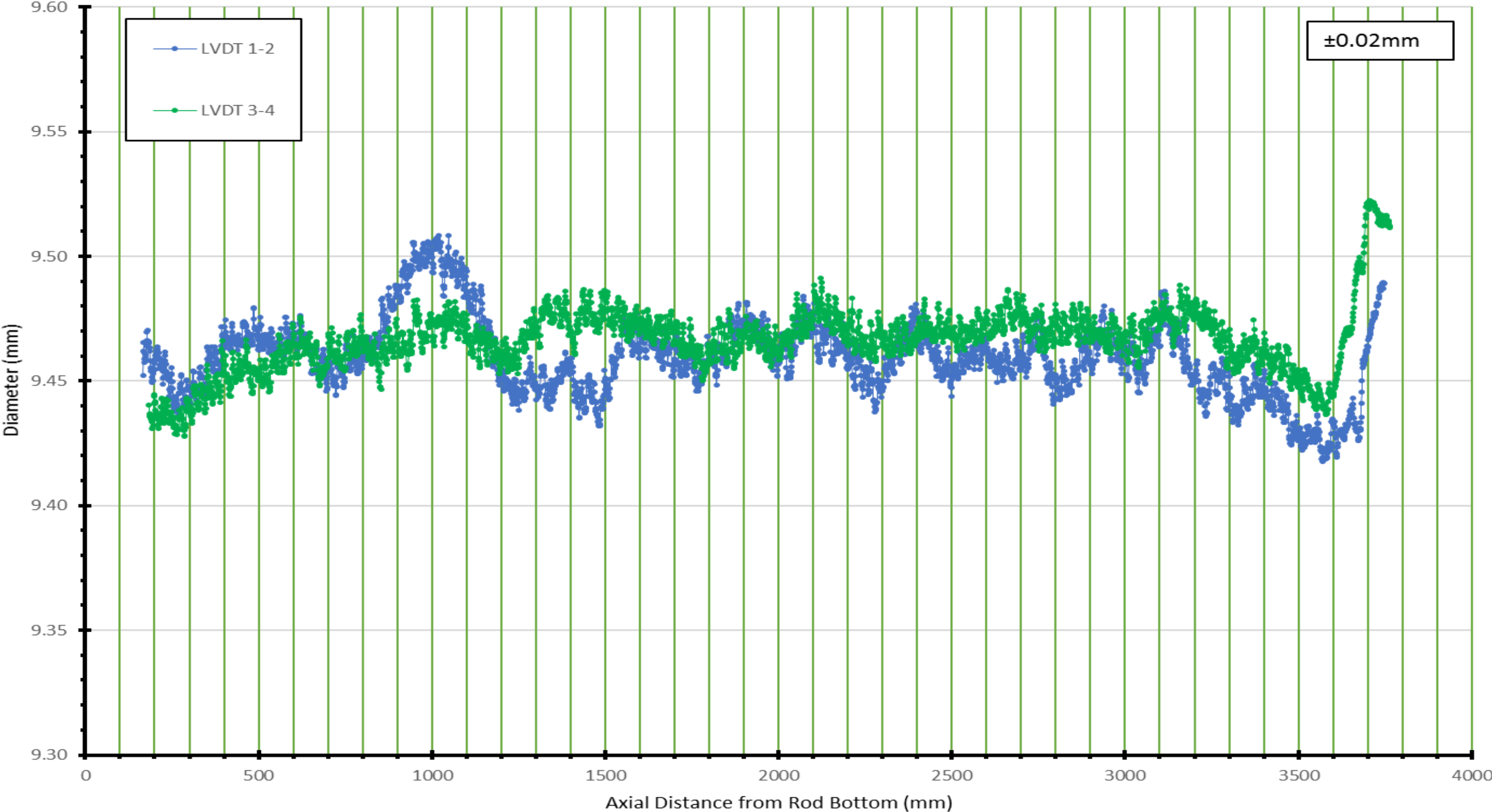


Figure 75. Individual LVDT Measurements for Rod 30AG09 Illustrating the Difference in Measurements for the Two Pairs between 900 and 1,600 mm.

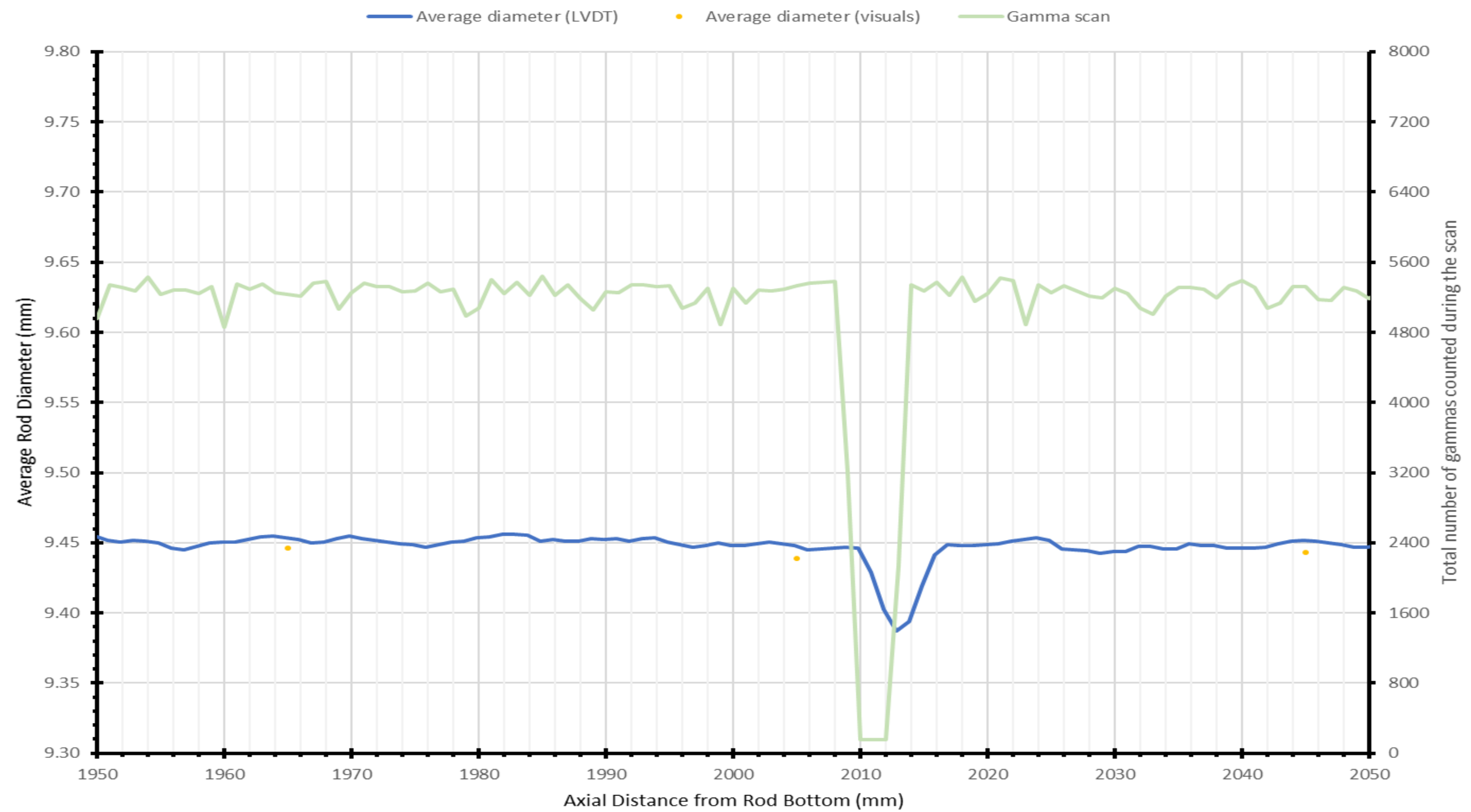


Figure 76. Average Diameter Reduction in Rod 6U3P16; This Reduction Nearly Aligns with the Pellet Stack Gap Noted in the Gamma Scan.

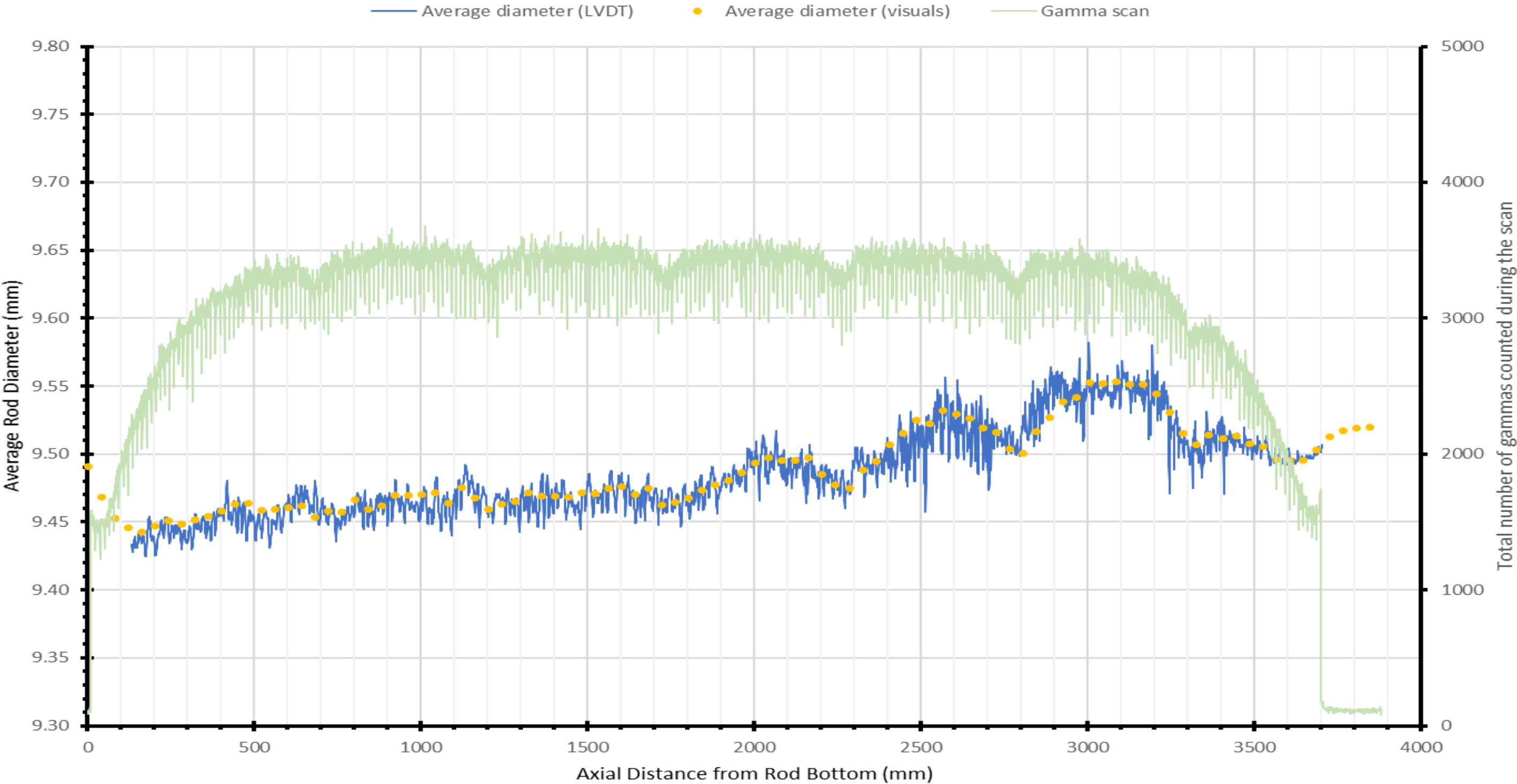


Figure 77. Example of LVDT Measurements and Visuals Diameter Measurements as Compared with Features Indicated by the Gamma Scans for Rod F35K13.

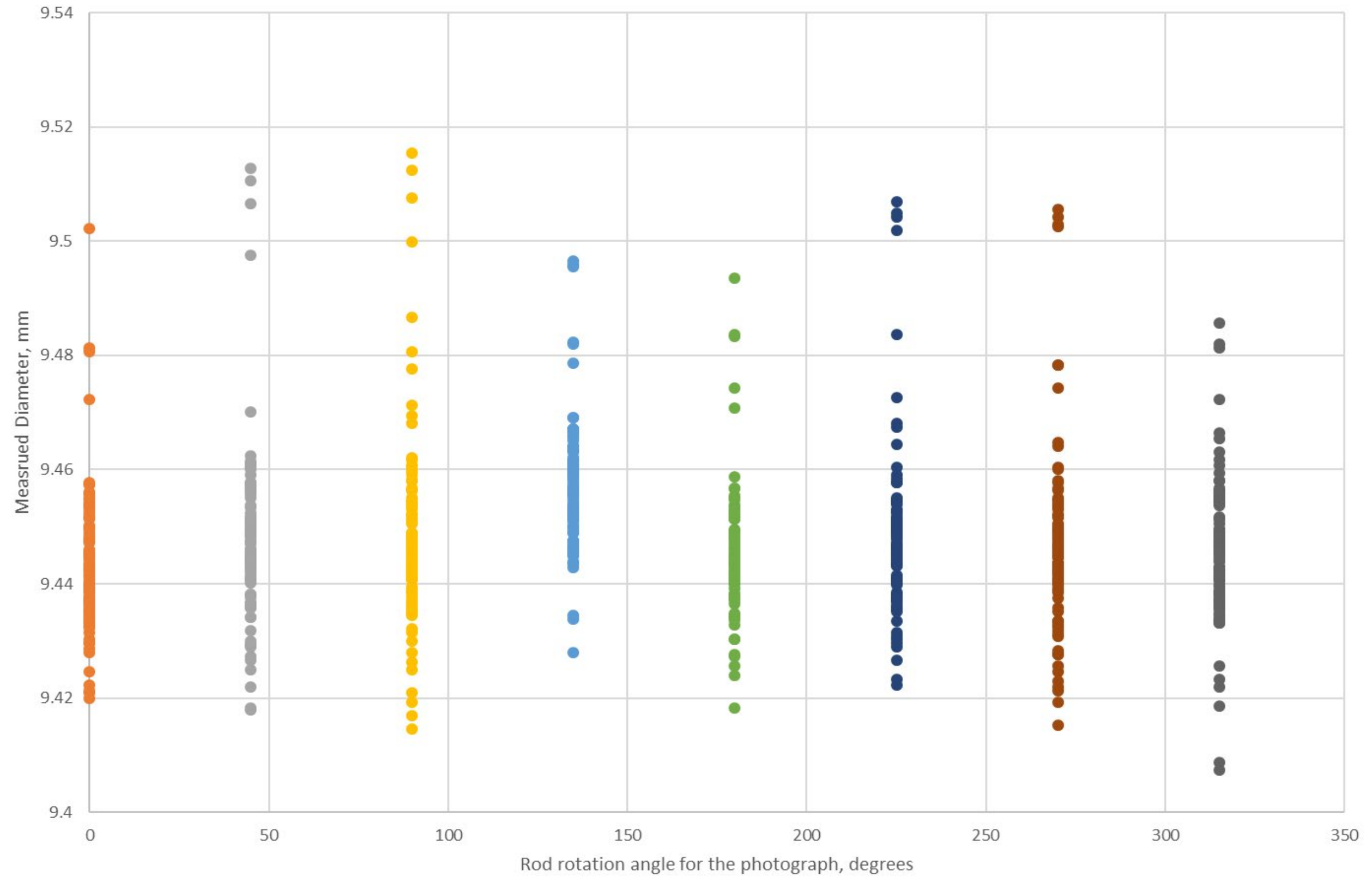


Figure 78. Observed Sinusoidal Trend in Visual Profilometry Data with Angle of Rod Rotation.

3.6 NDE.06: Surface Temperature Measurements

Several sister rod surface temperature measurements were taken intermittently over the course of year. The initial measurements were taken in the open hot cell environment using a clamp on thermocouple, but it was difficult to obtain a reliable measurement with that configuration, since the convection by the hot cell's air flow dramatically affected the thermocouple temperature.

To eliminate the effects of the hot cell air flow, an isolation housing was fabricated using 3D printing. The housing included a through-hole for rod insertion and a cavity for the U-shaped thermocouple probe, as illustrated in Figure 79.

Using the isolation housing, the surface temperature of several rods was measured at the axial mid-plane over several days. The maximum temperature measured, for sister rod 5K7P02, was 31.1 °C. Although the temperature was observed to vary in the daytime hours, the variation was not significant and did not appear to correlate with outdoor conditions. Rather, it is likely that the variation is related to the times when the lights are on in the hot cell, as the lights in the cell produce quite a bit of heat. Measurements during a cycle of approximately 24 hours are shown in Figure 80.

Additionally, the surface temperatures of two rod locations in the storage array (with a rod inserted) were measured at the axial mid-plane over several weeks. The maximum temperature that was recorded was for sister rod 5K7P02 at 31.2 °C. Because the heat produced by individual fuel rods is quite low, the resulting temperature differential from ambient is small and difficult to monitor in the hot cell environment. Since the temperatures of the rods in the hot cell are near ambient, it is unlikely that temperature-related factors will be an issue for any of the ambient temperature DE.

It is anticipated that additional surface temperature measurements will be taken as the rods are punctured during the DE.

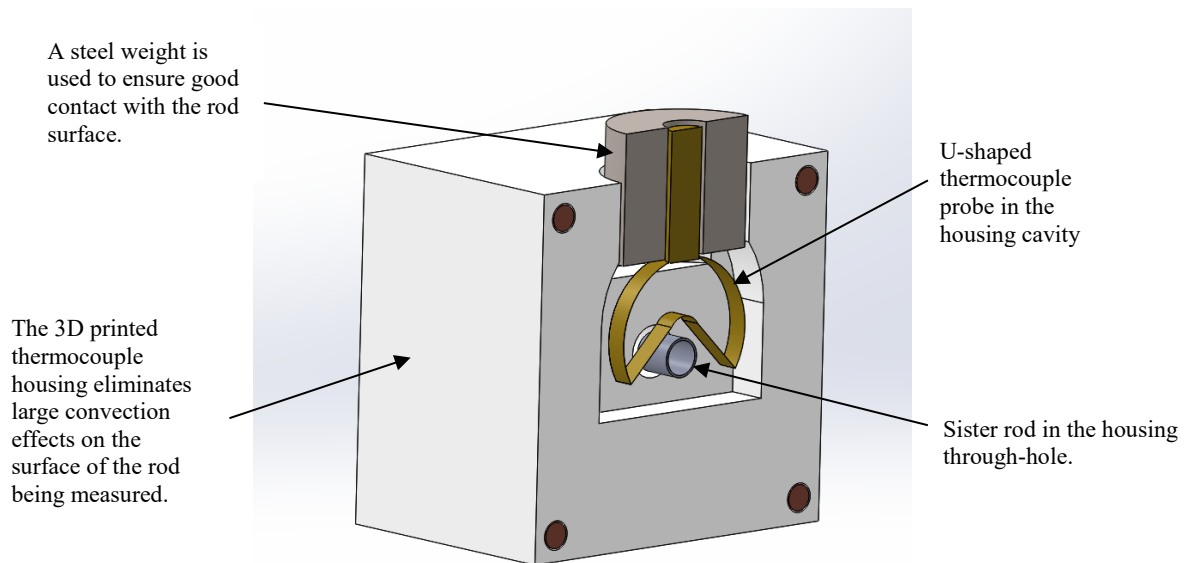


Figure 79. Cross-Sectional View of the Thermocouple Isolation Housing Used to Measure the Surface Temperature of Selected Sister Rods.

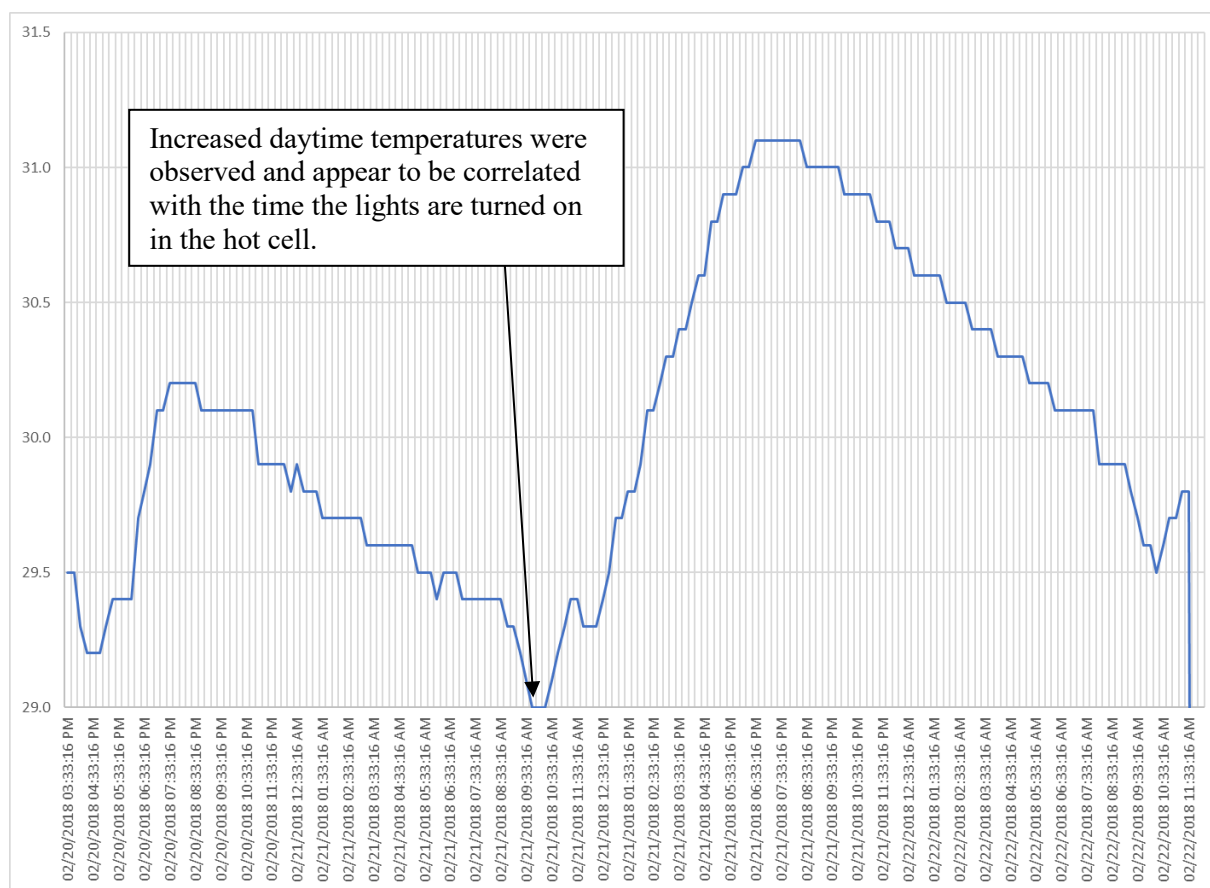


Figure 80. 24-Hour Measurement of Surface Temperature of Sister Rod 5K7P02 at Midplane, in the Temperature Housing and on the ADEPT (Not in the Storage Array).

4. SUMMARY OF RESULTS

The NDE scope and general findings are summarized in Table 9.

Waterside surface features relevant to the specification of future NDE and DE were identified via visual examination and tabulated. No weld failures, obvious cladding breaches, or other significant defects were observed. A typical striated surface texture appearance which is visible in the images as alternating axial light and dark bands is present to varying degrees in all cases, with the more heavily oxidized rods having the appearance of deeper striations. The Zirc-4 and LT Zirc-4 rods appear to have very heavy oxide layers, extensive spalling, and oxide flaking in the HBU elevations of the rod. The visual examination indicated that shallow GTRF marks are common, and a few ZIRLO rods appear to have moderate to deep GTRF marks. Several rods appear to have patches of CRUD and/or spalling oxide. Peeling oxide was identified on ZIRLO sister rods and the M5 rods have oxide rings with some peeling at the center. Long axial rod insertion and/or rod removal scratches are visible on most rods.

The one-dimensional gamma scans of all 25 sister rods performed specifically for the sister rod project exhibited the expected trends without any sign of fission product accumulation or migration and graphs of the data are available in Appendix A. The axial profiles of the rods were as expected, and depressions in burnup were easily observed at the spacer grid locations. Pellet-pellet interface locations were also observable, so an estimate of the number of pellets in each rod could be made. The spring in the plenum region was visible, so an estimate of the length of the plenum region was also made and is provided in Table 4. Some fuel stack gaps, as listed in Table 5, were observed via the gamma scanning. The largest was estimated as 5 mm on sister rod 6U3P16. A summary of the length and gap data derived using the NaI gamma scans are available in Tables 4 and 5, respectively.

The overall length of each sister rod was measured multiple times by ADEPT and was within the expected range. Table 4 provides the average length of each sister rod based on all overall rod length measurements.

Profilometry measurements were taken using two pairs of LVDTs to measure the fuel rod diameter as a function of axial location, and graphs of the data obtained are available in Section 3.5 and Appendix B. Bambooning was observed in all rods. No significant ovality was noted in the rods. In general, the expected diametrical trends were observed, however, some rods having very thick oxide layers have locally erratic diameter measurements where the LVDT moves into and out of spalled areas. A long ($\sim 3/4$ pellet length) reduced diameter (~ 0.5 mm) region was noted in the profilometry scan for rod 6U3P16 that is associated with the ~ 5 mm pellet-pellet gap identified during gamma scanning. This same pellet-pellet gap was also detected by the traditional eddy current measurements.

Two eddy current examinations were completed: (1) a campaign using traditional eddy current methods to measure oxide/CRUD thickness and remaining cladding thickness and to identify flaws, and (2) an EPRI campaign using their F-SECT technique to measure the hydrogen content of the cladding. The traditional eddy current measurements were completed in November 2017 and the F-SECT measurements were completed late in July 2017. The EPRI F-SECT measurements indicated an alloy-average maximum lift-off of ~ 130 , 105, 45, and 17 μm for the Zirc-4, LT Zirc-4, ZIRLO and M5-clad rods, respectively, while the traditional eddy current examinations performed indicated an alloy-average maximum lift-off of 146, 151, 48, and 19 μm on the Zirc-4, LT Zirc-4, ZIRLO and M5-clad rods, respectively. The differences in results obtained using the two different techniques are likely related to the fact that the F-SECT technique measured only selected locations, while the traditional eddy current measurements were more exhaustive. Rotational scans indicate circumferential variations in lift-off, with as much as 30 μm of variation around the circumference of some rods in the HBU elevations. In spalled sections of Zirc-4 and LT Zirc-4 rods local peaks indicate a maximum lift-off up to 173 μm . Significant wall thinning (17 – 22%) due to uniform oxidation was observed in the Zirc-4 and LT Zirc-4 rods in the

higher burnup regions of the rod, and the minimum remaining cladding wall thickness was measured as ~0.462 mm on these rods.

A comparison of previously-reported poolside measurements of the two F35 sister rods in 2002 with the traditional eddy current lift-off measured in hot cell yields an average difference of 15 – 25%. As circumferential variation in the oxide thickness is expected and these two very HBU Zirc-4-clad sister rods have a very large amount of oxide spalling from their 4-cycles in reactor, a conclusion about the veracity of either the EPRI or the ORNL data cannot be drawn. The metallography samples that will be examined during the destructive examinations of the sister rods are expected to provide a definitive oxide thickness measurement for each sister rod. Therefore, while the NDE lift-off data appear to be valid for use in the primary purpose of guiding the DE specimen selection process, it should not be cited where a precision measurement of the total oxide thickness is required. The EPRI F-SECT technique estimated a maximum hydrogen content of just under 1,000 wppm at an elevation of ~3,000 mm on a Zirc-4 rod. The elevation of the maximum hydrogen is consistent with the elevation of the peak lift-off measured using traditional eddy current methods.

No deep defects that would indicate through-wall penetration were noted during the encircling coil scans. Several defect scan indications were characteristic of pellet-pellet gaps or large GTRF marks and tended to confirm the visual, gamma scanning, and profilometry findings.

The surface temperature of several rods was measured at the axial mid-plane over several days. The maximum temperature measured, for sister rod 5K7P02, was 31.2 °C in the hot cell storage array.

All sister rods were extensively photographed during the visual examination, and the data was used as second method of diameter measurement. Although these measurements are not considered to be as accurate as the LVDT measurements in total, they are useful in verifying trends, measuring the ends of the rods that cannot be measured with the LVDTs, and for additional observations around the circumference of the rod. Overall, this method gives reasonable agreement with the LVDT data, and the overall accuracy appears to be better than 0.05 mm. Optimization of the optical path and camera optics, along with a fixed reference point for picture-by-picture calibration, could lead to a non-contact fast measurement system.

Table 9 Summary of Findings

NDE	NDE Findings
NDE.01: Visuals of the complete exterior surface of each rod with a digitally created user-viewable montage of the surface, and the location and appearance of any physical abnormalities (e.g., chemical attack, blisters, cracks, heavy or uneven oxide layers, weld failures, or clad distortions)	No apparent cladding breach. Several rods appear to have patches of CRUD and/or spalling oxide. Peeling oxide was identified on M5 and ZIRLO sister rods. Pellet-pellet gaps (confirmed by gamma scan) are visible as dark bands on the surface of rods 3D8E14, 6U3P16, and F35P17. GTRF marks are visible on almost every sister rod. The complete set of images are only available in digital format and are stored on ORNL's CURIE resource [3].
NDE.02: Gamma scanning to nondestructively: a. obtain relative axial burnup profiles b. identify any gross migration of fission products or large pellet cracks c. identify any pellet stack gaps d. measure the pellet stack height e. identify the location and magnitude of any burnup depressions due to grid spacers	The scan signals exhibited the expected behavior without any sign of fission product accumulation or migration. The axial profile of the rods was as expected, and depressions in burnup were easily observed at the spacer grid locations. Pellet-pellet interface locations were also observable, so an estimate of the number of pellets in each rod could be made. The spring in the plenum region was visible, so an estimate of the length of the plenum region was also made. Three relatively large fuel stack gaps (>3 mm) were observed on rods 6U3P16, 3D8E14, and F35P17. The measured pellet stack length varied from 3,674 to 3,699 mm.
NDE.03: Fuel rod overall length measurements	The overall rod length varied from 3,881 to 3,894 mm.
NDE.04: Eddy current scans to obtain information on clad mechanical macroscopic defects and estimate oxide/CRUD waterside thickness	Significant wall thinning (17 – 22%) due to uniform oxidation was observed in the Zirc-4 and LT Zirc-4 rods in the higher burnup regions of the rod, and the minimum remaining cladding wall thickness was measured as ~0.462 mm on these rods. The largest cladding defect noted was a 7% reduction in cladding total cross-sectional volume related to an identified pellet-pellet gap on rod F35P17, detected with eddy current as a cladding OD reduction (indicated as a 35% through wall flaw). Several 1 – 3% cladding total cross-sectional volume reductions were indicated at observed GTRF marks on other rods. The maximum rod average measured lift-off for M5-clad, ZIRLO-clad, and Zirc-4/LT Zirc-4-clad sister rods was 27, 69, and 164 μm , respectively.
NDE.05: Profilometry measurements providing the rod OD as a function of axial location	The maximum OD measured for M5-clad, ZIRLO-clad, and Zirc-4/LT Zirc-4-clad sister rods was 9.52, 9.55, and 9.63 mm, respectively.
NDE.06: Rod surface temperature measurements	The maximum waterside surface temperature measured on the sister rods in the hot cell (in storage and on the ADEPT) was 31.2 °C.

5. REFERENCES

1. EPRI. *High Burnup Dry Storage Cask Research and Development Project: Final Test Plan*. Contract No.: DE-NE-0000593. Electric Power Research Institute, Palo Alto, California, 2014.
2. Montgomery, R. A., et al. *Post-irradiation Examination Plan for High Burnup Demonstration Project Sister Rods*, SFWD-SFWST-2017-000090 ORNL/SR-2016/708, UT-Battelle, LLC, Oak Ridge National Laboratory, December 30, 2016.
3. Joseph, R., A. Myers, J. Jarrell, K. Banerjee, and J. Peterson. *SNF Data Visualization on the Centralized Used Fuel Resource for Information Exchange (CURIE) Website*, Transactions of the American Nuclear Society, Vol. 116, San Francisco, California, June 11–15, 2017, 225–228.
4. Smith, S. K., A. Nicholson, S. Croft, and G. Nutter. *Measurement of Pressurized Water Reactor Spent Nuclear Fuel Rods by High-Resolution Gamma Spectroscopy for Burnup Code Verification*, ORNL/SPR-2017/381, UT-Battelle, LLC, Oak Ridge National Laboratory, 2017.
5. Rooney, B., S. Garner, P. Felsher, and P. Karpus. PeakEasy 4.91 [Computer Program], Los Alamos National Laboratory, Los Alamos, NM, Release LA-CC-13-040. Available: <https://PeakEasy.lanl.gov>, 2015.
6. Broadhead, B. and C. F. Weber. “Validation of Inverse Methods Applied to Forensic Analysis of Spent Fuel,” 51st Annual Meeting of the Institute of Nuclear Materials Management, Baltimore, MD, 2010.
7. Chu, S. Y. F, L. P. Ekström, and R. B. Firestone. *WWW Table of Radioactive Isotopes, database version 1999-02-28*. Accessible from URL <http://nucldata.nuclear.lu.se/toi/>, 1999.
8. IAEA, *Safeguards Techniques and Equipment: 2011 Edition*, IAEA, http://www-pub.iaea.org/MTCD/Publications/PDF/nvs1_web.pdf, Vienna, 2011.
9. Balfour, M. G., et al. *Corrosion of Zircaloy-Clad Fuel Rods in High-Temperature PWRs: Measurement of Waterside Corrosion in North Anna Unit 1, Interim Report, March 1992*, prepared by Westinghouse Electric Corporation for Electric Power Research Institute, TR-1004008, Tier 2 Research Project 2757-1, 1992.

This page is intentionally left blank.

Appendix A

Traces for Both LVDT pairs

Figure A.1 through Figure A.25 show the individual LVDT diameter measurements for the rods. They consist of two sets of LVDT measurements with each pair of LVDTs 90° apart. The rod's angular orientation is random, so there is no information that can be related back to a specific grid direction.

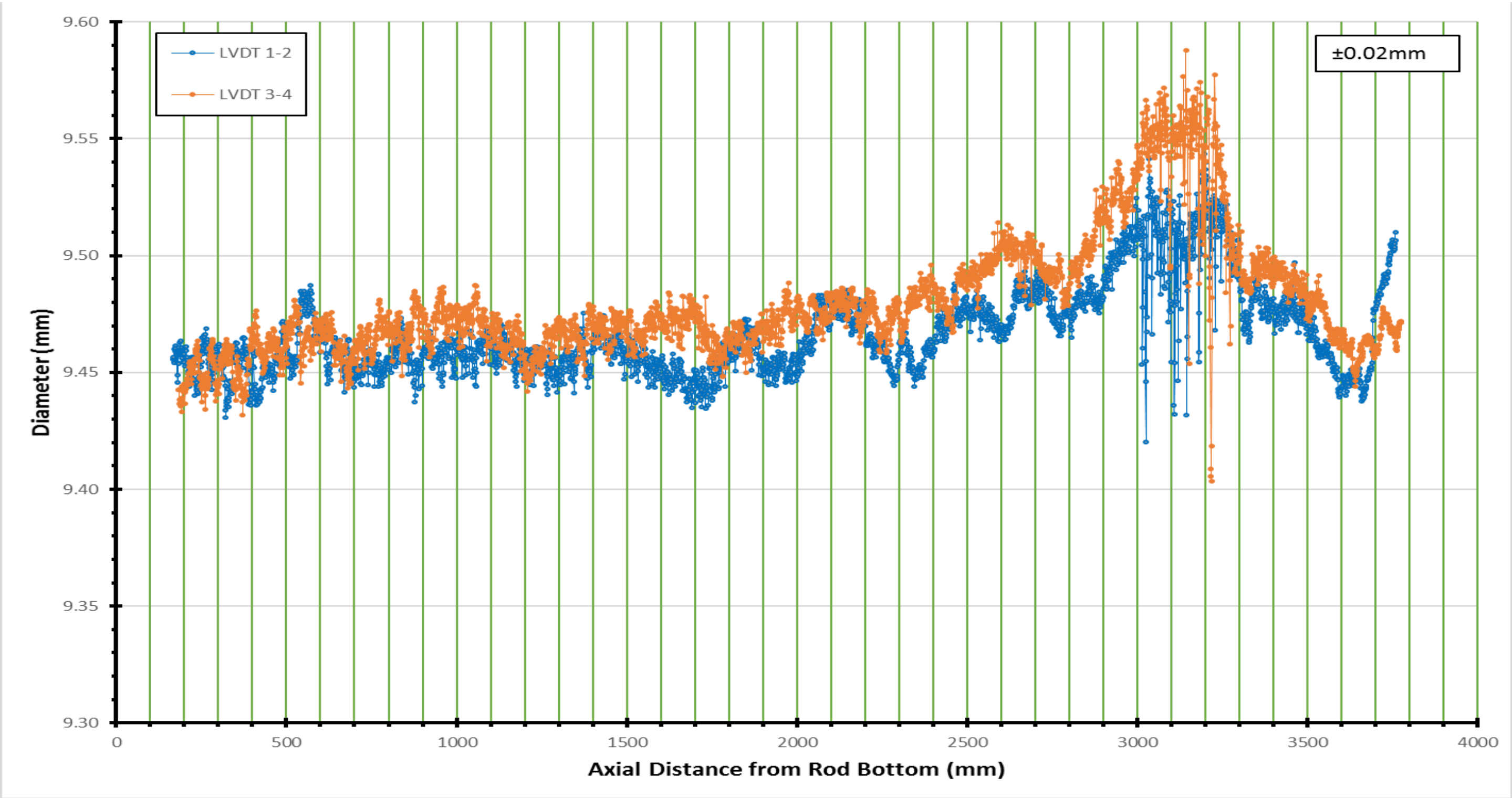


Figure A.1. Rod 3A1B16 LVDT Diameter Measurements.

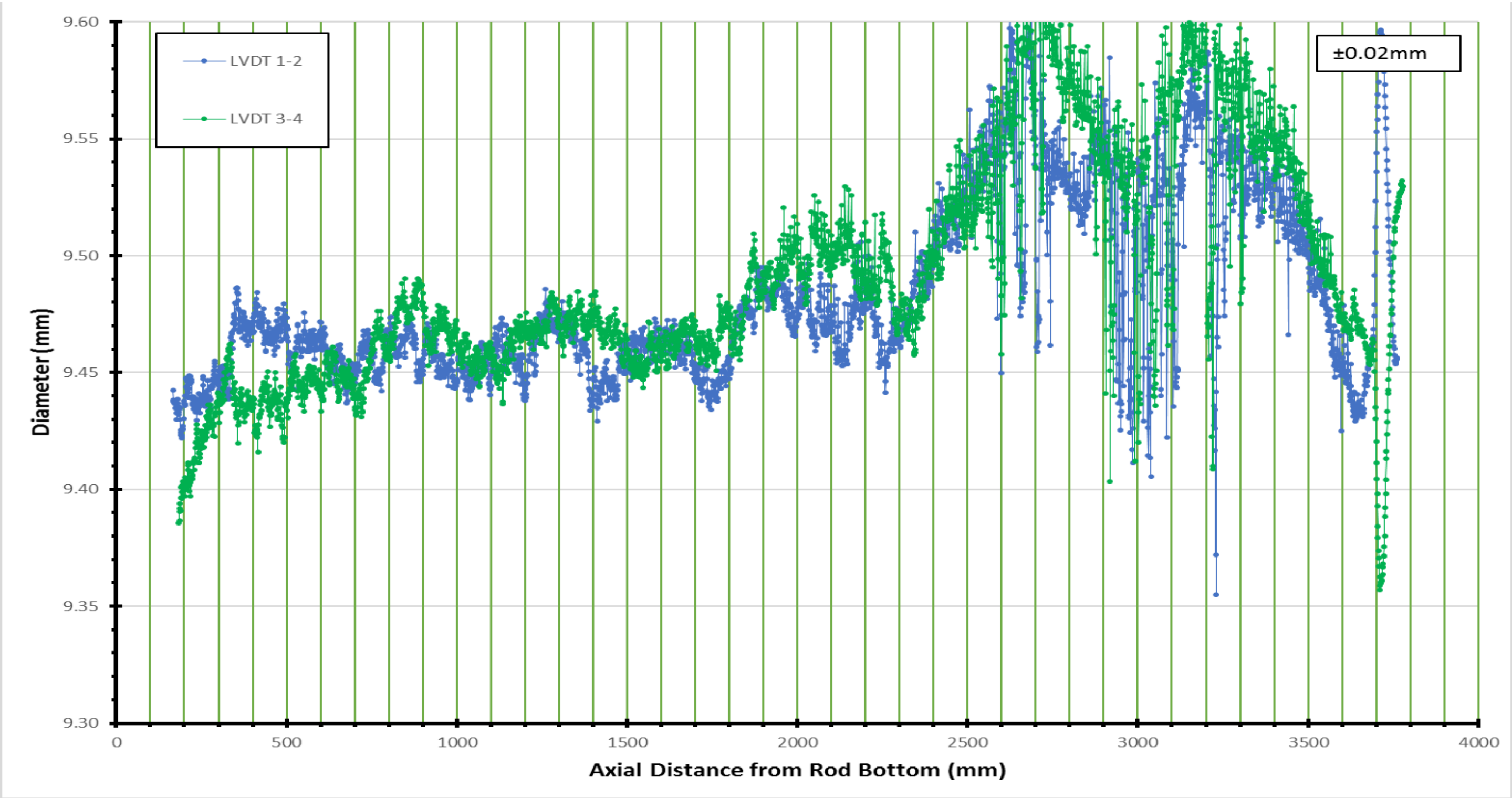


Figure A.2. Rod 3A1F05 LVDT Diameter Measurements.

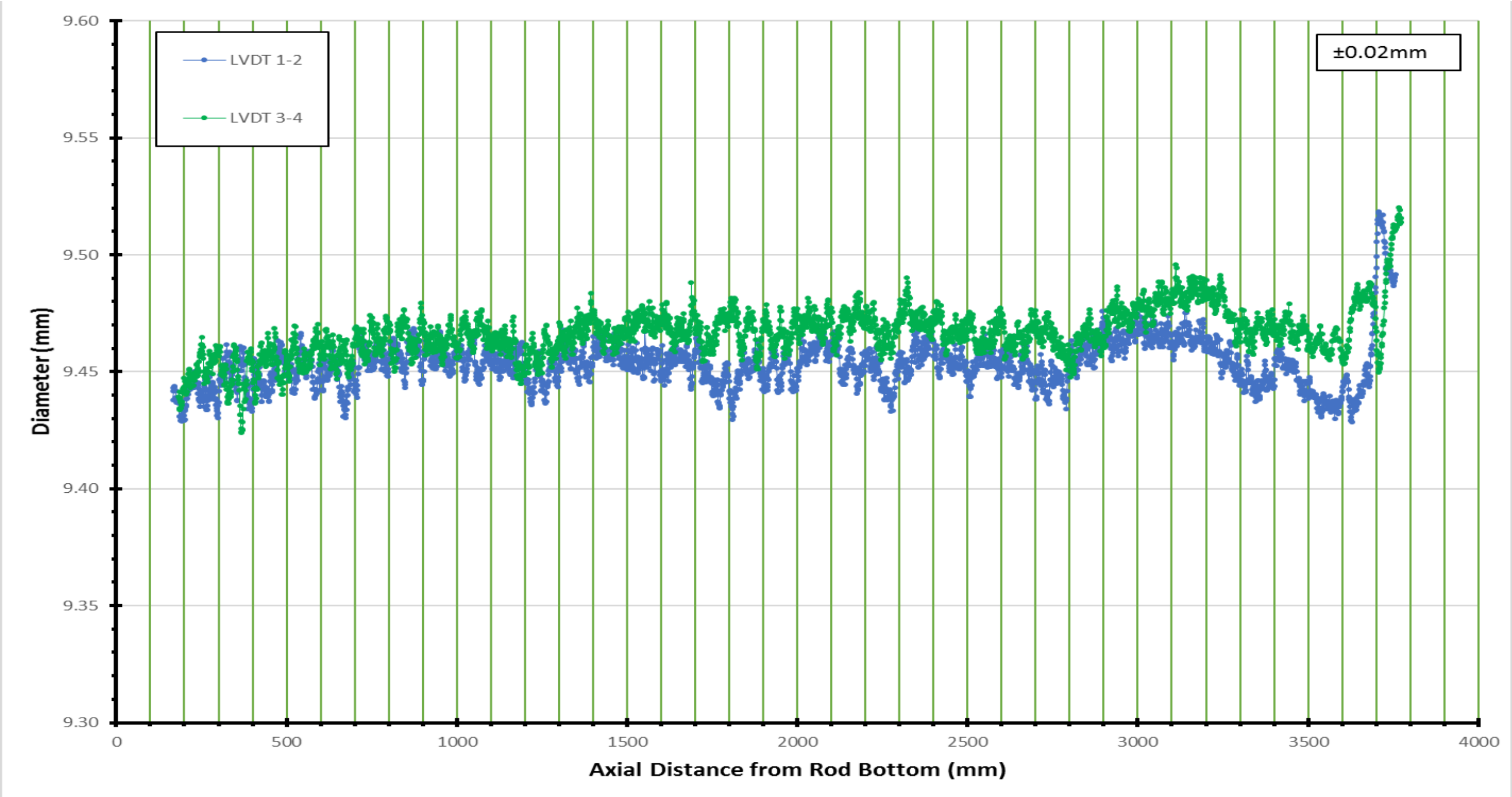


Figure A.3. Rod 3D8B02 LVDT Diameter Measurements.

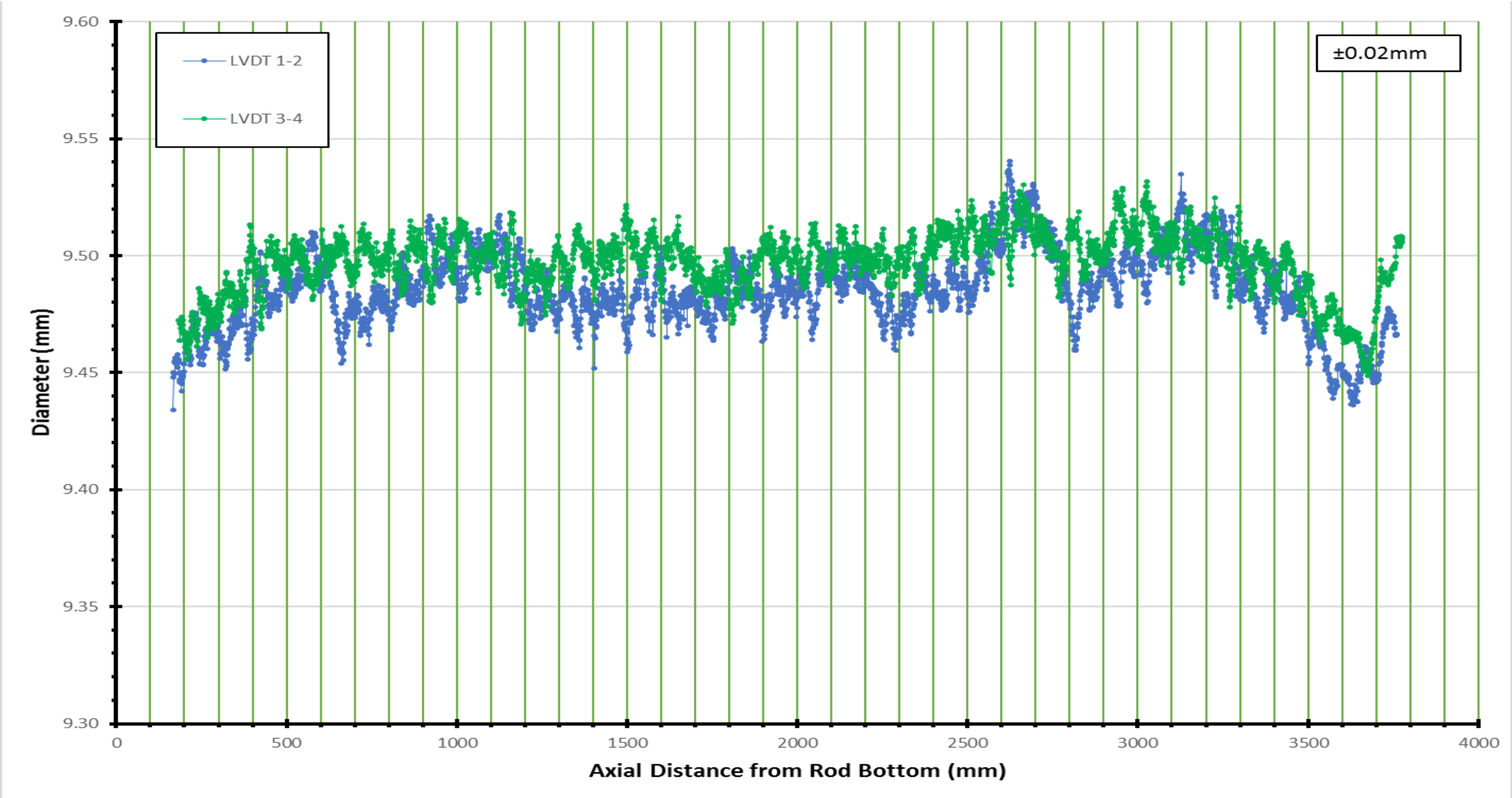


Figure A.4. Rod 3D8E14 LVDT Diameter Measurements.

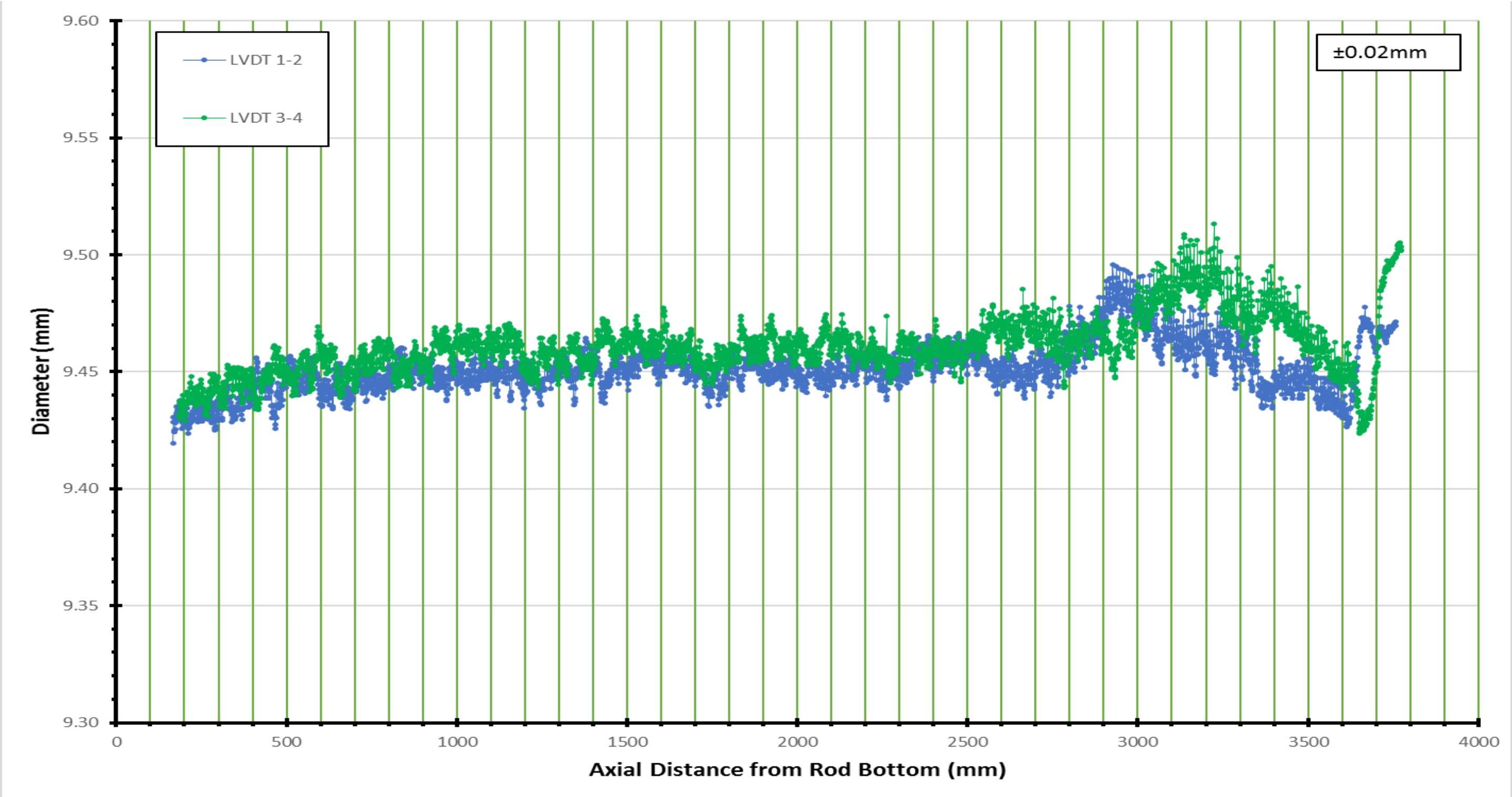


Figure A.5. Rod 3F9D07 LVDT Diameter Measurements.

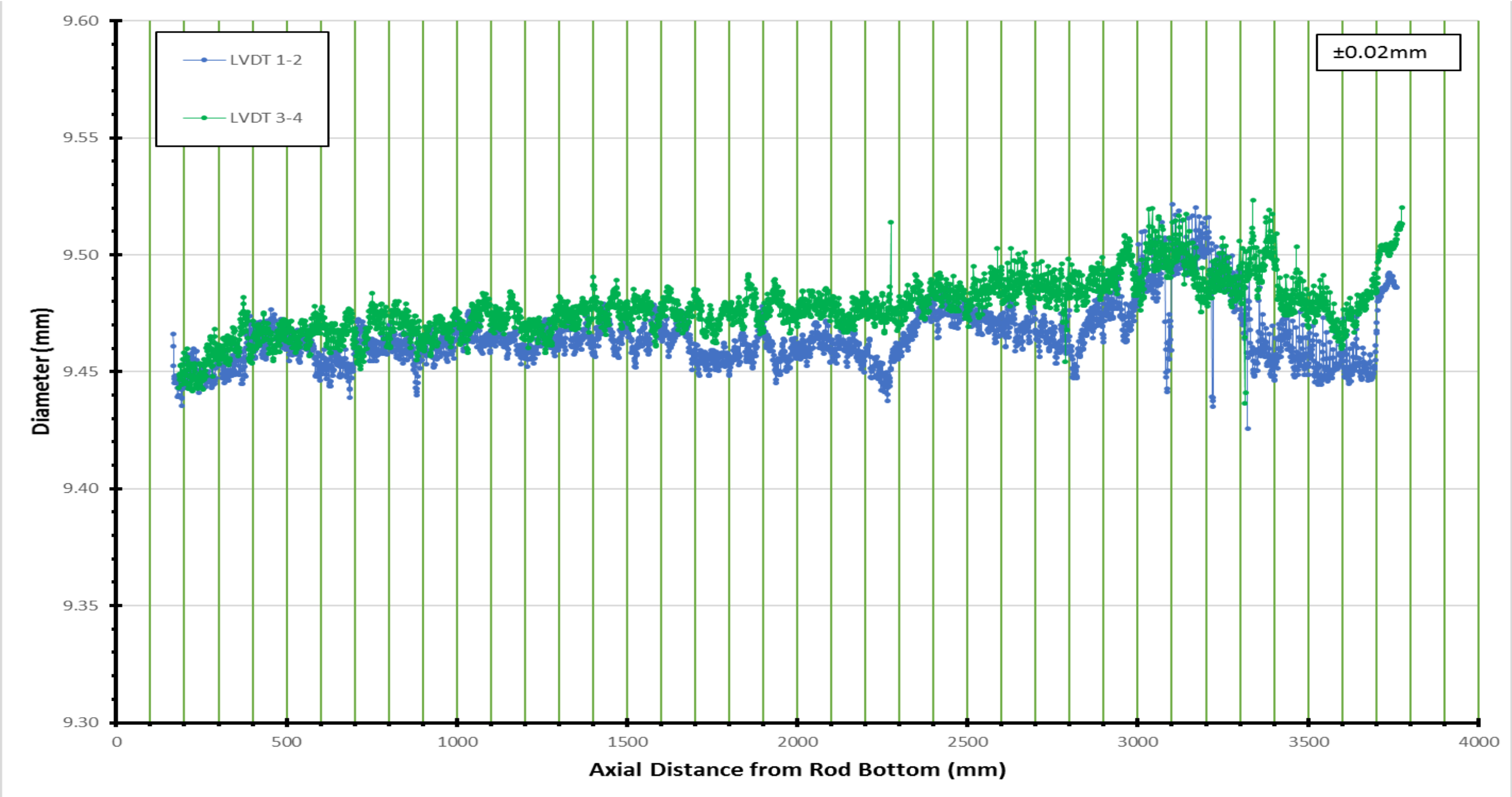


Figure A.6. Rod 3F9N05 LVDT Diameter Measurements.

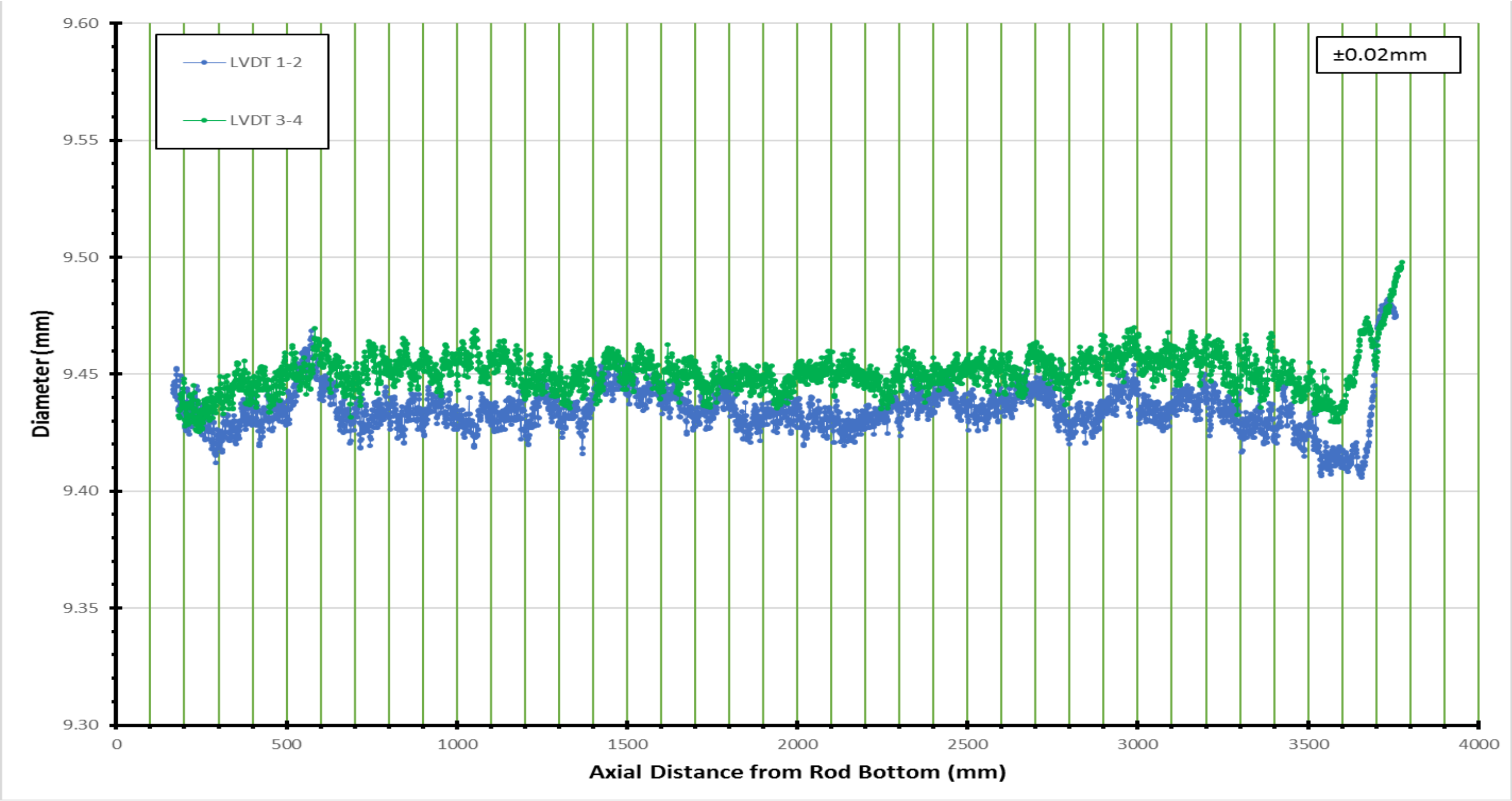


Figure A.7. Rod 3F9P02 LVDT Diameter Measurements.

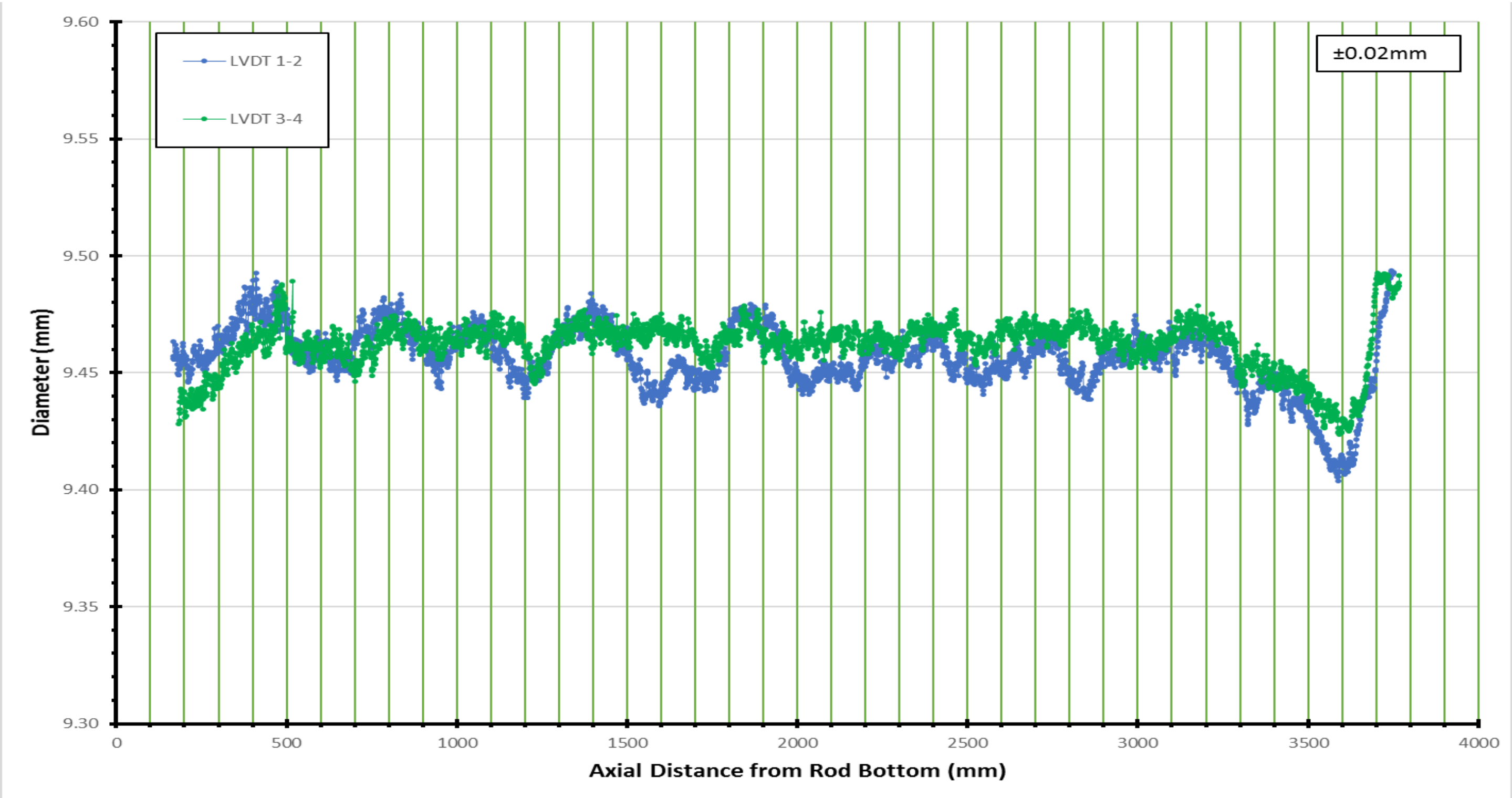


Figure A.8. Rod 5K7C05 LVDT Diameter Measurements.

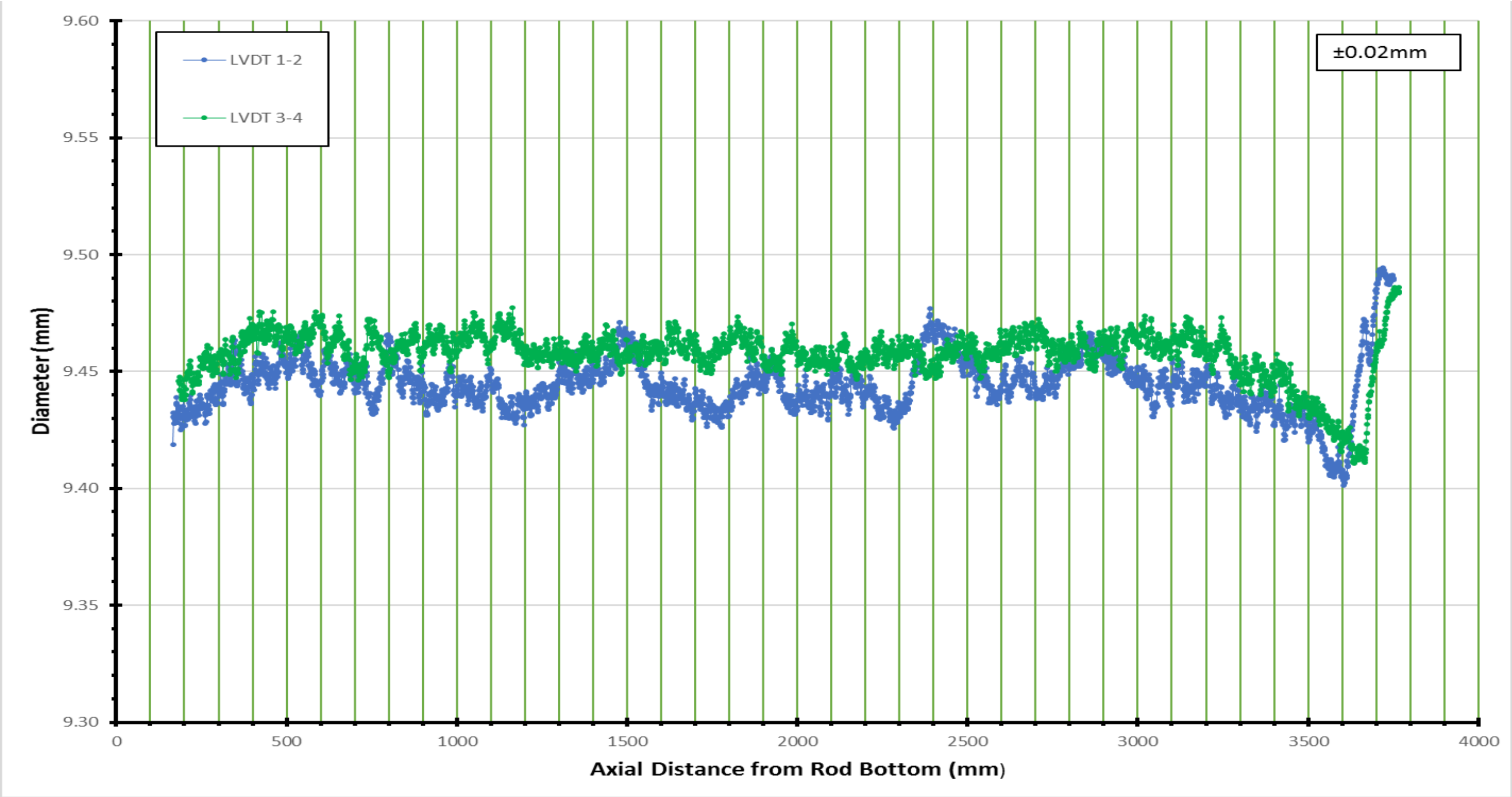


Figure A.9. Rod 5K7K09 LVDT Diameter Measurements.

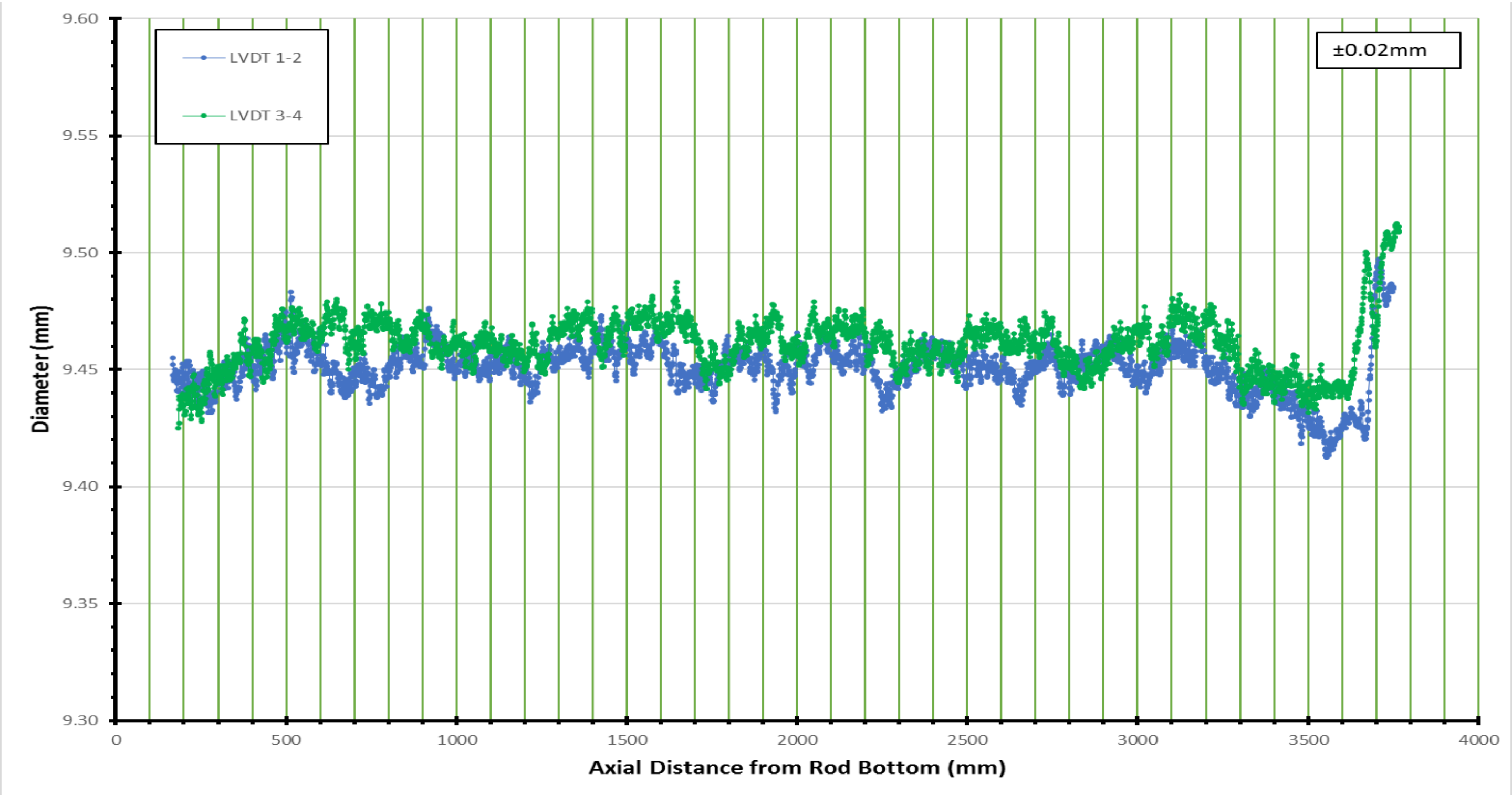


Figure A.10. Rod 5K7O14 LVDT Diameter Measurements.

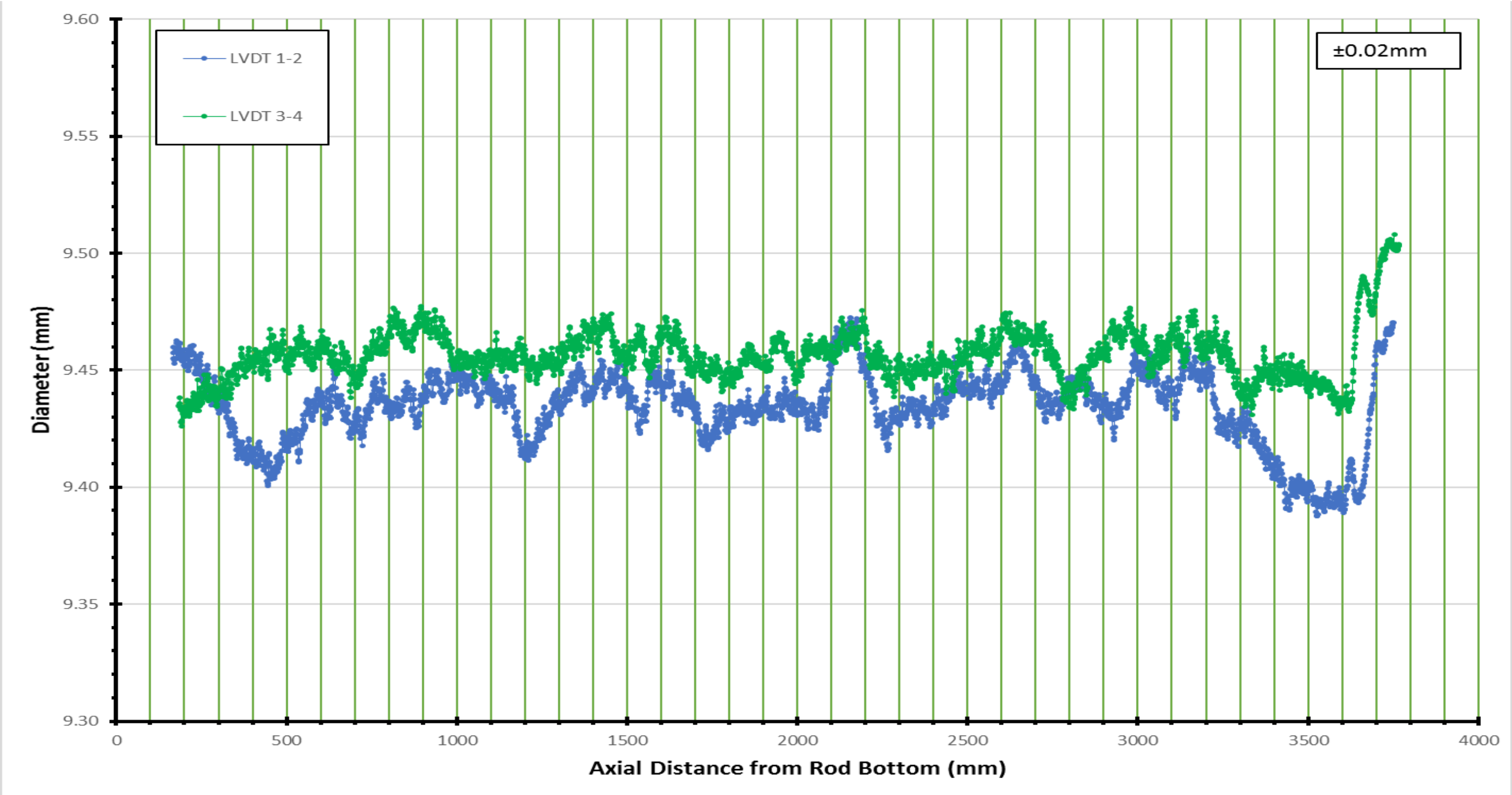


Figure A.11. Rod 5K7P02 LVDT Diameter Measurements.

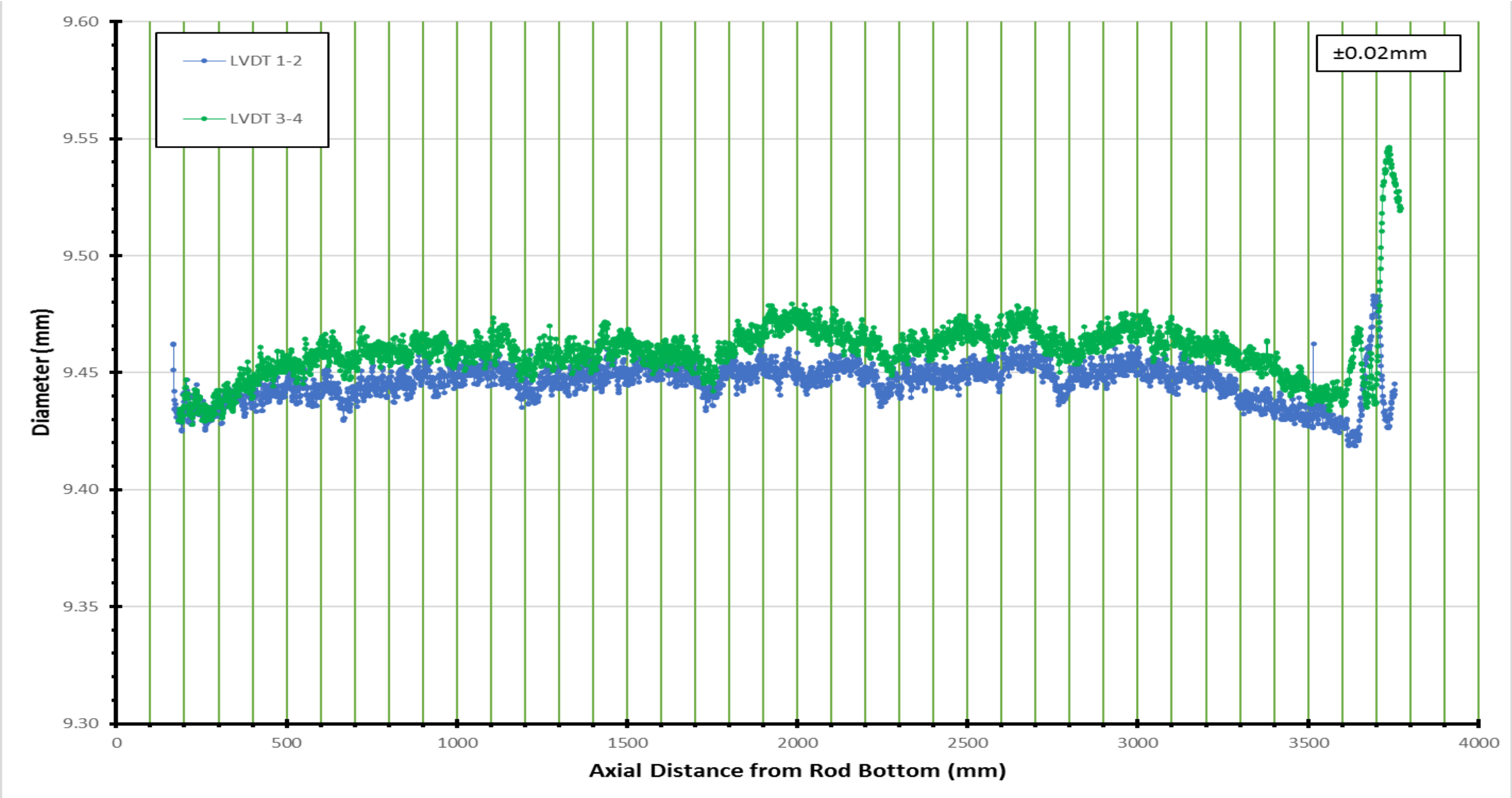
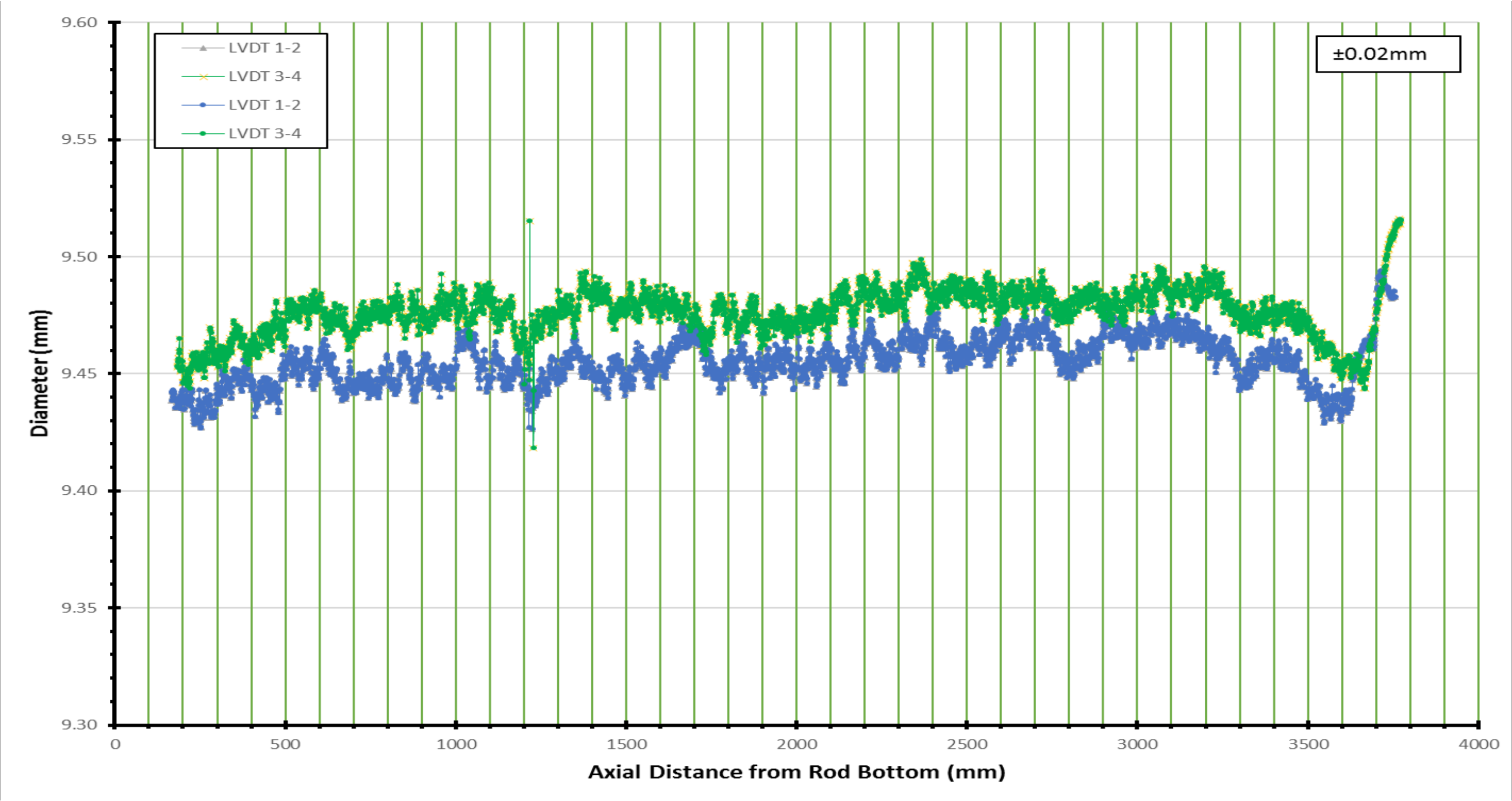


Figure A.12. Rod 6U3I07 LVDT Diameter Measurements.



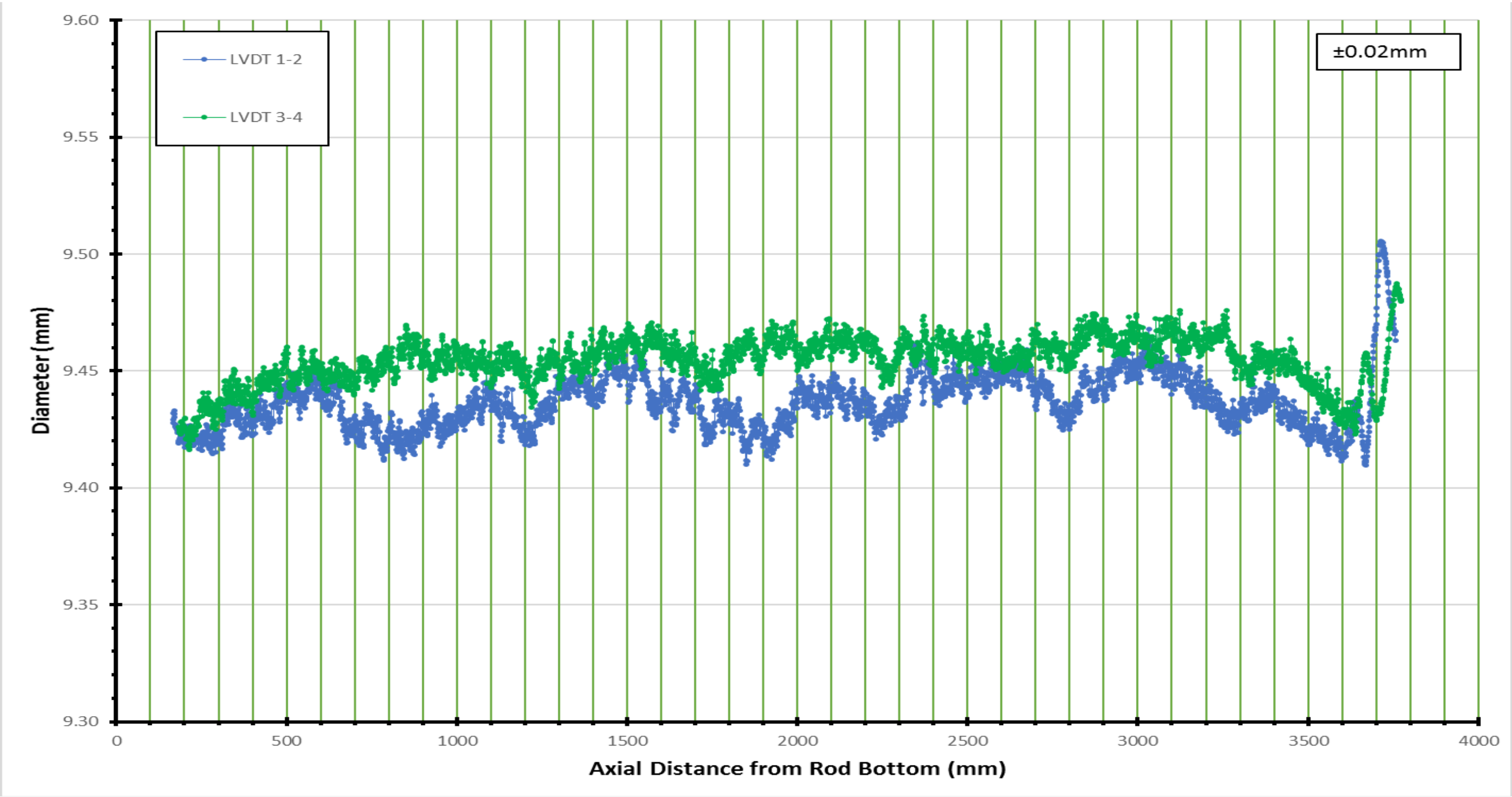


Figure A.14. Rod 6U3L08 LVDT Diameter Measurements.

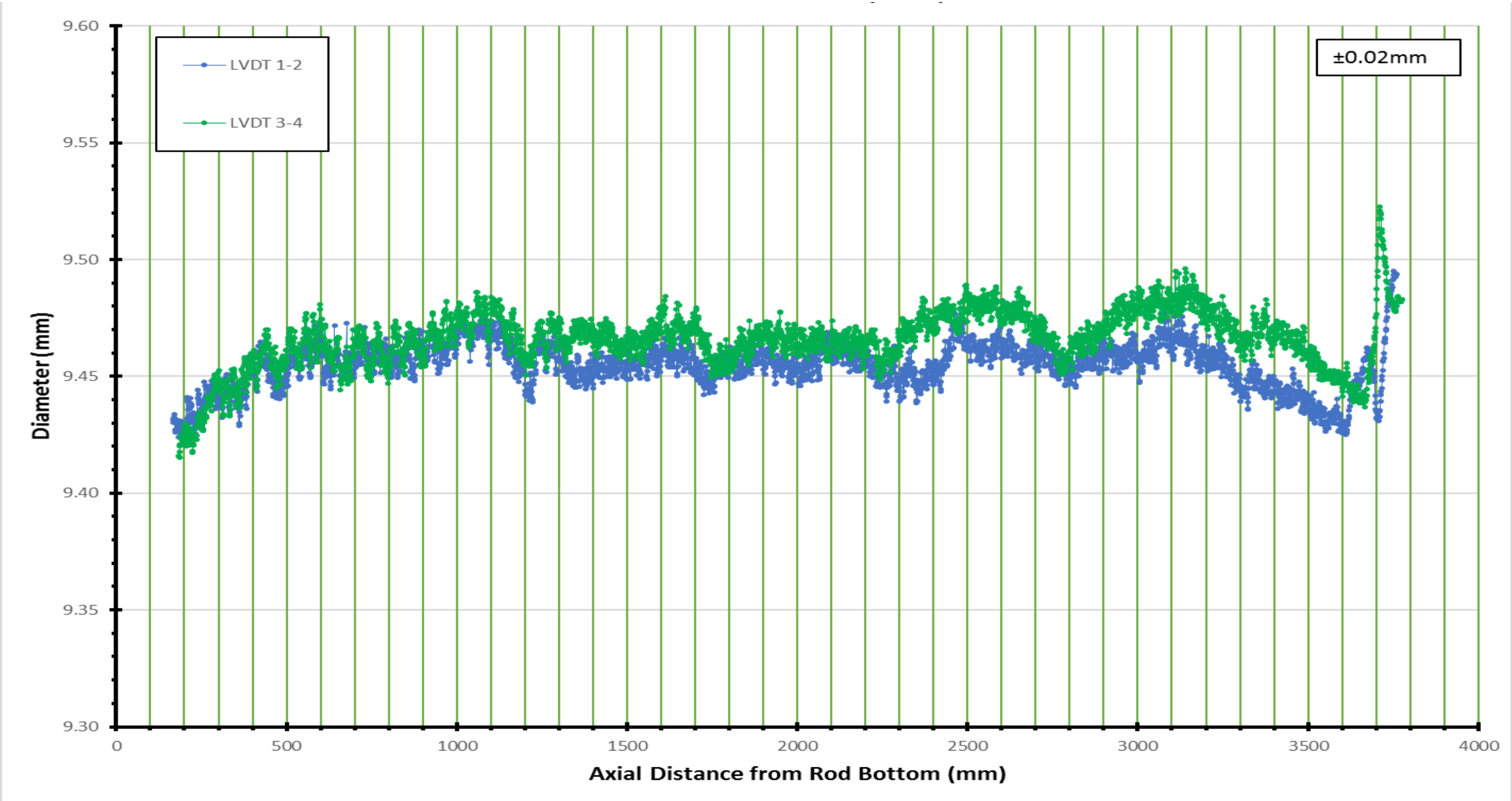


Figure A.15. Rod 6U3M03 LVDT Diameter Measurements.

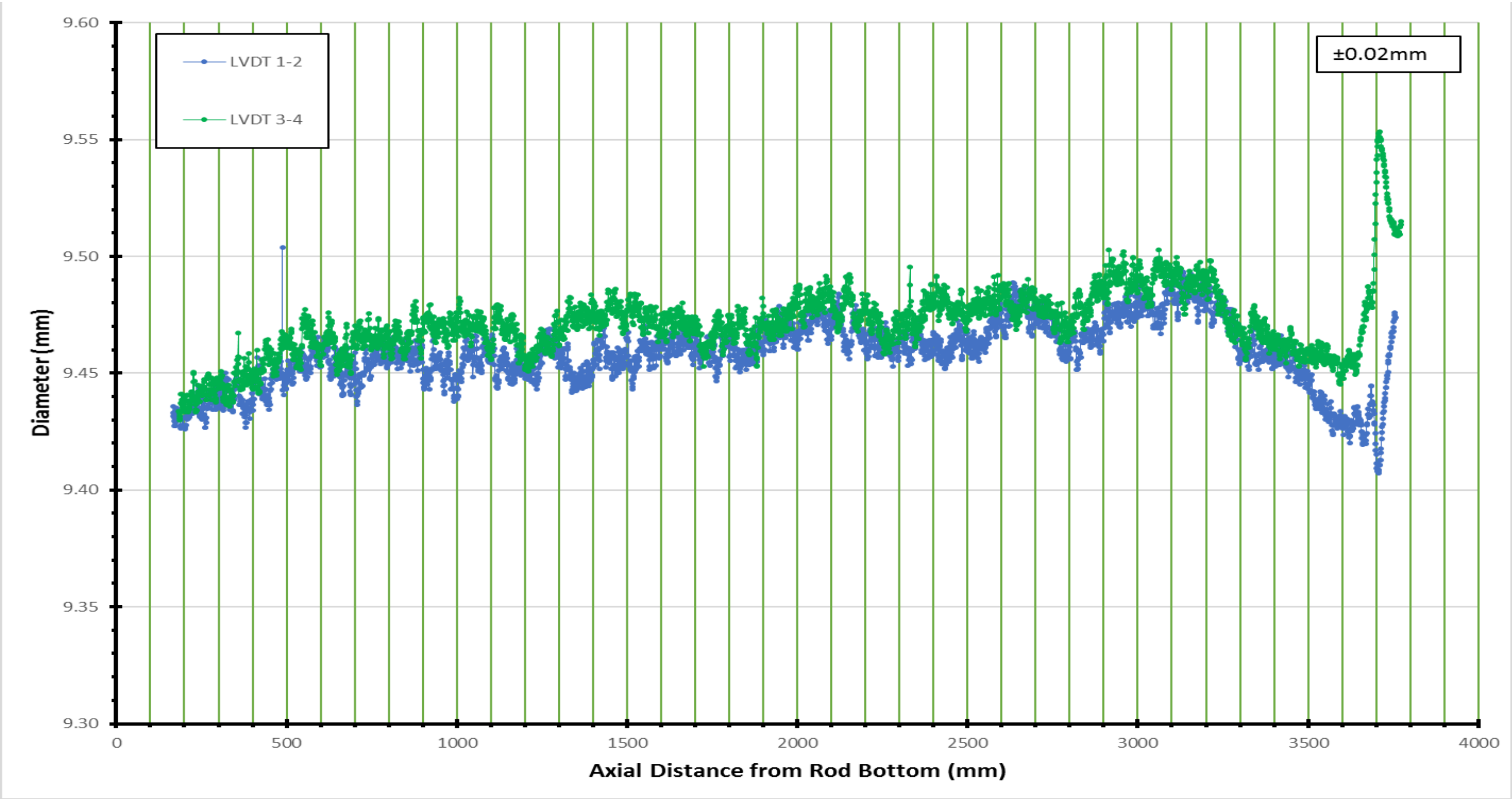


Figure A.16. Rod 6U3M09 LVDT Diameter Measurements.

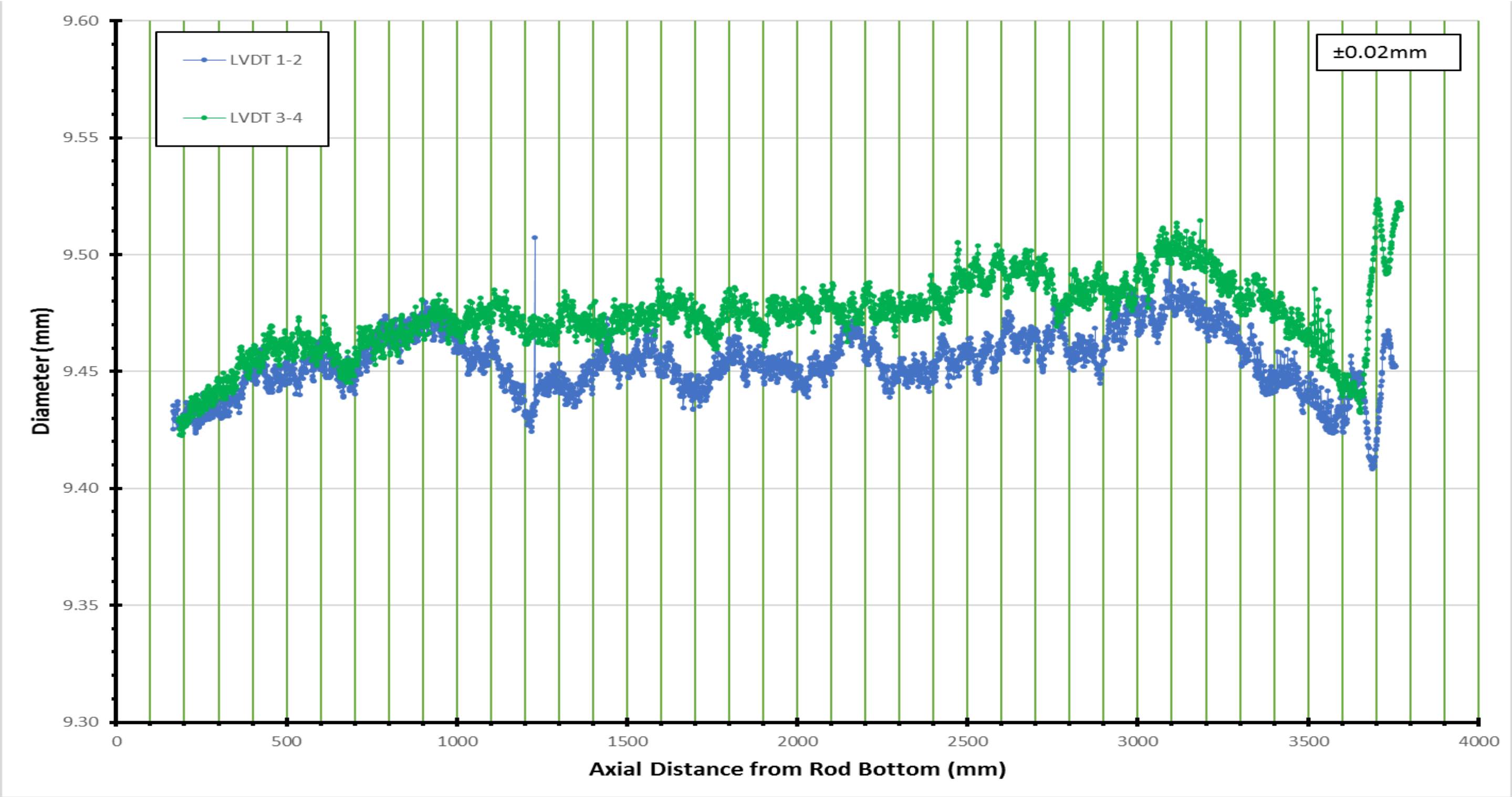


Figure A.17. Rod 6U3O05 LVDT Diameter Measurements.



Figure A.18. Rod 6U3P16 LVDT Diameter Measurements.

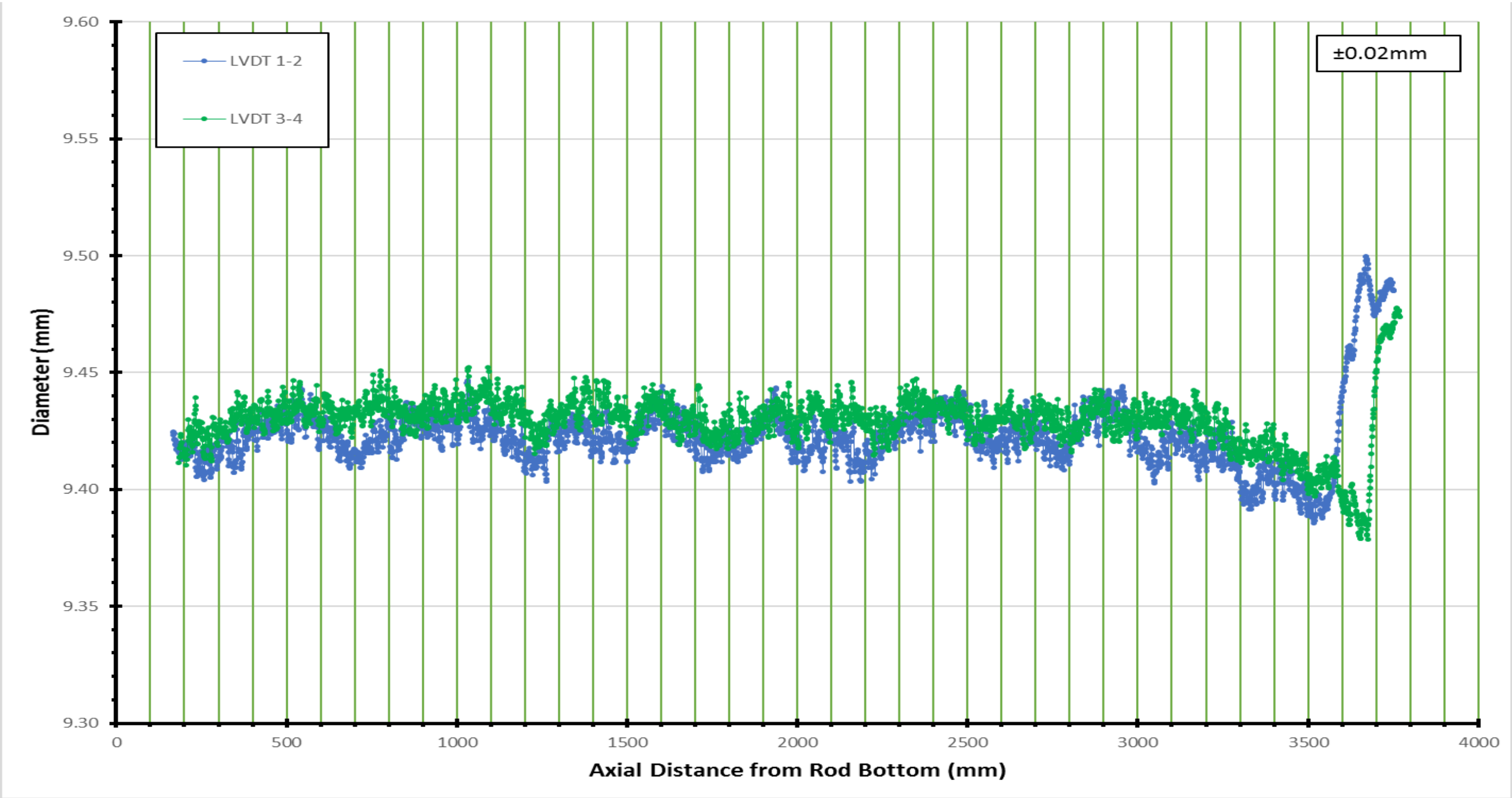


Figure A.19. Rod 30AD05 LVDT Diameter Measurements.

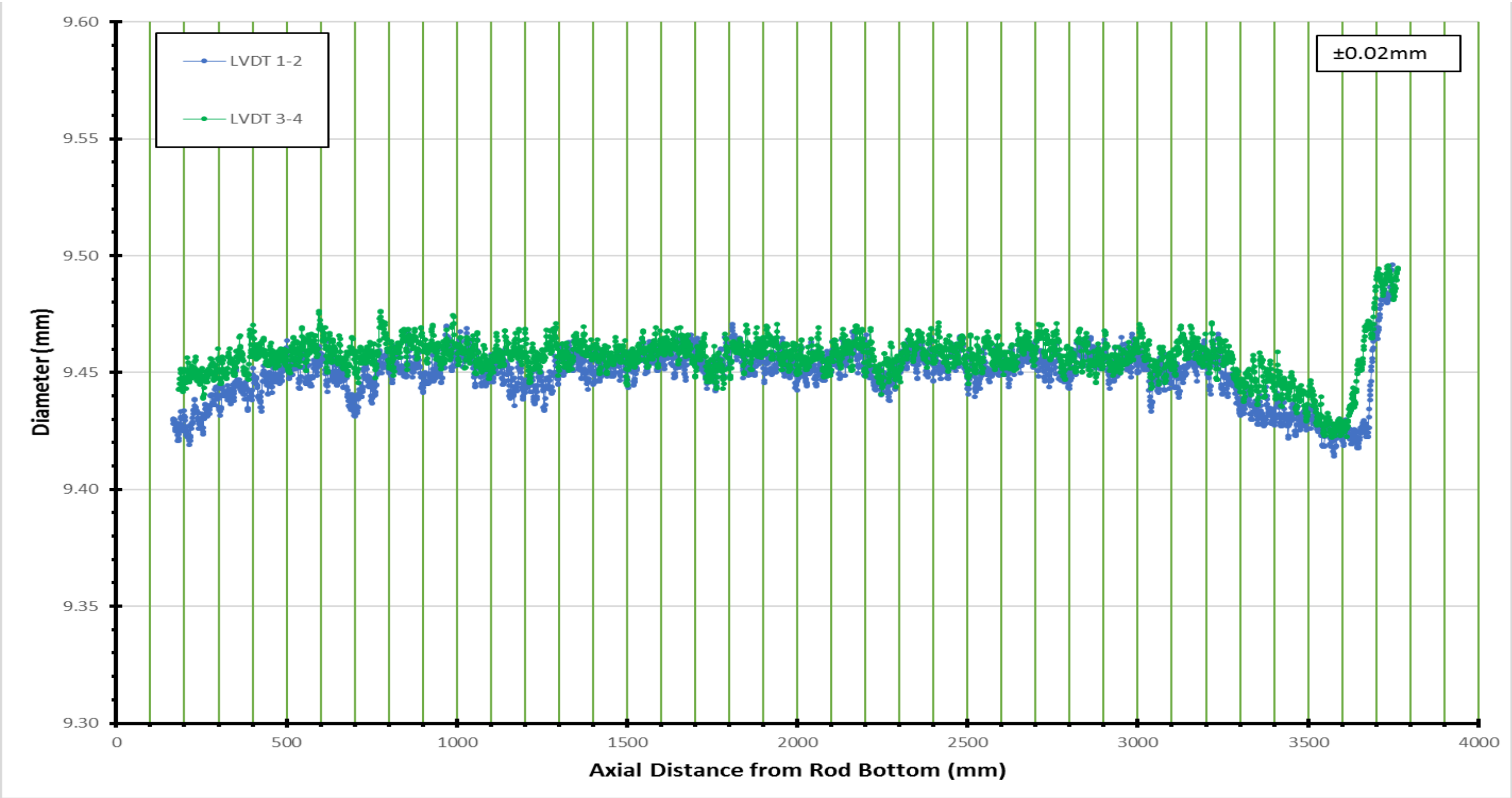


Figure A.20. Rod 30AE14 LVDT Diameter Measurements.



Figure A.21. Rod 30AG09 LVDT Diameter Measurements.

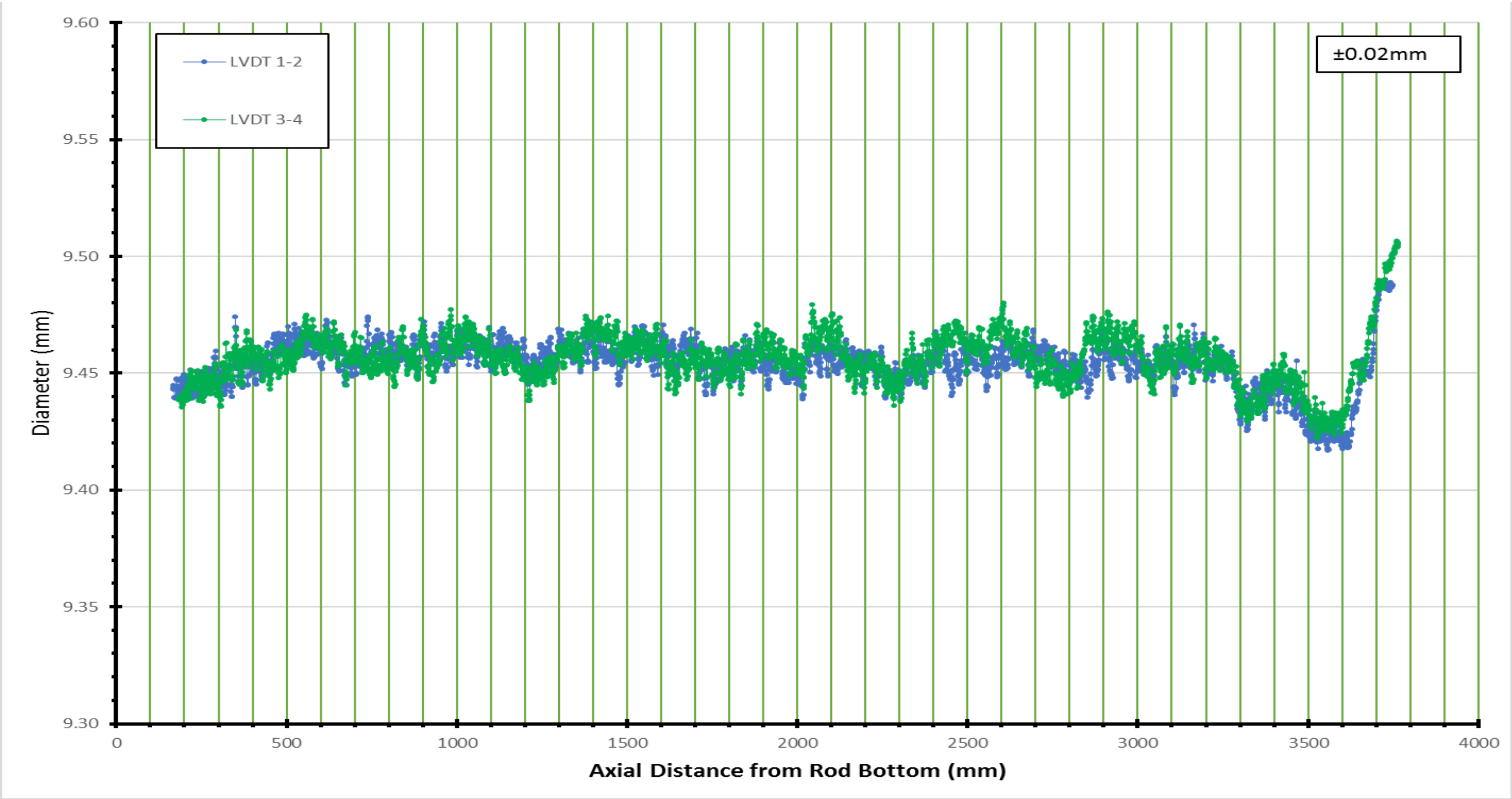


Figure A.22. Rod 30AK09 LVDT Diameter Measurements.



Figure A.23. Rod 30AP02 LVDT Diameter Measurements.

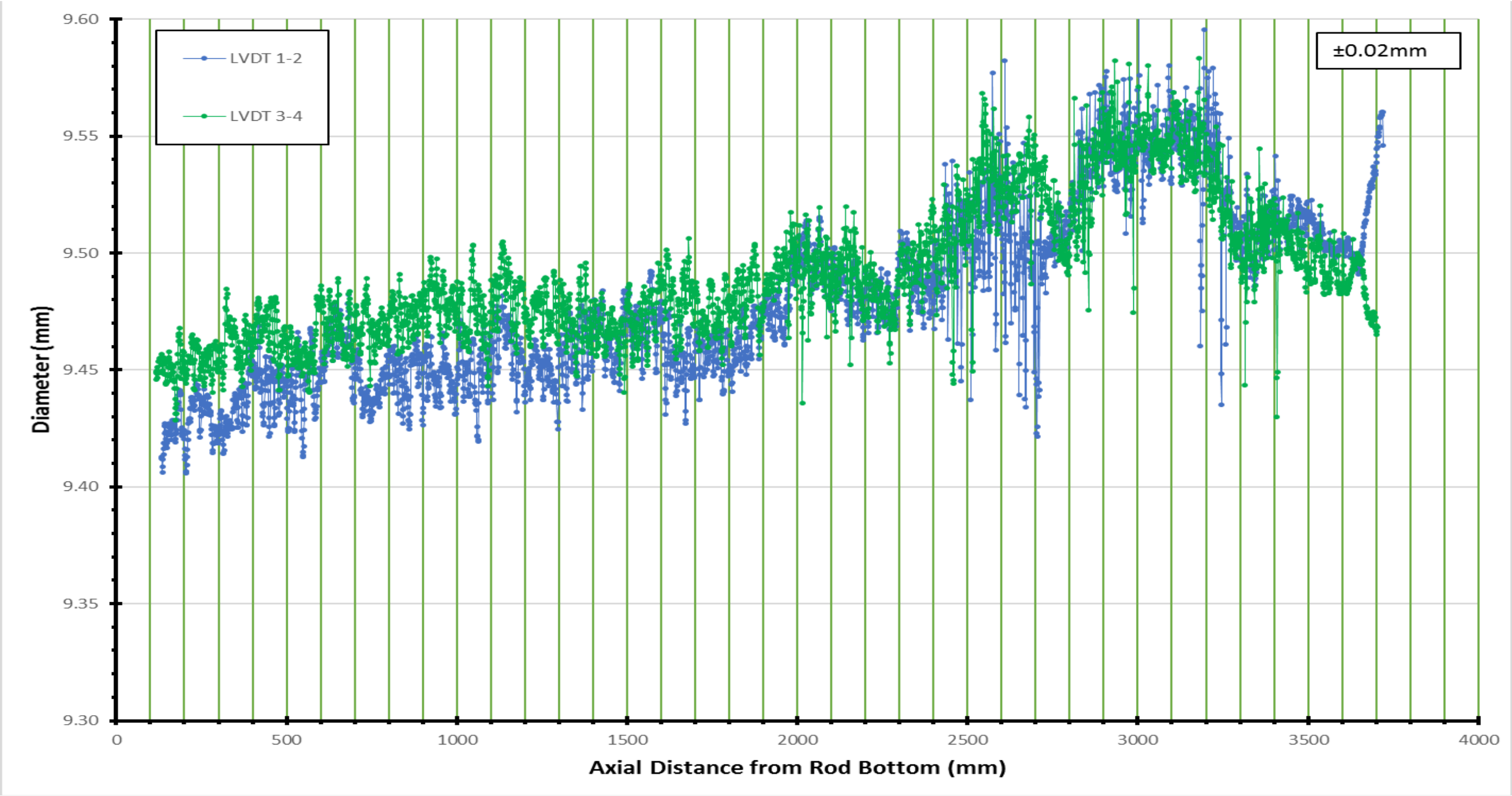


Figure A.24. Rod F35K13 LVDT Diameter Measurements.

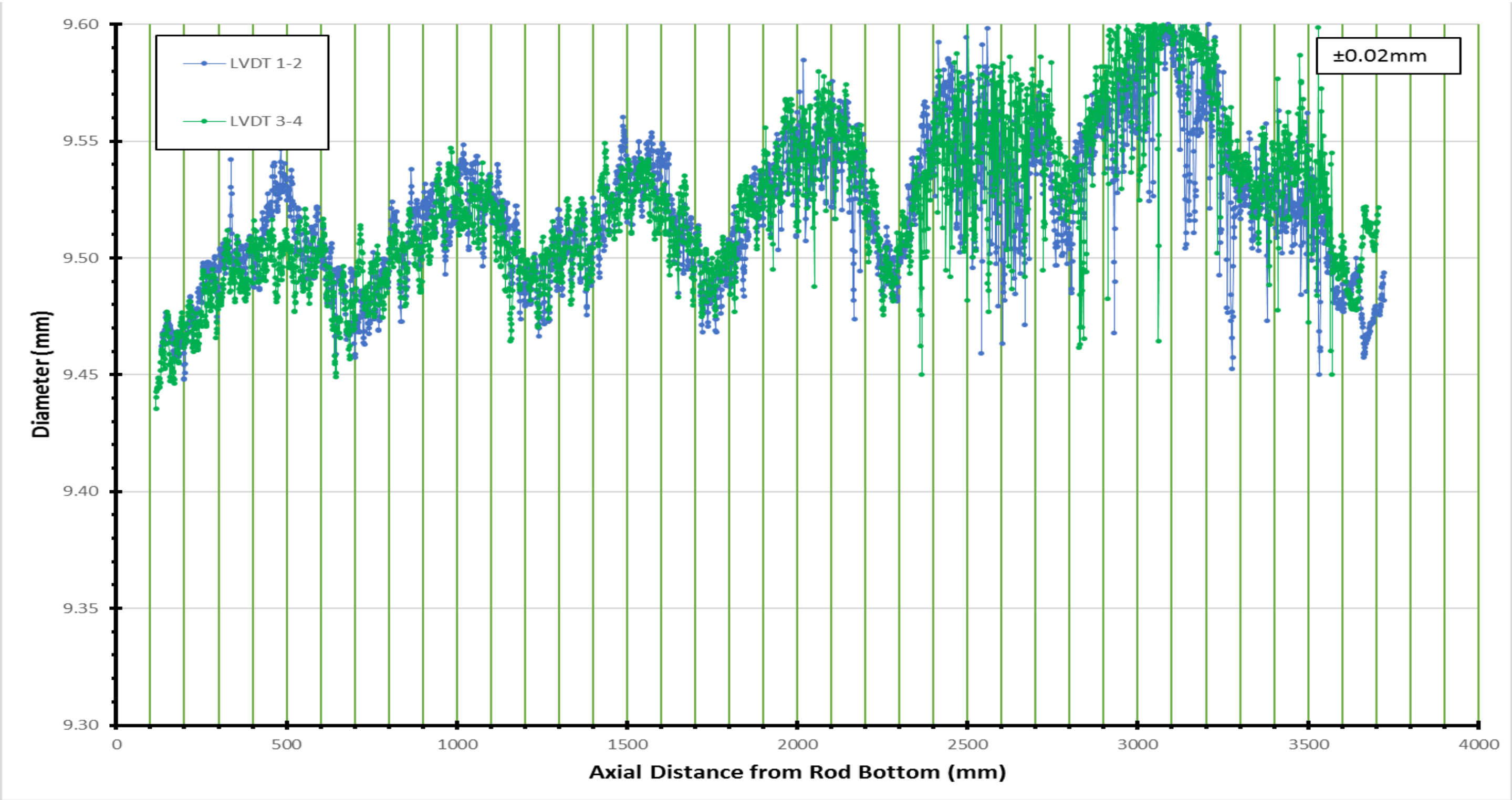


Figure A.25. Rod F35P17 LVDT Diameter Measurements.

Appendix B

Gamma Scan, Average LVDT Profilometry, and Visual Profilometry Feature Comparison

Figures B-1 through B-25 show the overlay of gamma scan data with the LVDT average diameter measurements and visually derived diameter measurements for each rod. Rod angular orientation is random, so there is no information that can be related back to a specific operational rod orientation in its fuel assembly.

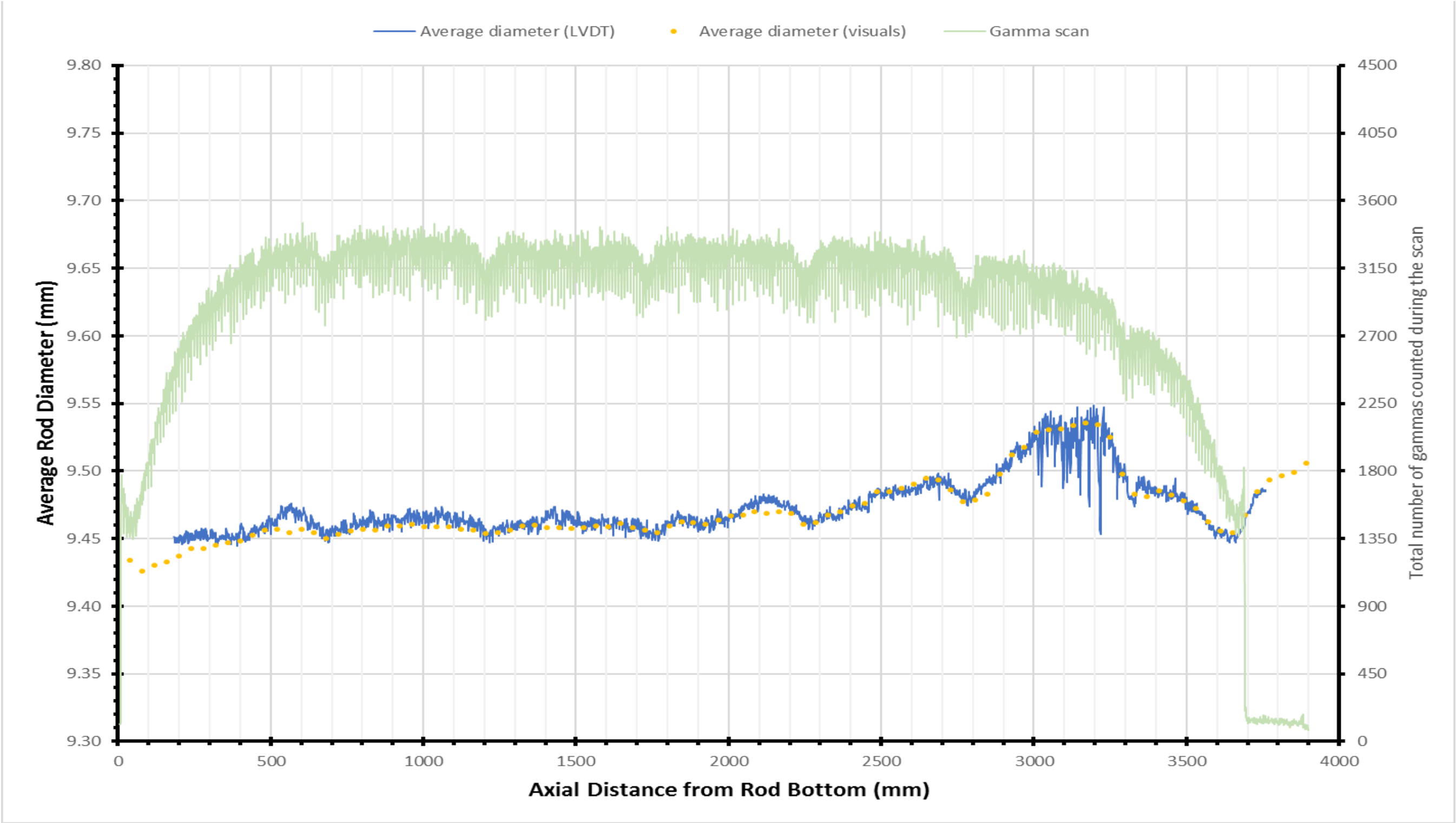


Figure B.1. Rod 3A1B16 LVDT Profilometry, Visual Profilometry, and Gamma Scan Data.

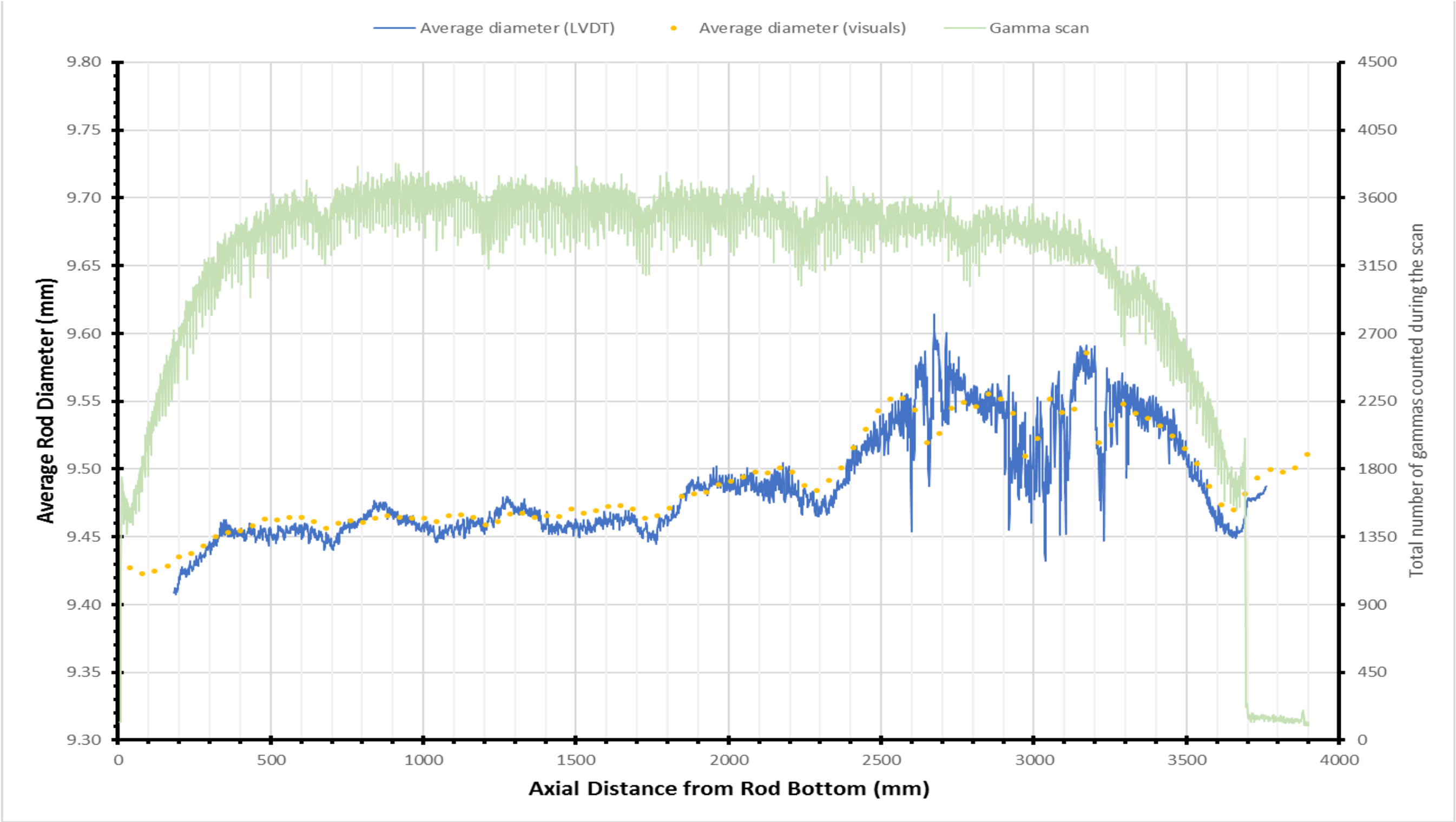


Figure B.2. Rod 3A1F05 LVDT Profilometry, Visual Profilometry, and Gamma Scan Data.

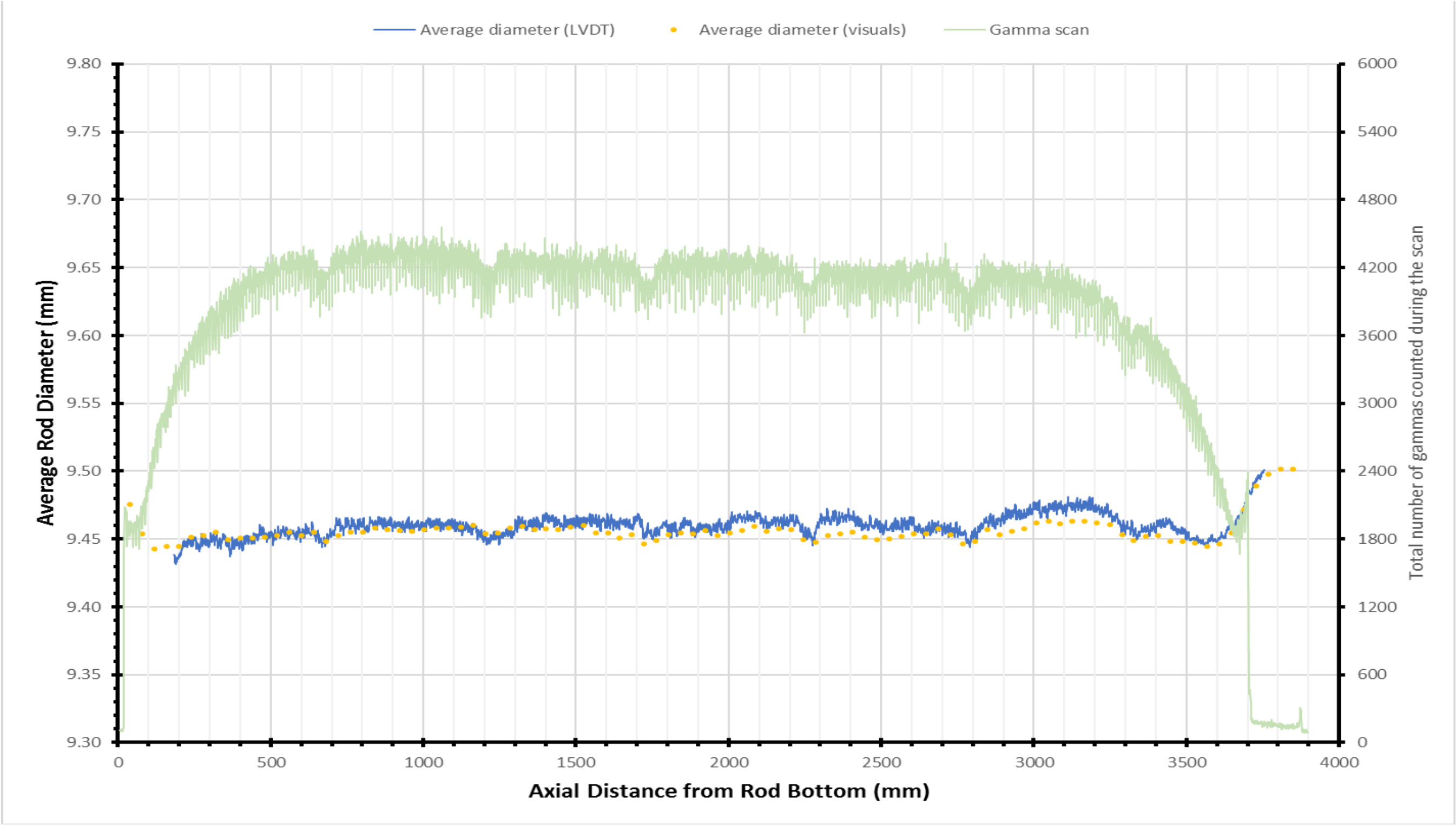


Figure B.3. Rod 3D8B02 LVDT Profilometry, Visual Profilometry, and Gamma Scan Data.

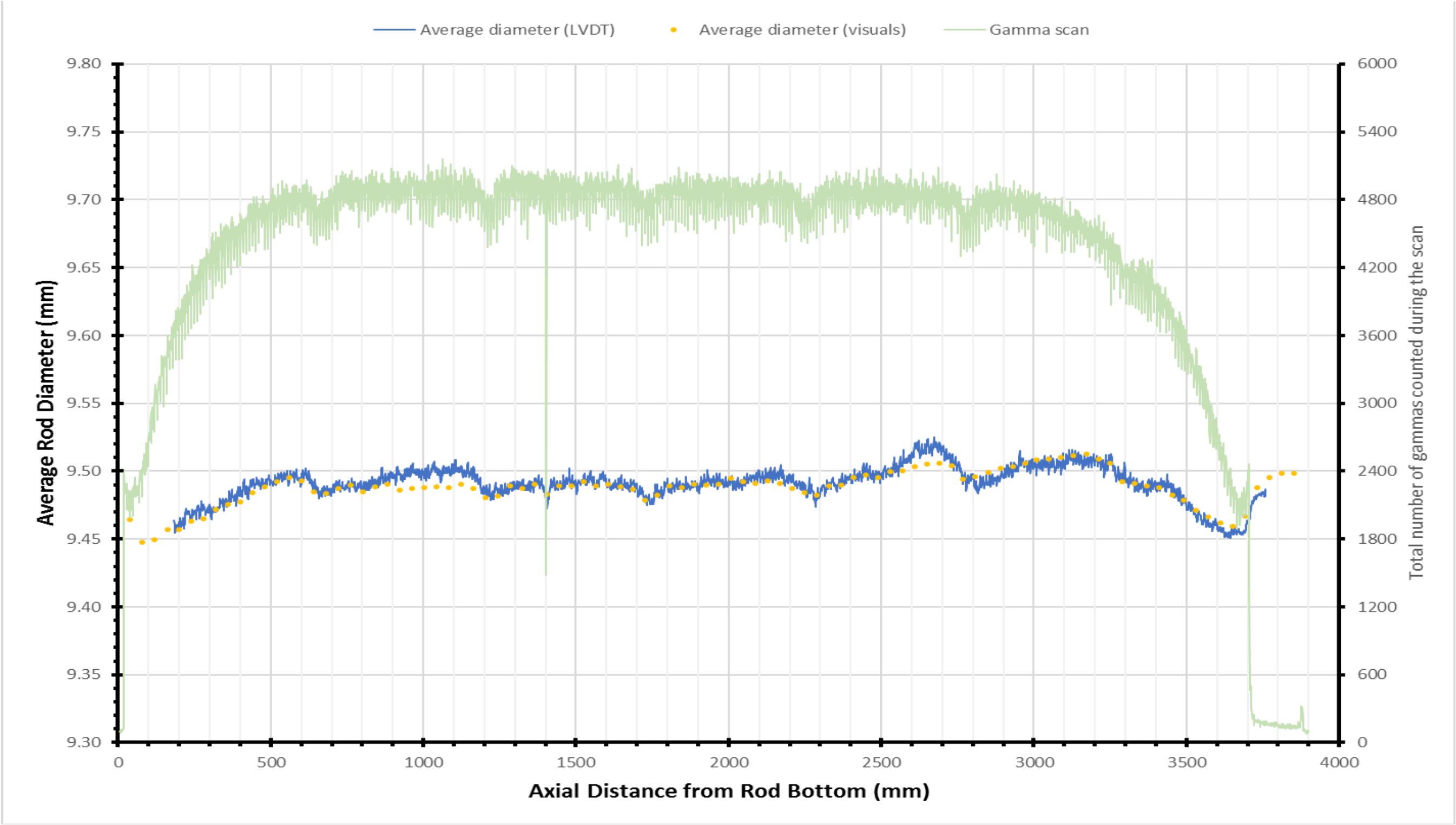


Figure B.4. Rod 3D8E14 LVDT Profilometry, Visual Profilometry, and Gamma Scan Data.

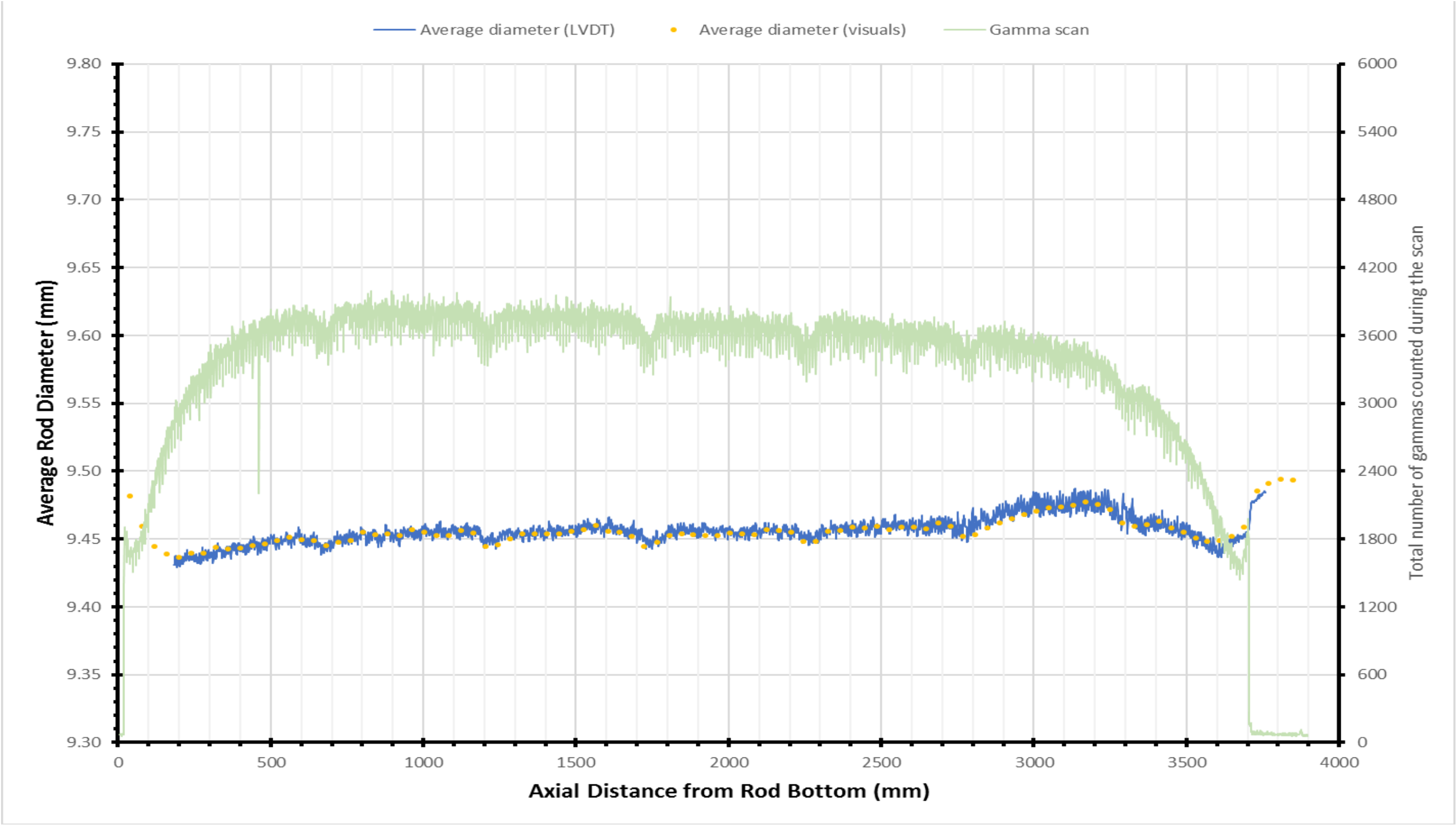


Figure B.5. Rod 3F9D07 LVDT Profilometry, Visual Profilometry, and Gamma Scan Data.

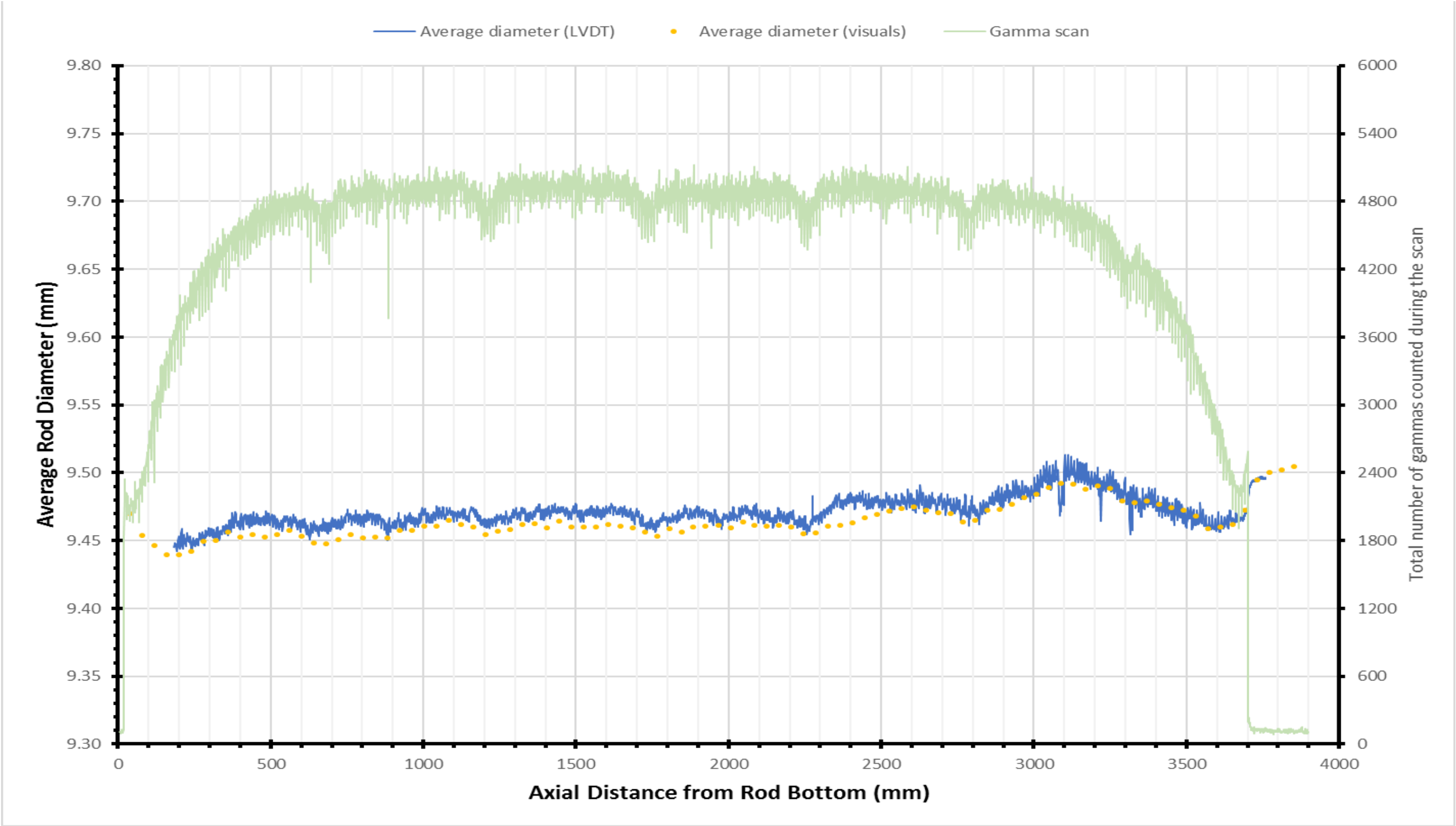


Figure B.6. Rod 3F9N05 LVDT Profilometry, Visual Profilometry, and Gamma Scan Data.

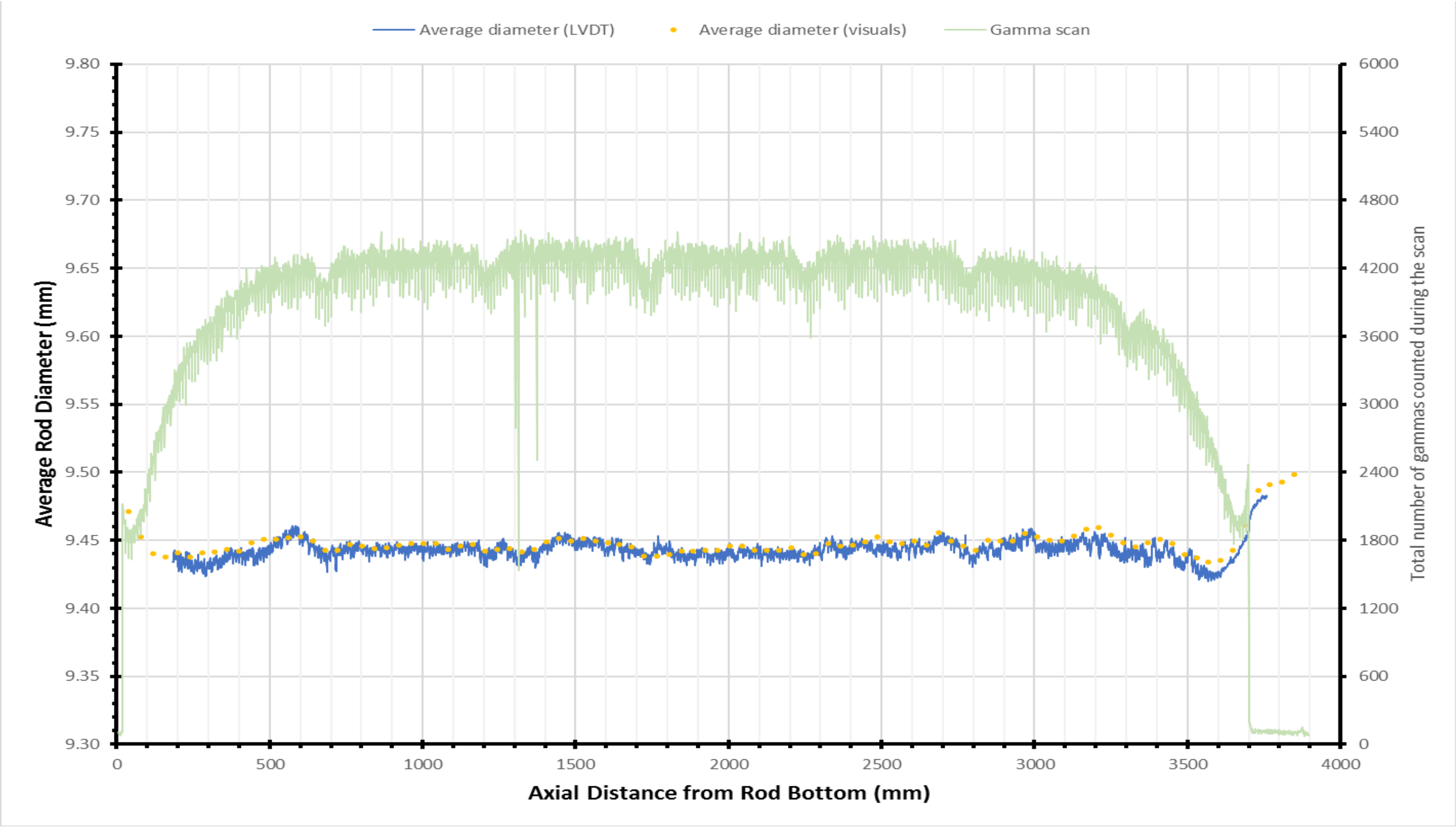


Figure B.7. Rod 3F9P02 LVDT Profilometry, Visual Profilometry, and Gamma Scan Data.

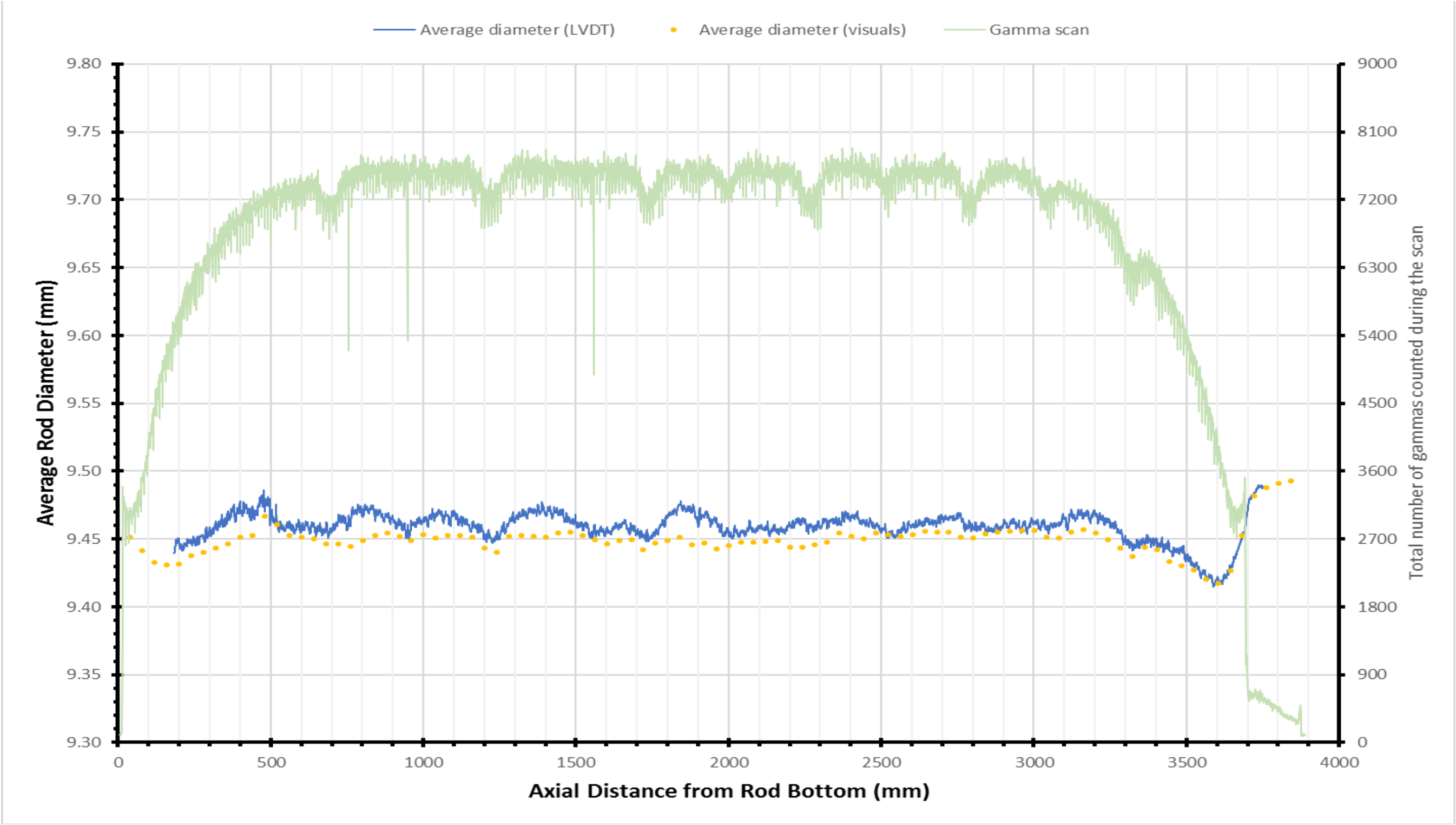


Figure B.8. Rod 5K7C05 LVDT Profilometry, Visual Profilometry, and Gamma Scan Data.

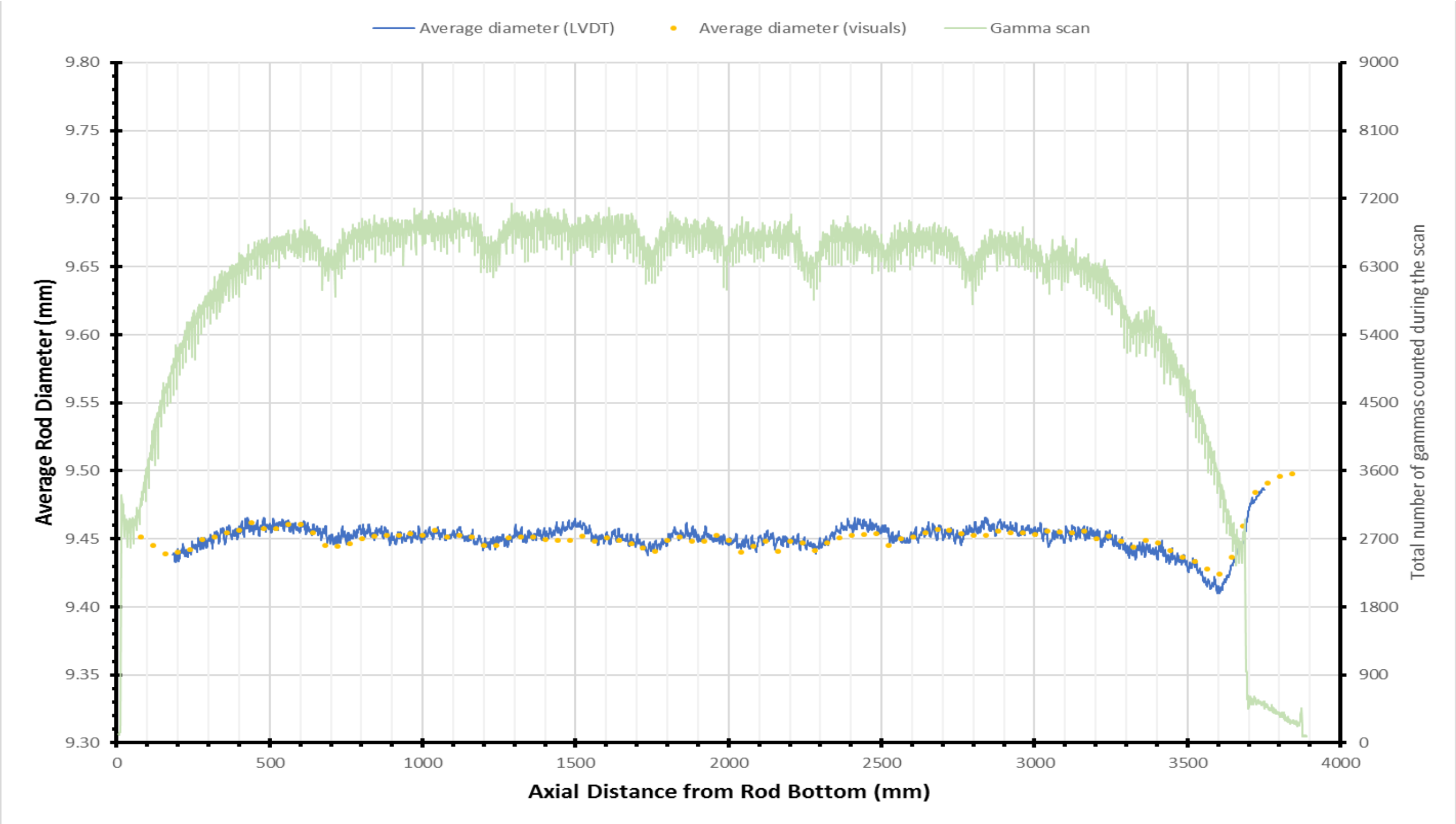


Figure B.9. Rod 5K7K09 LVDT Profilometry, Visual Profilometry, and Gamma Scan Data.

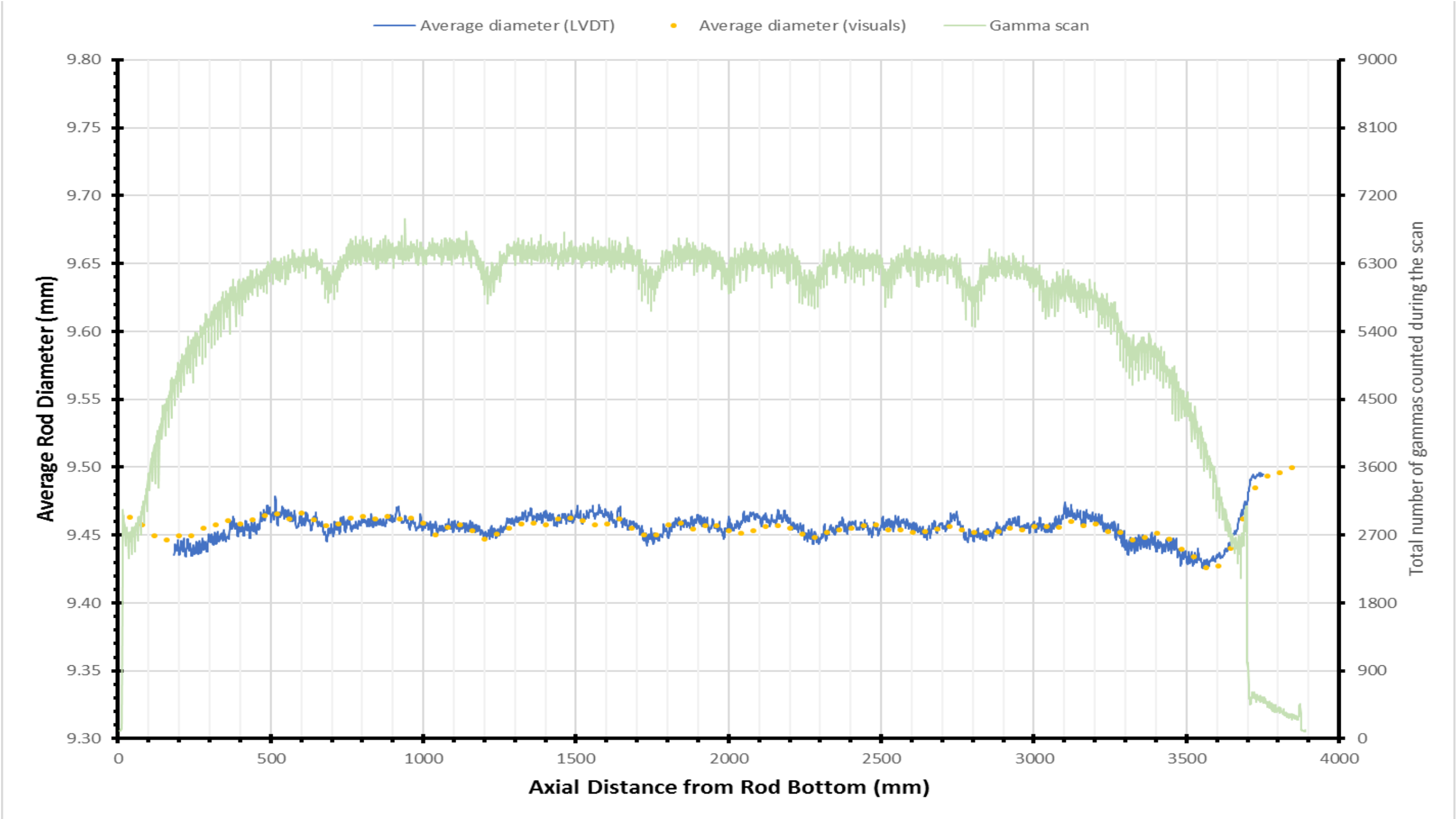


Figure B.10. Rod 5K7O14 LVDT Profilometry, Visual Profilometry, and Gamma Scan Data.

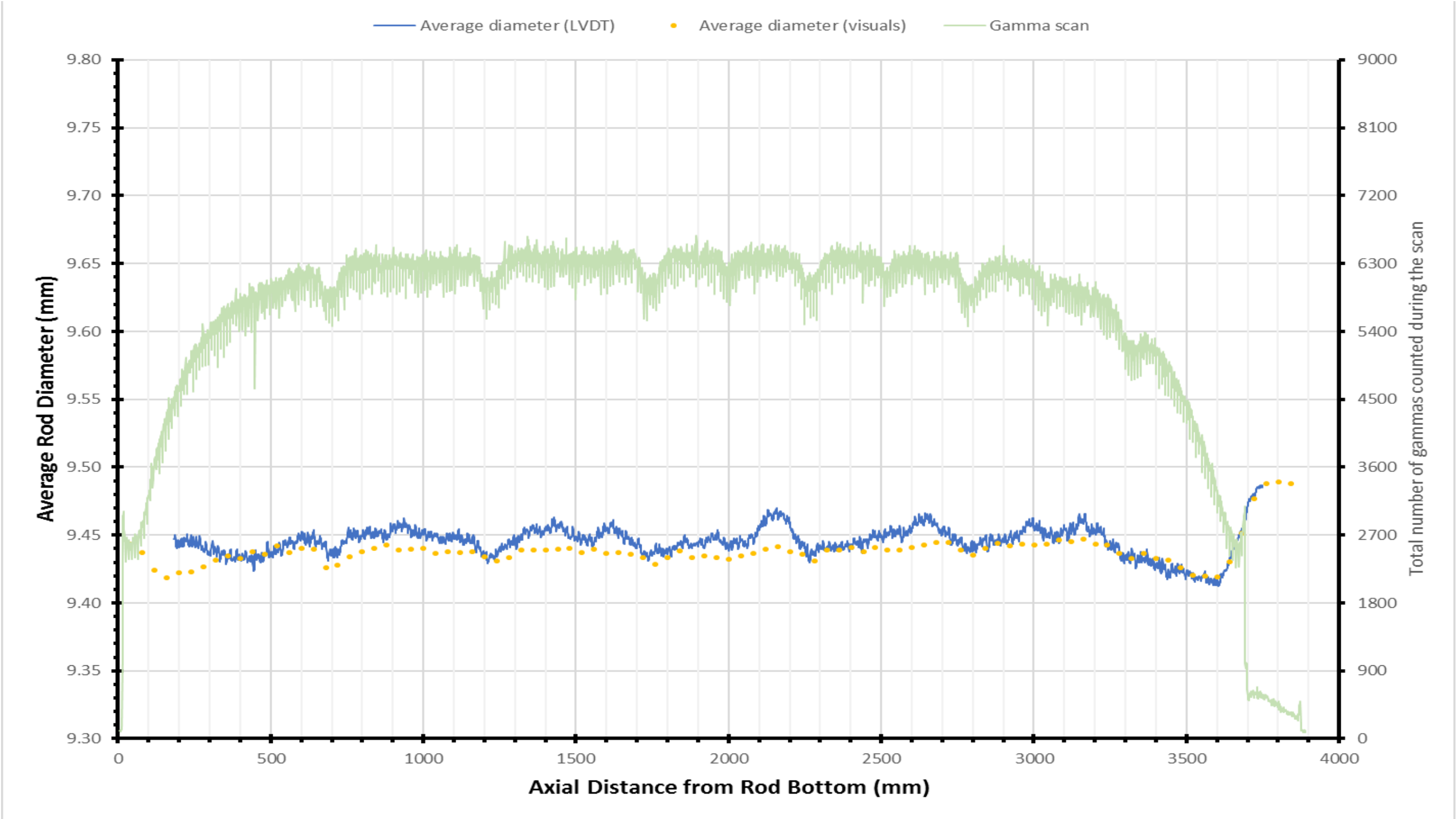


Figure B.11. Rod 5K7P02 LVDT Profilometry, Visual Profilometry, and Gamma Scan Data.

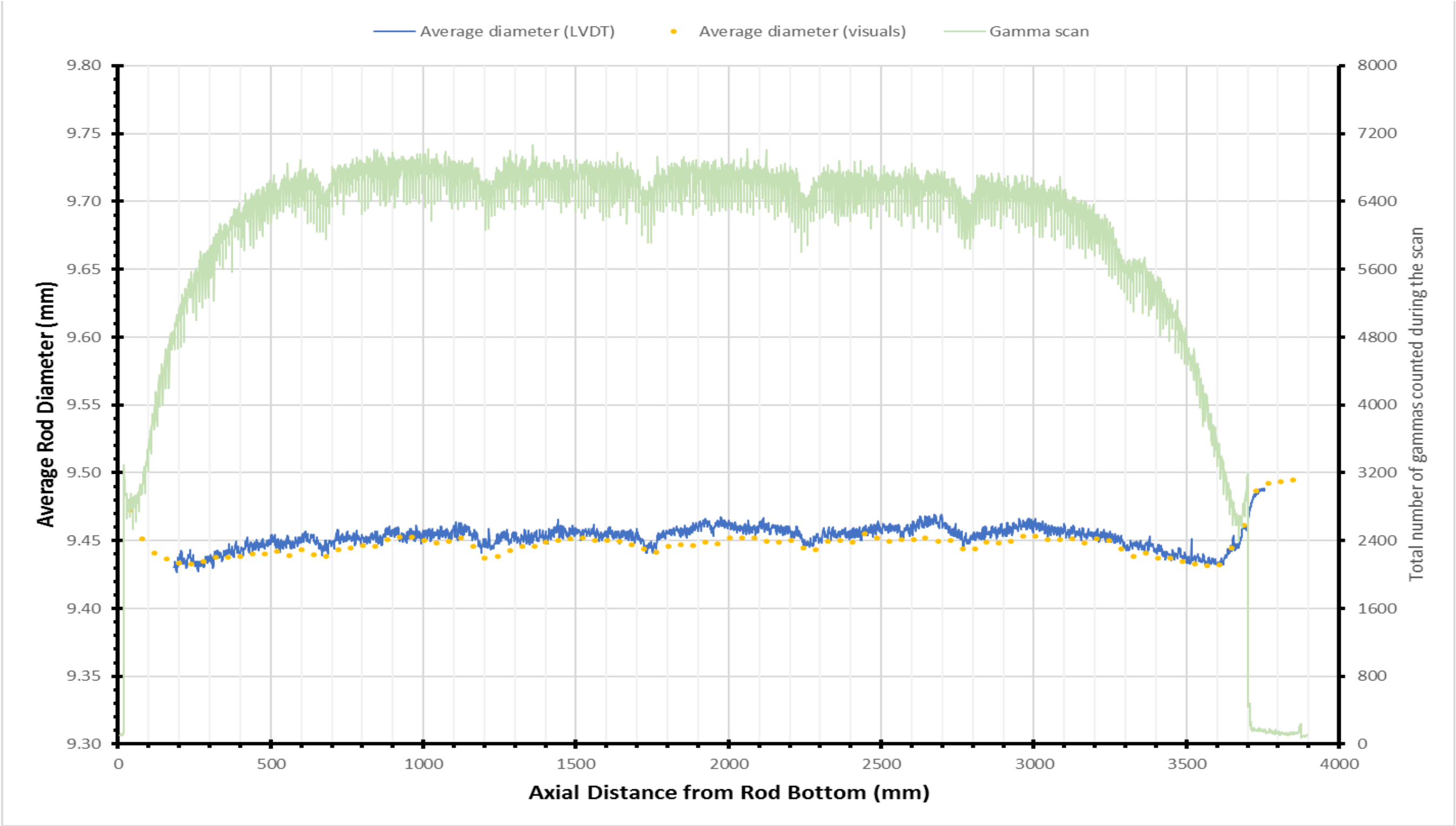


Figure B.12. Rod 6U3I07 LVDT Profilometry, Visual Profilometry, and Gamma Scan Data.

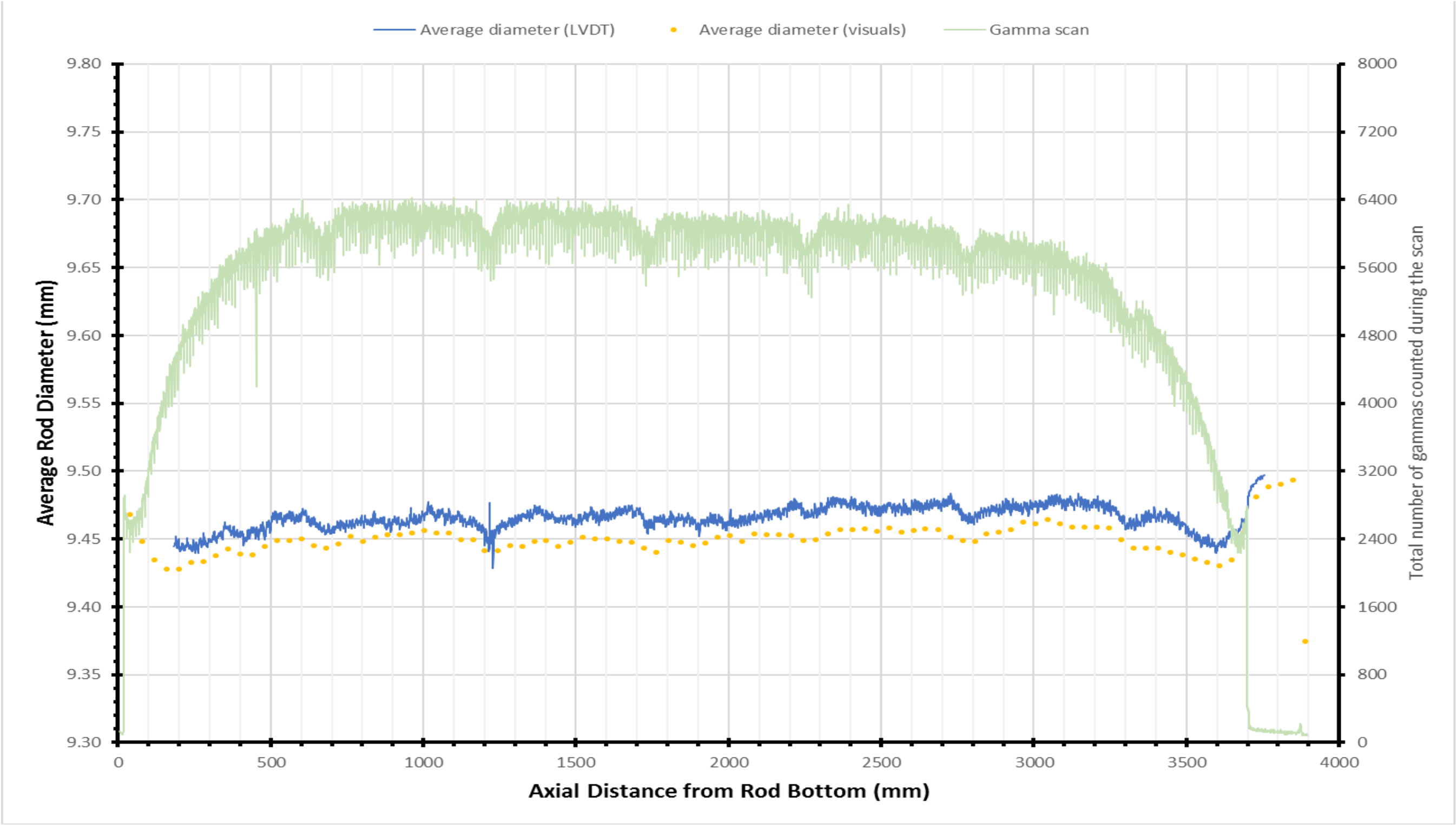


Figure B.13. Rod 6U3K09 LVDT Profilometry, Visual Profilometry, and Gamma Scan Data.

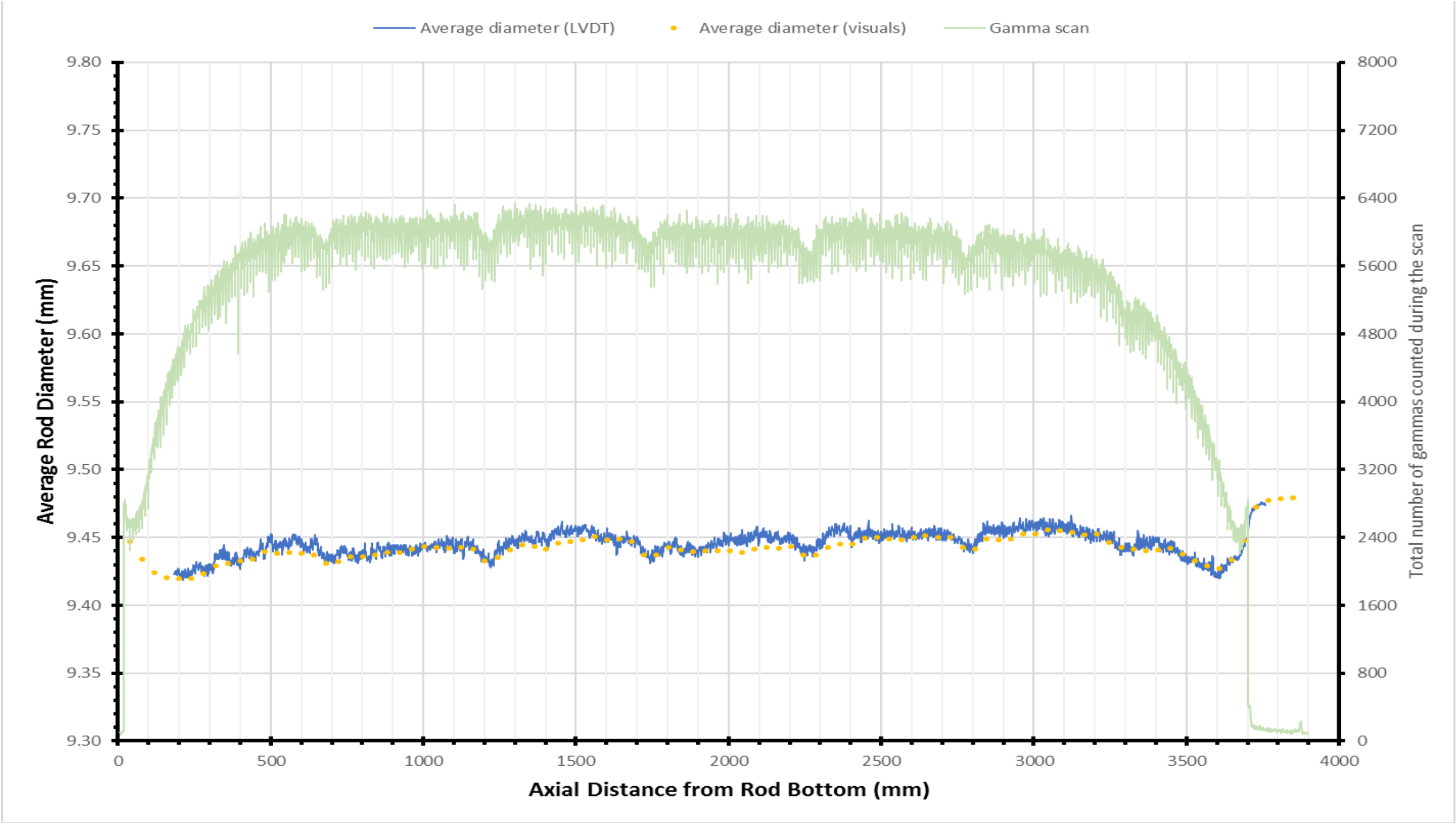


Figure B.14. Rod 6U3L08 LVDT Profilometry, Visual Profilometry, and Gamma Scan Data.

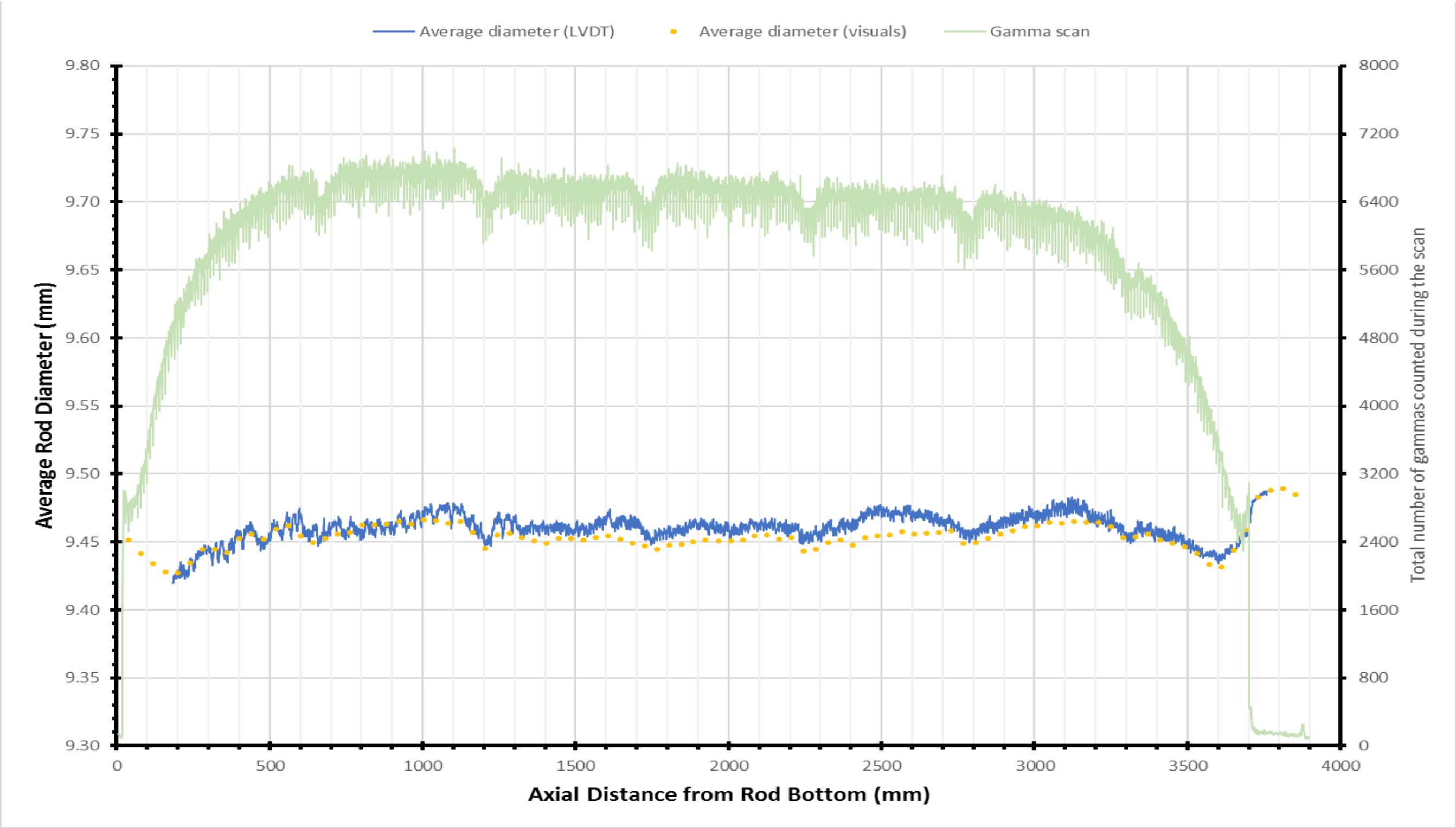


Figure B.15. Rod 6U3M03 LVDT Profilometry, Visual Profilometry, and Gamma Scan Data.

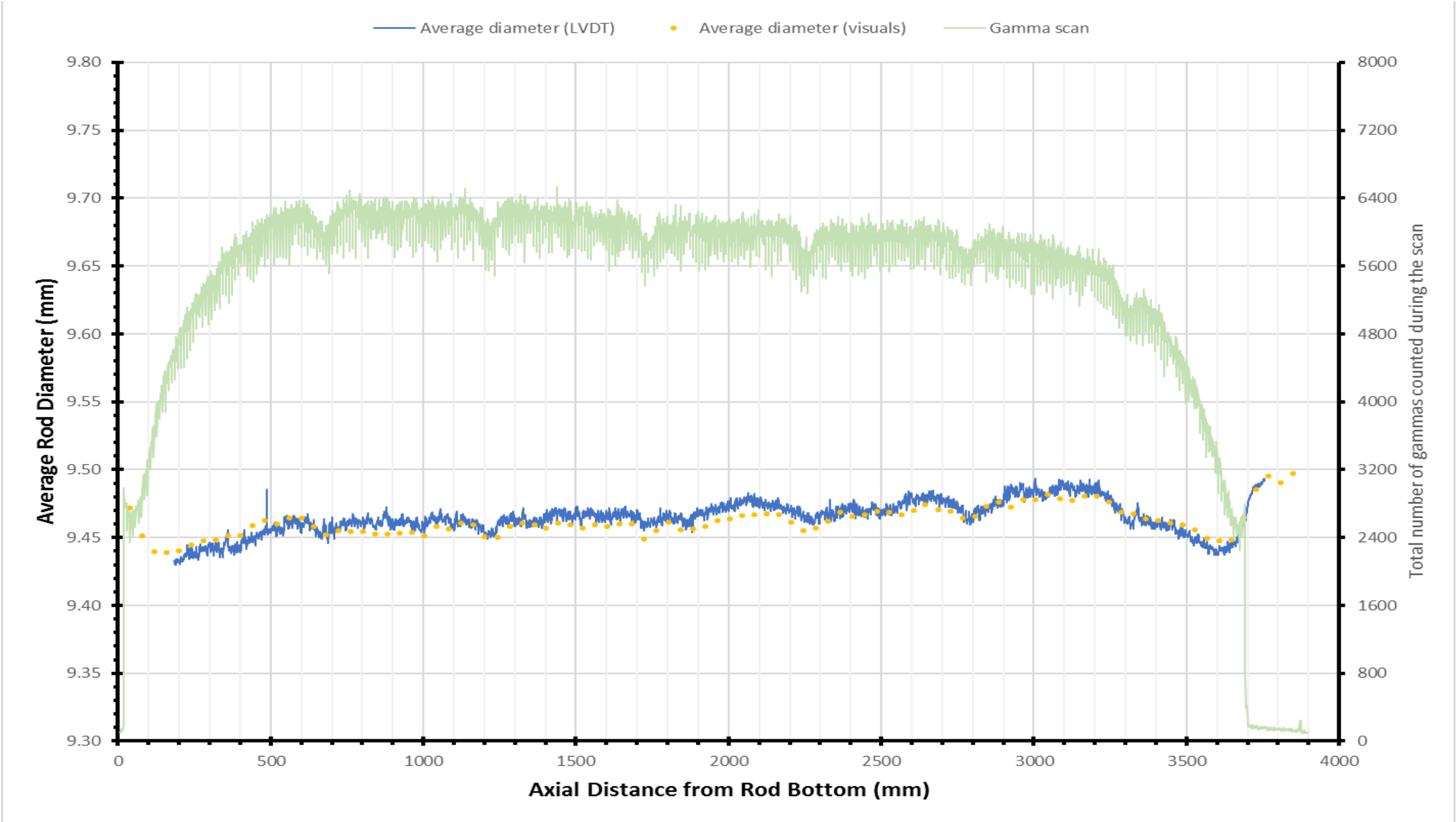


Figure B.16. Rod 6U3M09 LVDT Profilometry, Visual Profilometry, and Gamma Scan Data.

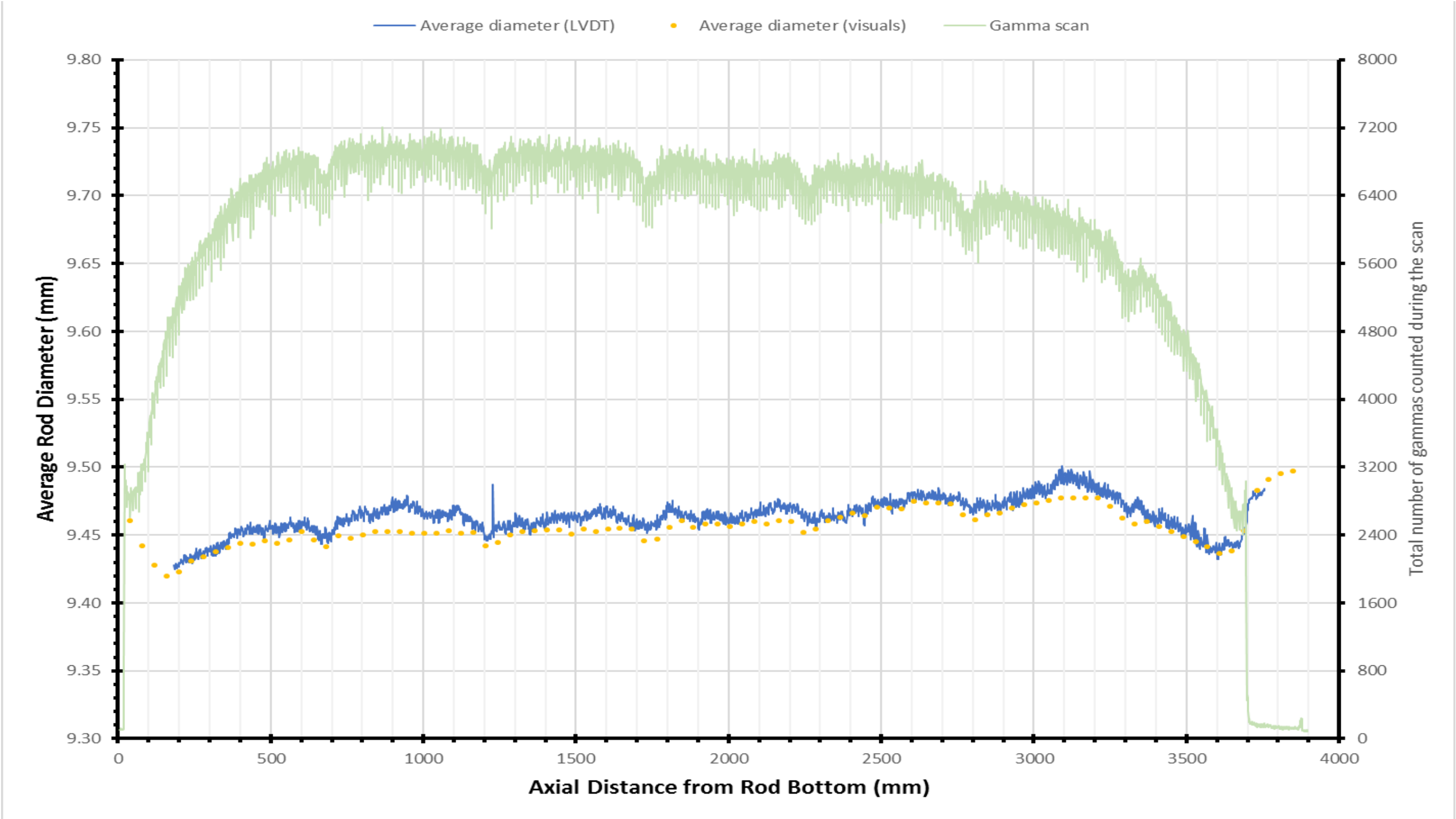


Figure B.17. Rod 6U3O05 LVDT Profilometry, Visual Profilometry, and Gamma Scan Data.

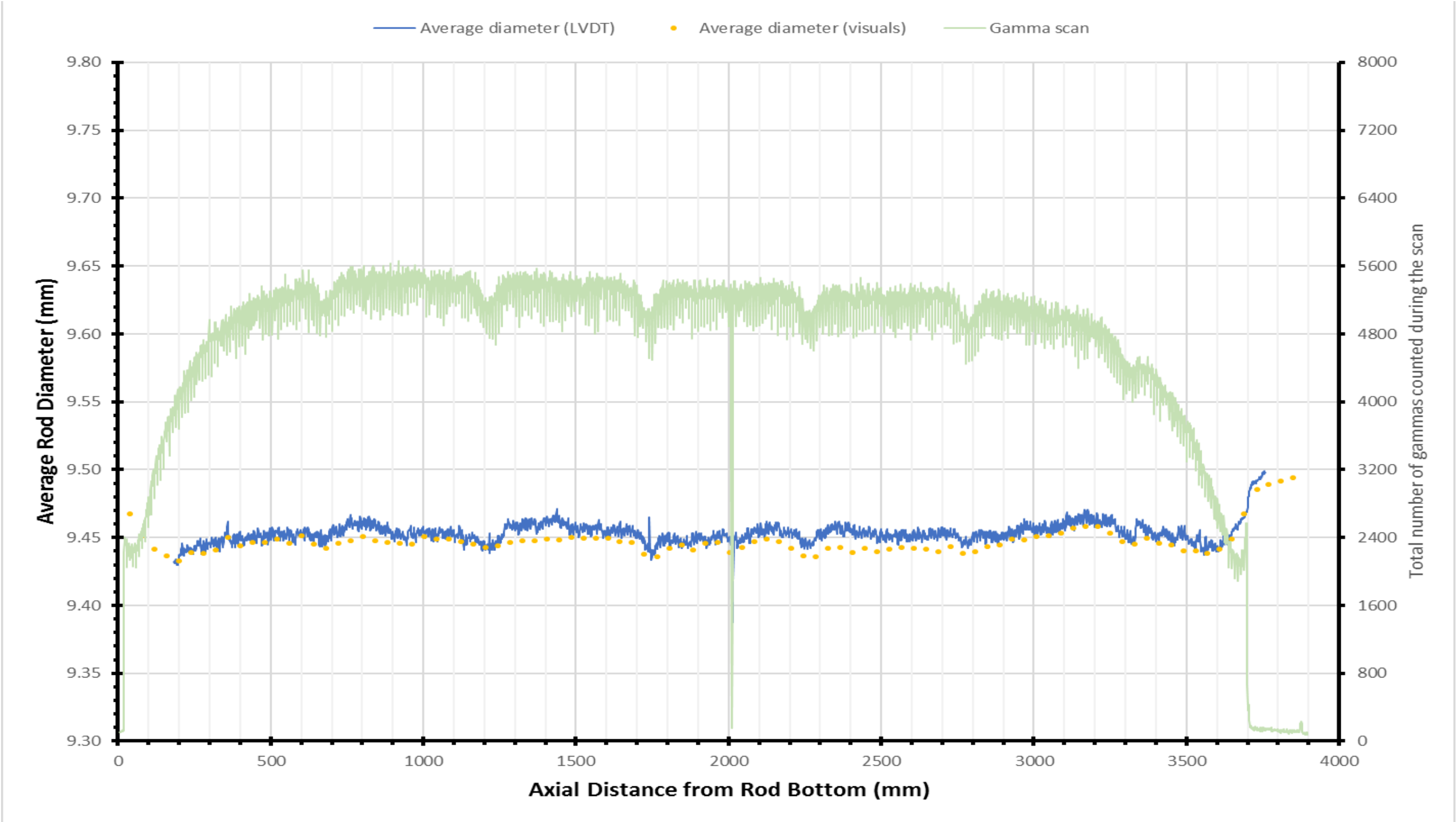


Figure B.18. Rod 6U3P16 LVDT Profilometry, Visual Profilometry, and Gamma Scan Data.

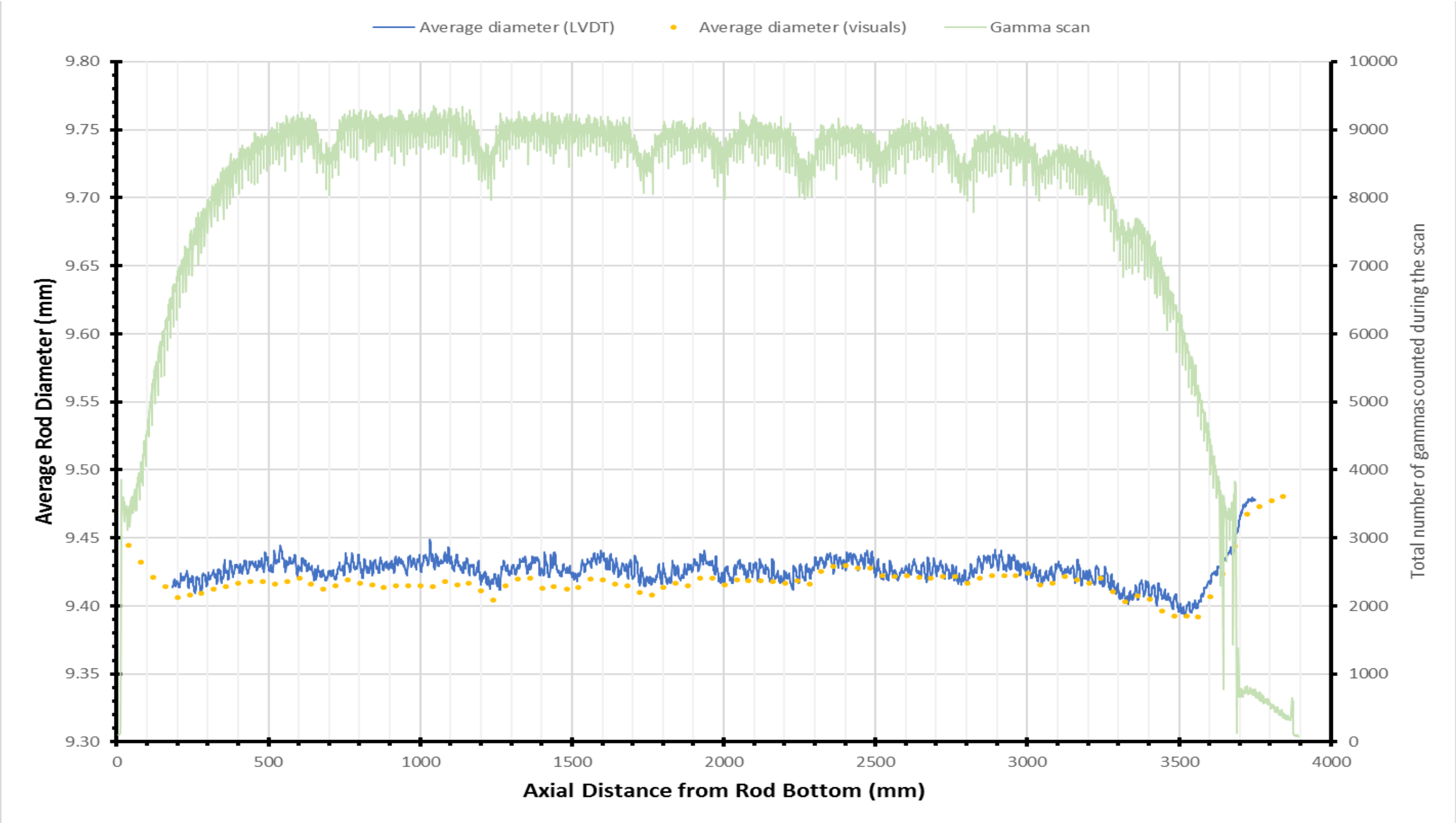


Figure B.19. Rod 30AD05 LVDT Profilometry, Visual Profilometry, and Gamma Scan Data.

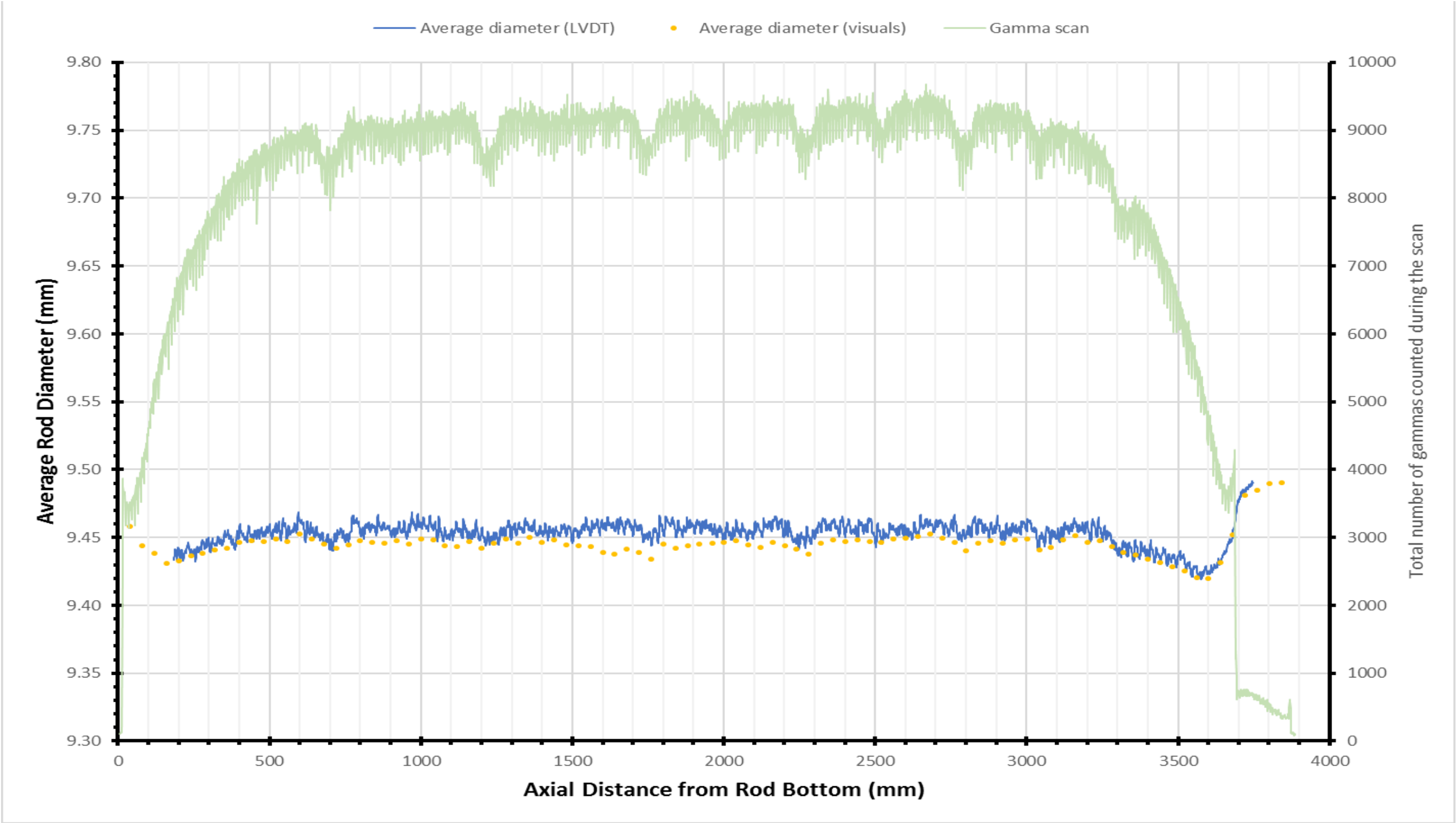


Figure B.20. Rod 30AE14 LVDT Profilometry, Visual Profilometry, and Gamma Scan Data.

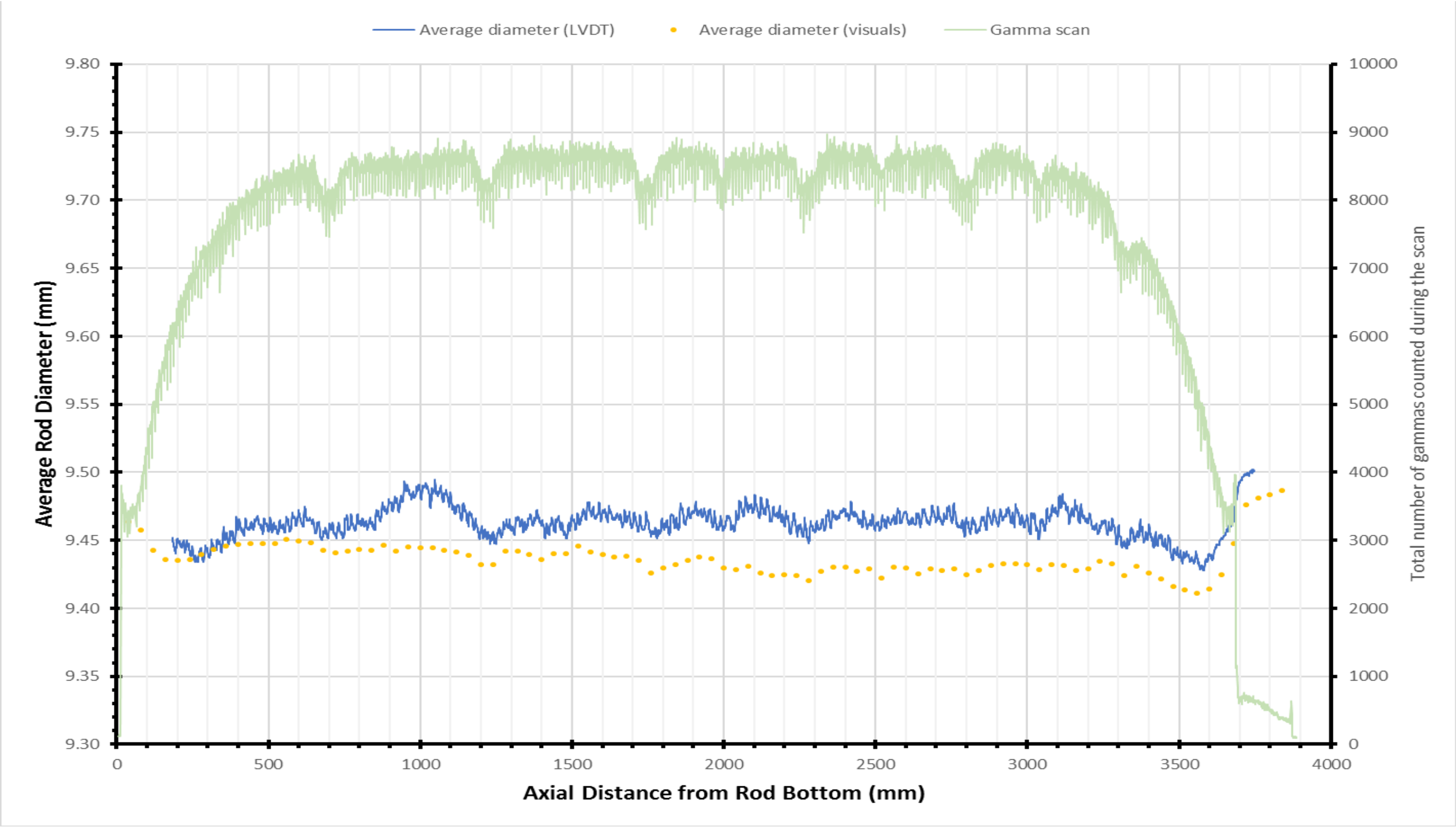


Figure B.21. Rod 30AG09 LVDT Profilometry, Visual Profilometry, and Gamma Scan Data.

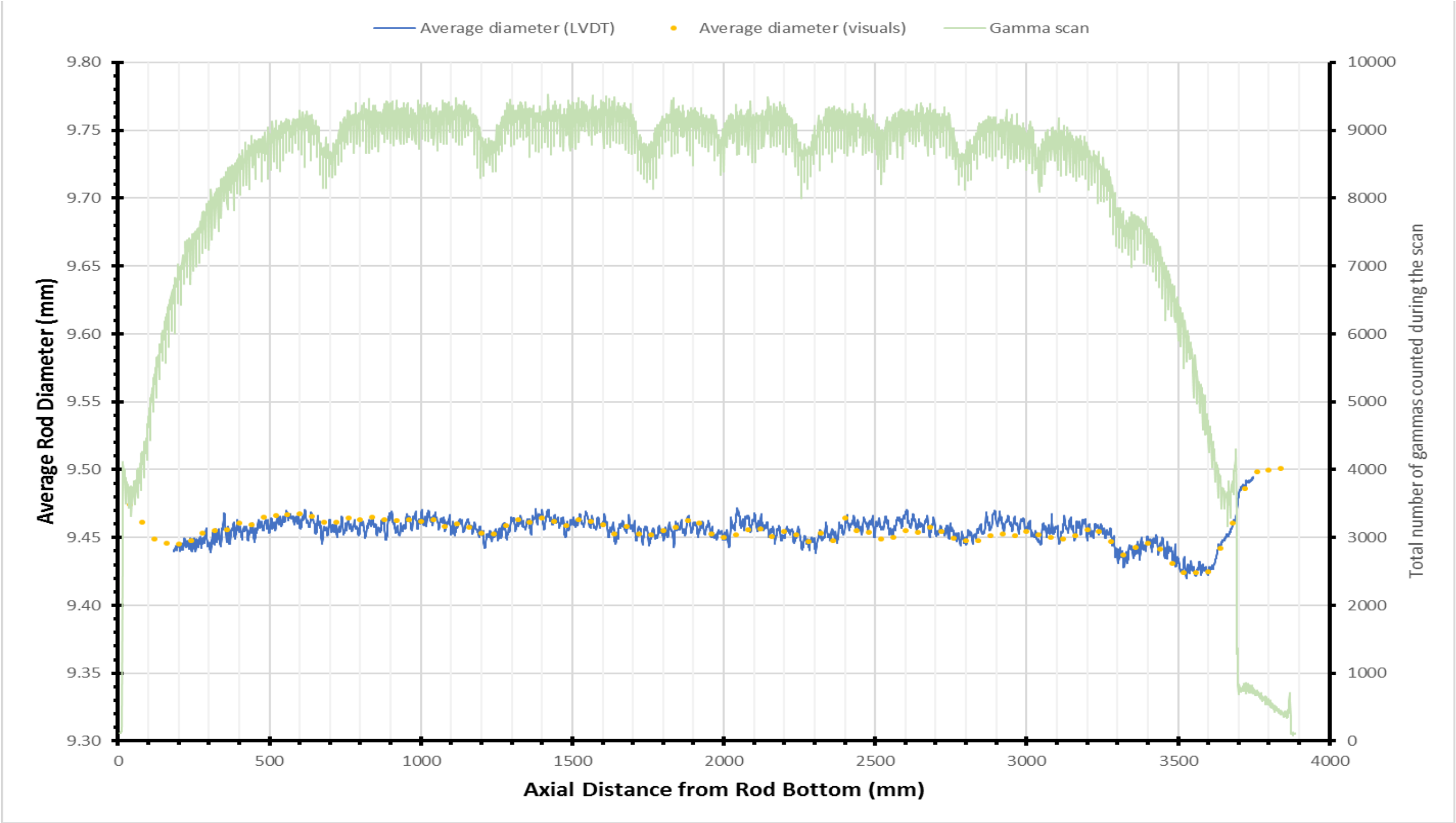


Figure B.22. Rod 30AK09 LVDT Profilometry, Visual Profilometry, and Gamma Scan Data.

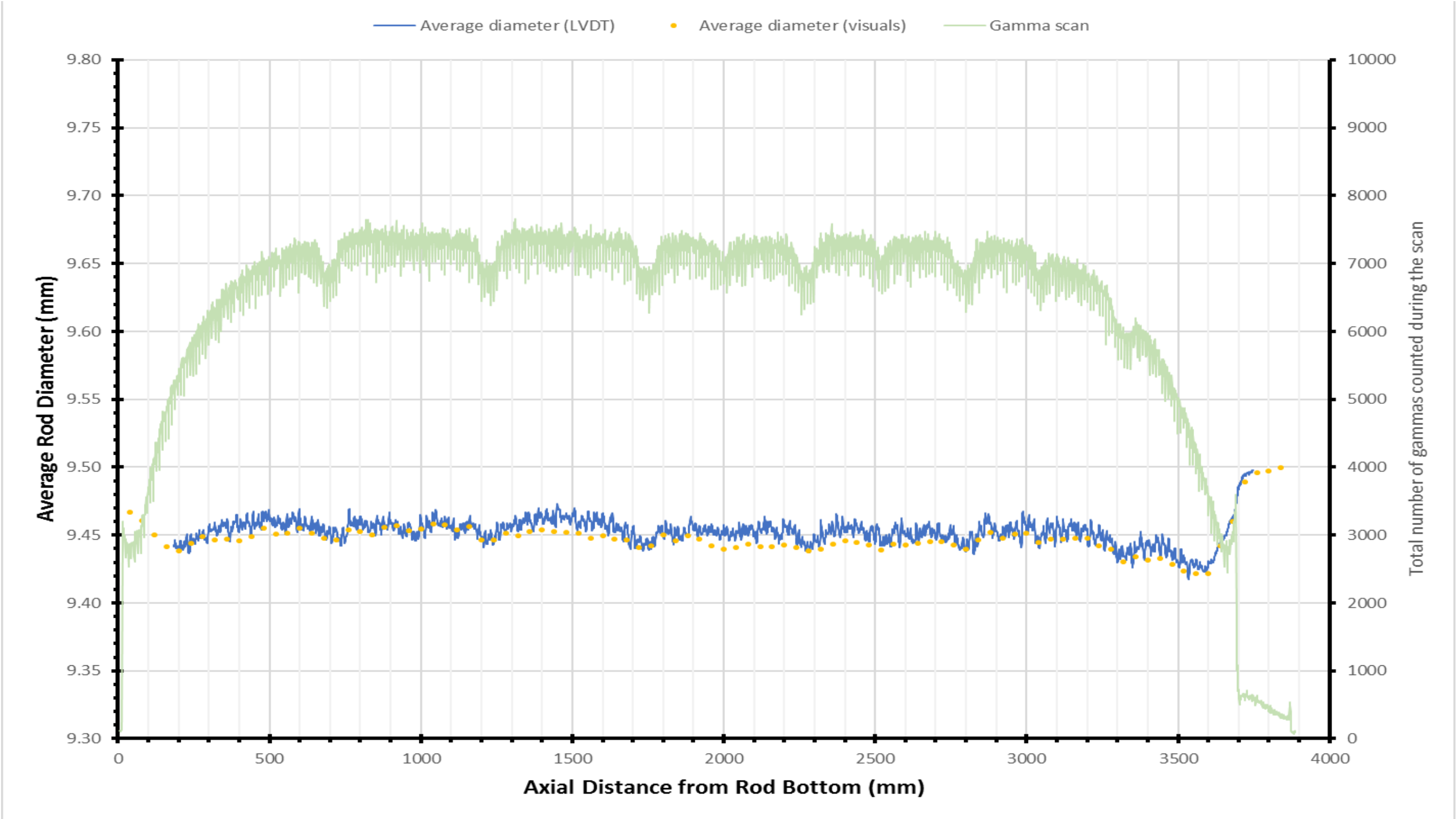


Figure B.23. Rod 30AP02 LVDT Profilometry, Visual Profilometry, and Gamma Scan Data.

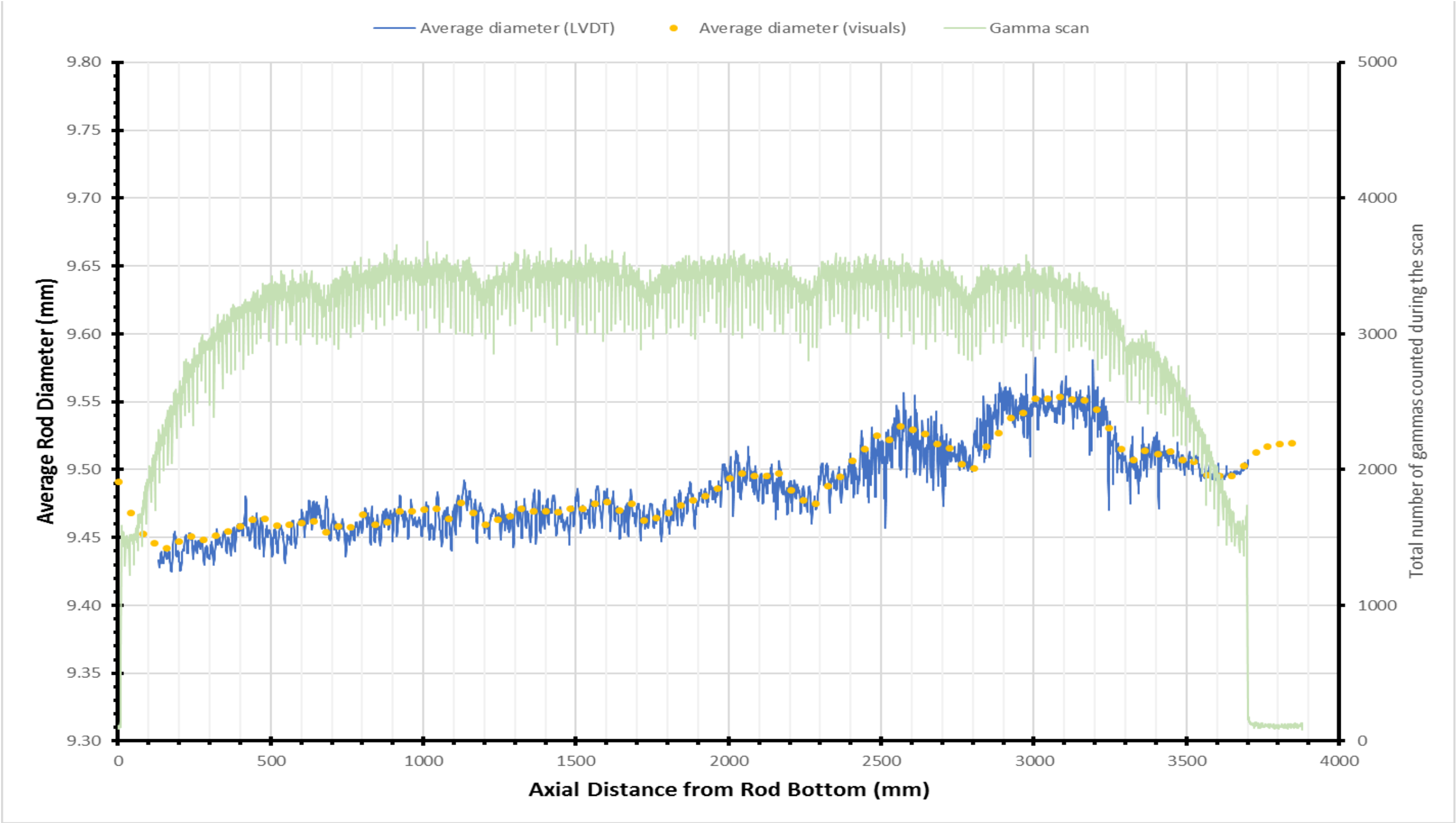


Figure B.24. Rod F35K13 LVDT Profilometry, Visual Profilometry, and Gamma Scan Data.

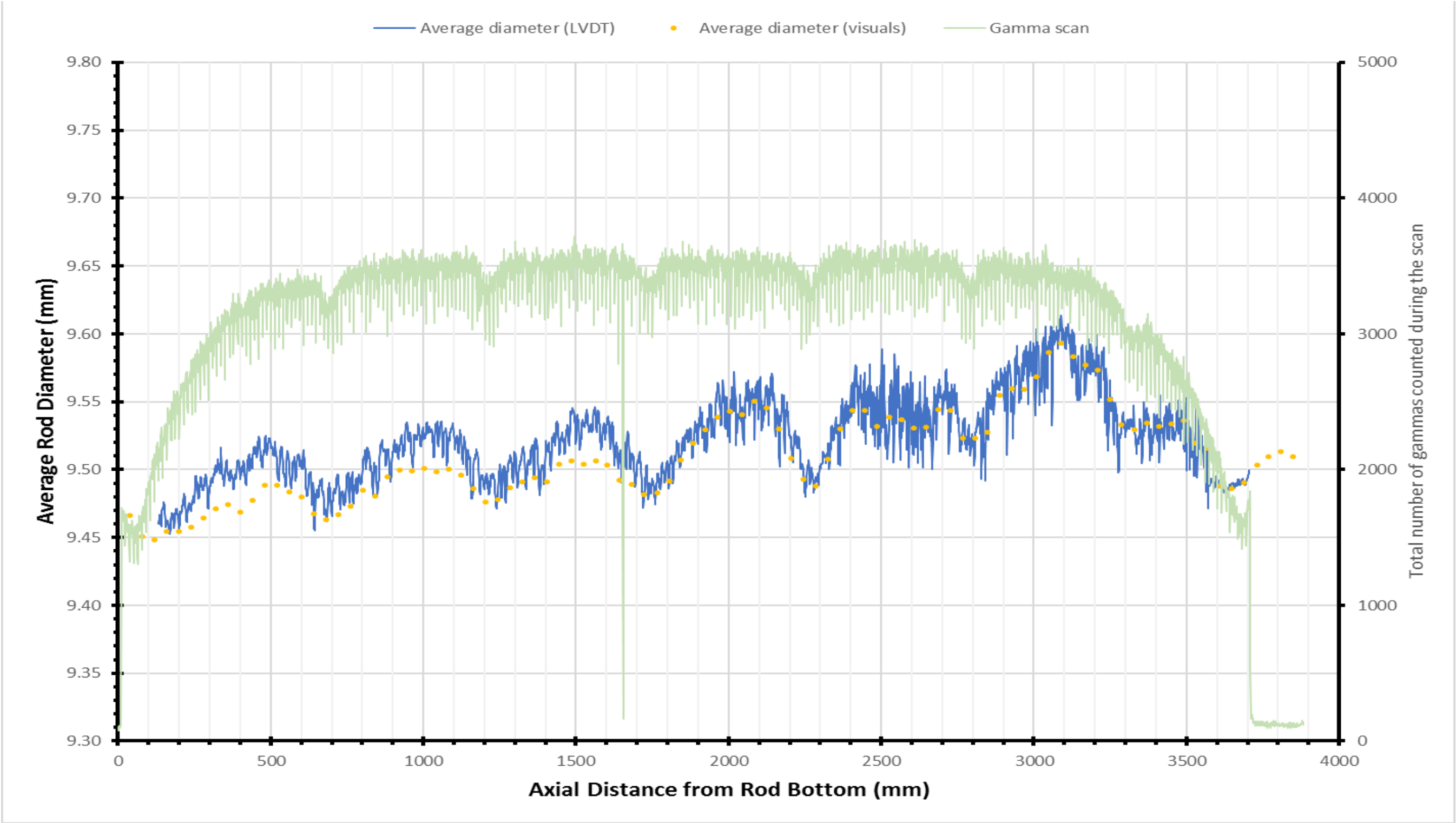


Figure B.25. Rod F35P17 LVDT Profilometry, Visual Profilometry, and Gamma Scan Data.

Appendix C

Traces for Four Quadrant Lift-Off Measurements and Rotational Lift-Off Scans

As each sister rod was scanned for the first time, an arbitrarily selected 0° orientation was marked and in later eddy current exams this 0° orientation was maintained. However, this was not tracked in other NDE and the rod's angular orientation cannot be referenced back to other NDE. Additionally, it is not known what the orientation was in reactor, so there is no information that can be related back to an operational azimuthal location in reactor, although it is possible to orient the rod generally to the spacer grid using visible fretting marks and axial rod removal/insertion scratches on the sister rods.

Figure C.1 through Figure C.25 show the individual lift-off traces for all 25 sister rods. They consist of four sets of lift-off measurements with each of the four measurements ~90° apart.

Additionally, many rotational scans were completed to investigate possible variations in oxide/CRUD thickness around the rod circumference due to expected rod burnup or temperature variations in reactor, or due to some feature (e.g., spalling, GTRF) observed in other NDEs. Plots of these lift-off measurements are provided in Figure C.26 through Figure C.63.

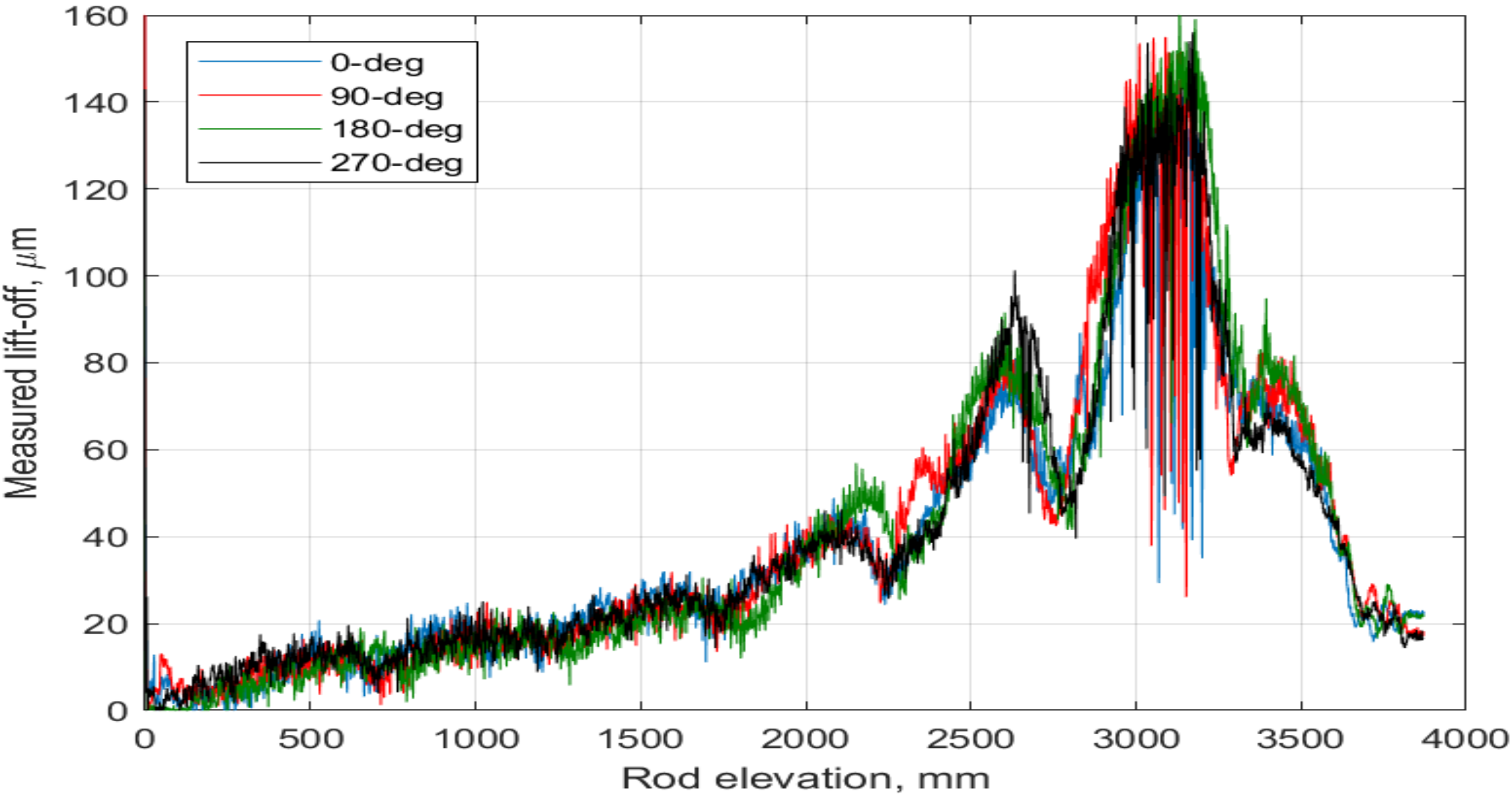


Figure C.1. Lift-Off Measured in All Four Quadrants, Sister Rod 3A1B16.

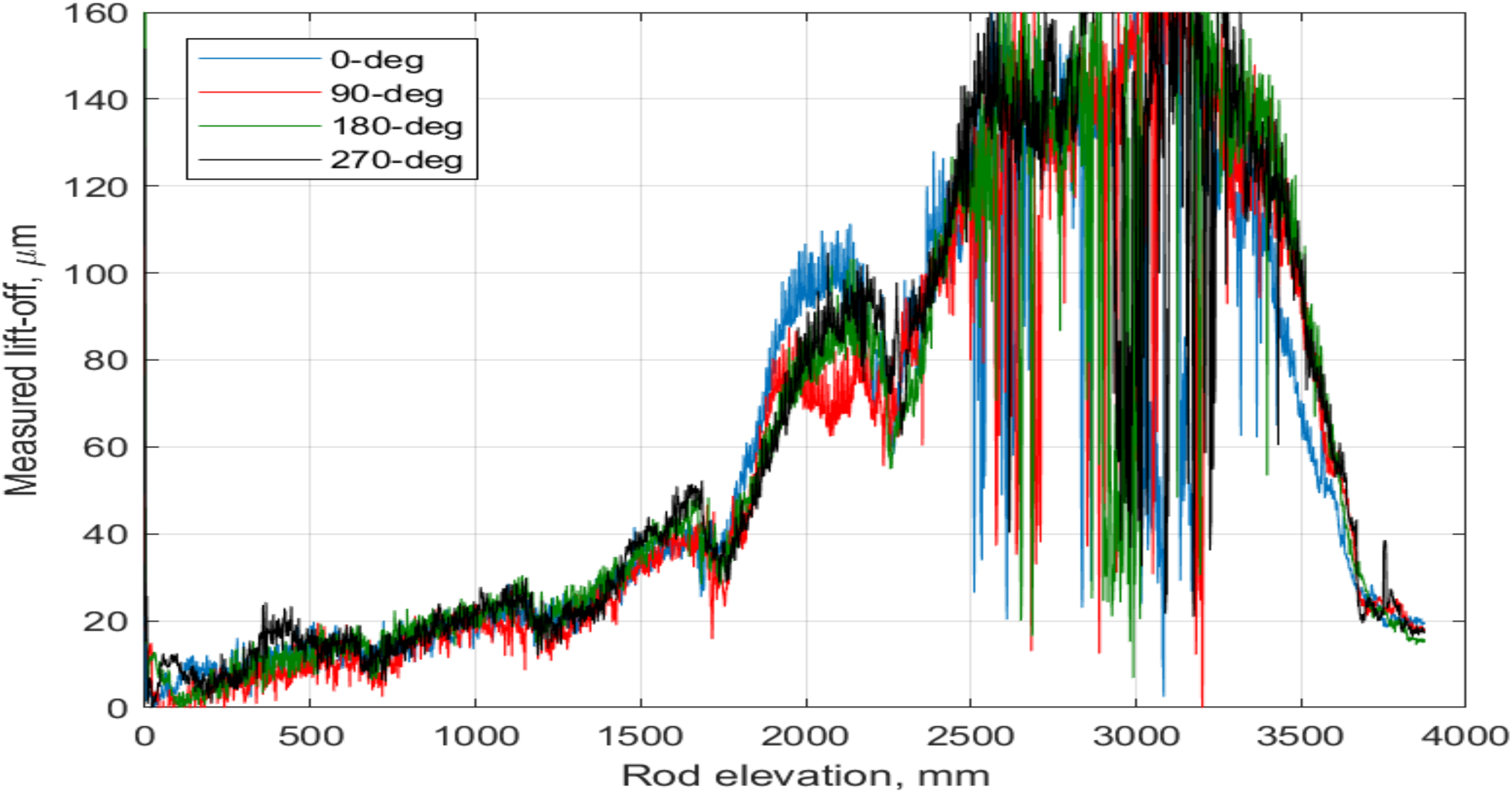


Figure C.2. Lift-Off Measured in All Four Quadrants, Sister Rod 3A1F05.

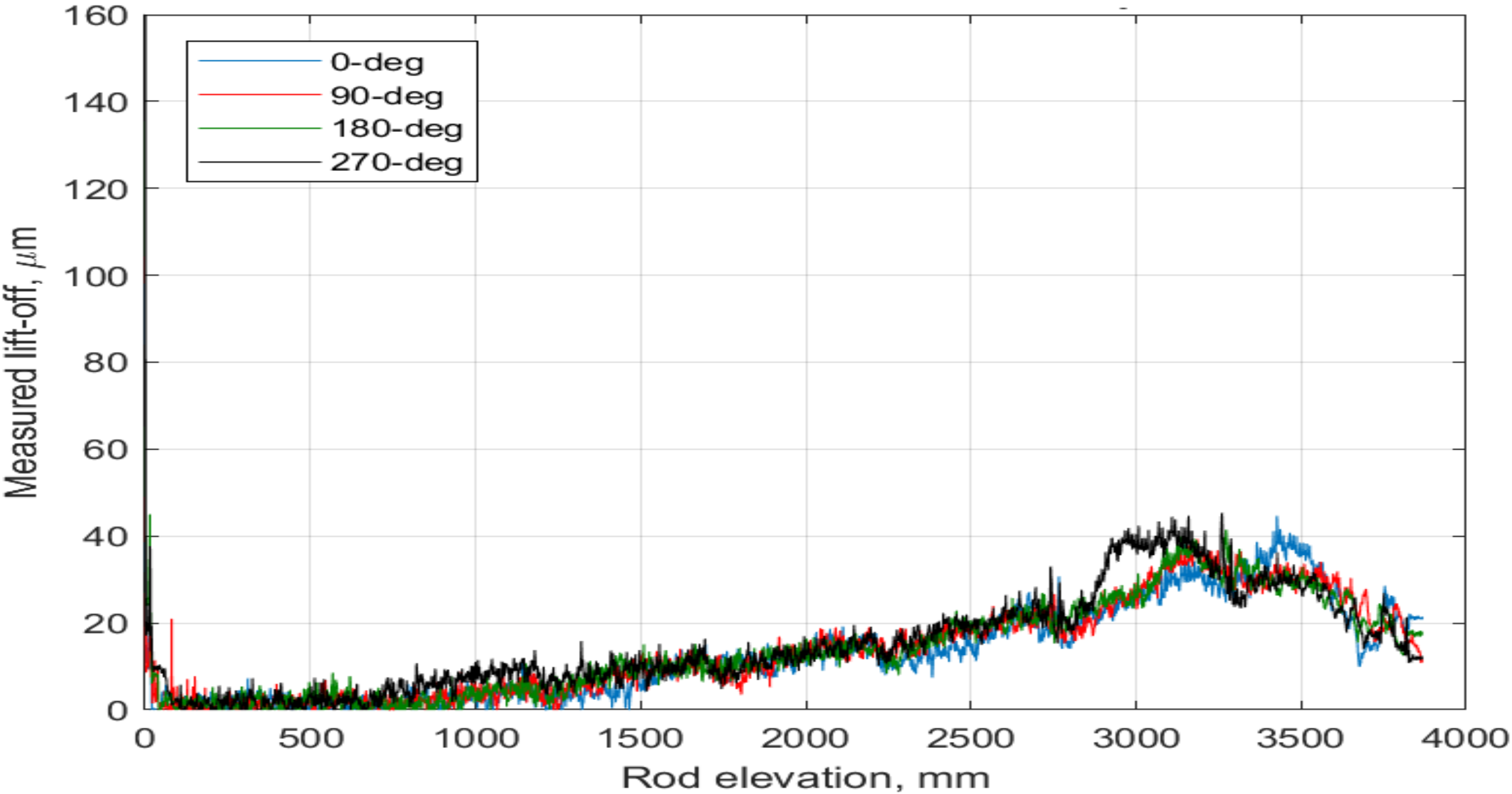


Figure C.3. Lift-Off Measured in All Four Quadrants, Sister Rod 3D8B02.

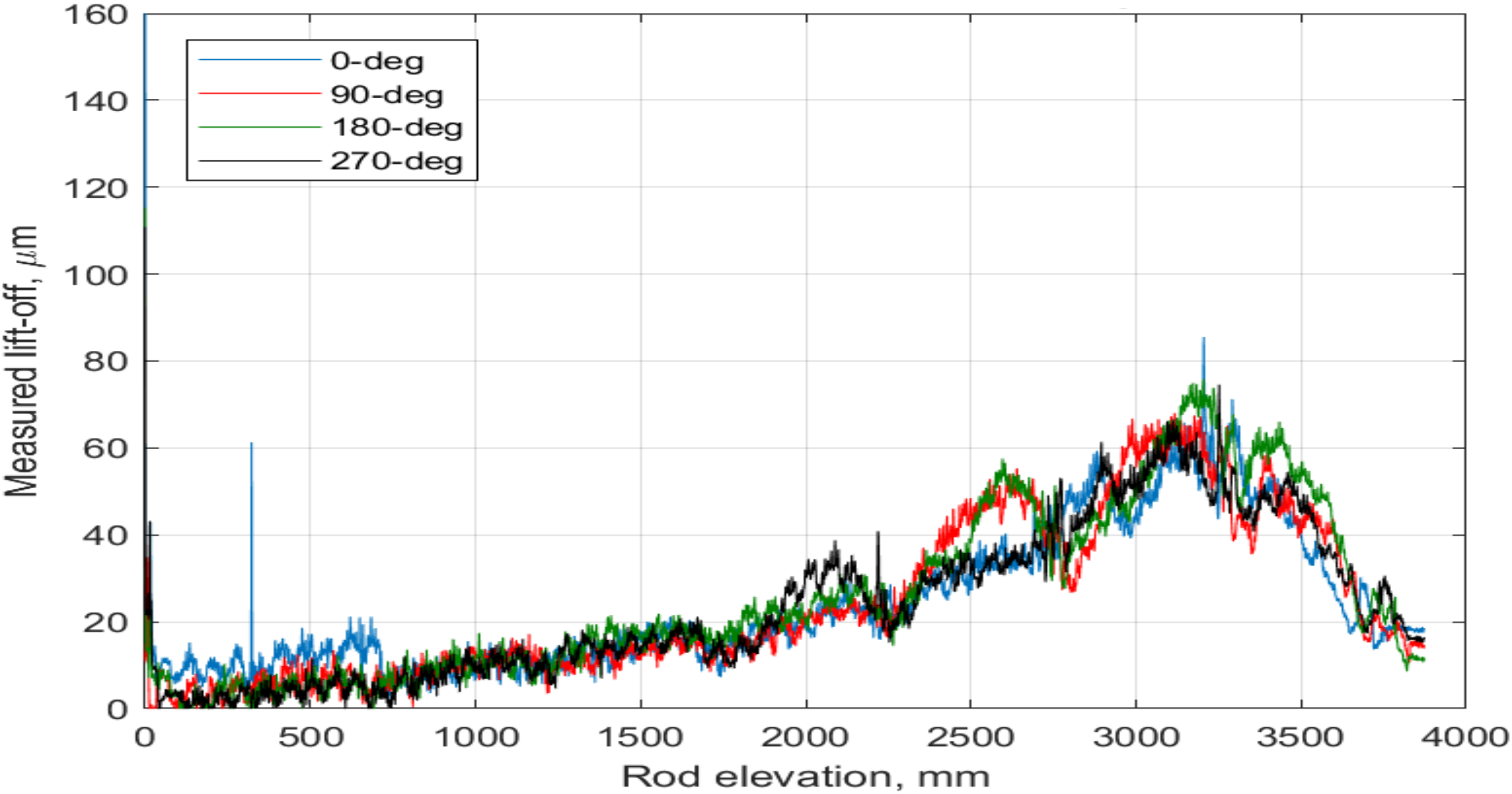


Figure C.4. Lift-Off Measured in All Four Quadrants, Sister Rod 3D8B14.

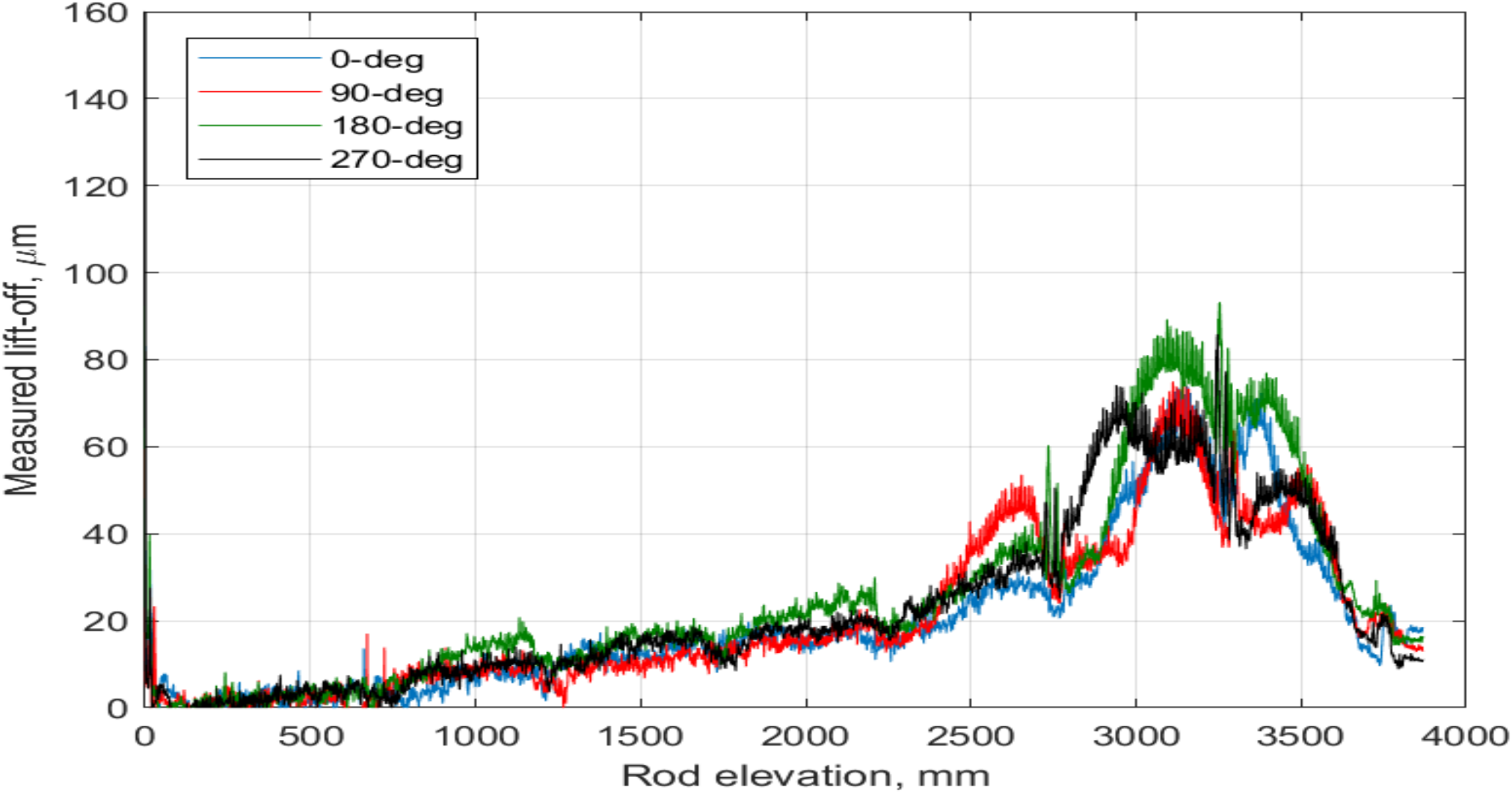


Figure C.5. Lift-Off Measured in All Four Quadrants, Sister Rod 3F9D07.

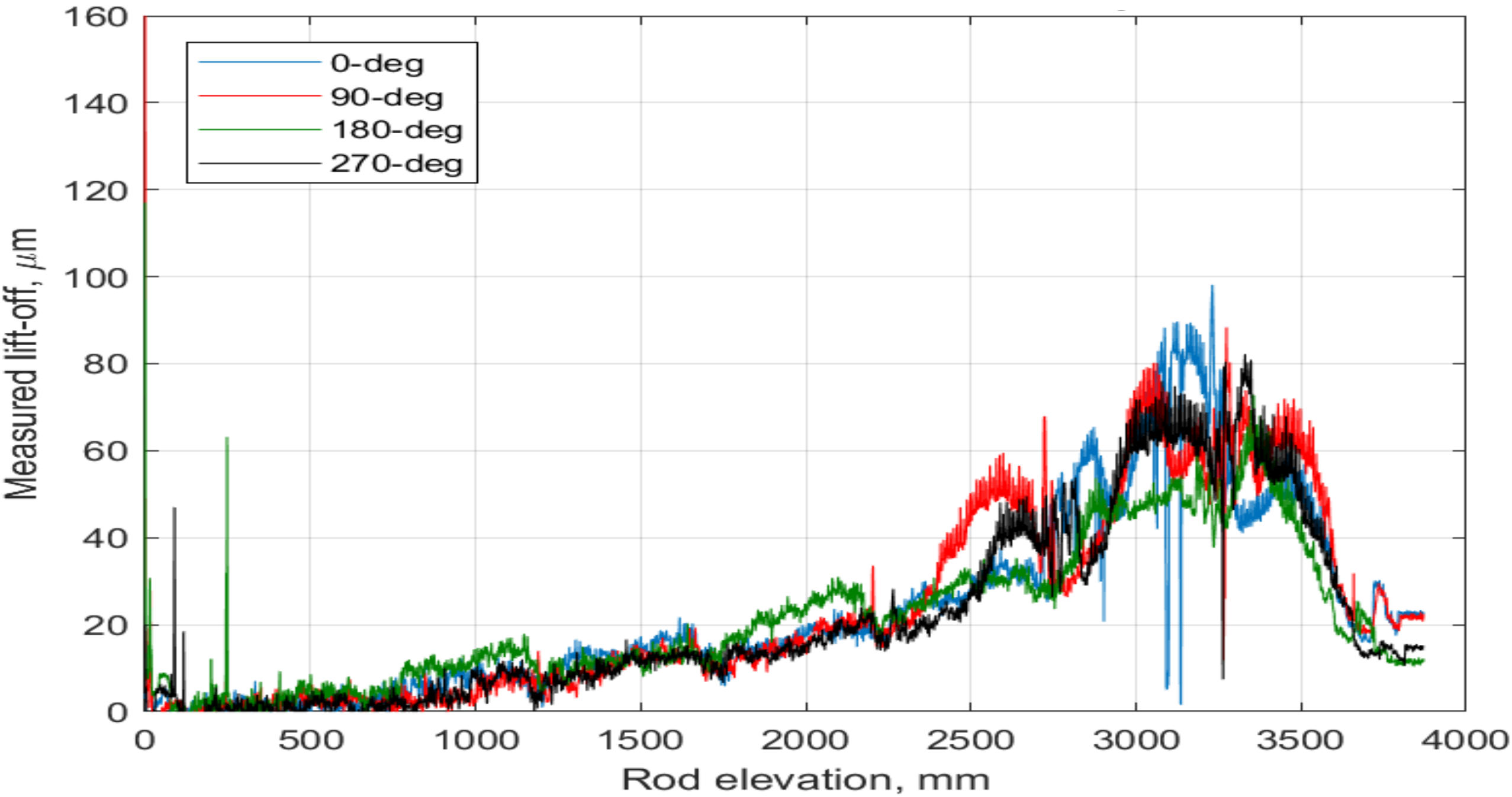


Figure C.6. Lift-Off Measured in All Four Quadrants, Sister Rod 3F9N05.

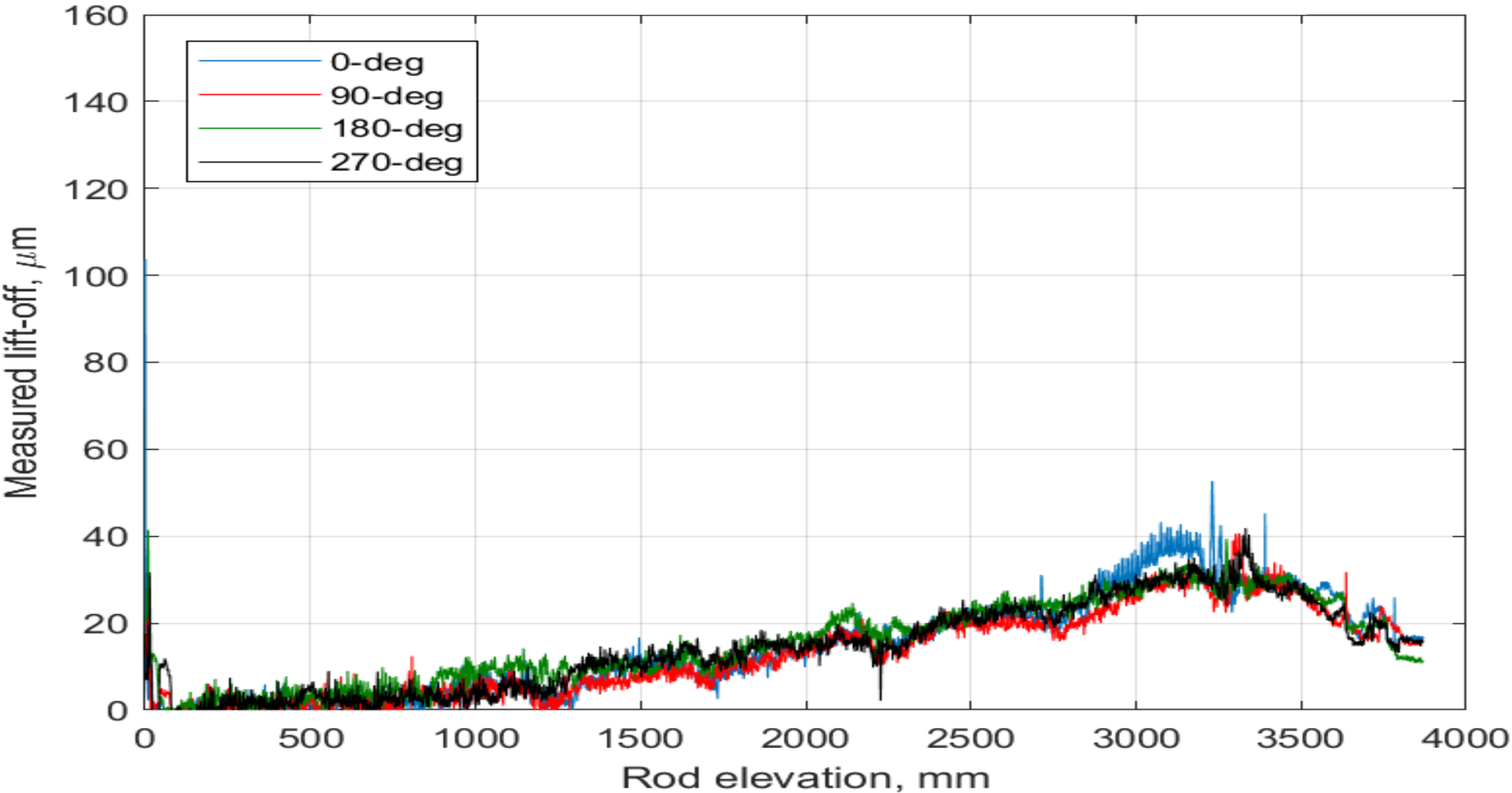


Figure C.7. Lift-Off Measured in All Four Quadrants, Sister Rod 3F9P02.

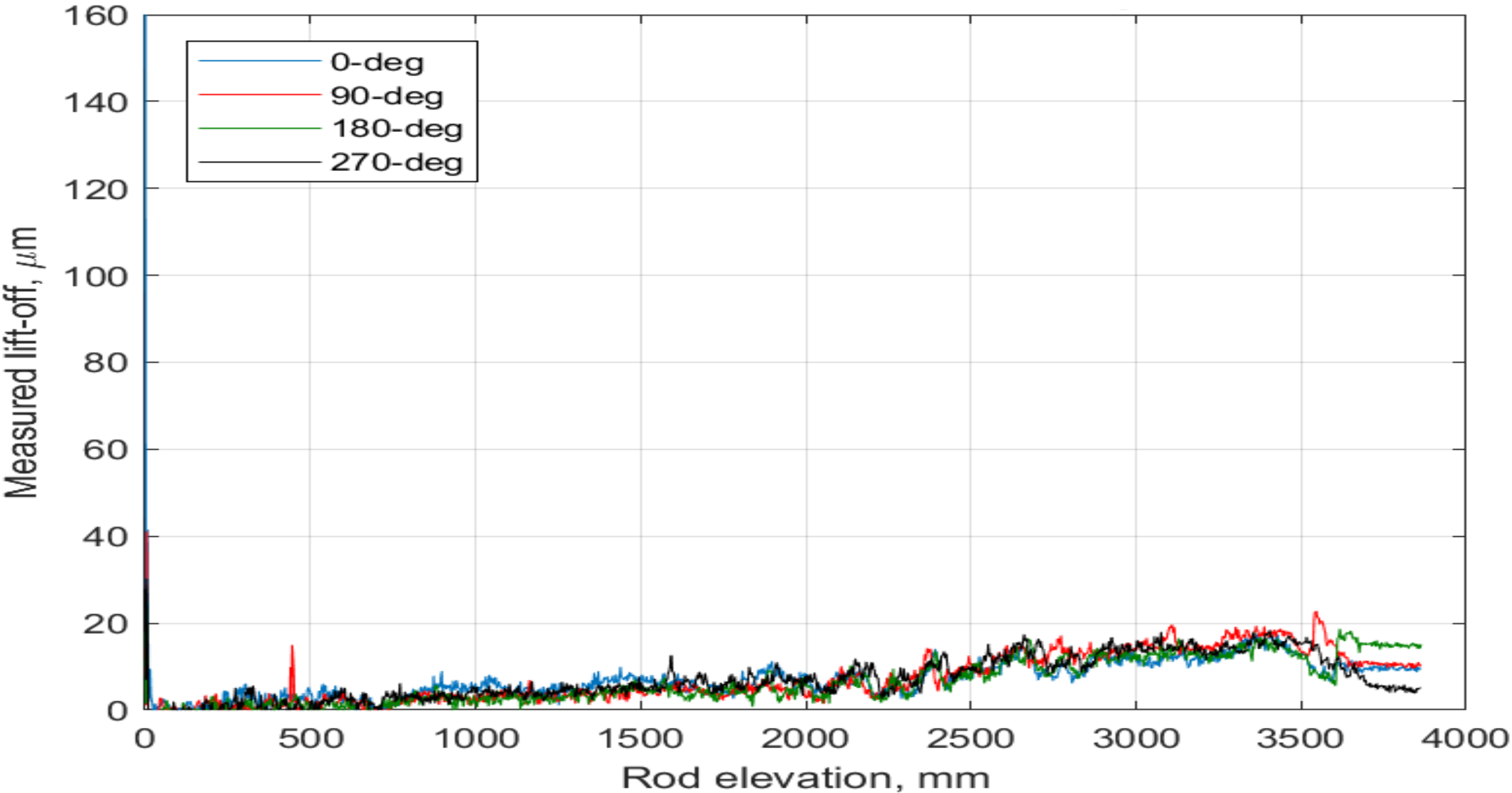


Figure C.8. Lift-Off Measured in All Four Quadrants, Sister Rod 5K7C05.

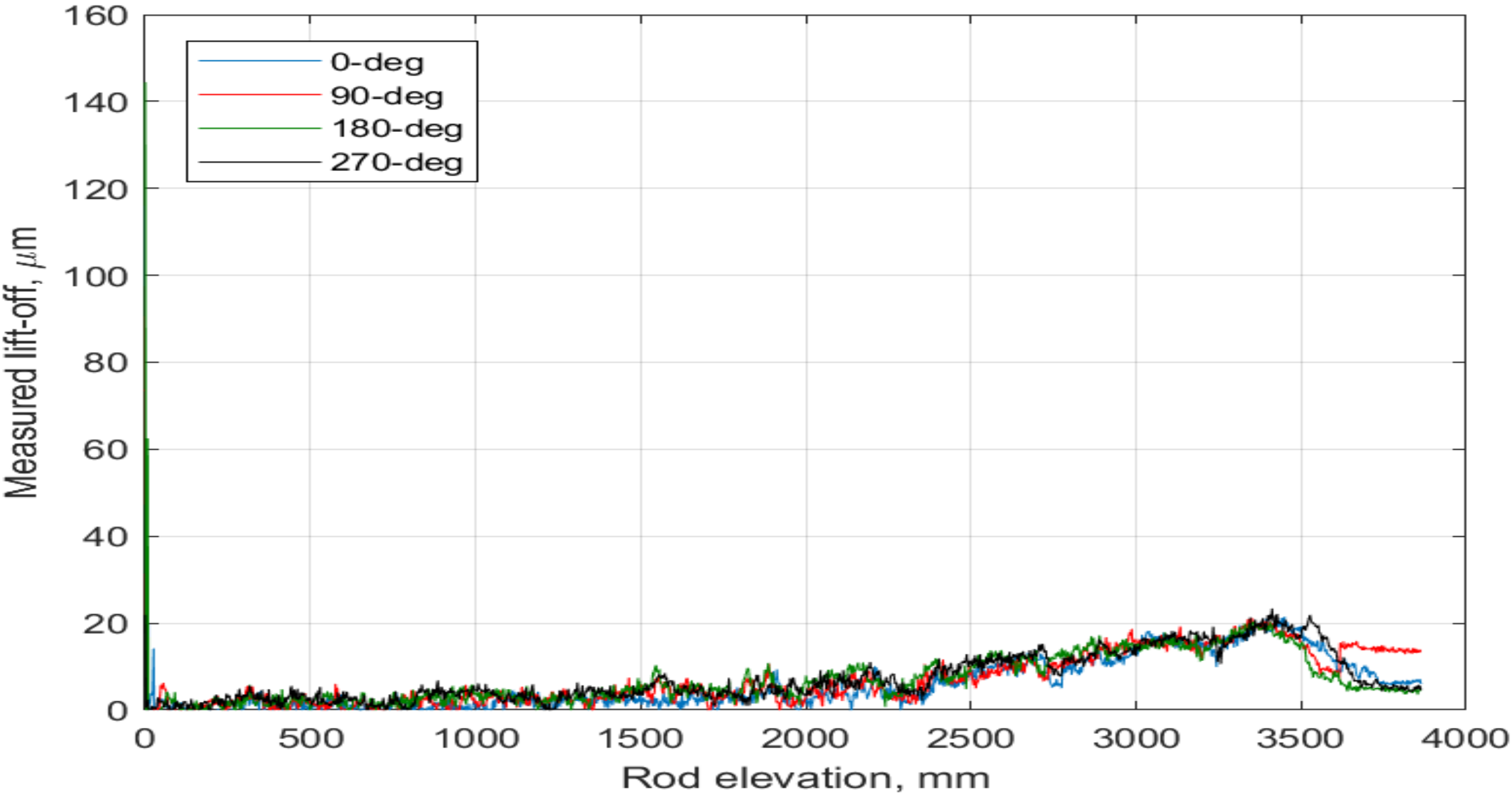


Figure C.9. Lift-Off Measured in All Four Quadrants, Sister Rod 5K7K09.

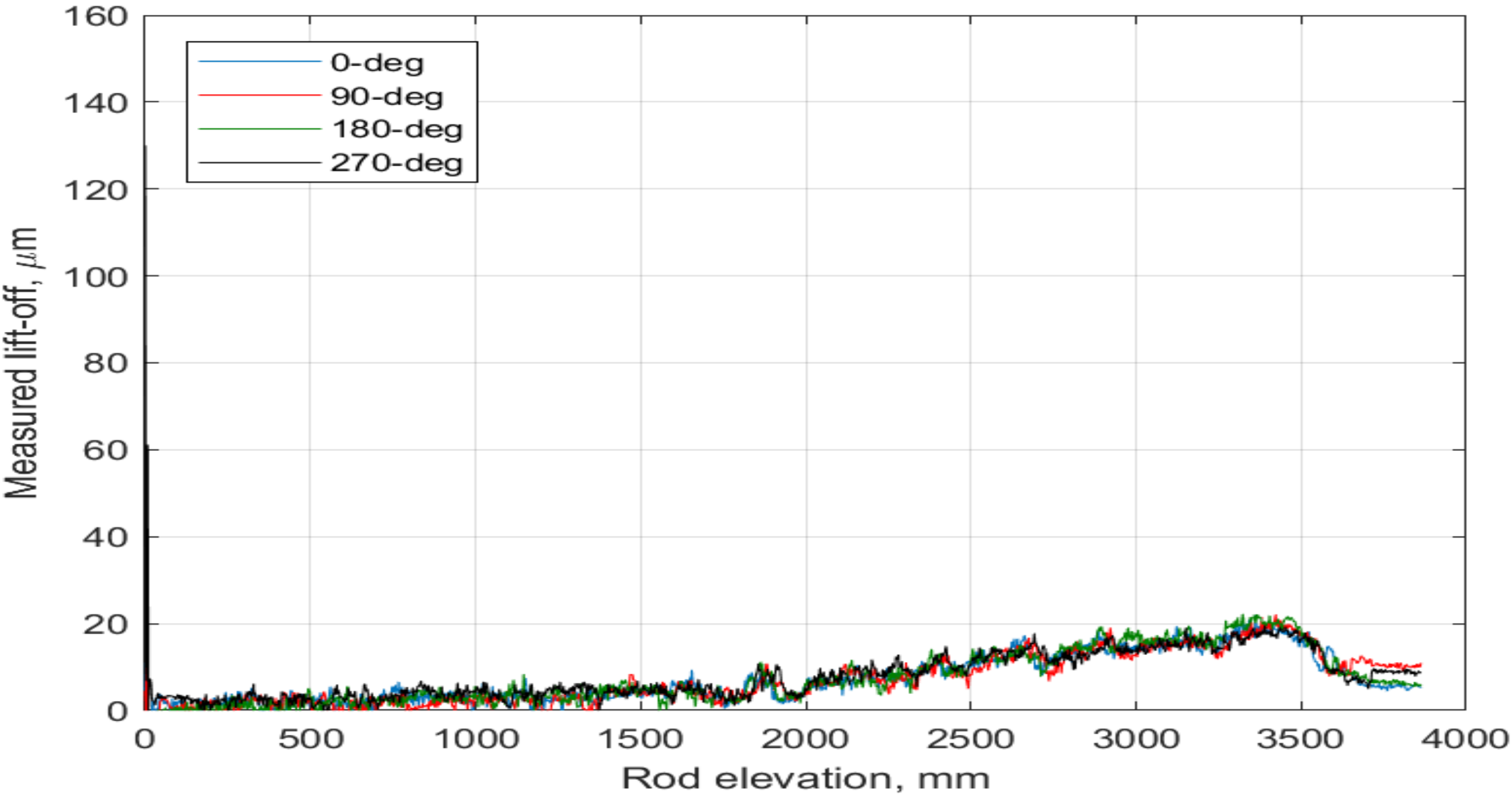


Figure C.10. Lift-Off Measured in All Four Quadrants, Sister Rod 5K7O14.

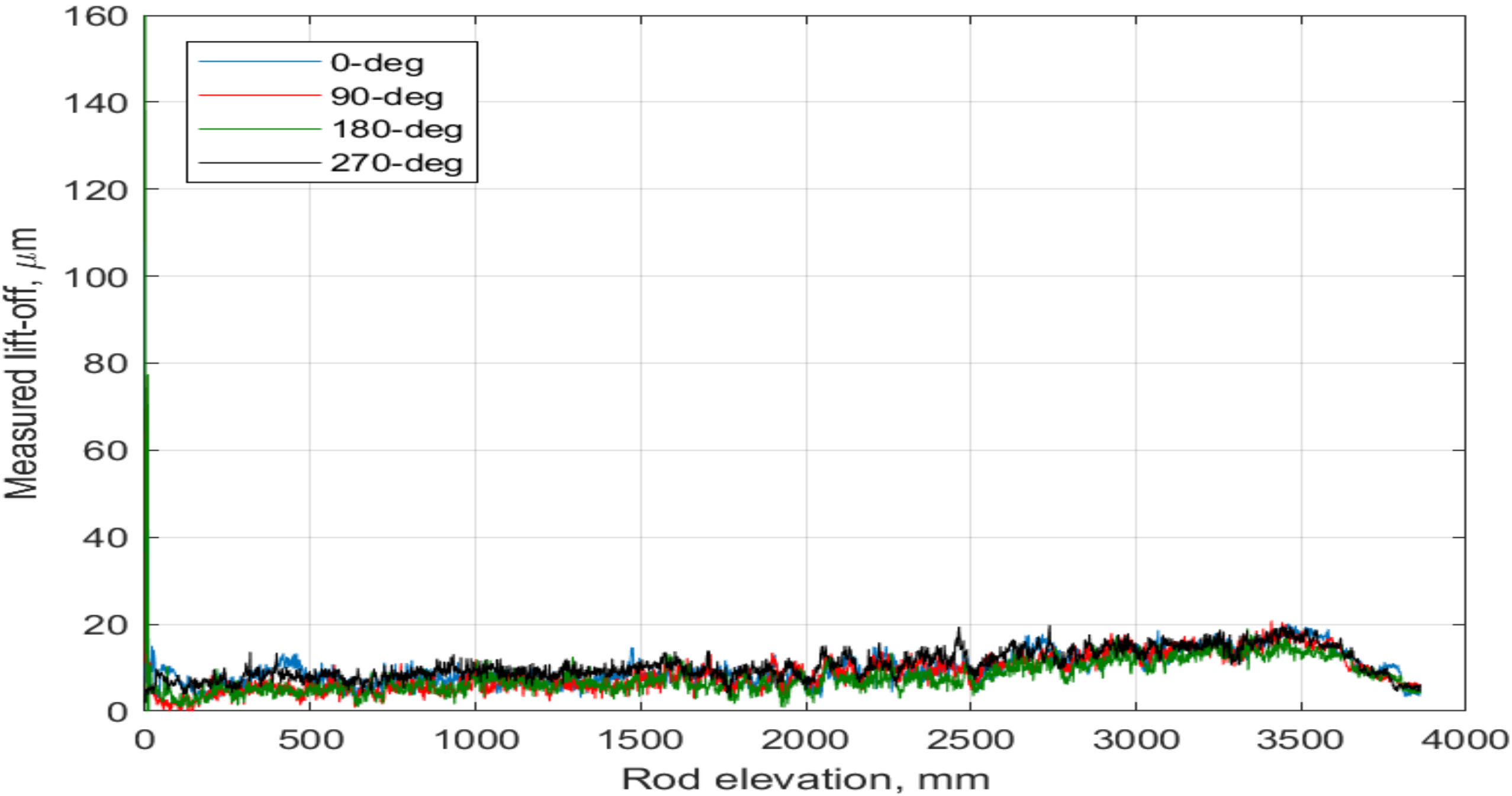


Figure C.11. Lift-Off Measured in All Four Quadrants, Sister Rod 5K7P02.

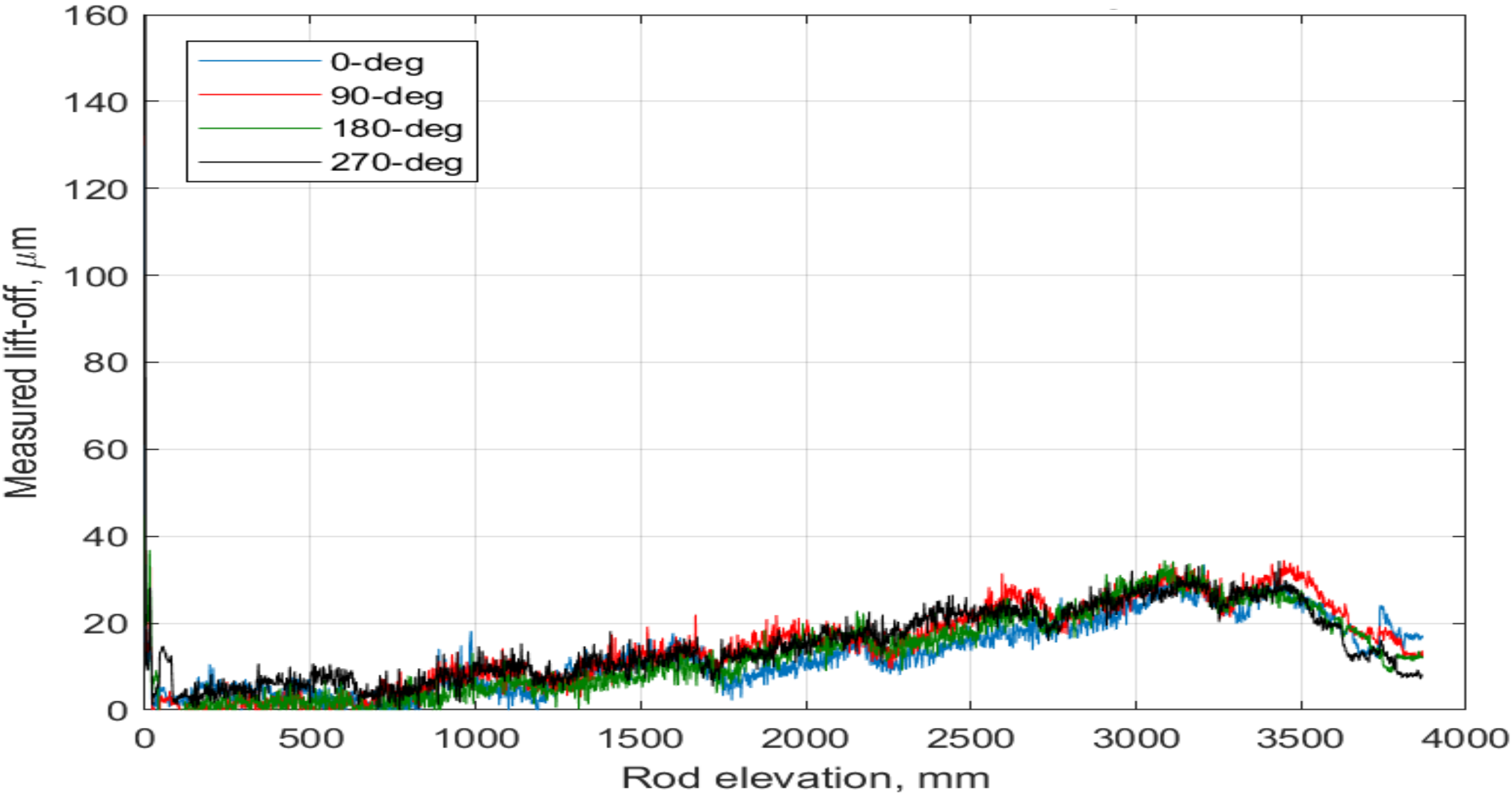


Figure C.12. Lift-Off Measured in All Four Quadrants, Sister Rod 6U3I07.

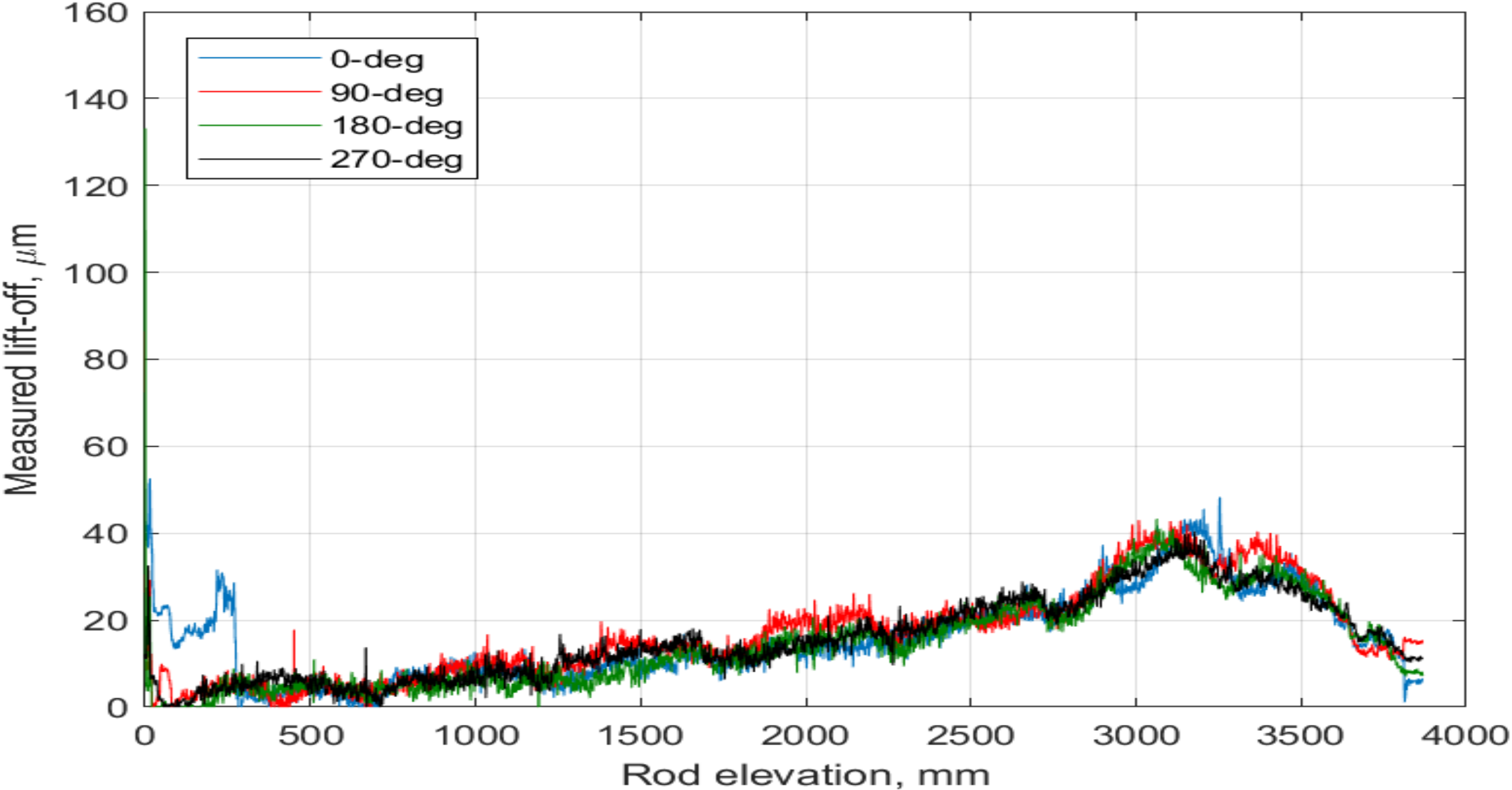


Figure C.13. Lift-Off Measured in All Four Quadrants, Sister Rod 6U3K09.

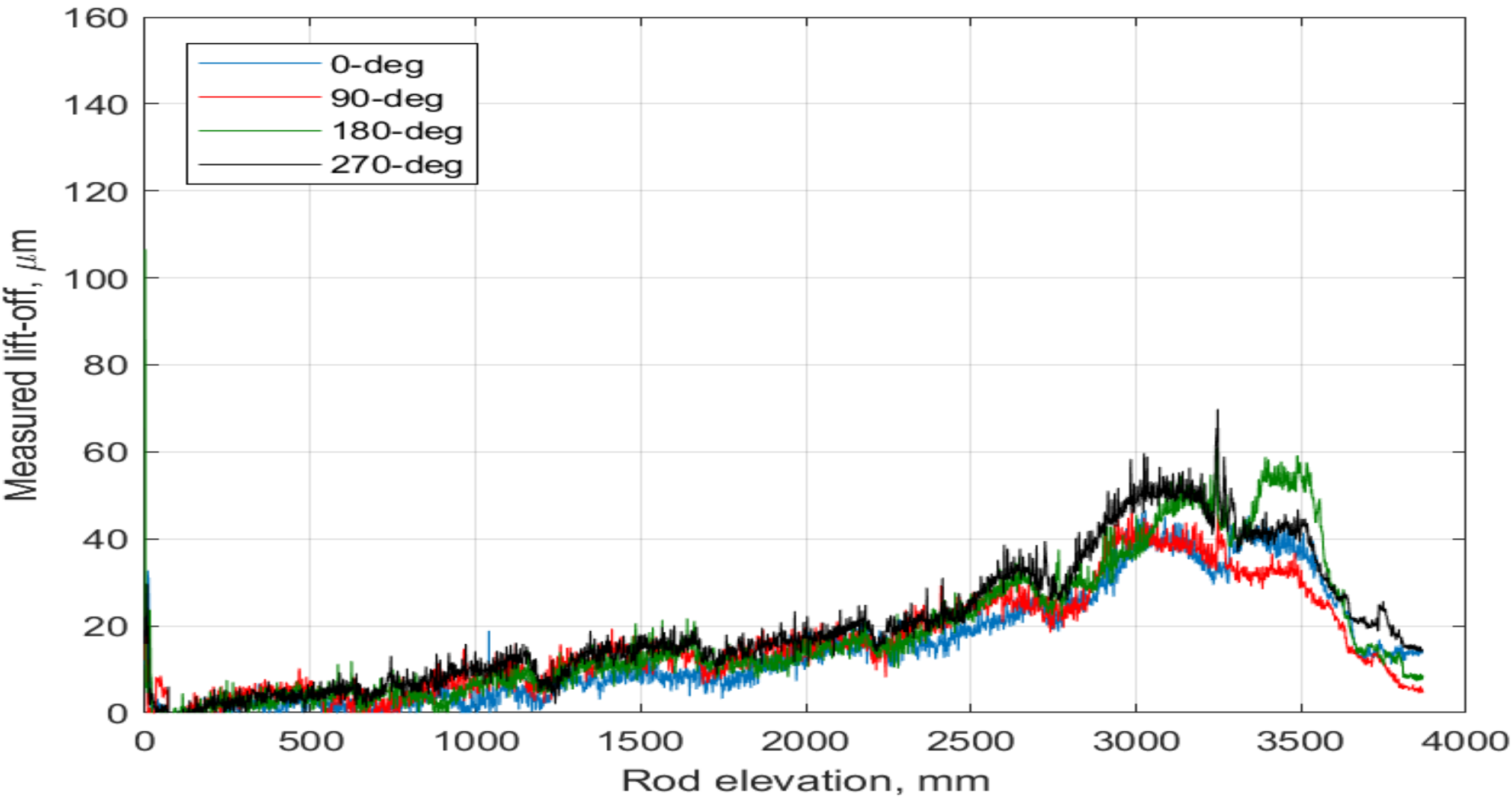


Figure C.14. Lift-Off Measured in All Four Quadrants, Sister Rod 6U3L08.

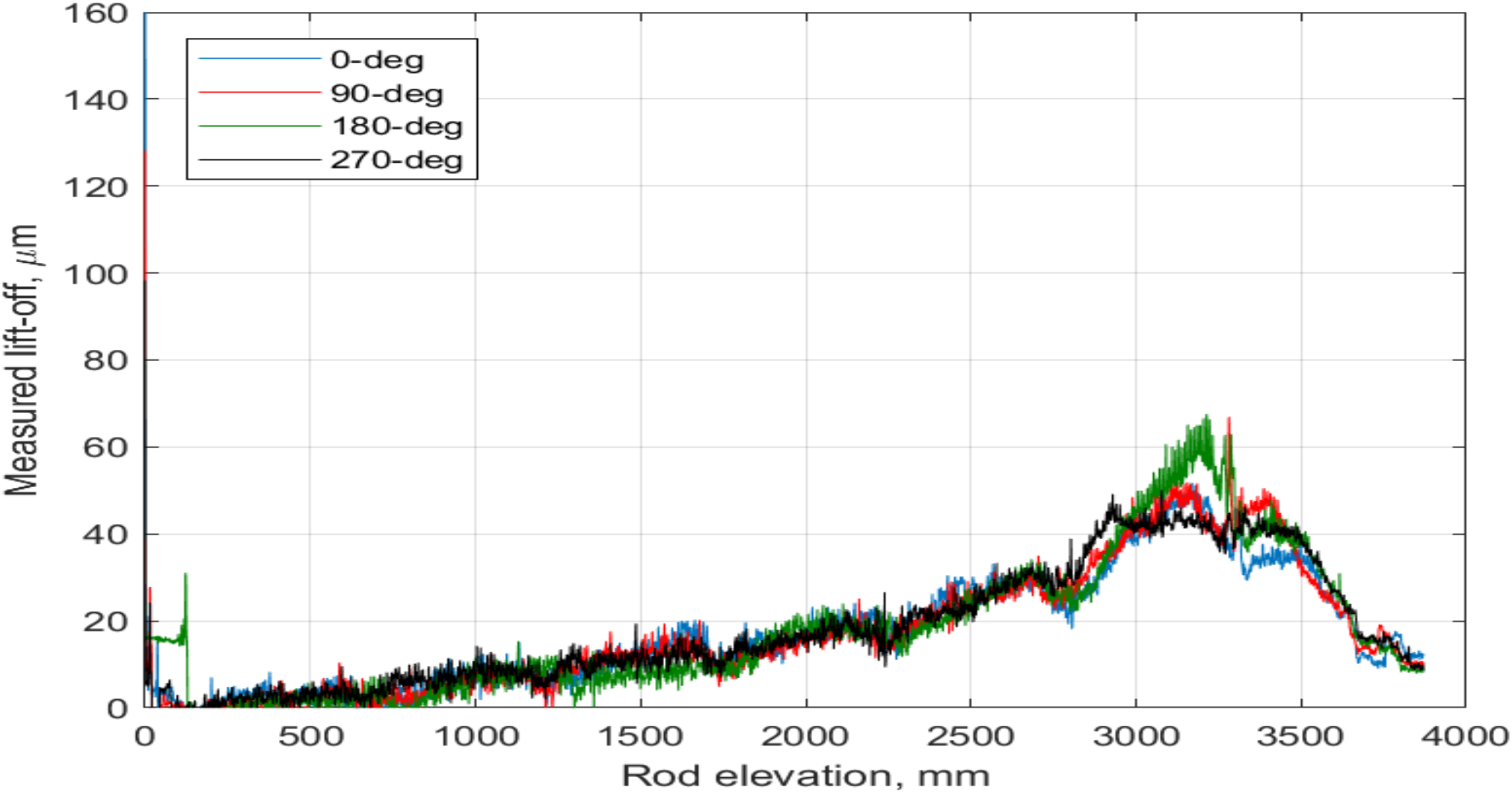


Figure C.15. Lift-Off Measured in All Four Quadrants, Sister Rod 6U3M03.

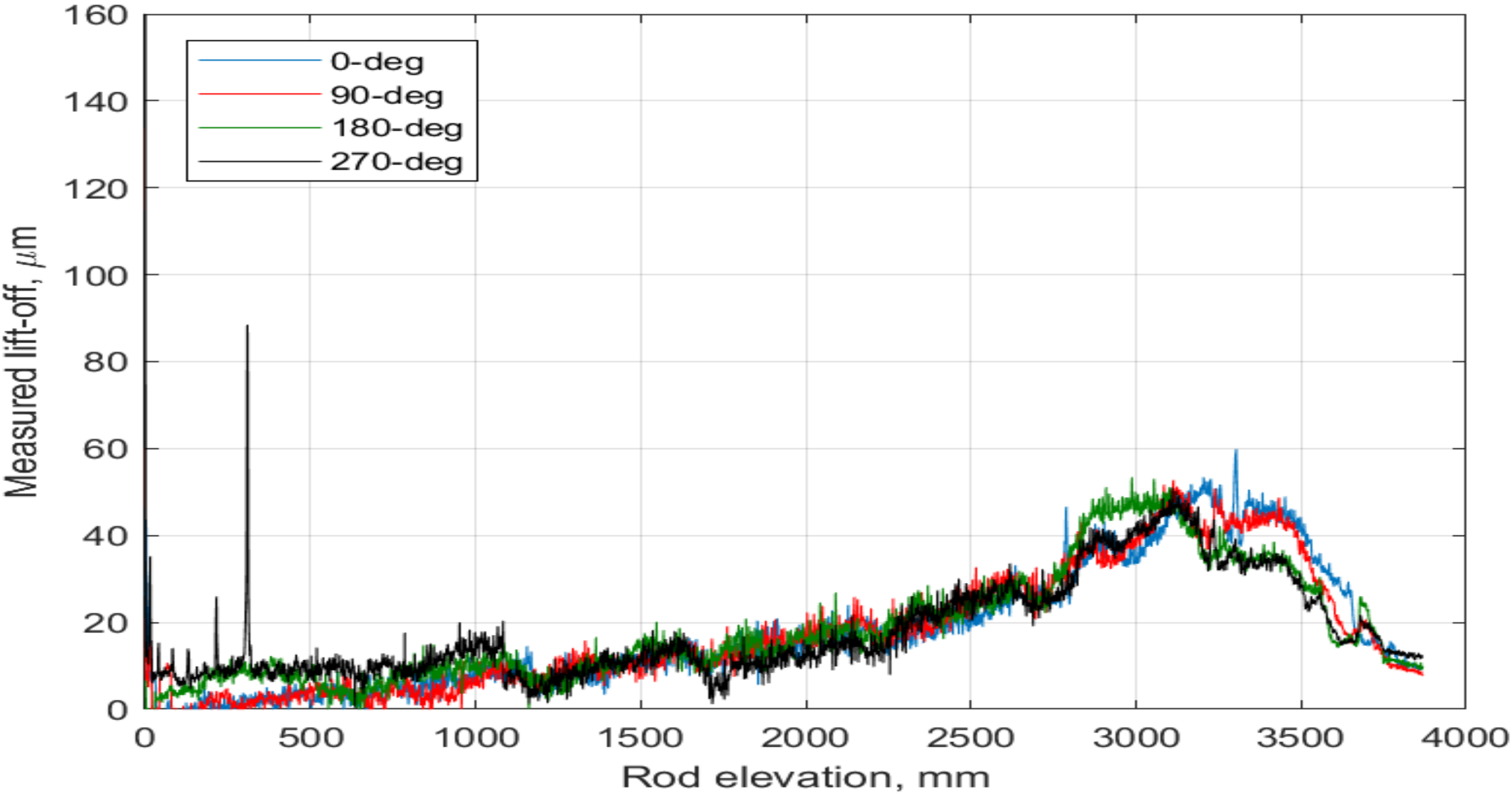


Figure C.16. Lift-Off Measured in All Four Quadrants, Sister Rod 6U3M09.

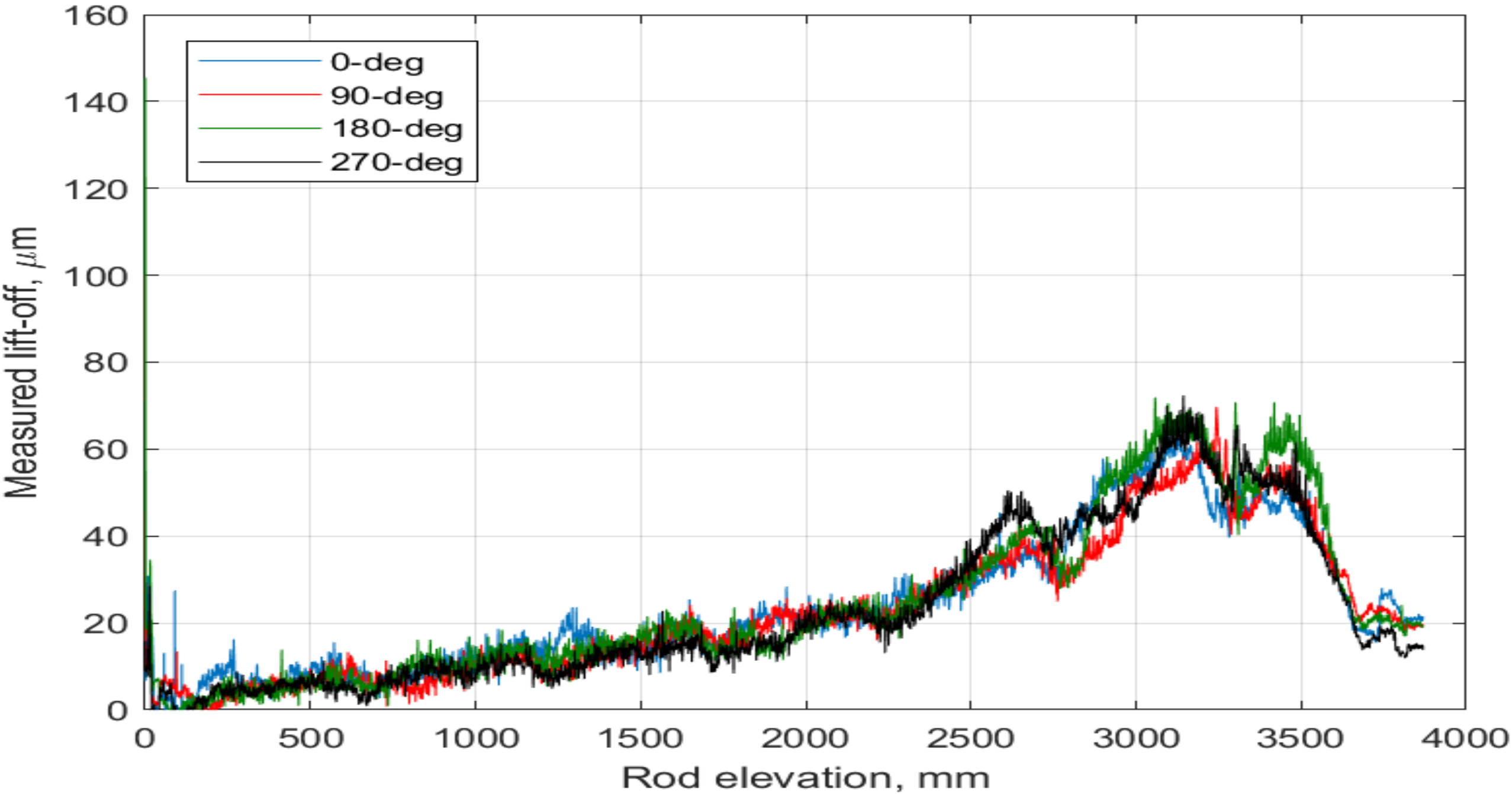


Figure C.17. Lift-Off Measured in All Four Quadrants, Sister Rod 6U3O05.

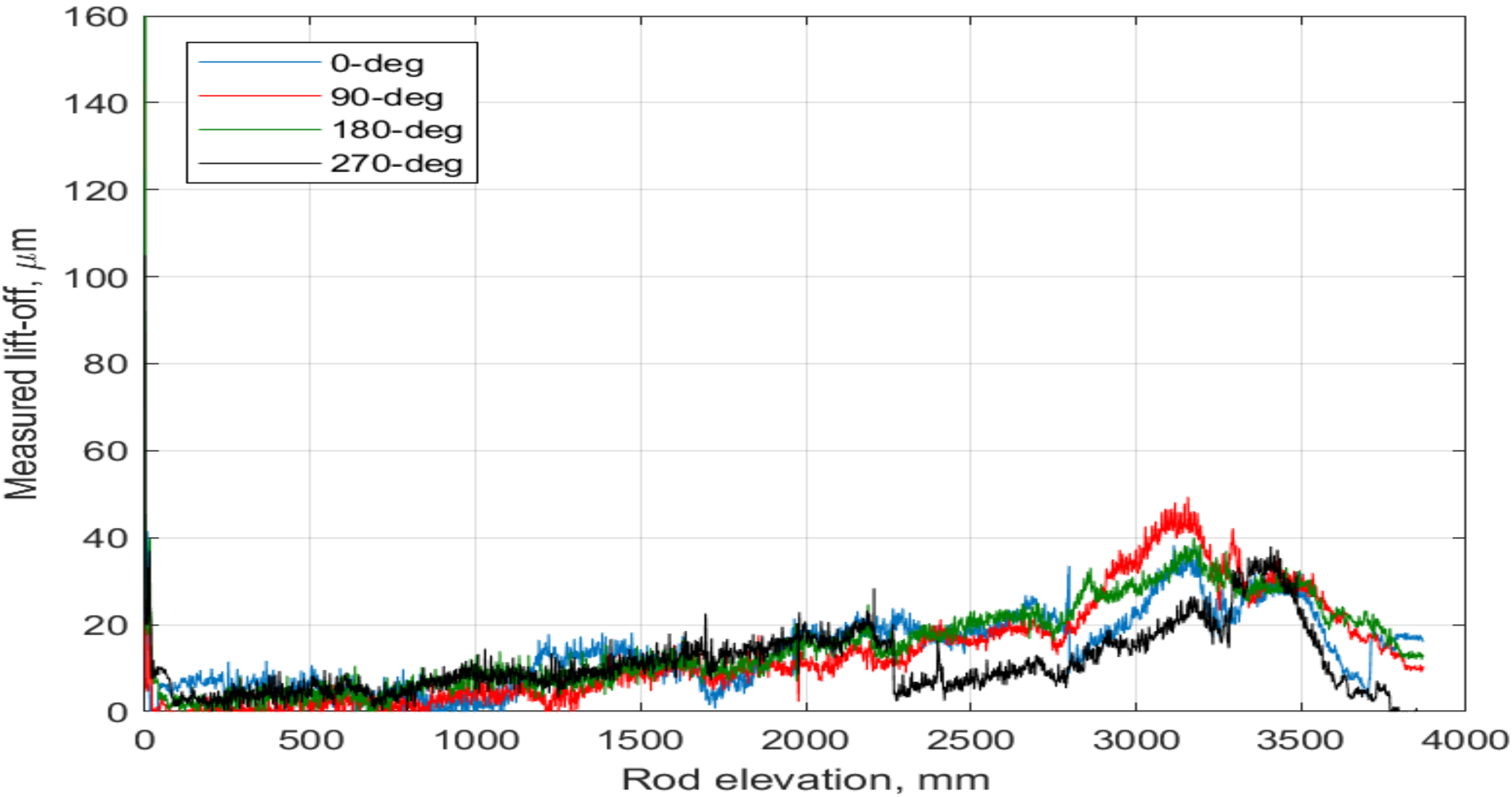


Figure C.18. Lift-Off Measured in All Four Quadrants, Sister Rod 6U3P16.

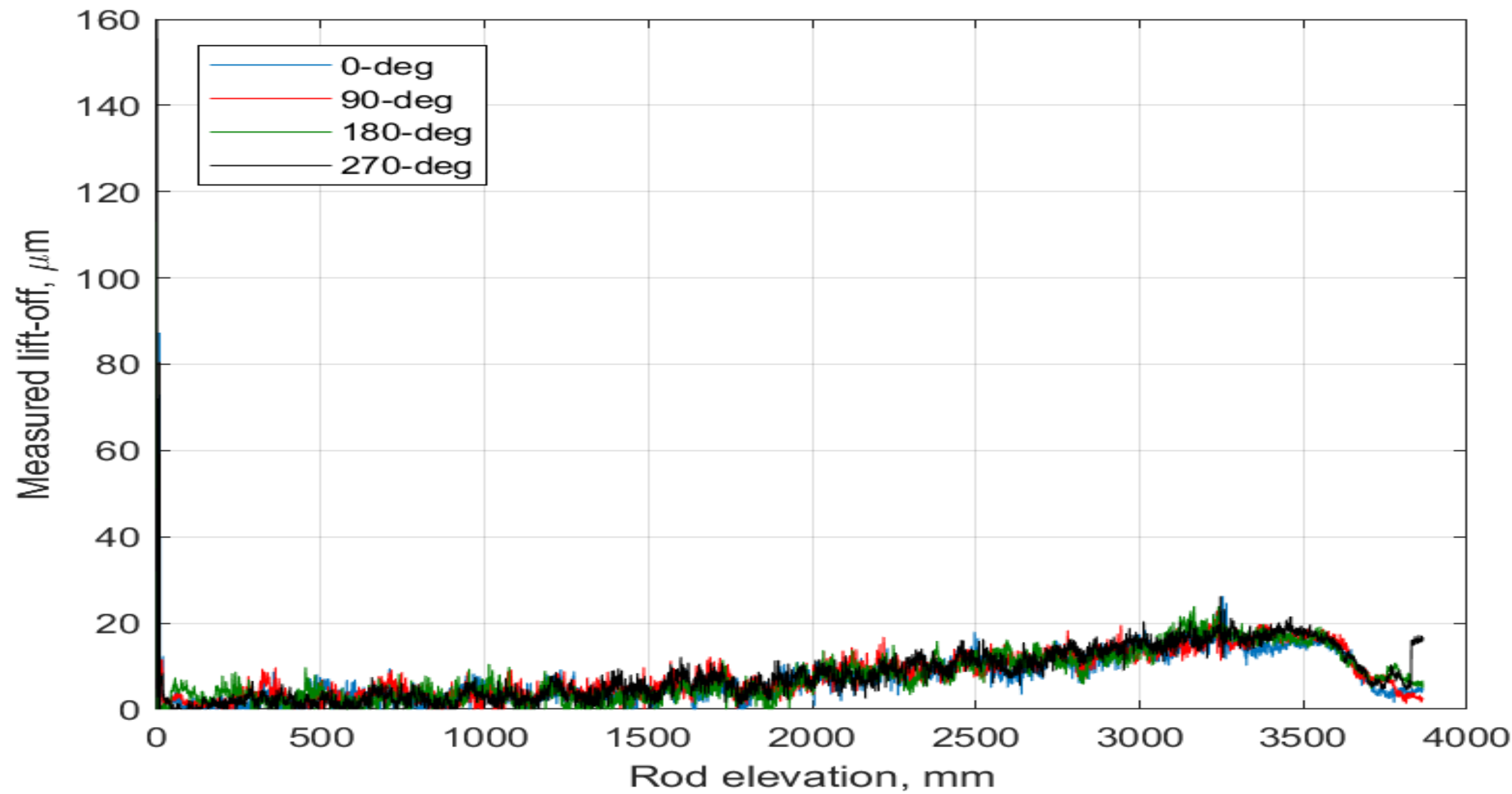


Figure C.19. Lift-Off Measured in All Four Quadrants, Sister Rod 30AD05.

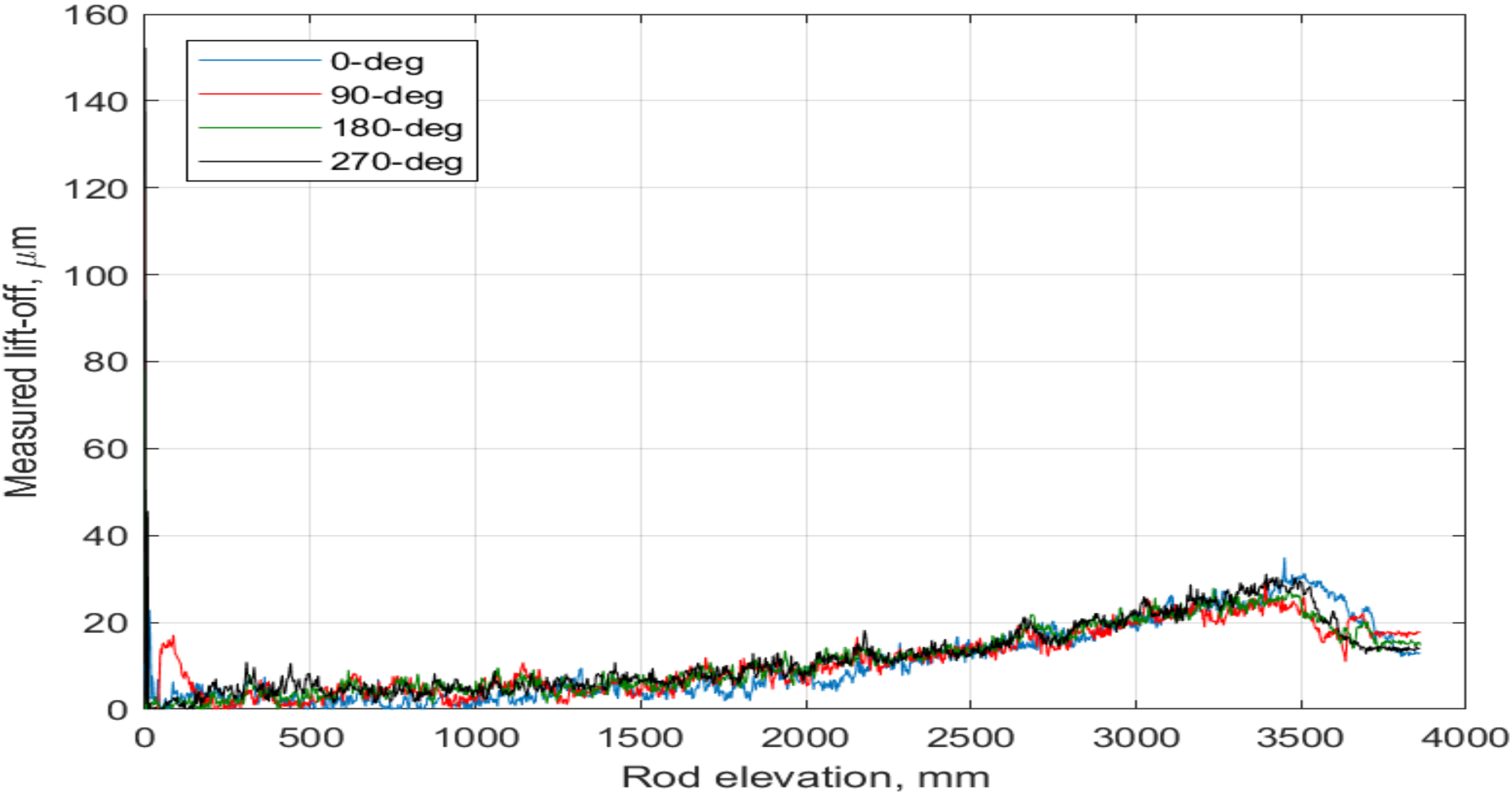


Figure C.20. Lift-Off Measured in All Four Quadrants, Sister Rod 30AE14.

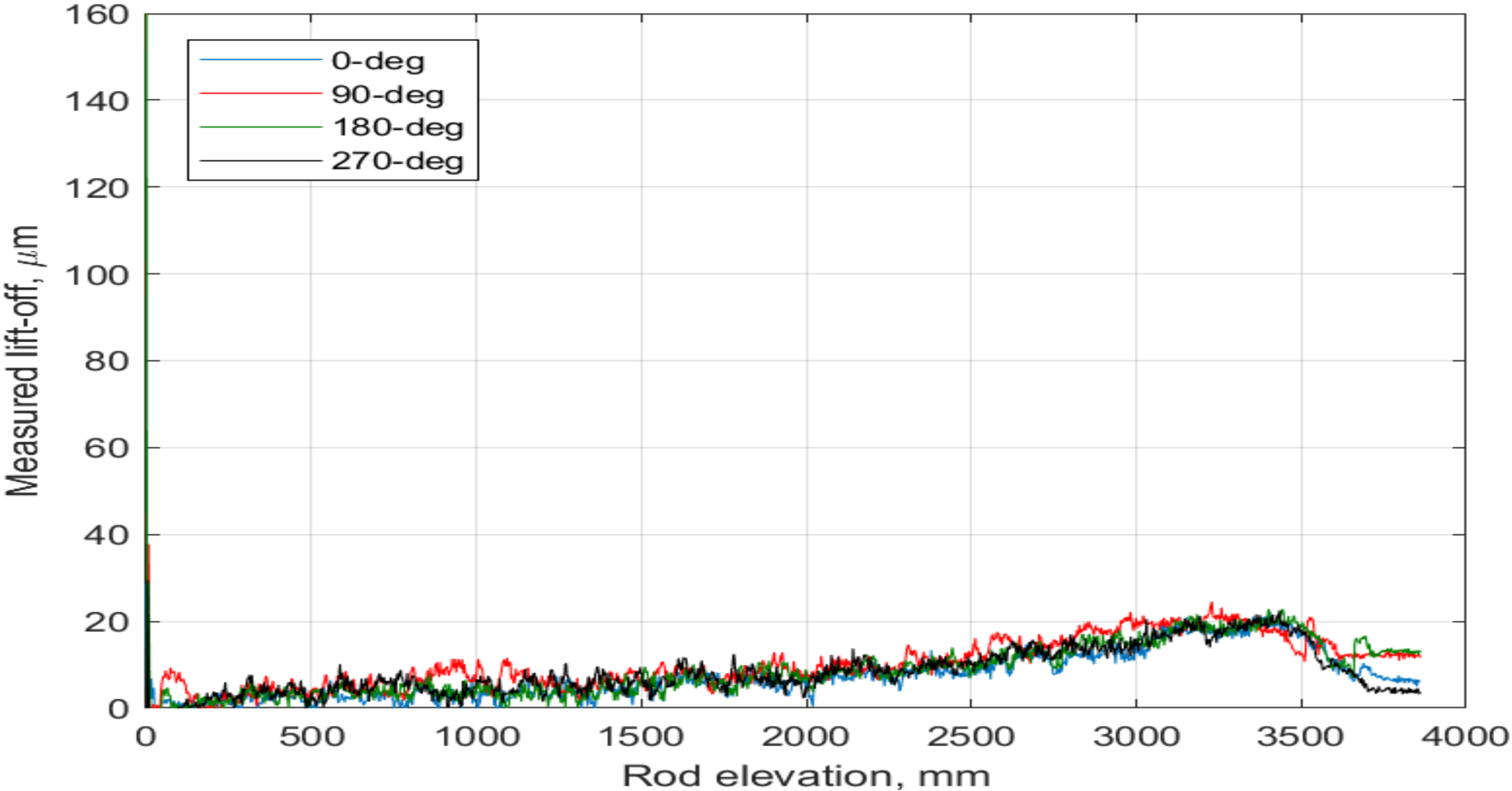


Figure C.21. Lift-Off Measured in All Four Quadrants, Sister Rod 30AG09.

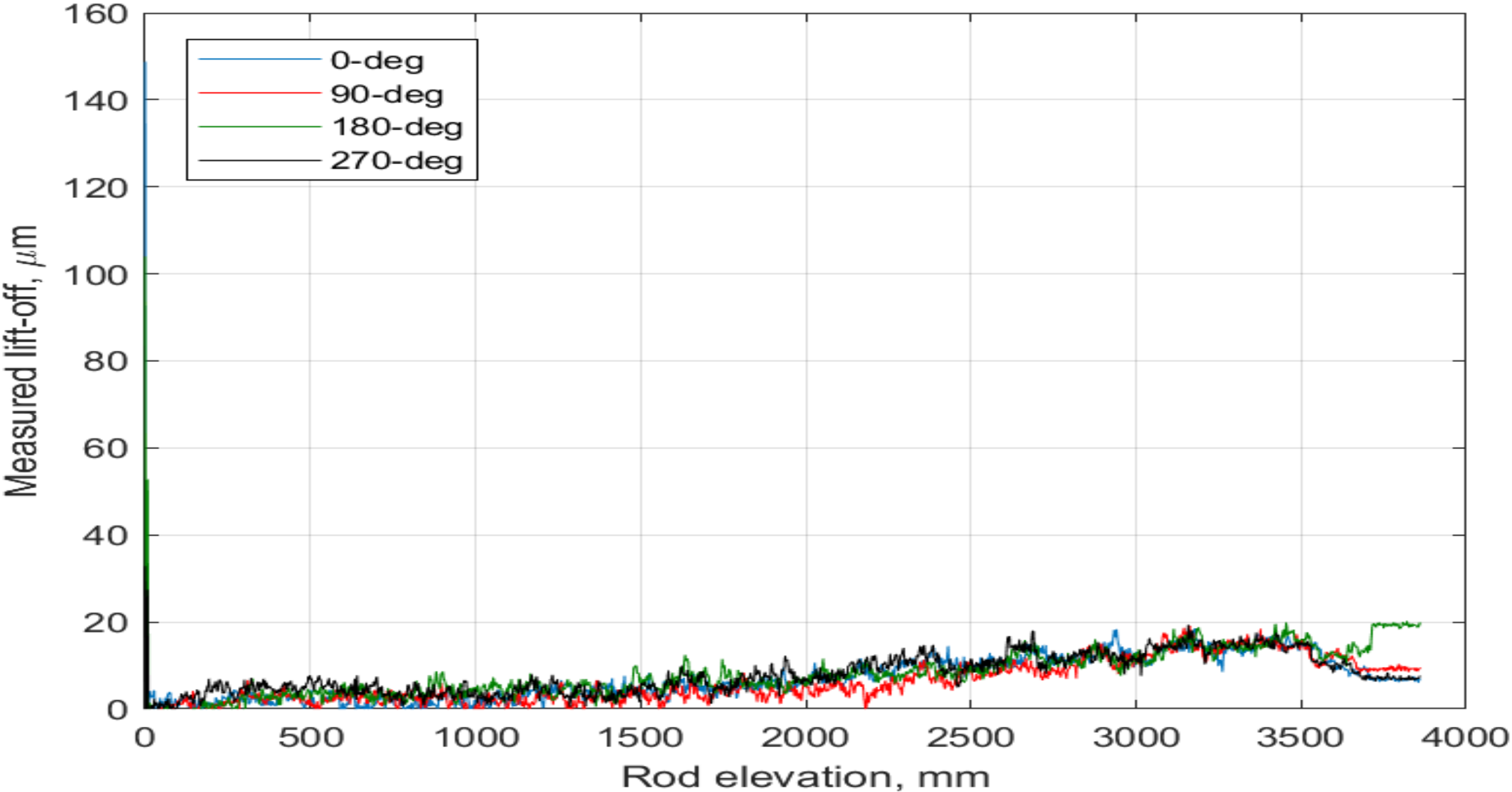


Figure C.22. Lift-Off Measured in All Four Quadrants, Sister Rod 30AK09.

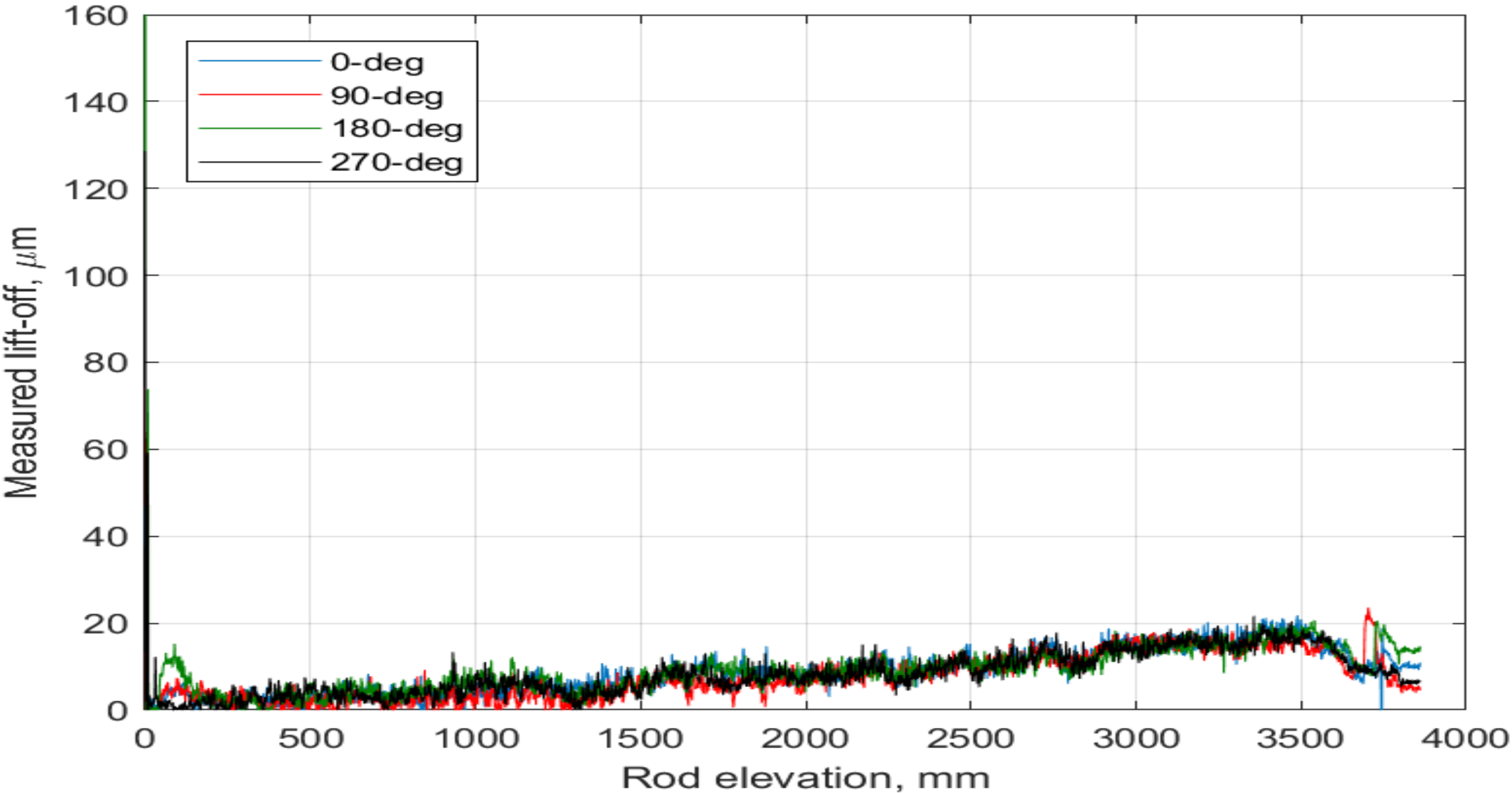


Figure C.23. Lift-Off Measured in All Four Quadrants, Sister Rod 30AP02.

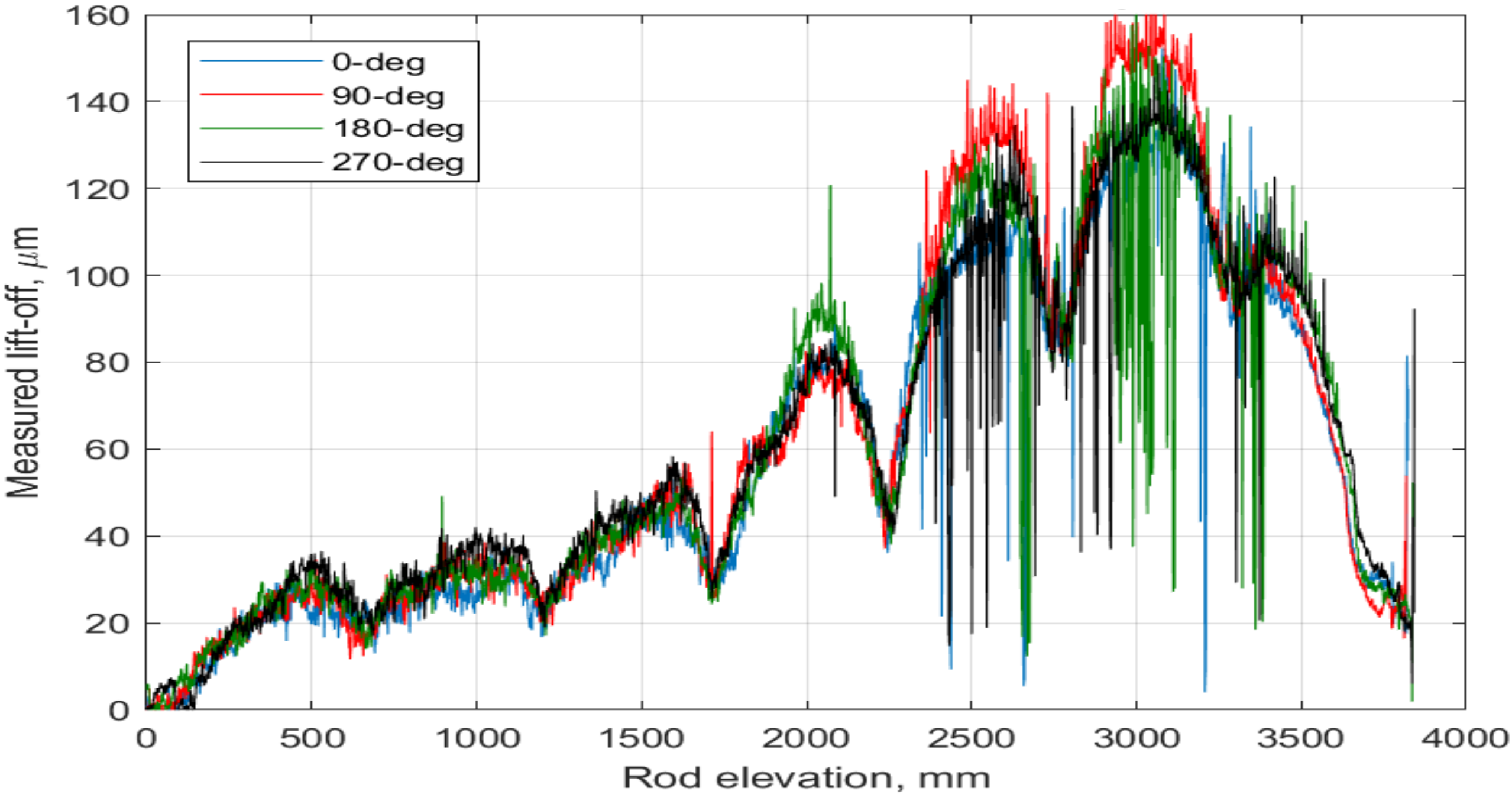


Figure C.24. Lift-Off Measured in All Four Quadrants, Sister Rod F35K13.

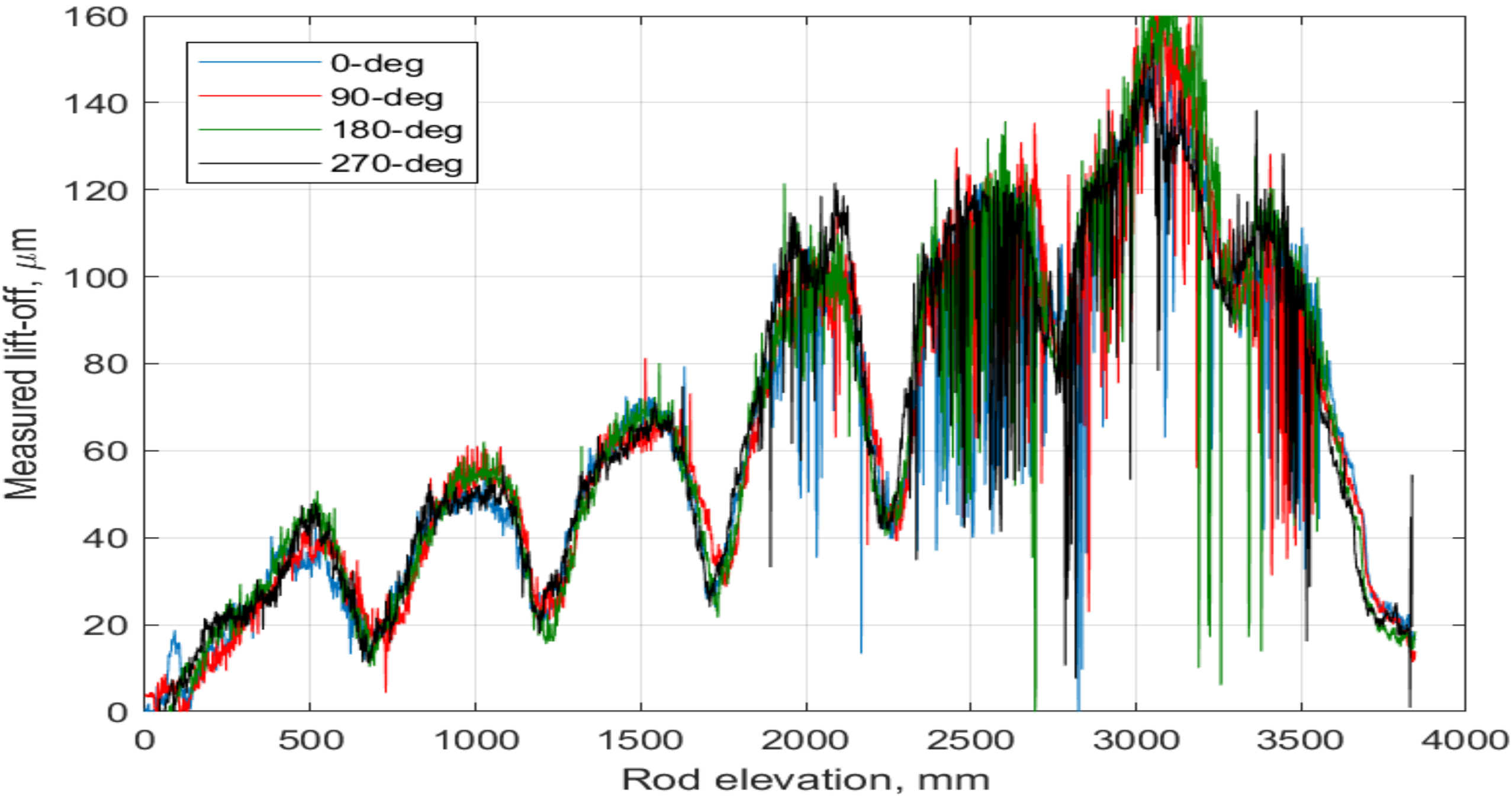


Figure C.25. Lift-Off Measured in All Four Quadrants, Sister Rod F35P17.

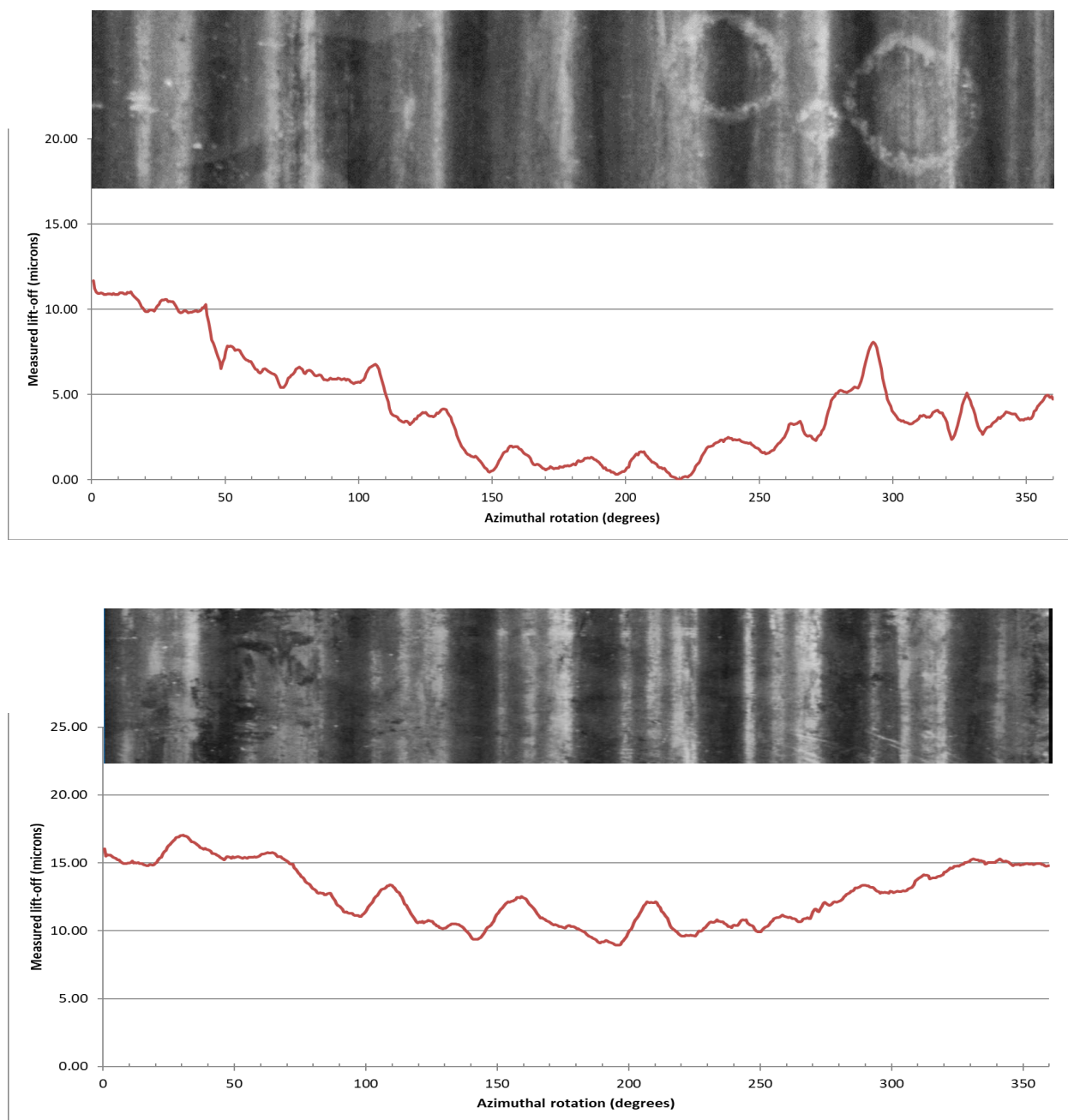


Figure C.26. Rotational Eddy Current Lift-Off Scans for 30AE14 at Elevations of 229 mm (Top) and 3,861 mm (Bottom).

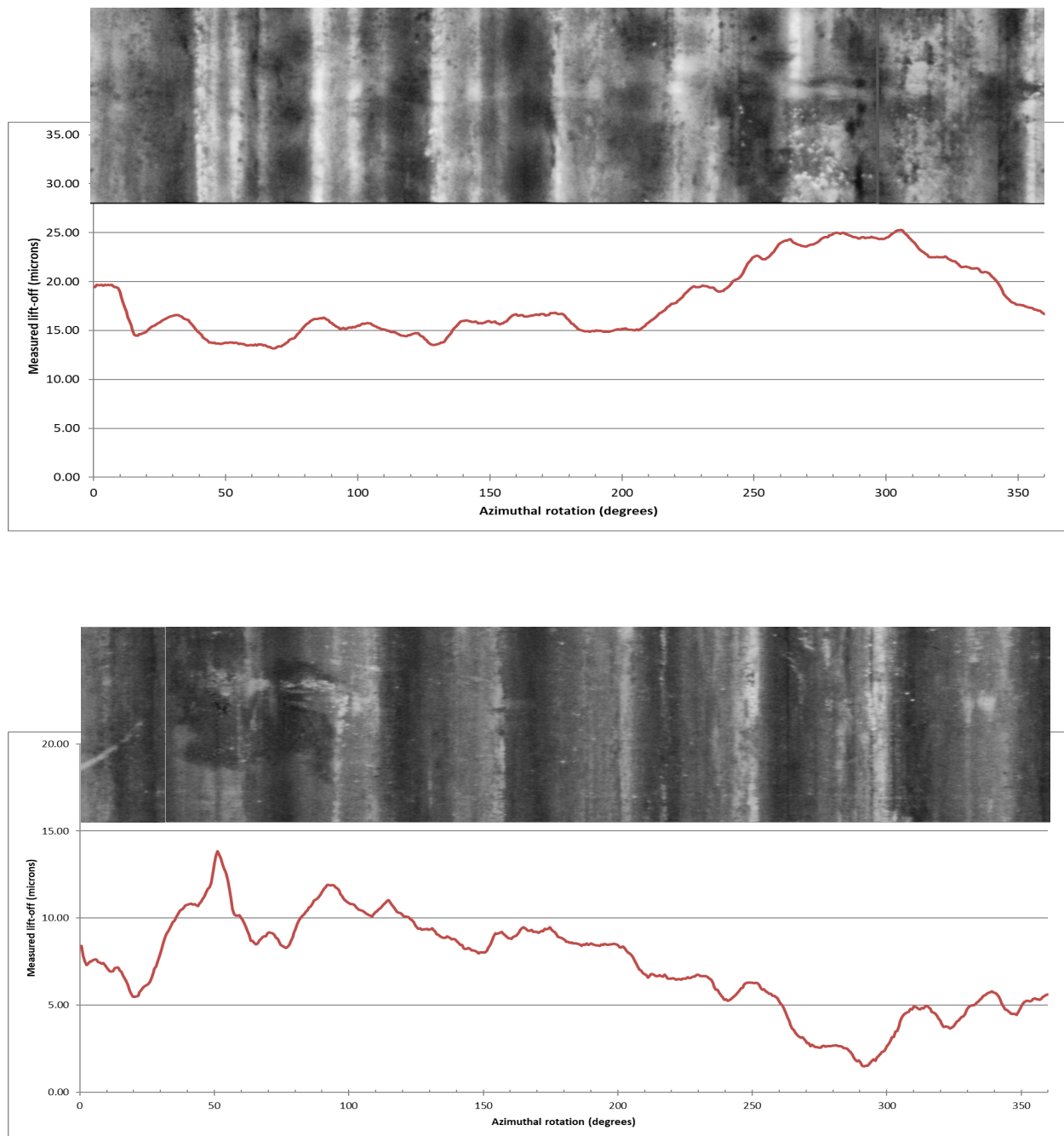


Figure C.27. Rotational Eddy Current Lift-Off Scans for 30AE14 at Elevations of 3,781 mm (Top) and 2,461 mm (Bottom).

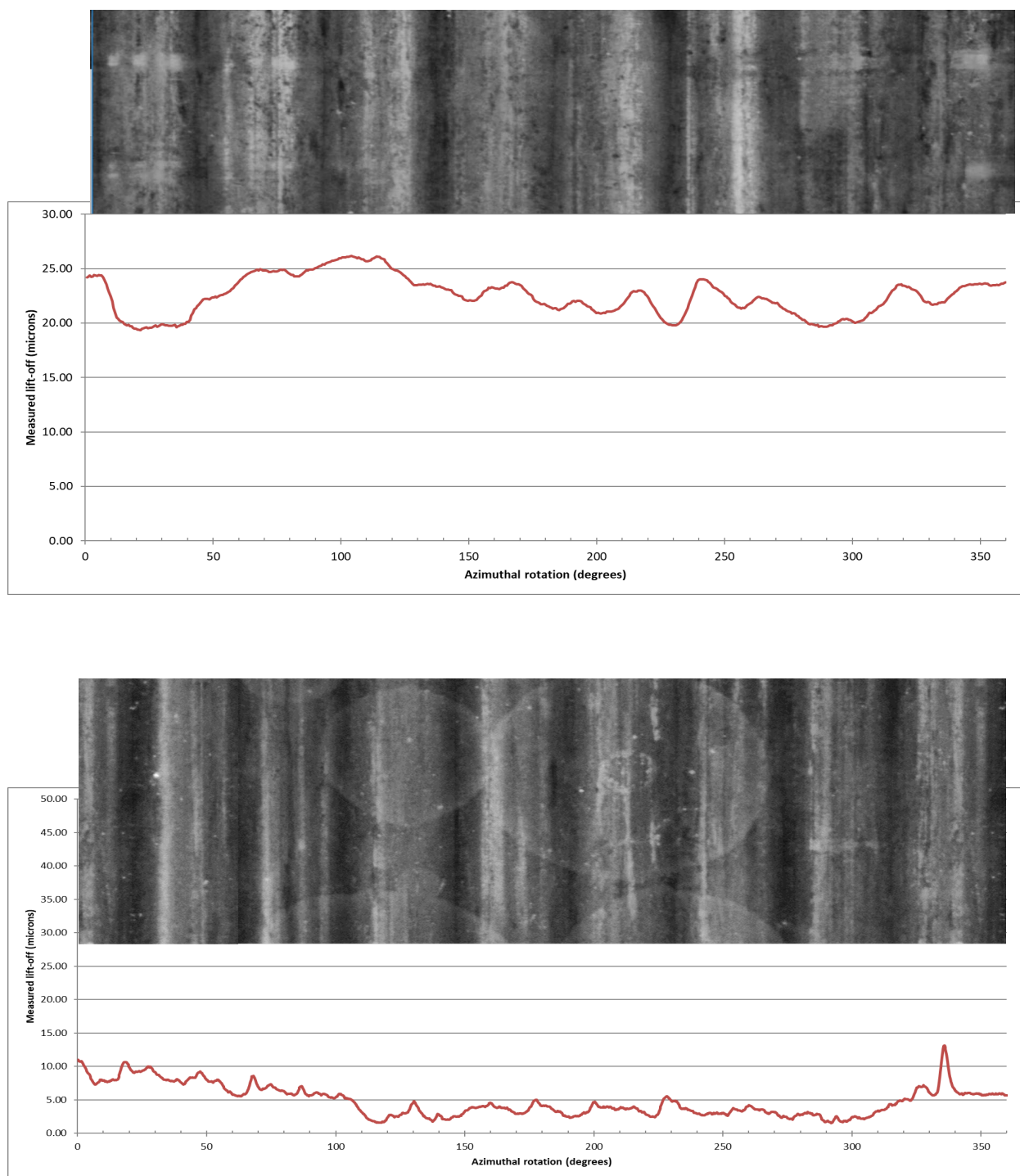


Figure C.28. Rotational Eddy Current Lift-Off Scans for 30AE14 at Elevations of 3320 mm (Top) and 235 mm (Bottom).

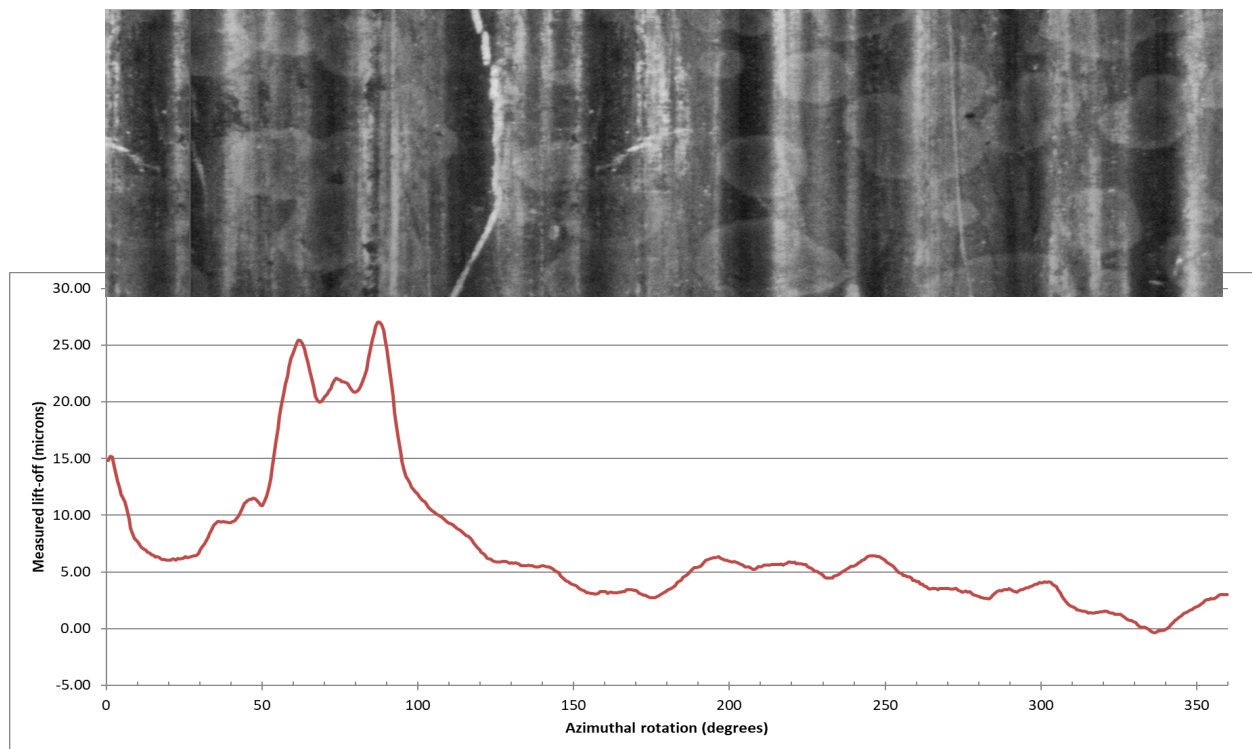


Figure C.29. Rotational Eddy Current Lift-Off Scans for 30AE14 at elevation of 33 mm.

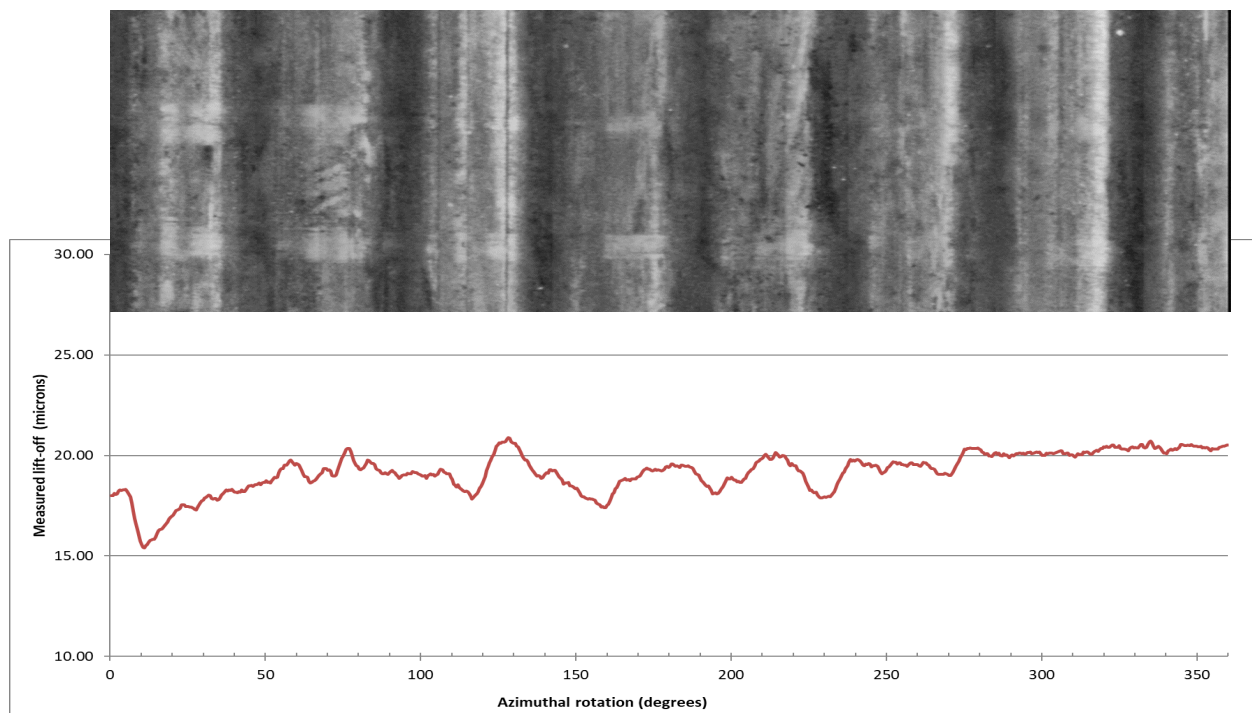


Figure C.30. Rotational Eddy Current Lift-Off Scans from 30AG09 at 530 mm.

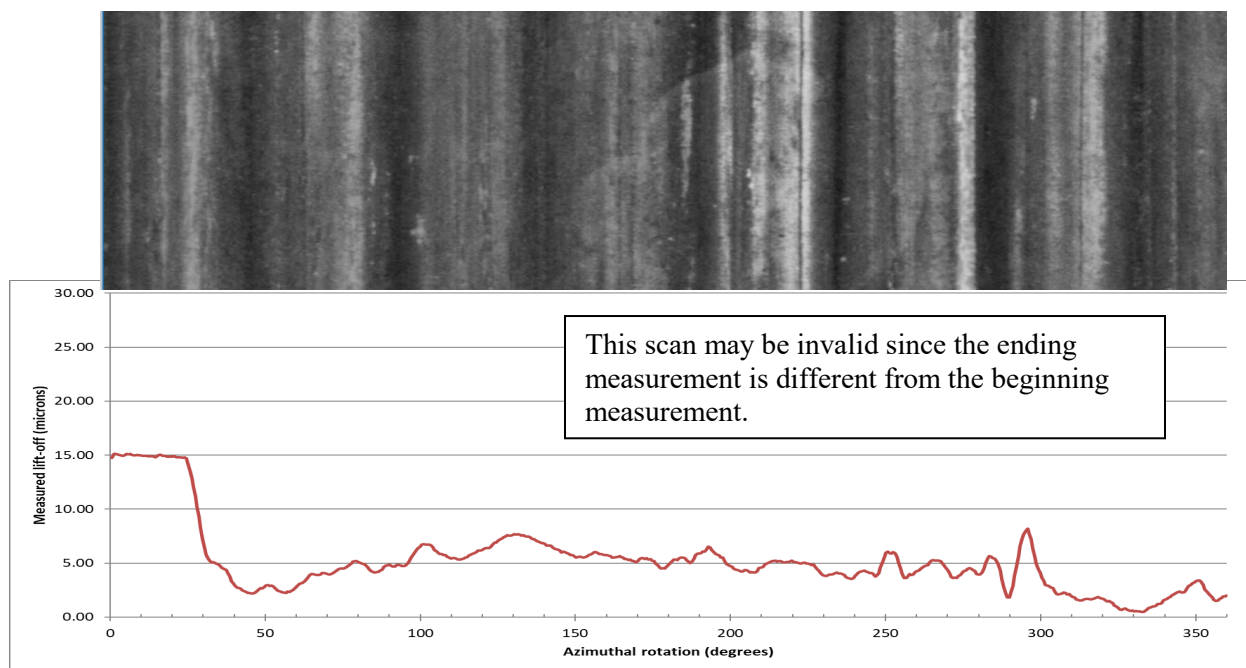


Figure C.31. Rotational Eddy Current Lift-Off Scans from 30AG09 at 670 mm.

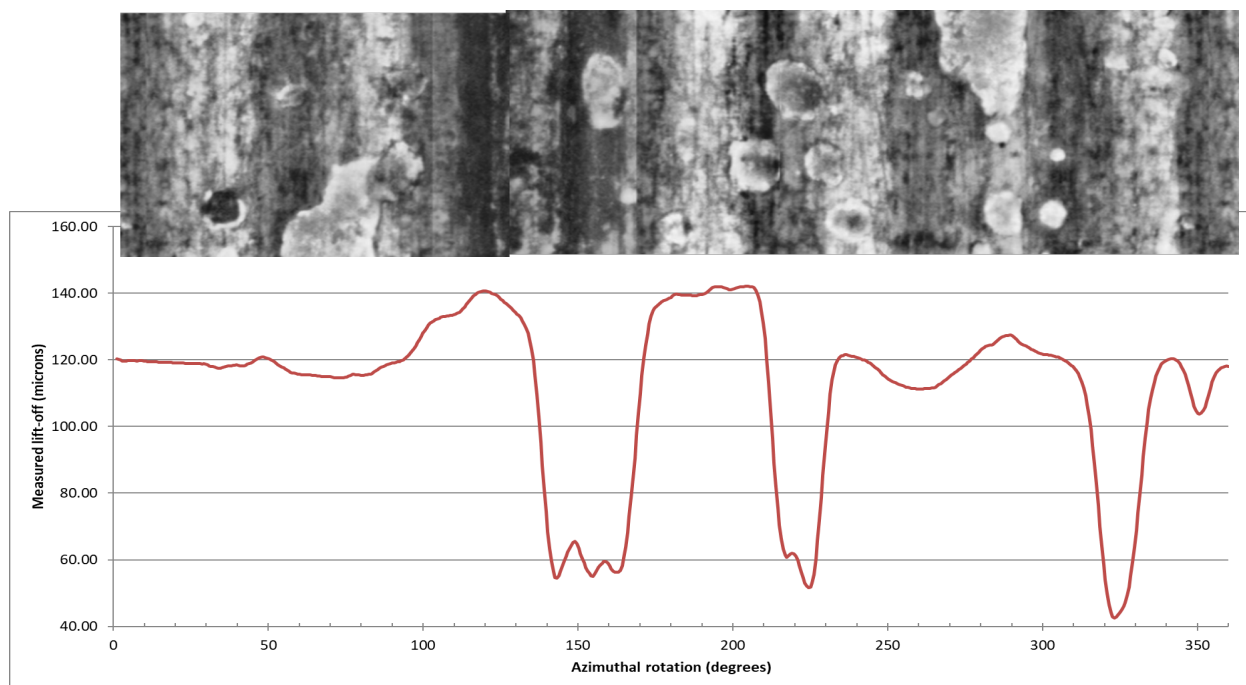


Figure C.32. Rotational Eddy Current Lift-Off Scans of 3A1B16 at 3,100 mm.

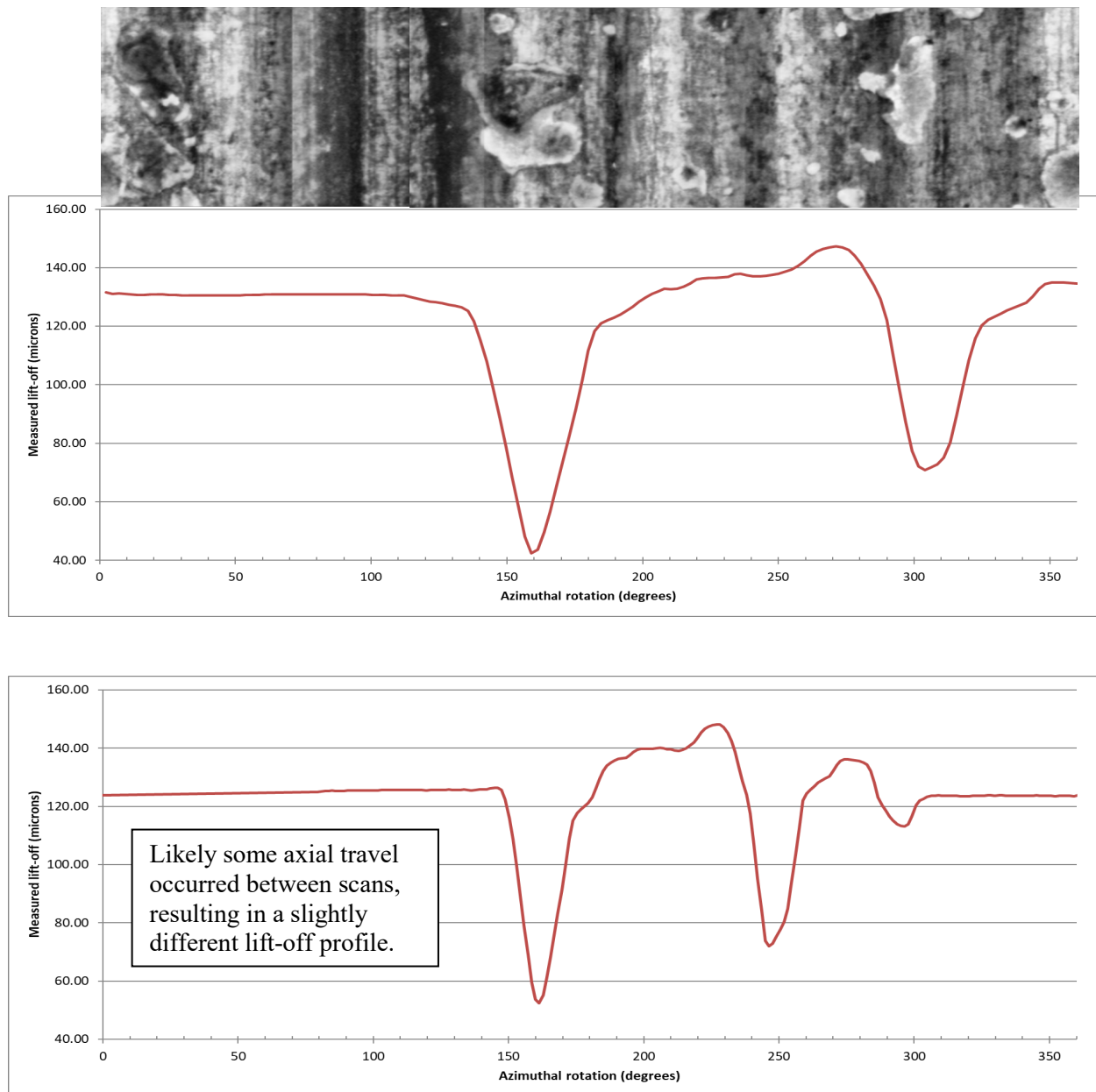


Figure C.33. Rotational Eddy Current Lift-Off Scans of 3A1B16 at 3,100 mm at 1 RPM (Top) and 10 RPM (Bottom).

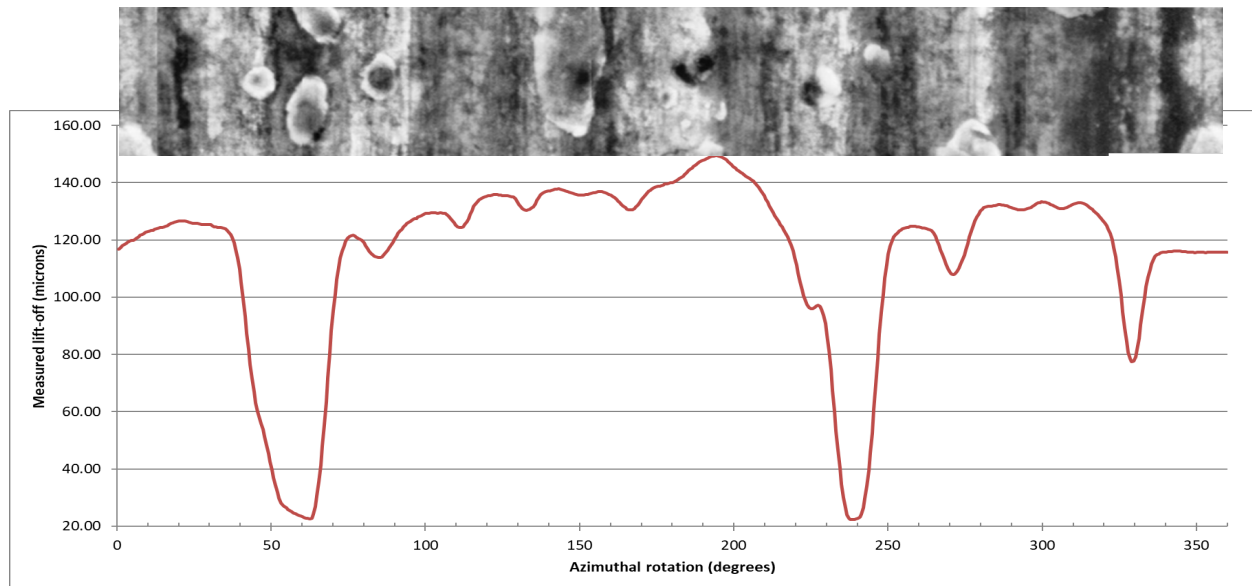


Figure C.34 Rotational Eddy Current Lift-Off Scans of 3A1B16 at 791 mm.

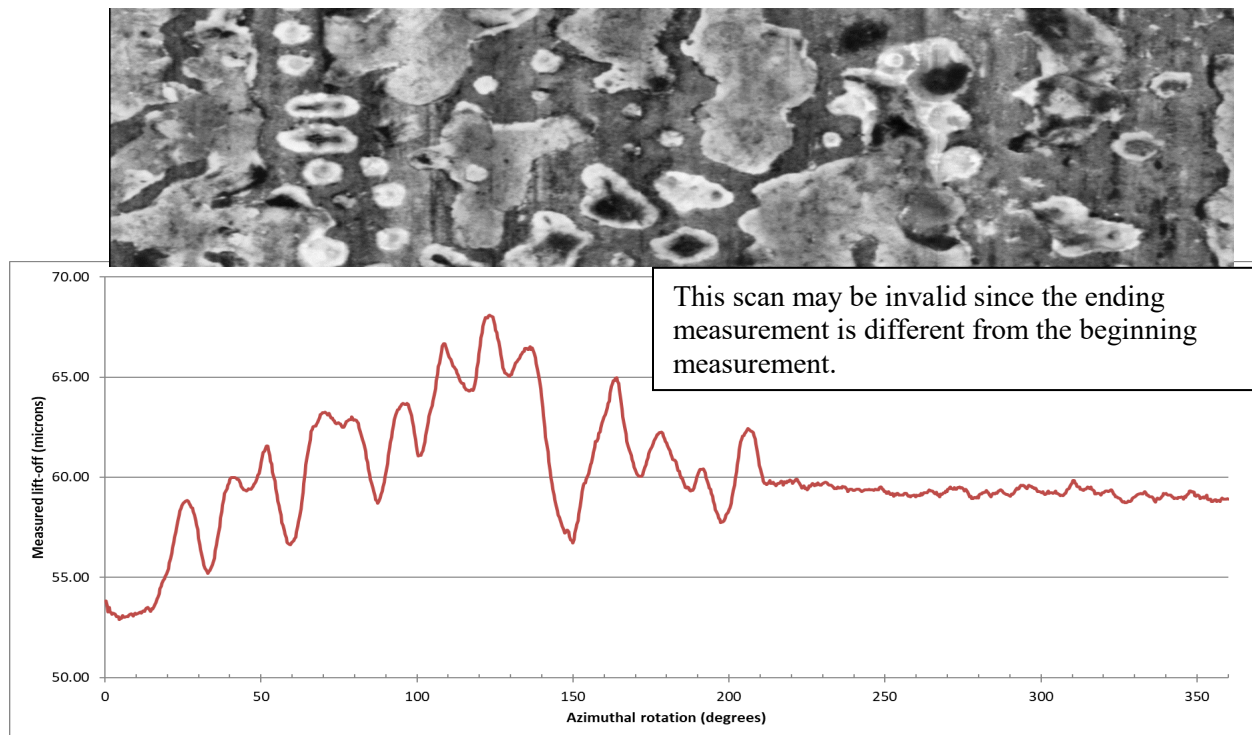


Figure C.35. Rotational Eddy Current Lift-Off Scans of F35P17 at 1,365 mm.

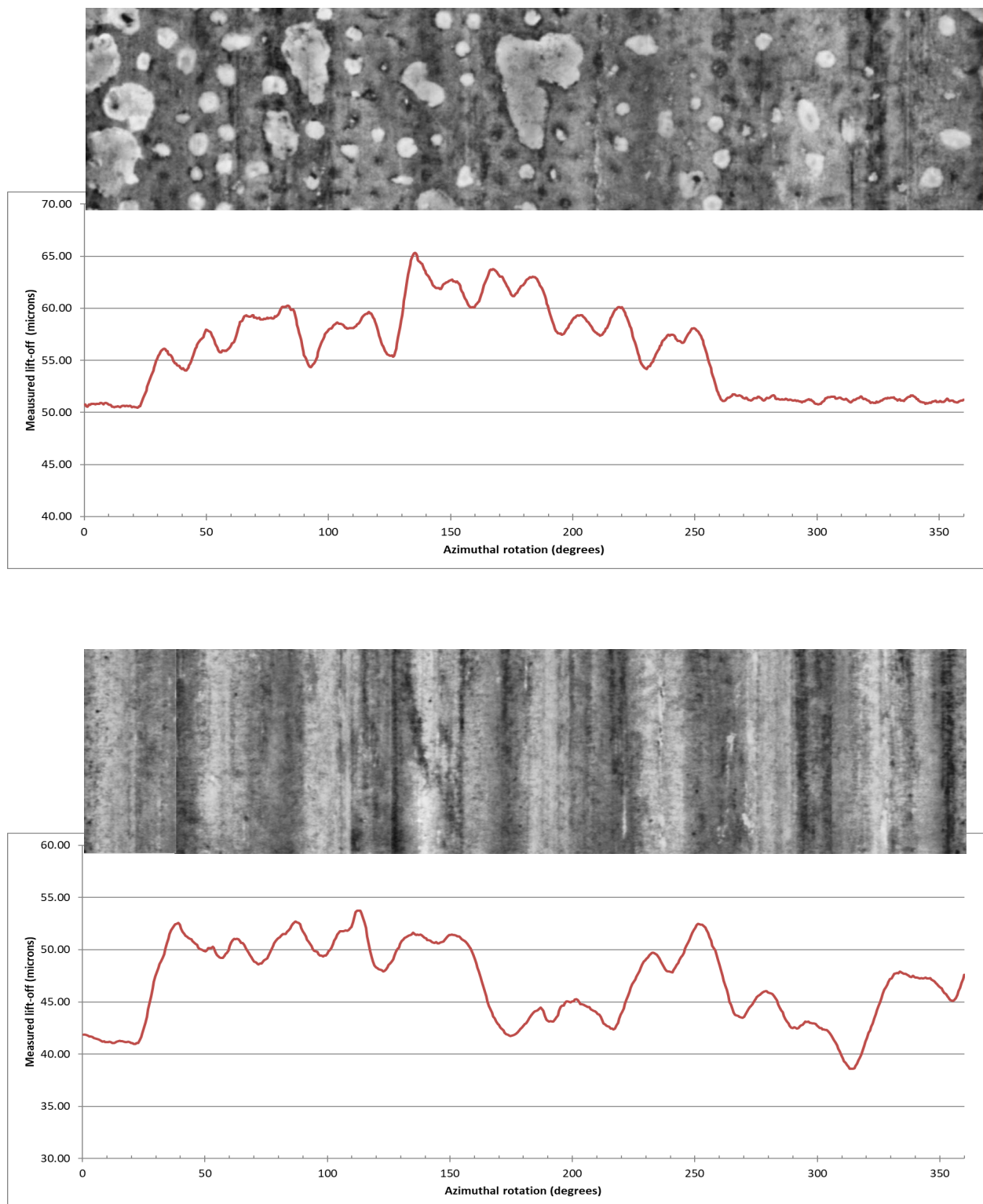


Figure C.36. Rotational Eddy Current Lift-Off Scans of F35P17 at 1,805 mm (Top) and 2,263 mm (Bottom).

December 21, 2018

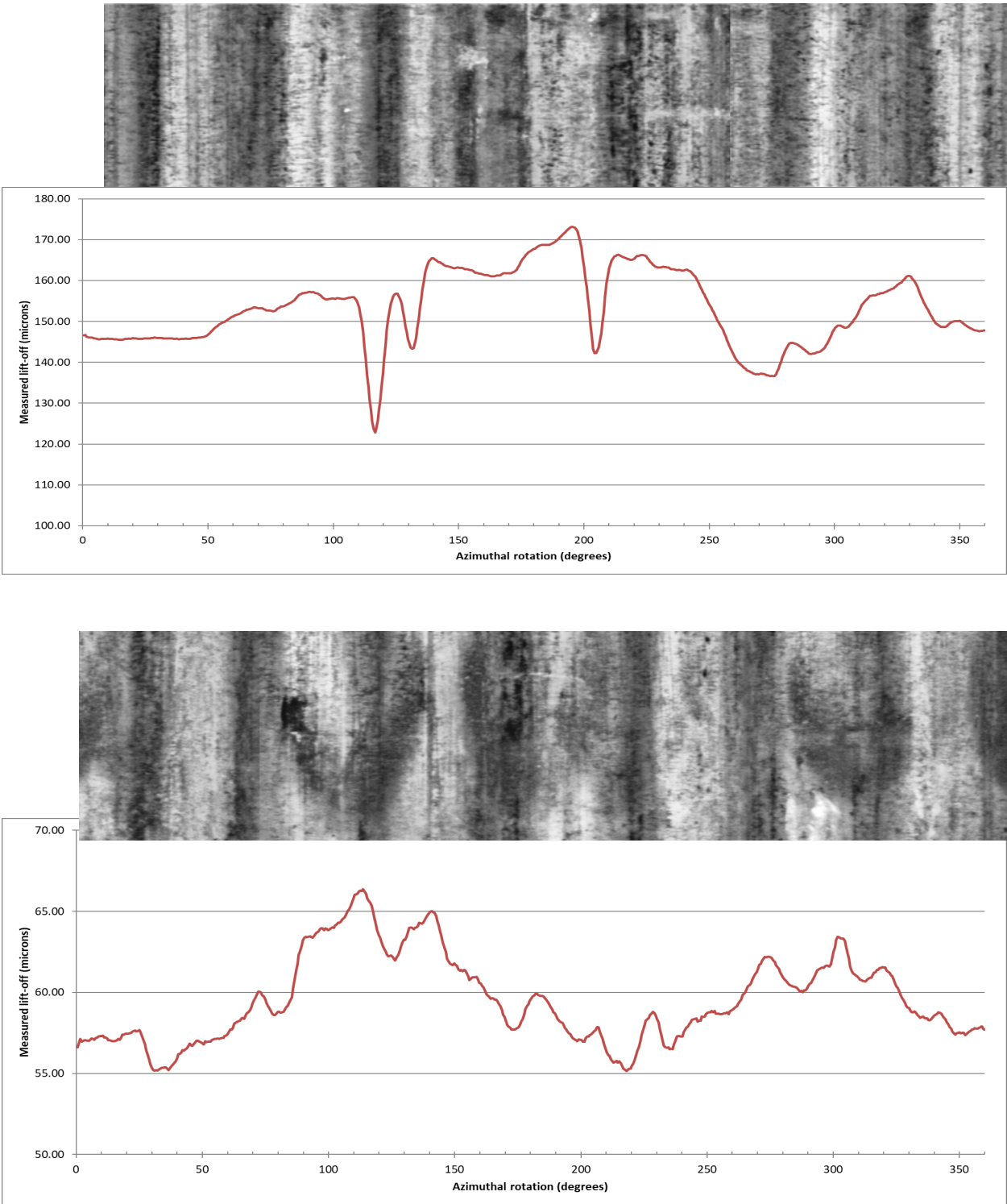


Figure C.37. Rotational Eddy Current Lift-Off Scans of F35P17 at 3,080 mm (Top) and 3,650 mm (Bottom).

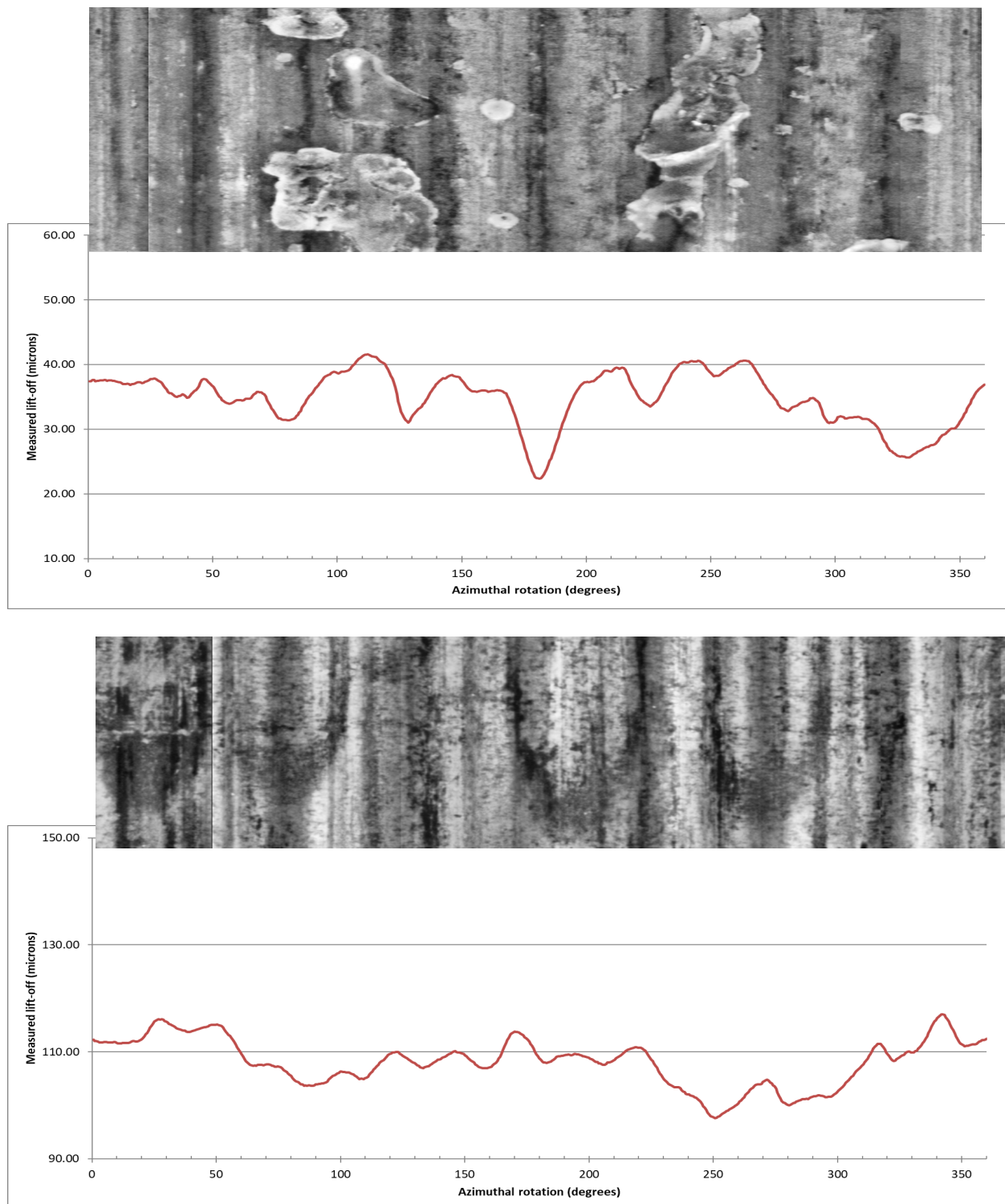


Figure C.38. Rotational Eddy Current Lift-Off Scans of F35K13 at 1,139 (Top) and 3,403 mm (Bottom).

December 21, 2018

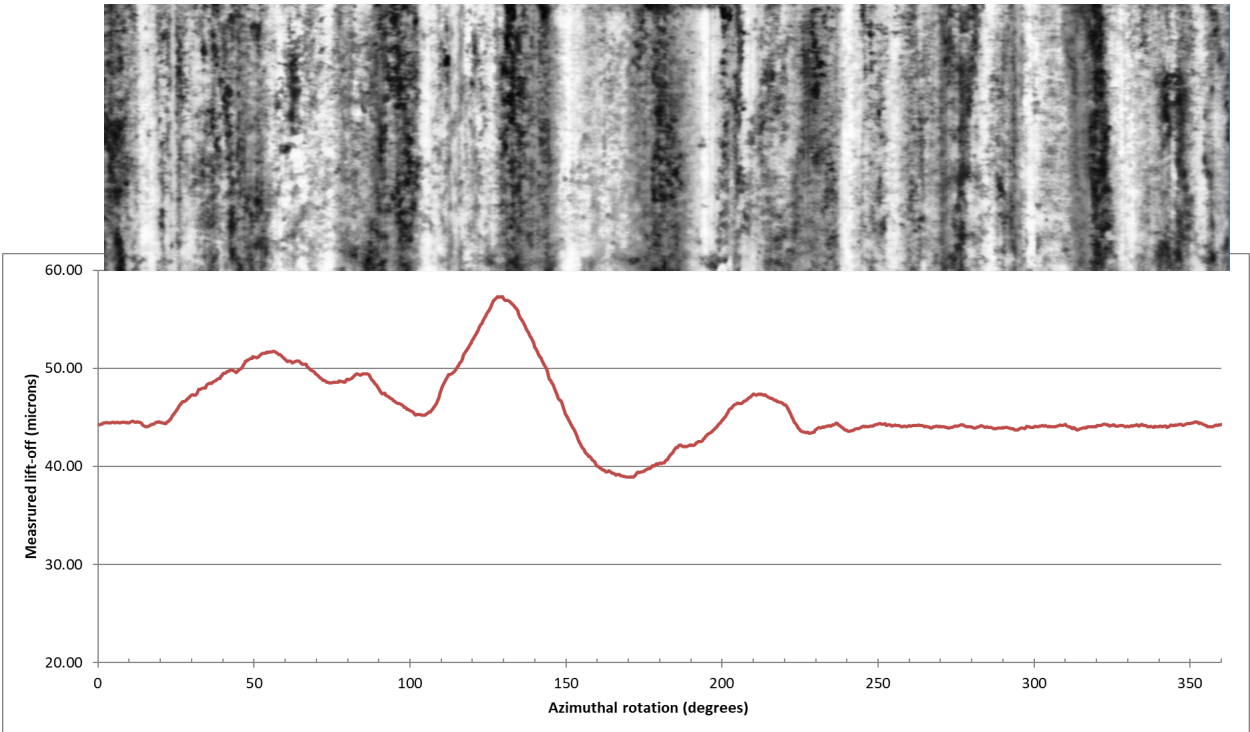


Figure C.39. Rotational Eddy Current Lift-Off Scans of 6U3M03 at 3213mm

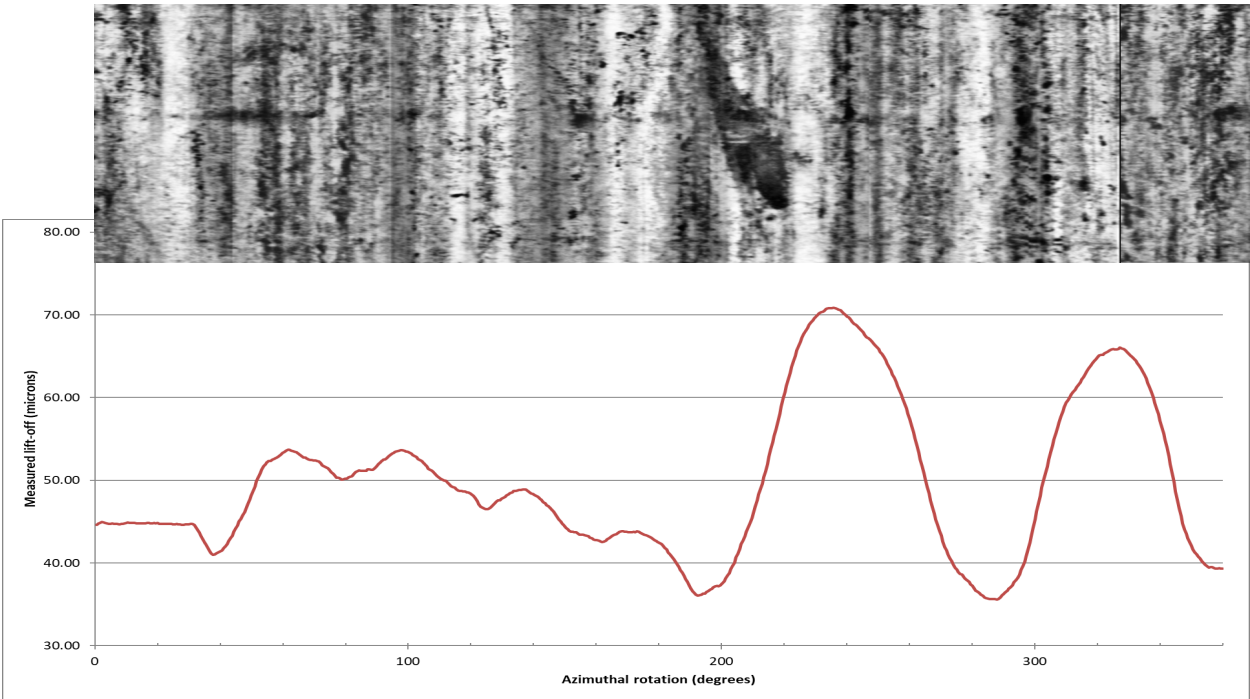


Figure C.40. Rotational eddy current lift-off scan of 3F9D07 at 3,333 mm.

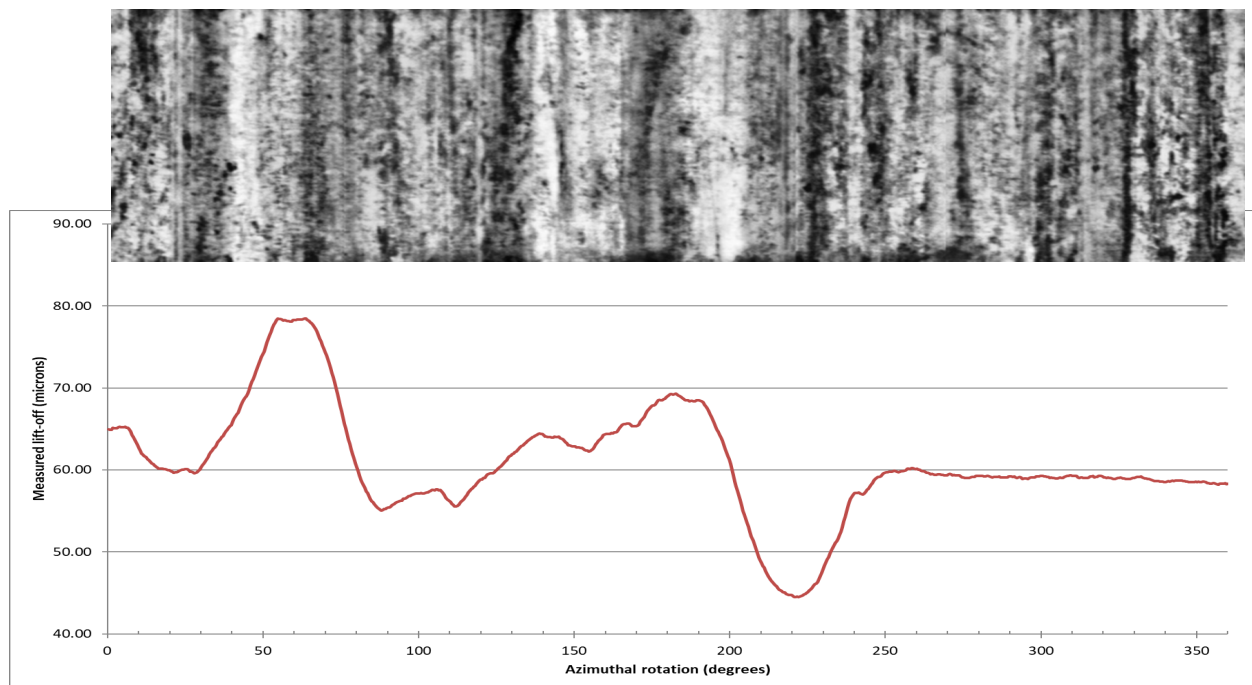


Figure C.41. Rotational eddy current lift-off scan of 3F9D07 at 3,200 mm.

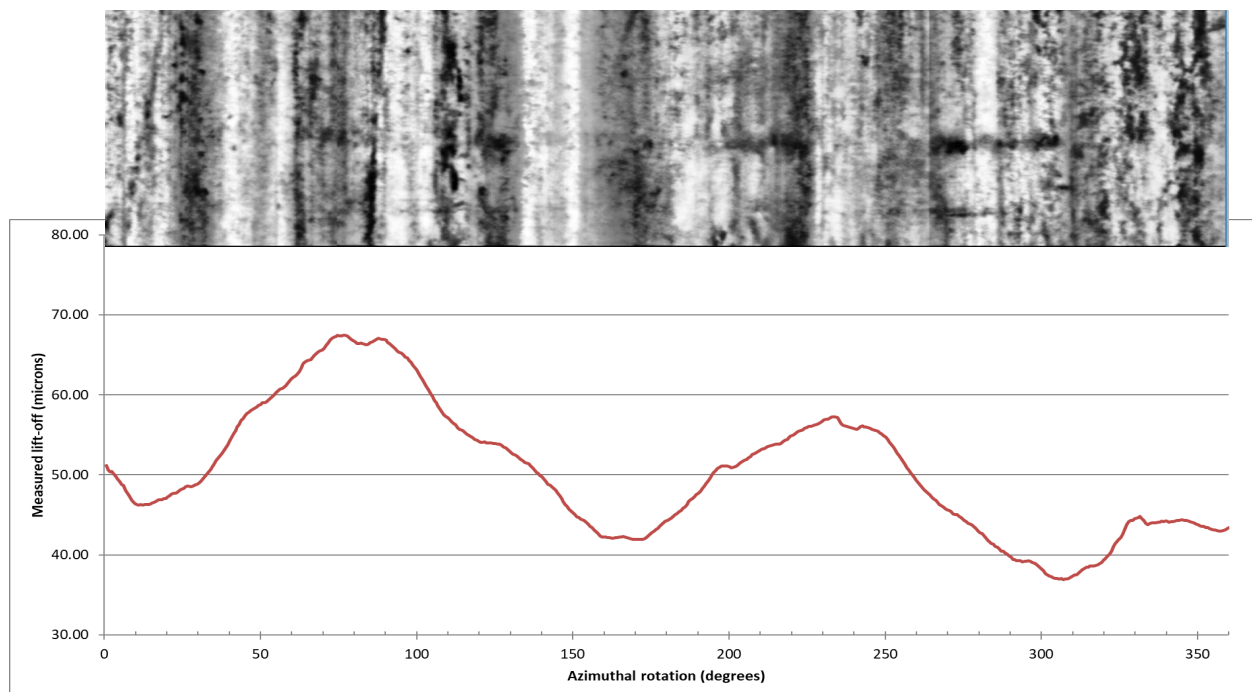


Figure C.42. Rotational eddy current lift-off scan of 3F9D07 at 3,295 mm.

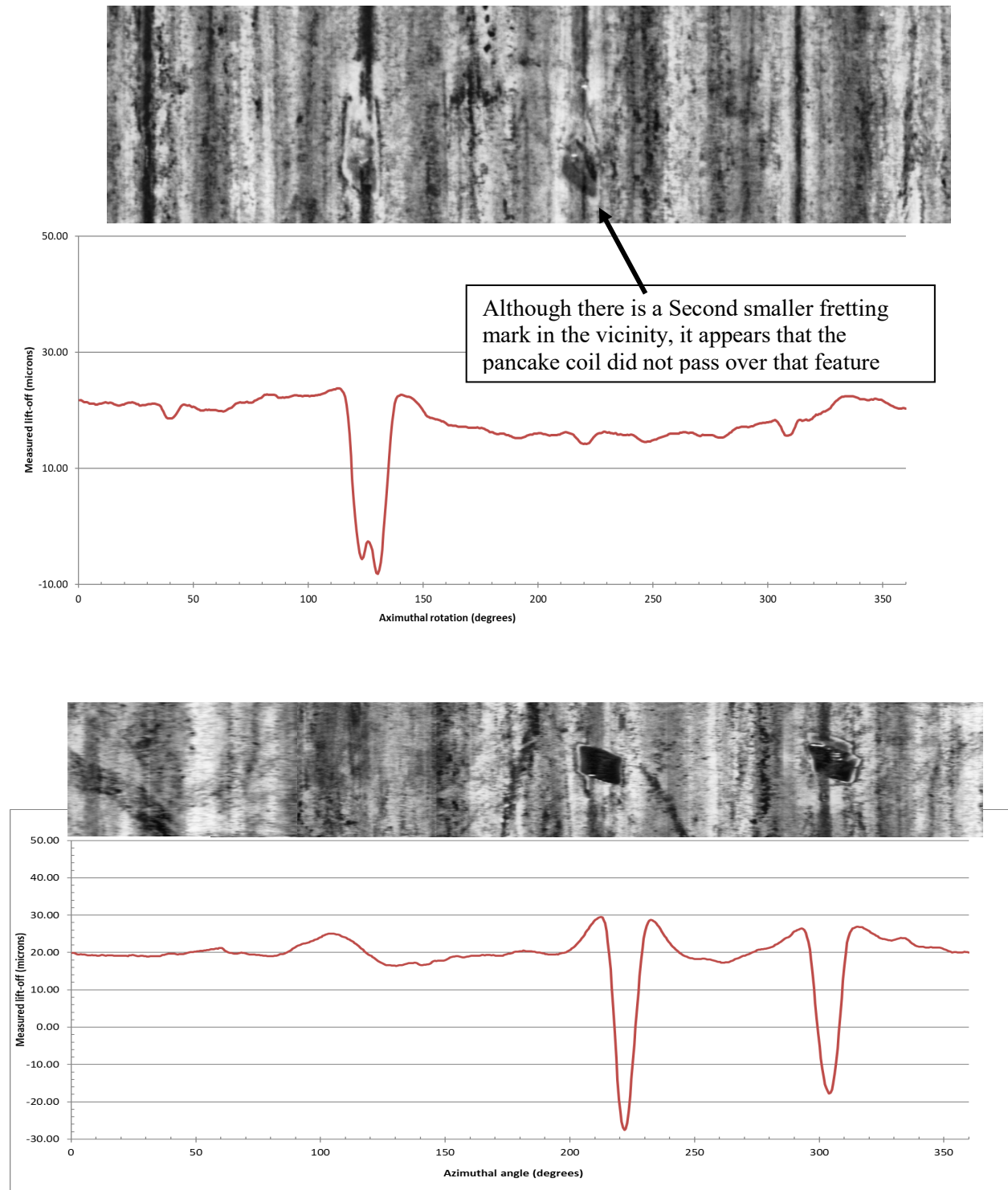


Figure C.43. Rotational Eddy Current Lift-Off Scans of 3F9D07 at 1,765 mm (Top) and 2,279 mm (Bottom).

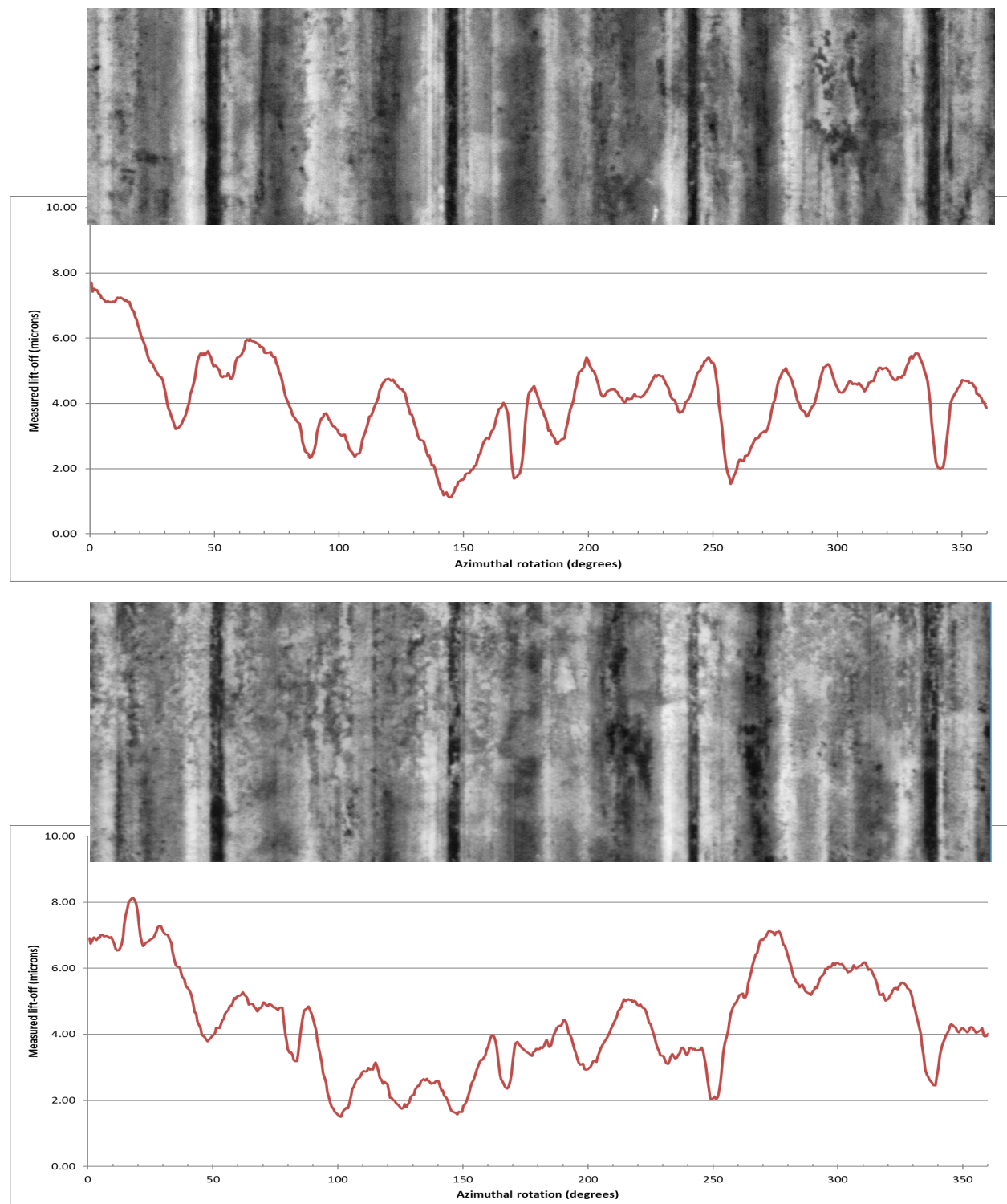


Figure C.44. Rotational Eddy Current Lift-Off Scans of 6U3K09 at 310 mm (Top) and 322 mm (Bottom).

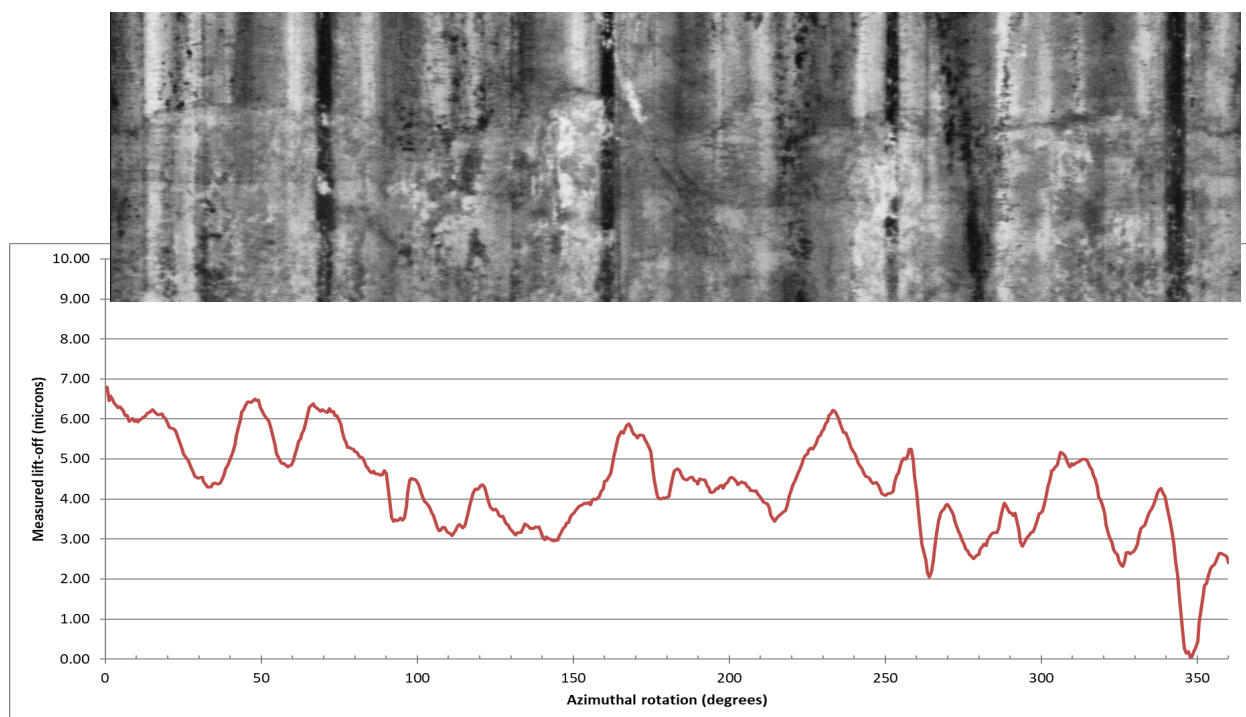


Figure C.45. Rotational eddy current lift-off scan of 6U3K09 at 330 mm.

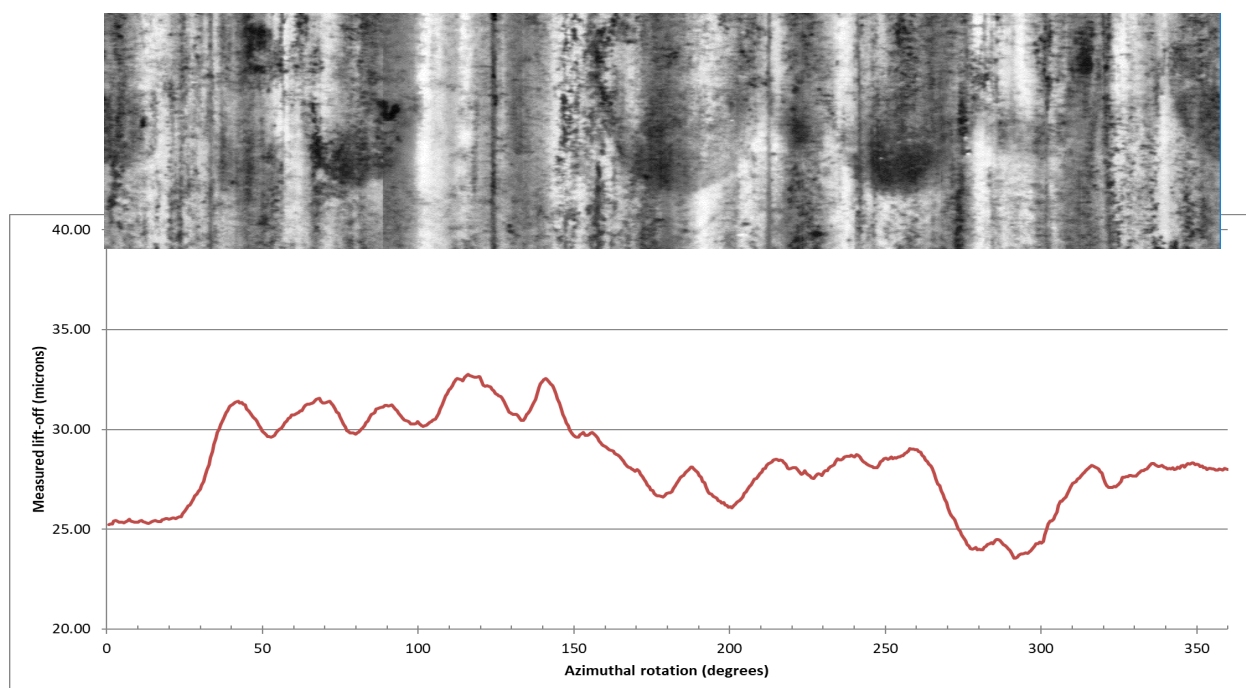


Figure C.46. Rotational eddy current lift-off scan of 6U3K09 at 3630 mm.

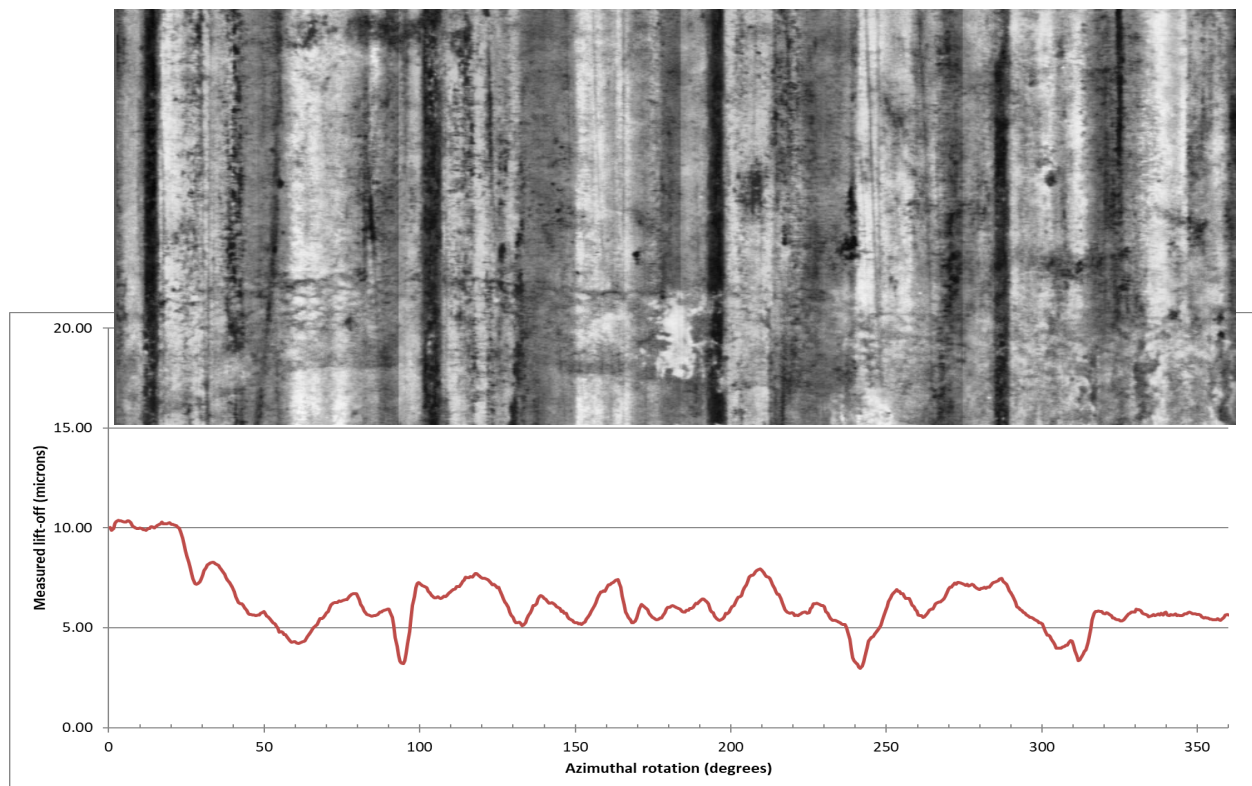
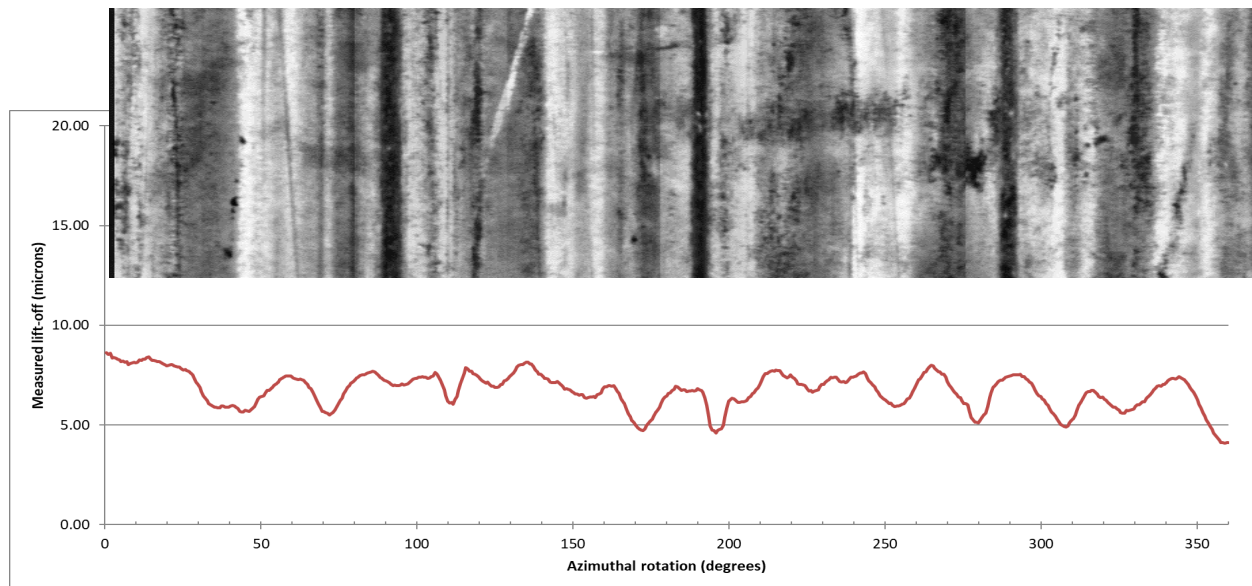


Figure C.47. Rotational Eddy Current Lift-Off Scans of 6U3K09 at 371 mm (Top) and 3537 mm (Bottom).

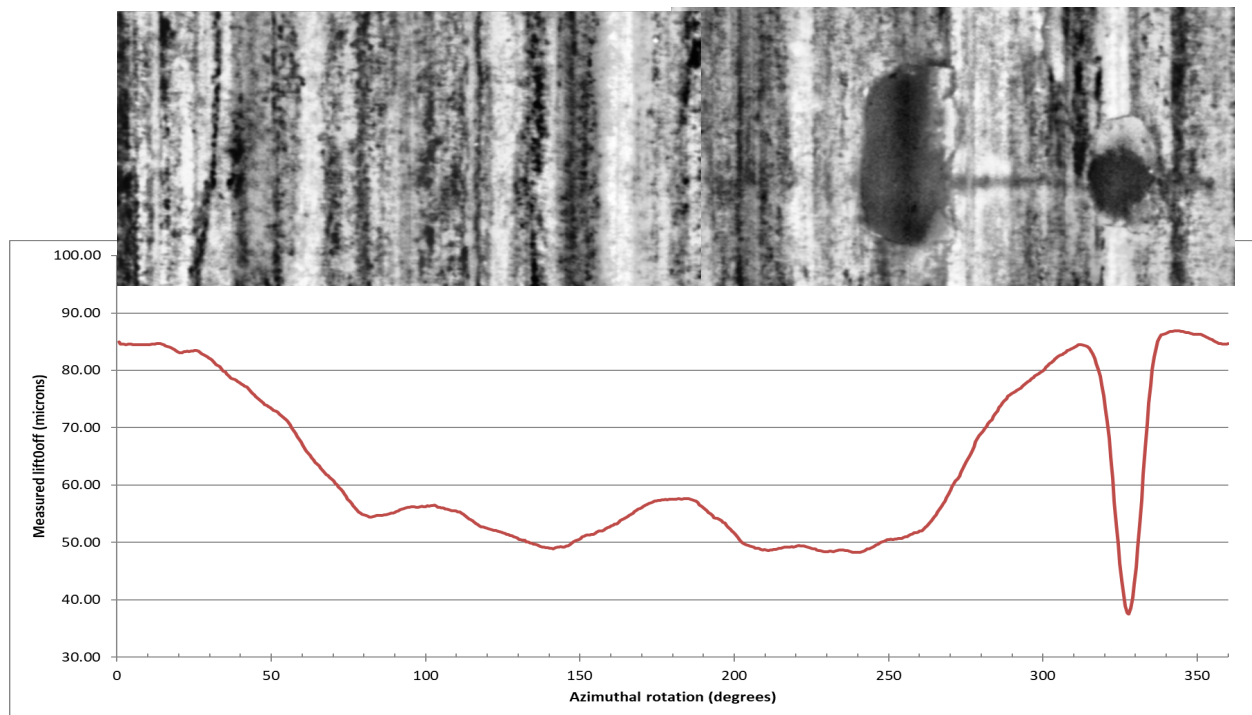


Figure C.48. Rotational eddy current lift-off scan of 3F9N05 at 3209 mm

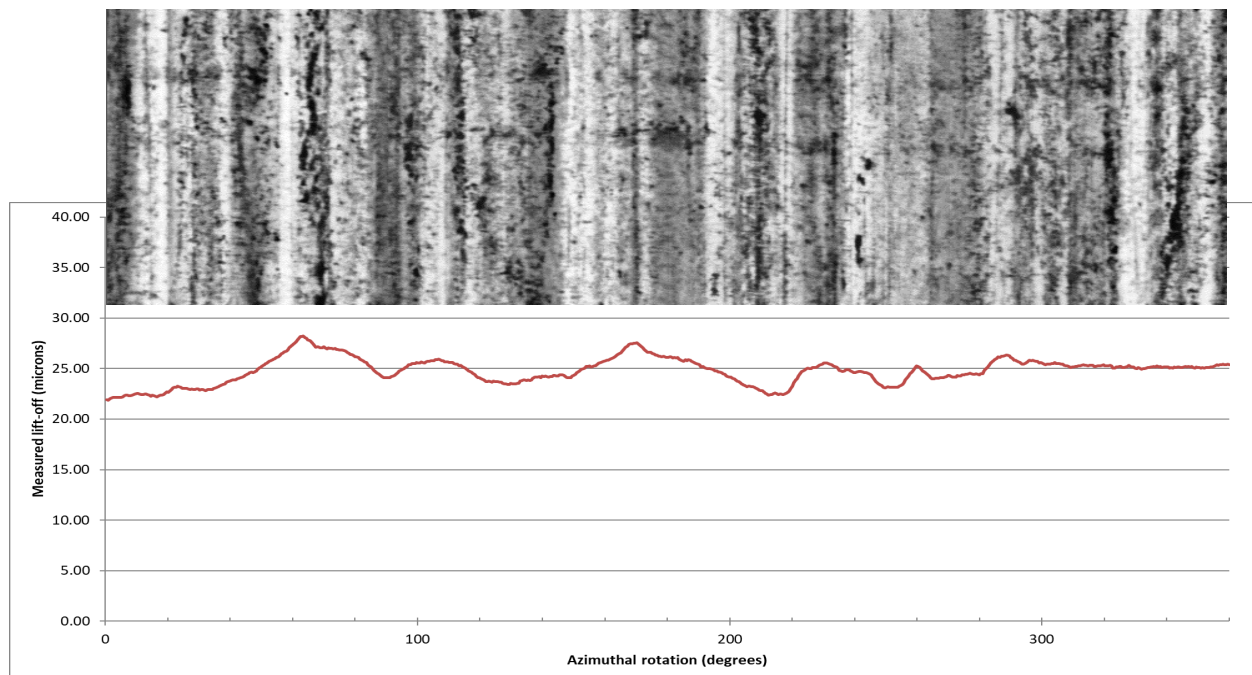


Figure C.49. Rotational eddy current lift-off measurement of 6U3I07 at 3432 mm.

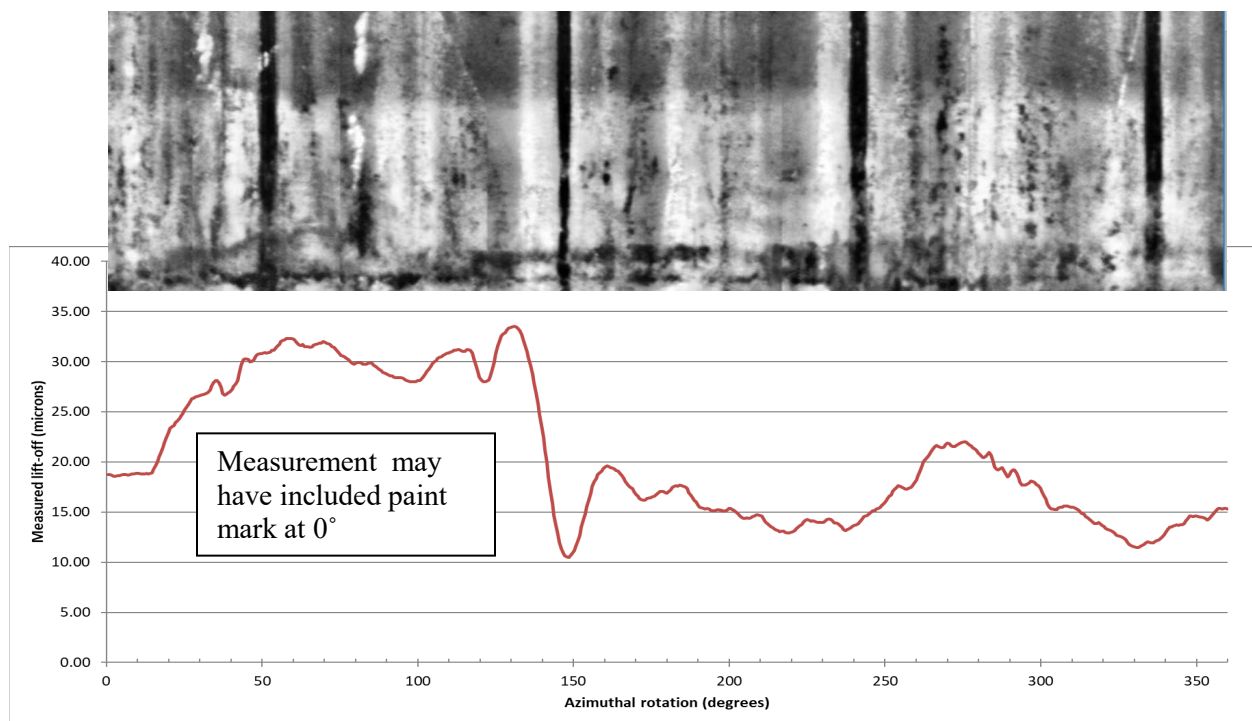


Figure C.50. Rotational eddy current lift-off measurements of 6U3I07 at 35 mm (lower end cap).

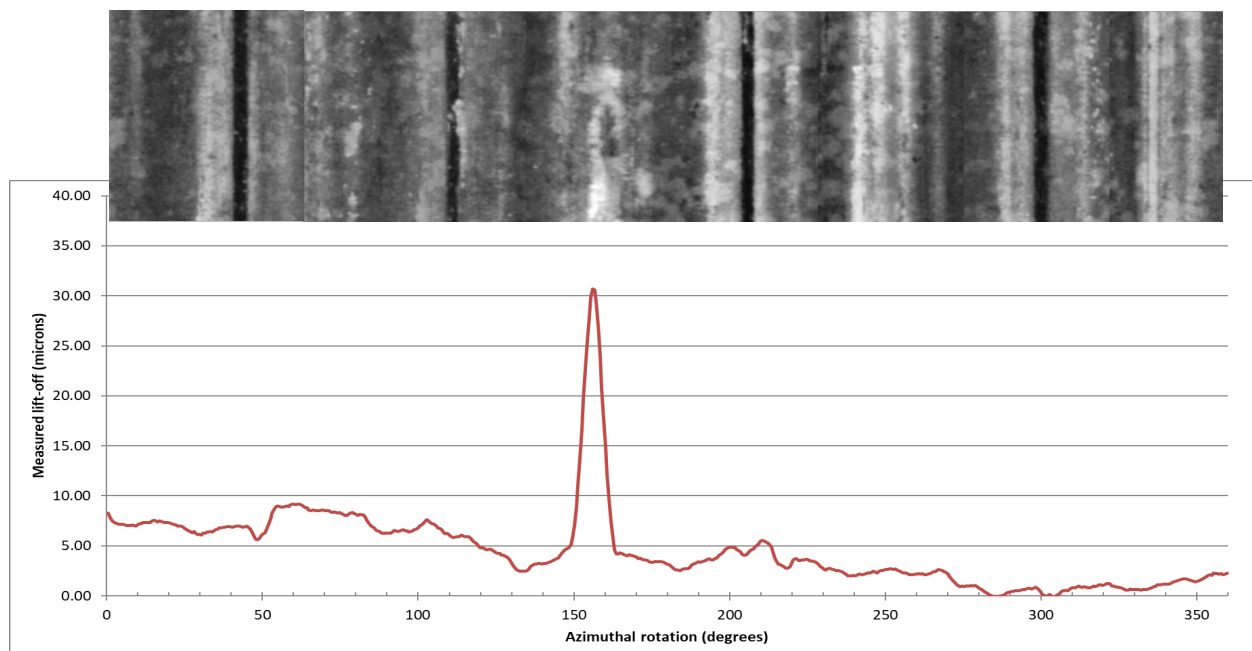


Figure C.51. Rotational eddy current lift-off measurements of 6U3I07 at 65 mm.

December 21, 2018

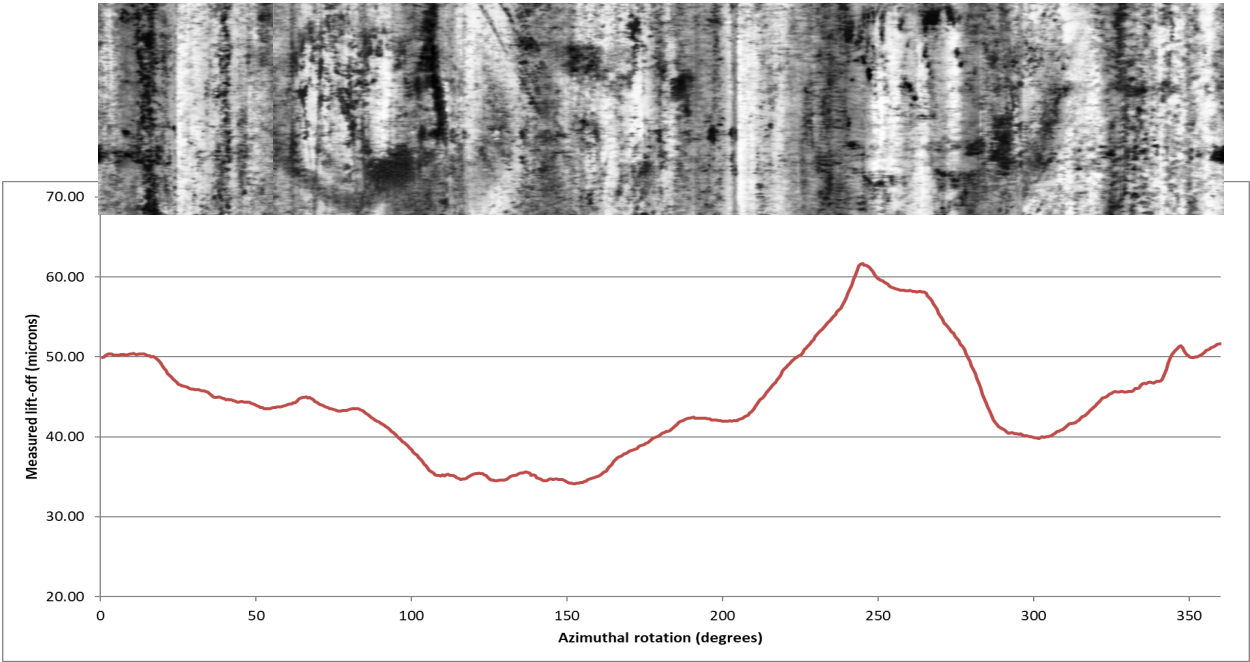
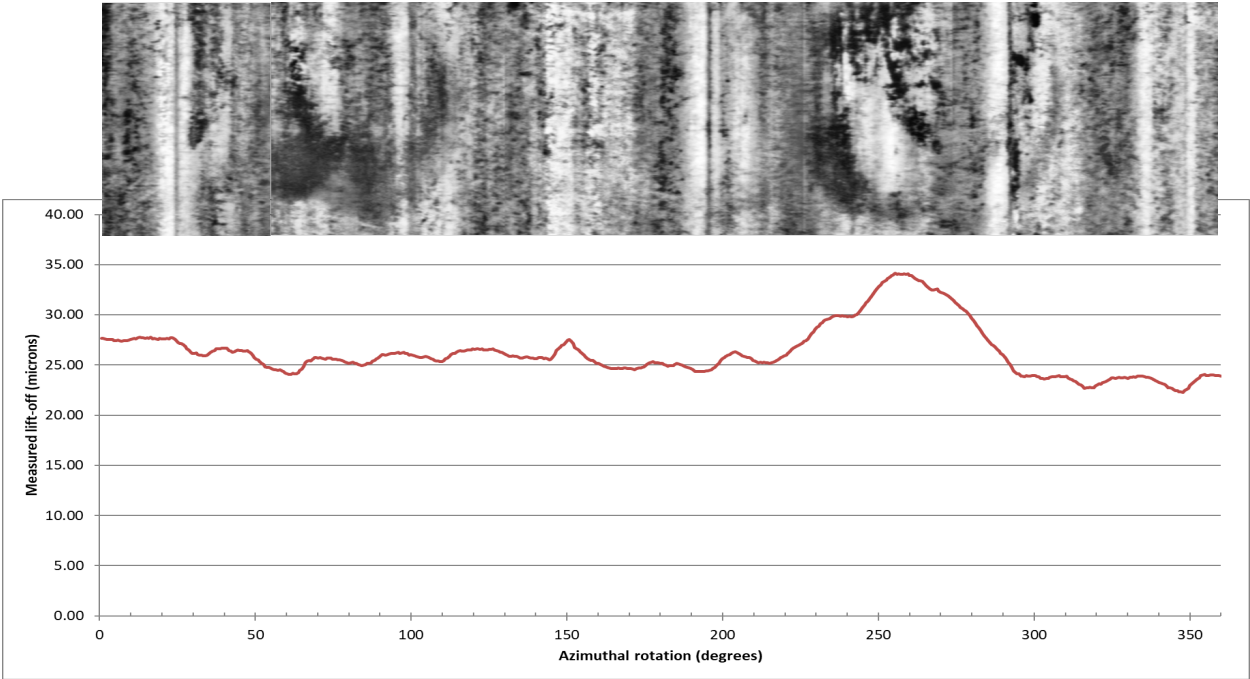


Figure C.52. Rotational Eddy Current Lift-Off Scans of 6U3L08 at 3659 mm (Top) and 3435 mm (Bottom).

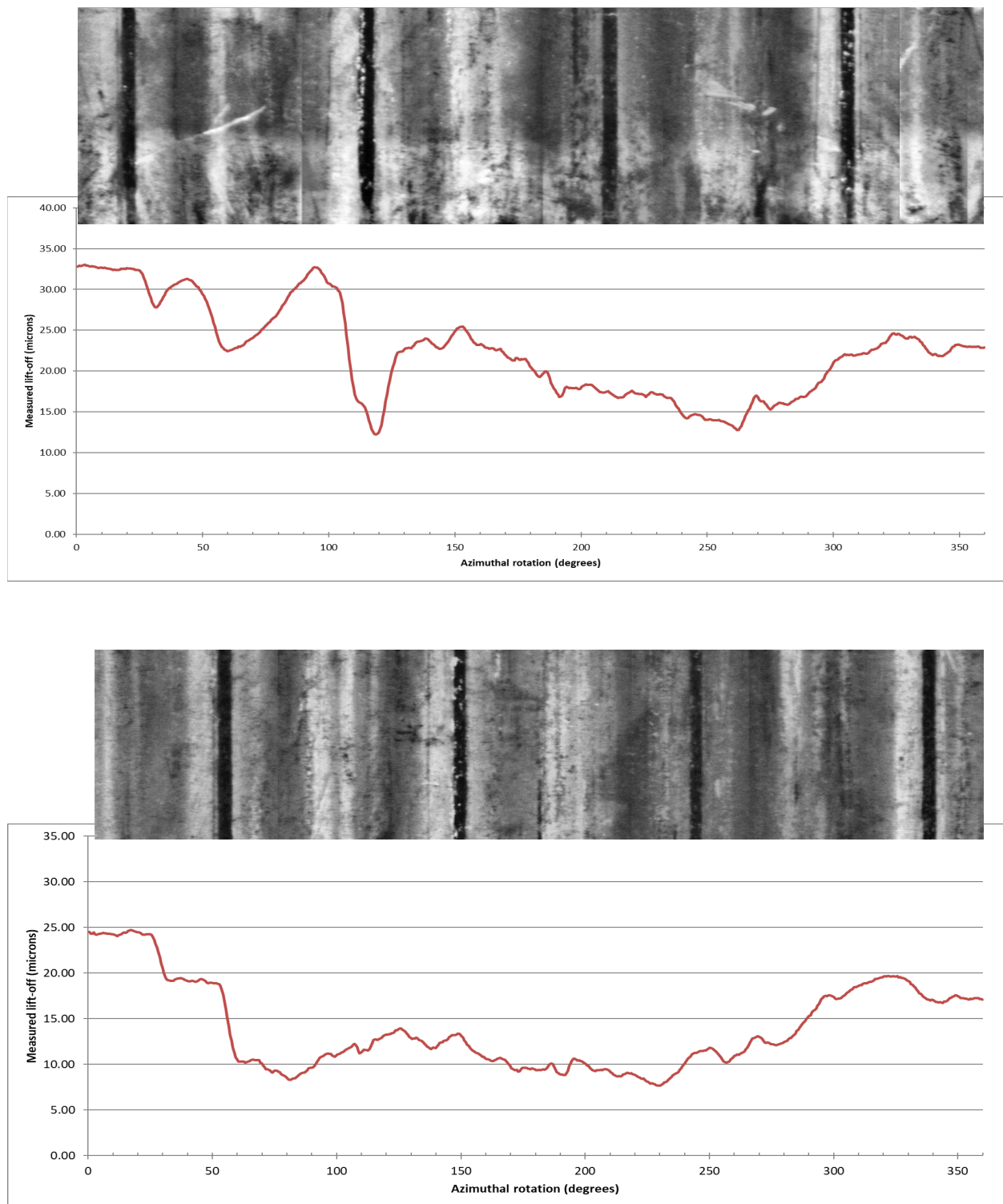


Figure C.53. Rotational Eddy Current Lift-Off Scans of 6U3L08 at 35 mm (Top) and 38 mm (Bottom).

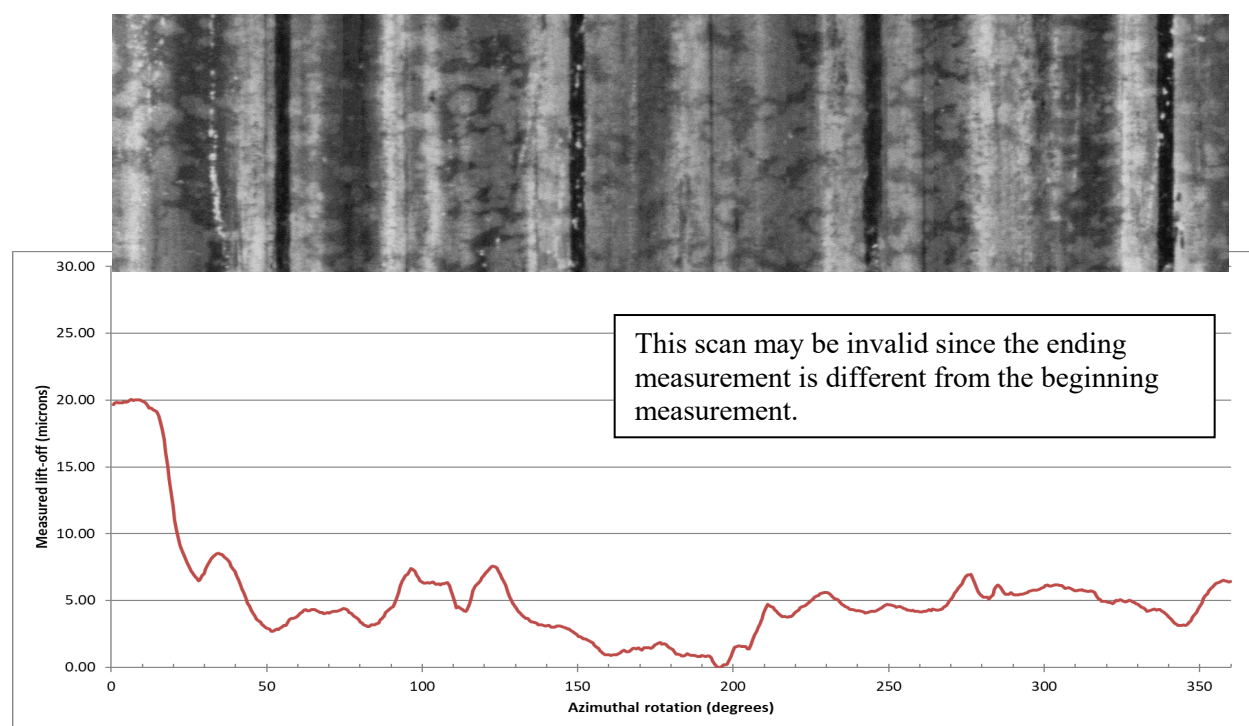


Figure C.54. Rotational eddy current lift-off scan of 6U3L08 at 55 mm.

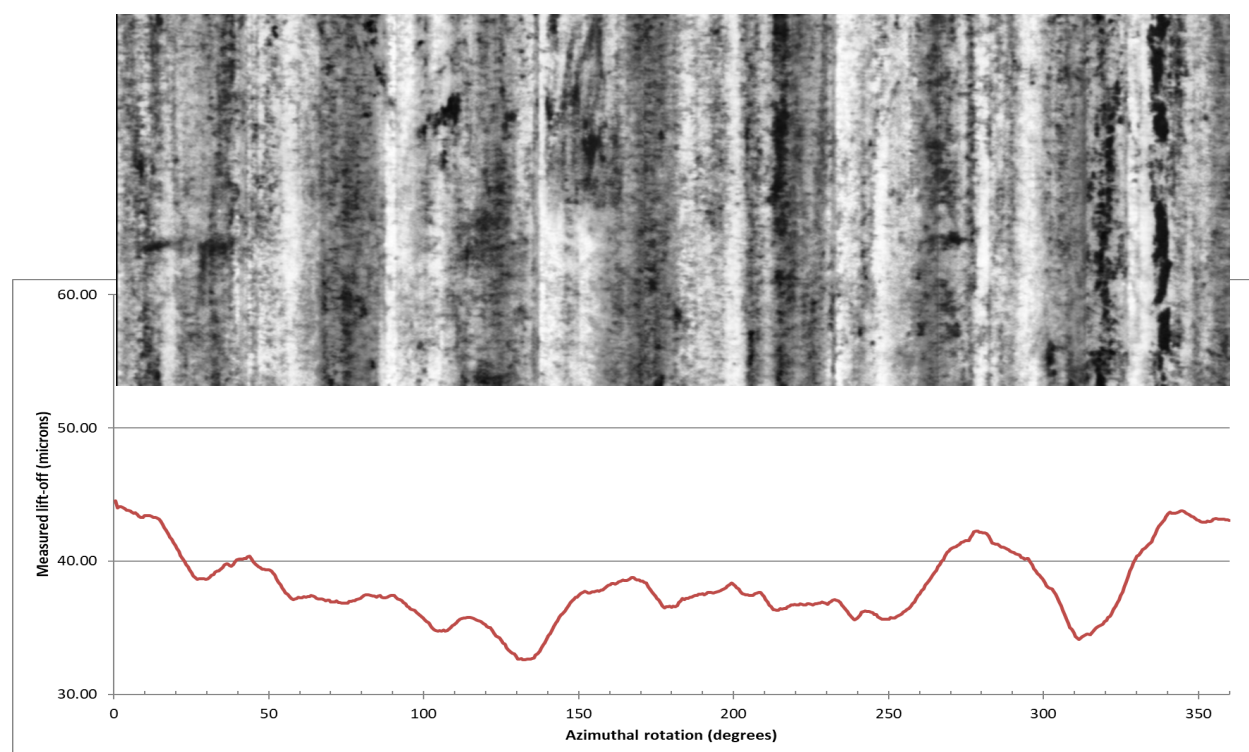


Figure C.55. Rotational Eddy Current Lift-Off Scans of 6U3L08 at 3,364 mm.

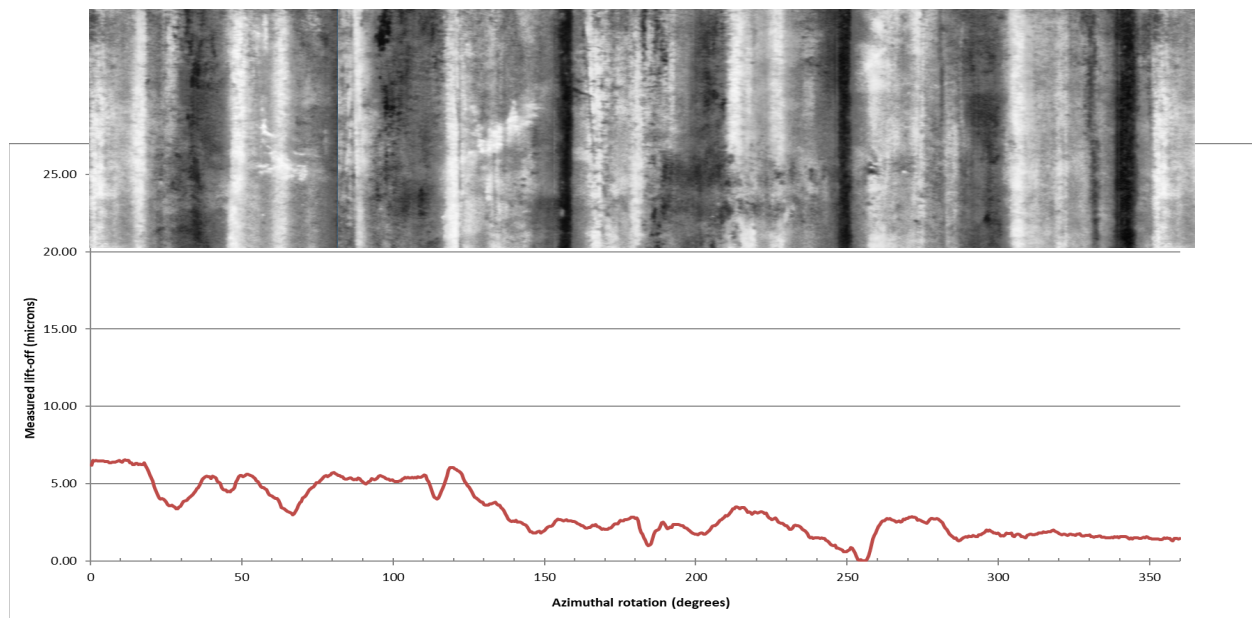
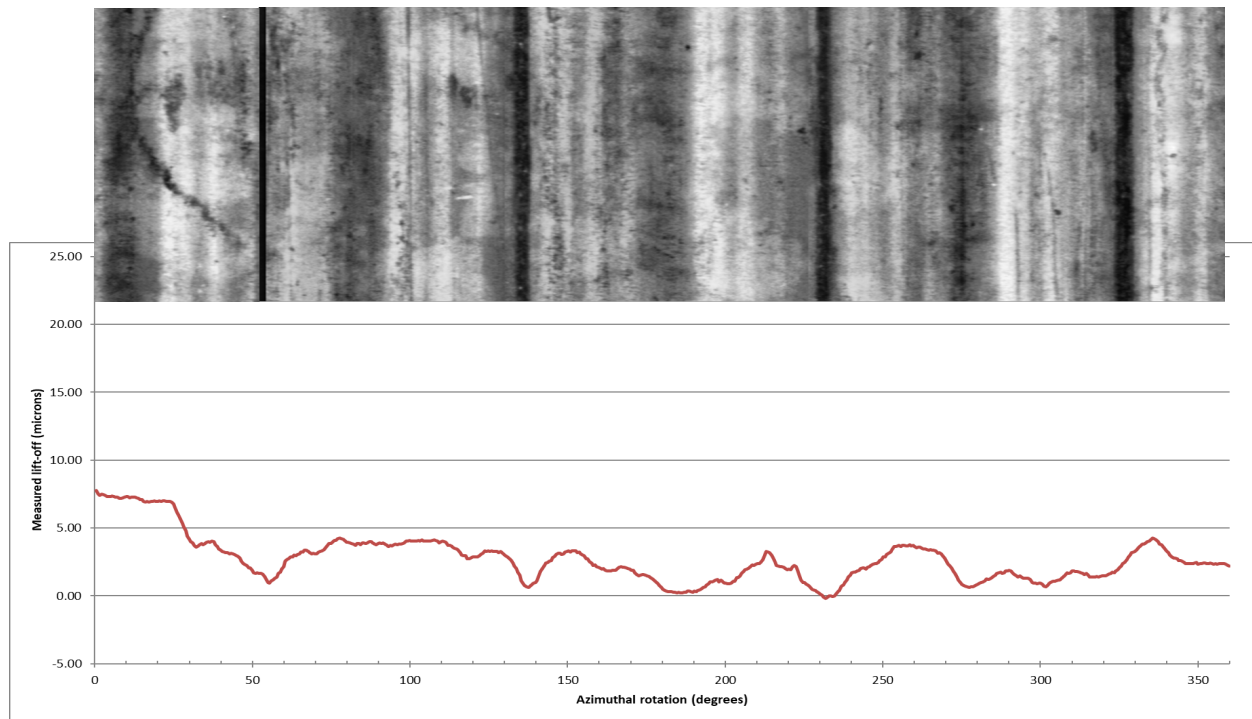


Figure C.56. Rotational Eddy Current Lift-Off Scans of 6U3P16 at 449 mm (Top) and 516 mm (Bottom).

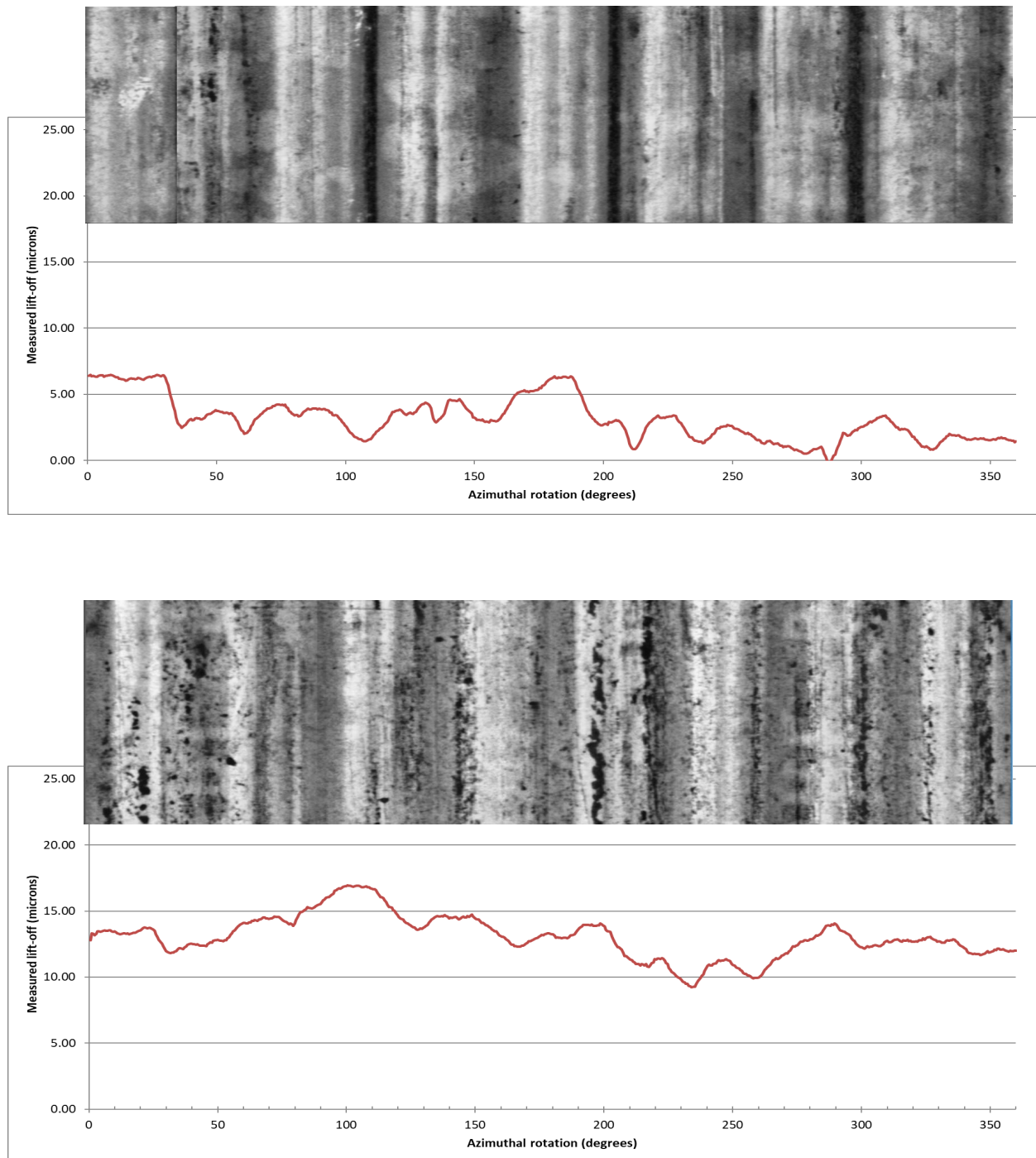


Figure C.57. Rotational Eddy Current Lift-Off Scans of 6U3P16 at 398 mm (Top) and 3835 mm (Bottom).

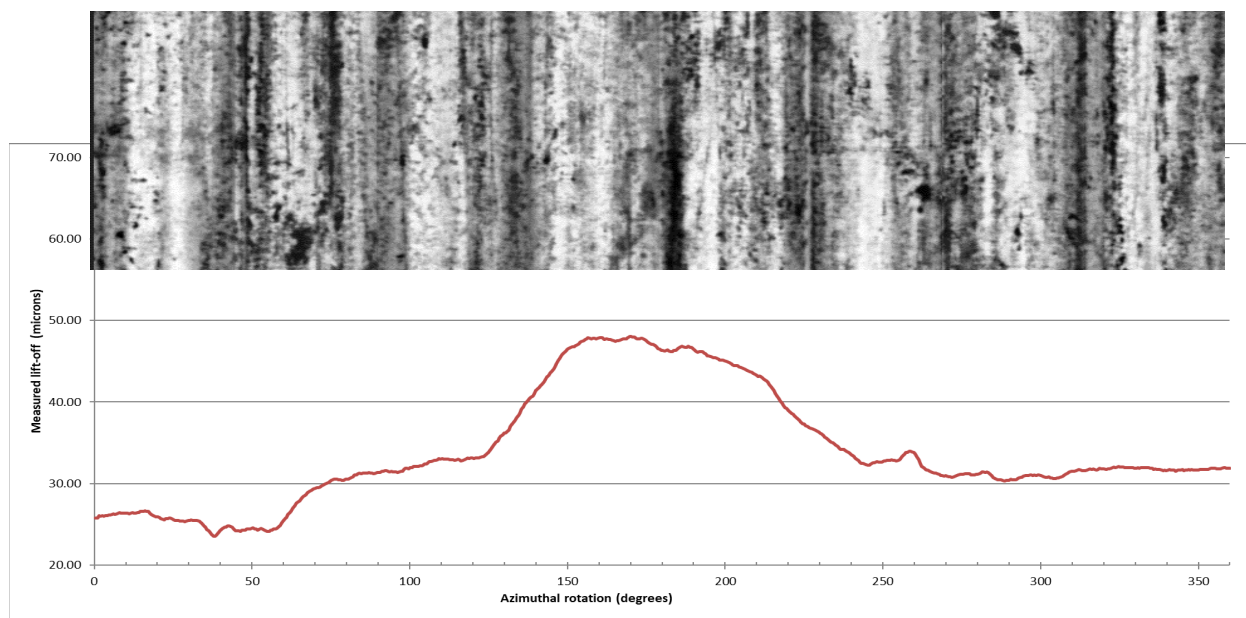


Figure C.58. Rotational eddy current lift-off scan of 6U3P16 at 3,434 mm.

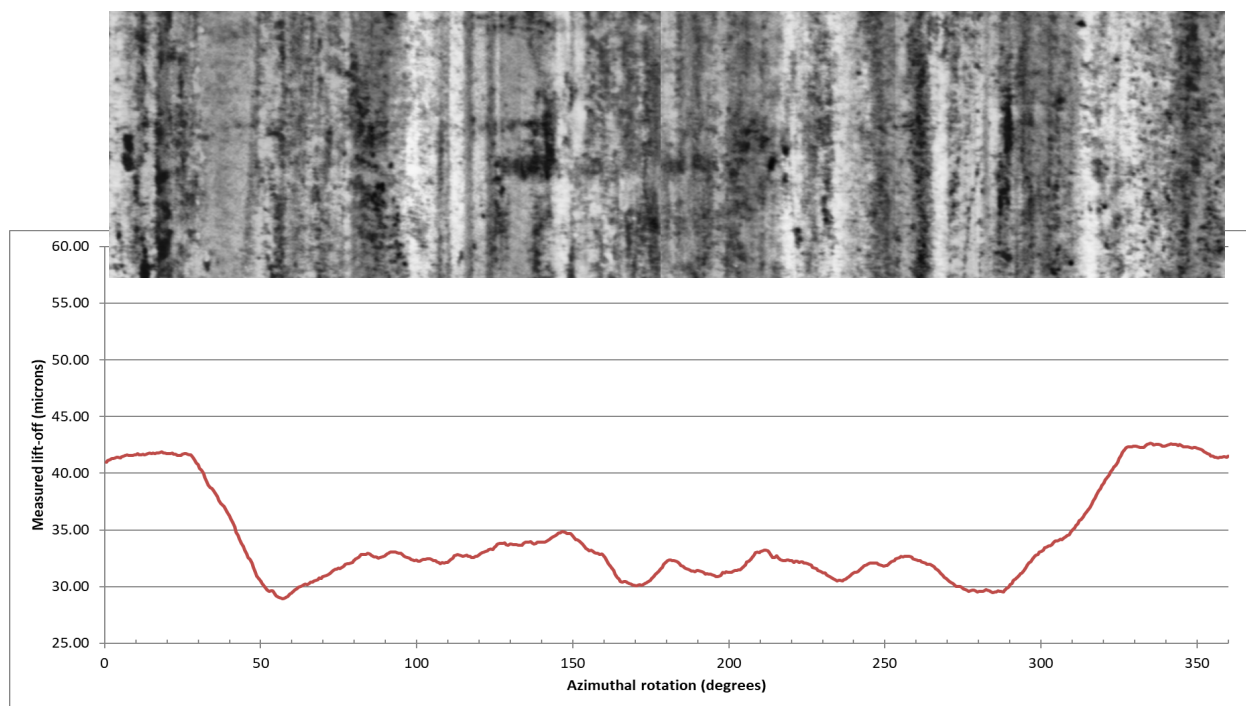


Figure C.59. Rotational eddy current lift-off scan of 3F9P02 at 3,201 mm.

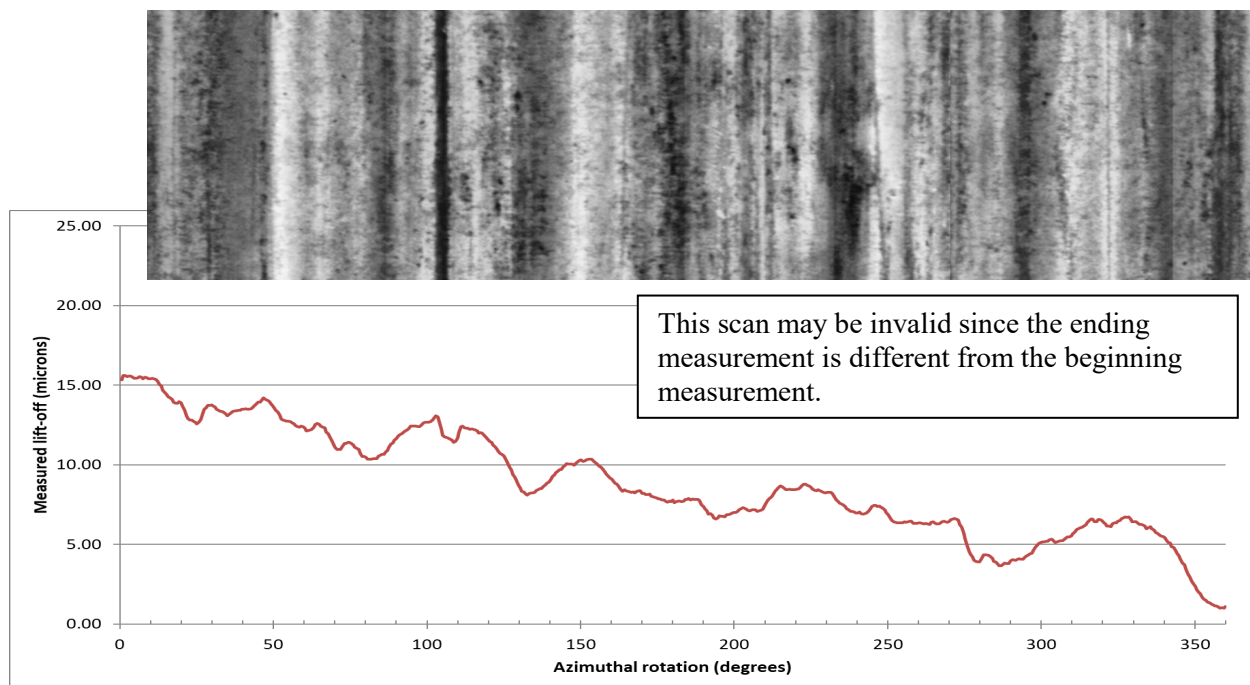
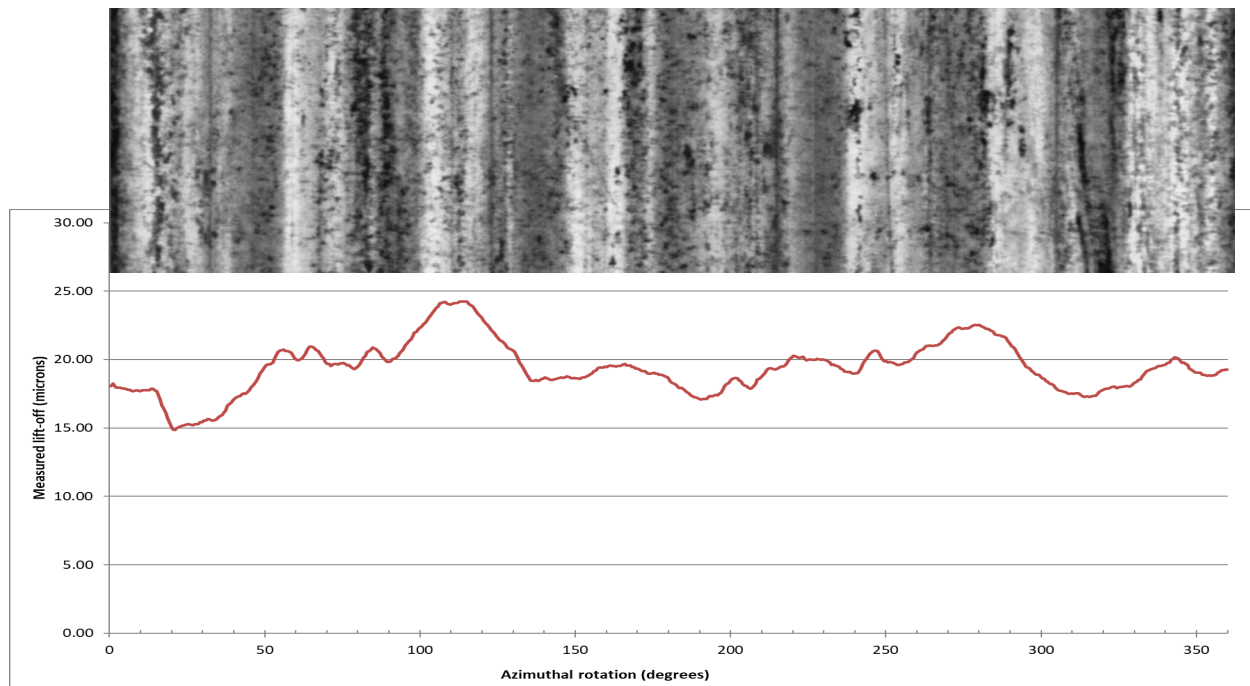


Figure C.60. Rotational Eddy Current Lift-Off Scans of 3F9P02 at 3664 mm (Top) and 2281 mm (Bottom).

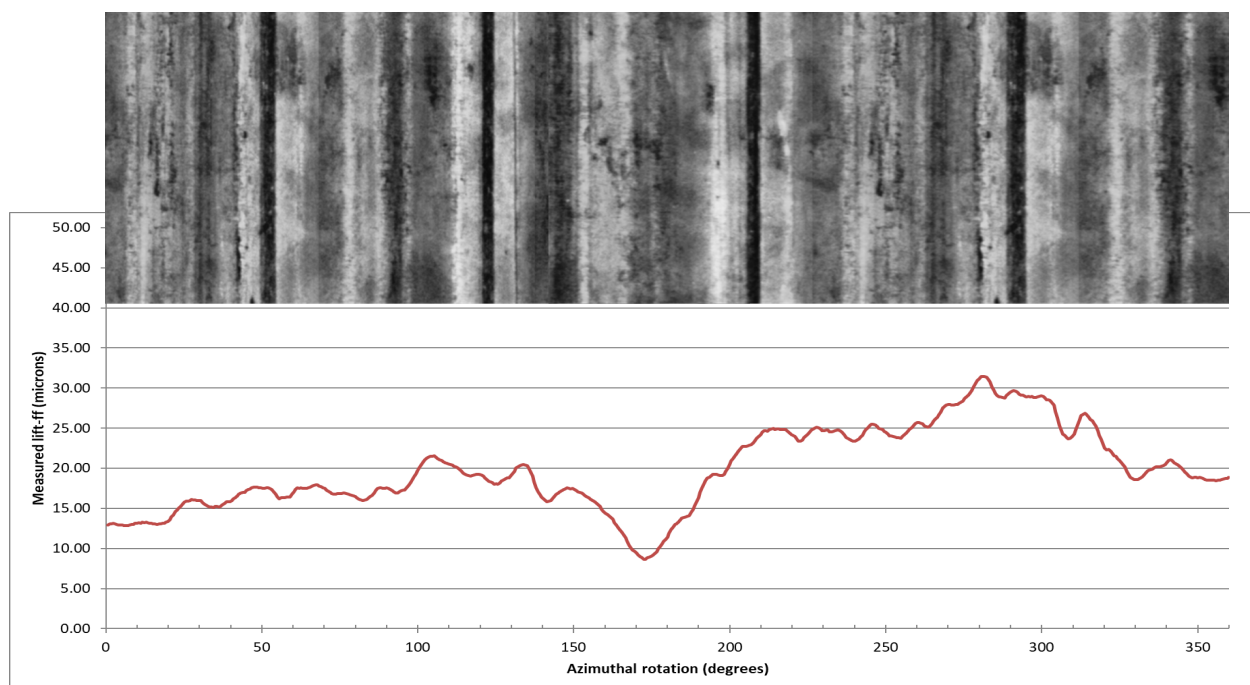
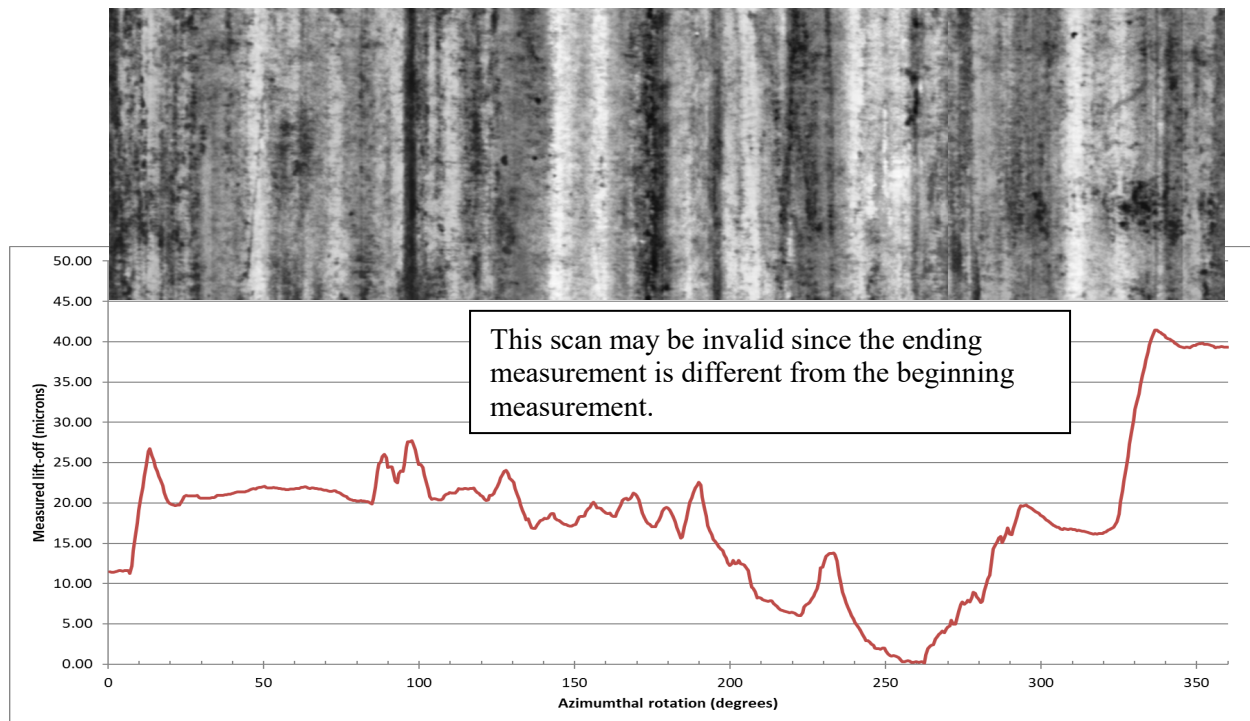


Figure C.61. Rotational Eddy Current Lift-Off Scans of 3F9P02 at 2116 mm (Top) and 307 mm (Bottom).

December 21, 2018

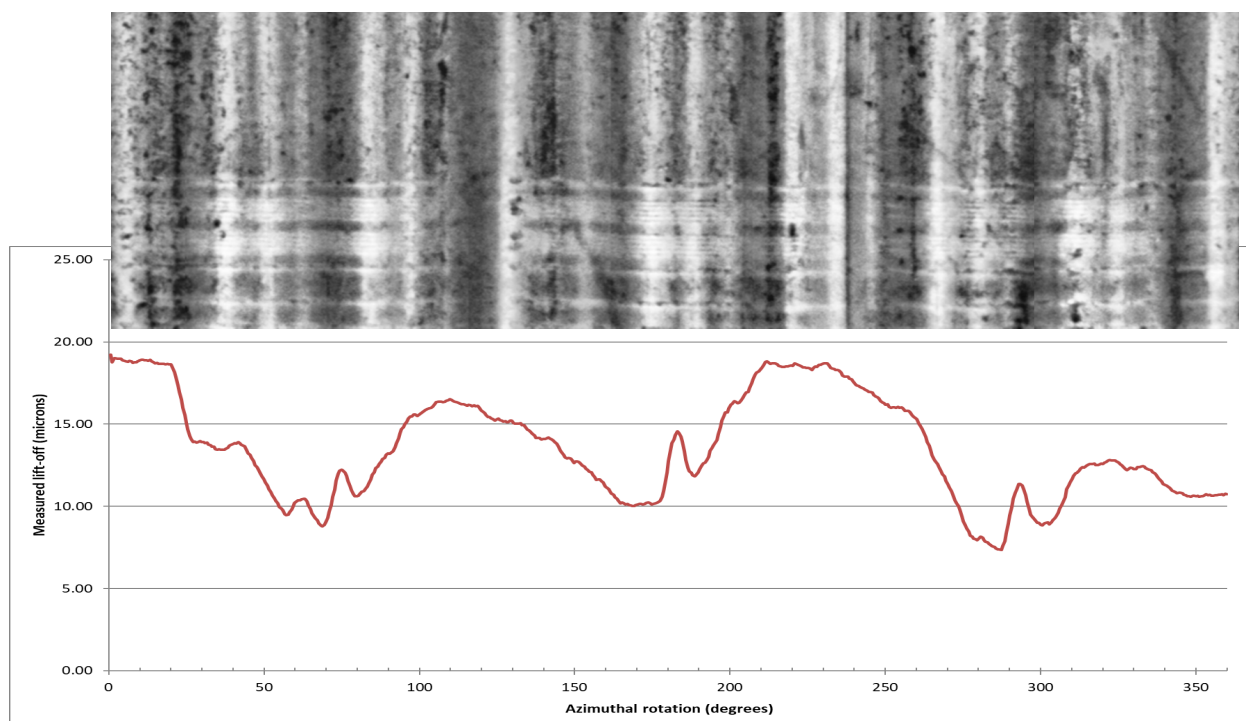


Figure C.62. Rotational eddy current lift-off scan of 3F9P02 at 3835 mm.

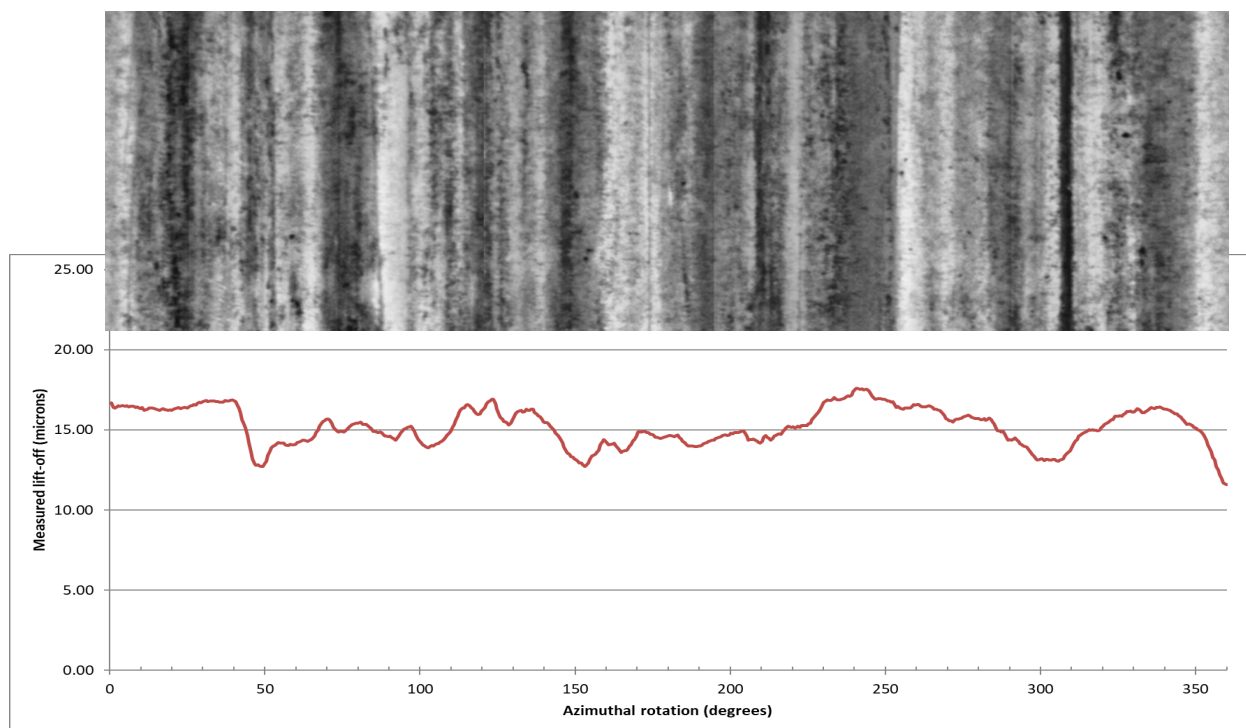


Figure C.63. Rotational Eddy Current Lift-Off Scans of 3F9P02 at 2281 mm (rescan).